Università degli studi di Messina

DIPARTIMENTO DI SCIENZE MATEMATICHE E INFORMATICHE, SCIENZE FISICHE E SCIENZE DELLA TERRA - MIFT
Dottorato di Ricerca in Fisica
PhD coordinator: Prof L. Torrisi

Wide-bandgap detectors for low-flux radiations and laser-generated plasma diagnostics

Tutor:
Prof.
L. TORRISI

PhD student:
A. CANNAVÓ

Cycle XXX
S.S.D. FIS 01
Academic Year 2016/2017

Acknowledgements

First of all I want to thank my tutor prof. Lorenzo Torrisi for his innumerable teachings, his availability, his attention and care to me. Work with him was a great opportunity for me and he helped me to understand the importance and beauty of this work, "the best work in the word" as he always tell us. Without his support and his continuing guidance, of course this thesis would not exist.

Special thanks also to Prof. Lucia Calcagno of the University of Catania and Dr. Antonella Sciuto of the CNR-IMM of Catania for their important suggestions, assistance and availability.

I would like to thank, for their practical support, all the technicians and assistants of the various laboratories, starting from Laboratori Nazionali del Sud of the INFN Institute of Catania, the CNR-IMM Insitute of Catania and the Department of Physics - MIFT of Messina, and in particular to Dr. Emanuele Morgana that help me in the optimization of the electronics and in the assembly work of the detectors.

Among the administrative staff of the University of Messina, I want to thank Dr. Paola Donato for her assistance in every circumstances, she gave me all the necessary support and encouragements during these years.

I can not forget to thanks my dear research team Nancy, Peppe Costa, Ceccio and Maria. With them I shared everything: anxiety and worry before any new experiment, the fatigue of working very often in unfavorable conditions, the carefree to spend happy moments out of the work ambit and the joy in achieving all the desired goals; for these reasons I am truly grateful to each of them.

Lastly, I would like to recall the loving presence of my family, Babbo, Mamma, Alby and Cri, who supported me with every means at their disposal, especially in the most difficult times of discomfort; they have been present in every special moment of my life and occupy the most important place in my heart: there are no rightful and complete words in the world to express my gratitude and my love for them.

Thanks to You that, through Your imperceptible touch and inscrutable support, You have been directing and bringing the invisible wires of my life.

Contents

Acknowledgements **i**

List of figures **v**

List of tables **xi**

List of symbols **xii**

Introduction **1**

1 Radiations detection **5**

1.1 Online radiations detectors 5

1.1.1 Ionization chamber 5

1.1.2 Scintillation detector 13

1.1.3 Photomultiplier 16

1.1.4 Semiconductor detector 21

1.2 Offline detection system 23

1.2.1 Photographic emulsion 24

1.2.2 Thermoluminescent Dosimeters TLD 25

1.2.3 Image Plates 27

1.2.4 Track-etch detectors 28

1.2.5 GAFchromic films 31

2 Semiconductor based detector **33**

2.1 Theory about Schottky junction 33

2.1.1 Schottky Barrier Height 33

2.1.2 Depletion Layer 37

2.1.3 Capacitance and Resistance in the depletion region 39

2.1.4 Schottky diode current 40

2.2 Silicon Carbide based detectors 42

2.2.1 Typical structure of a SiC Schottky barrier detector 43

2.2.2 SiC AZ 80 45

2.2.3 SiC AZ 25 46

2.2.4 SiC IAZ 4 46

2.2.5 Production of the silicon carbide detectors 47

2.3 Diamond detector 50

2.4 Gallium arsenide detector . . . 51

3 Application of detector in spectroscopic regime 53

3.1 Introduction . . . 53
3.2 Description of the electronic chain . . . 53
3.2.1 Preamplifier . . . 54
3.2.2 Spectroscopy linear amplifier . . . 56
3.2.3 Amptek MCA-8000D . . . 60
3.3 Detection of MeV α-particles . . . 61
3.3.1 Radioactive source . . . 61
3.3.2 Results with radioactive α-source . . . 62
3.3.3 Effects of Mylar absorbers . . . 63
3.3.4 Calibration process . . . 65
3.3.5 Effects of the detector bias voltage . . . 66
3.3.6 Energy resolution . . . 67
3.3.7 ΔE measurements . . . 69
3.4 Detection of sub-MeV He ions . . . 70
3.4.1 Ion Implanter . . . 70
3.4.2 Experimental results . . . 72
3.4.3 Variation of source energy and current . . . 75
3.4.4 Multilayer target . . . 76
3.4.5 Measurements with SiC IAZ 4 . . . 77
3.5 X-rays detection . . . 77
3.6 Characterization with β^- emitted from a radioactive source and electron gun . . . 81

4 SiC detectors for plasma-laser diagnostic 83

4.1 Introduction . . . 83
4.1.1 Plasma . . . 83
4.1.2 Non-equilibrium plasma generated by laser . . . 85
4.1.3 Backward Ion Acceleration, Target Normal Sheath Acceleration and Radiation Pressure Acceleration . . . 93
4.1.4 Estimation of radiations fluence . . . 94
4.2 Description of TOF technique . . . 96
4.2.1 Typical TOF spectra . . . 98
4.3 Comparison in the response of SiCs, Diamond and Silicon Detector . . . 103
4.4 Comparison with other plasma diagnostics . . . 105
4.4.1 Ion collector . . . 106
4.4.1.1 Analysis of a typical IC-TOF spectrum . . . 108
4.4.1.2 Comparison in the ion response between SiC and IC . . . 109
4.4.2 Ion Energy Analyser . . . 111
4.4.3 PVT Scintillator coupled to photomultiplier . . . 113
4.5 Use of SiC detectors in laser-plasma applications . . . 117
4.5.1 Laser Ion Source . . . 118
4.5.2 Fusion reaction . . . 122
4.5.3 Compact X-rays source . . . 125
4.5.3.1 Target influence . . . 126

4.5.3.2 Laser Parameters 128
4.5.4 Multi energetic ion implantation 130
4.6 Radiation hardness 137
4.6.1 Literature data 137
4.6.2 Plasma induced damage 140

Conclusion and future challenge **145**

Appendix **149**

A Common aspects of radiations detectors **150**

B Physics of semiconductor material **155**

C Density of states $N(E)$ **166**

Bibliography **168**

List of Figures

1.1 Variation of ion pair charge with applied voltage. . . . 7
1.2 Behaviour of potential 7
1.3 (a) Electrical circuit representation of a ionzation chamber; behaviour of the current (b) and of the voltage (b) as a function of the time. . . . 8
1.4 Multiplication factor, M, as a function of applied voltage for argon at pressures of 10 and 40 cm Hg, radius of center wire $a = 0.013\,\text{cm}$, radius of outer electrode $b = 1.105\,\text{cm}$. . . . 10
1.5 Schematic of a MWPC and distribution of the electric field lines around wire [20]. . . . 11
1.6 Track reconstruction through a multi-layer MWPC. . . . 11
1.7 Principle of operation of a drift chamber. . . . 12
1.8 Scheme of a TPC (a) and reconstruction of a particle trajectory (b). . . . 13
1.9 Scheme of a scintillators detector with a coupled photomultiplier. . . . 13
1.10 Energy levels in organic scintillators. . . . 14
1.11 Energy levels for inorganic scintillators 16
1.12 Scheme of a photomultiplier. . . . 17
1.13 Secondary emission ratio from Ref. [38]. . . . 18
1.14 Scheme of a voltage divider. . . . 19
1.15 Different typologies of dynode section from Ref. [38]. . . . 20
1.16 Schematic representation of a typical p-n junction. . . . 23
1.17 Processing a Photographic emulsion. . . . 24
1.18 Formation of an electron-hole pair (a), and illustration of the two possible modes of recombination (b). . . . 26
1.19 Thermoluminescent response as a function of absorbed dose in air for different X-rays radiations. . . . 26
1.20 Glow curve at a dose of 14.6 mGy for LiF:Mg,Cu,P 27
1.21 Typical readout system. . . . 28
1.22 Relative ionization rate as a function of the energy per nucleon or velocity. 29
1.23 On the top molecular structure model for the monomer of CR-39, while in the bottom an example of calibration curve, from Ref. [34], obtained from irradiations of ^{12}C (in the inset some typical etched tracks). . . . 30
1.24 (a) typical microscope images of 1 MeV proton tracks on CR-39; (b) proton track diameter as a function of incident mean energy for CR-39 etched for 6h in an 80°C solution of 6 N NaOH. . . . 30
1.25 Proton track diameter as a function of incident mean energy for various etch time (a) and etchant temperature (b). . . . 31
1.26 Structure of a GAFChromic EBT3 film. . . . 31
1.27 Calibration curve for EBT (a) and EBT3 (b) films. . . . 32

2.1 Representation of the band structure near the metal-semiconductor junction. 34
2.2 Deduction of the Schottky-Mott model. 34
2.3 Behaviour of charge density (a) , electric field (b), potential (c) and energy (d) across the junction. 37
2.4 Depletion layer thickness as a function of the reverse bias voltage. 38
2.5 Estimates of resistance and capacitance as a function of the reverse bias voltage. 39
2.6 Current density at room temperature (a) and comparison between current densities of 4H-SiC and Silicon at different temperatures (b). 41
2.7 Ionization energy and bandgap for various semiconductor detector. 42
2.8 Simplified structure of a silicon carbide detector. 43
2.9 Simulation of the Bragg peak for proton of 150 keV and 850 keV, respectively into a silicon carbide detector. 44
2.10 (a) Schematic of the geometry for the SiC AZ 80 diode, (b) picture of the device, (c) I-V curve characterization and (d) simulated efficiency curves for photons and protons. 45
2.11 (a) Schematic of the geometry for the SiC AZ 25 diode, (b) picture of the device, (c) I-V curve characterization and (d) simulated efficiency curves for photons and protons. 46
2.12 (a) Schematic of the geometry for the SiC IAZ 4 diode, (b) picture of the device, (c) I-V curve characterization and (d) simulated efficiency curves for photons and protons. 47
2.13 Intrinsic doping concentration versus the C/Si ratio, [17]. 48
2.14 Schematic structure of a typical SiC Schottky diode. 50
2.15 (a) Schematic of the geometry for the SiC IAZ4 diode, (b) picture of the device, (c) I-V curve characterization and (d) simulated efficiency curves for photons and protons. 51
2.16 Current-Voltage characteristics of Ryc's device presented in Ref.[108] . . . 52
2.17 Spectra of ^{241}Am radioisotope acquired at 295 K and 265 K. 52

3.1 Electronic chain used in spectroscopic regime. 54
3.2 Simplified block diagram of the circuitry in ORTEC 142 series. 55
3.3 CR-RC pulse shaping for unipolar output. 57
3.4 Doubly-Differentiated CR-RC-CR Shaping for bipolar output. 57
3.5 Pole-Zero cancellation network. 58
3.6 The diagram of the baseline restorer. 59
3.7 Schematic of the Pile-Up Rejector. 59
3.8 Unpiled-Up Amplifier Output Rate as a Function of the Input Rate for different values of shaping time constants. 60
3.9 Decay scheme and branching ratios of the multi-peaks alpha source. . . . 62
3.10 Photo of the vacuum chamber. 62
3.11 The four α spectra acquired with: a) traditional Silicon Surface Barrier Detector; (b Silicon Carbide detector AZ 25; c) Silicon Carbide AZ 80; (d Diamond detector. 63
3.12 a) Simulated transmitted energy of 15000 α-particles after 12 μm Mylar absorber; α spectra acquired with: b) traditional Silicon Surface Barrier Detector, (c Silicon Carbide detector AZ 80 and (d Diamond detector using 12, 18 μm Mylar absorbers. 64

3.13 Detection of α-particles emitted by a single peak Am source through Silicon (a) and SiC AZ 80 (b) detector at different bias voltage. 66
3.14 Ion range of 5.46 MeV α particles in SiC and detection of α-particles emitted by the three peak α-source through SiC AZ 80 (b), SiC AZ 25 (c) and Diamond (d) detector at different bias voltage. 67
3.15 Energy resolution for Silicon, SiC AZ 25, SiC AZ 80 and Diamond detector in the energy range between 200 keV and 6 MeV, compared with literature results of Ref. [109]. 68
3.16 Response of the SiC IAZ 4 to a single peak α-source (^{241}Am), changing the bias voltage and using a Mylar Absorber (12 μm thick). 69
3.17 Profile of the depletion layer at 0 V and (a) and -5 V (b). 70
3.18 Structure of the Ion Implanter in the Department of Physics of the University of Catania with photos of the Chamber ion source, of the electromagnetic deflecting system and of the End station. 71
3.19 Rutherford Backscattering Spectrometry. 72
3.20 Silicon a), c) and SiC IAZ25 b), d) spectra detecting Helium beam backscattered by Silicon, Au on Silicon, Ag on Silicon and Cu on Silicon target. . . 73
3.21 SiC spectra obtained by changing the source conditions in terms of ions energy and current. 75
3.22 Silicon (left) and SiC (right) spectra obtained irradiating a multilayer target. 76
3.23 Response of SiC IAZ 4 to He ions backscatterd from the Si + Au target a) and the multilayer target b). 77
3.24 a) Tabulated spectra given by Amptek site; b) measured yield as a function of current and voltage of tube; experimental spectra obtained by changing voltage c) and current d) of tube. 78
3.25 Response of M-SiC and I-SiC detectors to an x-ray source at 40 kV. 79
3.26 On the top spectra of ^{241}Am acquired at +27° and +100°C [12]; on the bottom energy resolution for two SiC detectors as a function of energy [48]. 80
3.27 SiC reverse current monitored as a function of the dose rate for exposition to a 20 kV X-ray tube and to 1.3 MeV γ-rays from the 60Co source. 81
3.28 Characteristics of the ^{90}Sr-^{90}Y β-source. 82
3.29 a) spectrum obtained from the ^{90}Sr-^{90}Y source or detecting electrons coming from an electron gun system b). 82

4.1 Ionization parameter as a function of the plasma temperature. 84
4.2 CCD image of a Cu plasma generated by a Nd:YAG laser. 85
4.3 Ablation yield as a functioon of the laser fluence [102]. 86
4.4 Description of the ponderomotive force. 87
4.5 Typical temperature, density and expansion velocity profiles of a plasma generated by irradiation of a solid target by a nanosecond laser pulse focused on target at an irradiance of 10^{14}W/cm^2 [64]. 88
4.6 Cross section dependence on the ratio between electron energy and ionization energy 90
4.7 Calculated cross section for C ions. 90
4.8 Maximum proton energy plotted as a function of $I\lambda^2$, experimental. . . . 92
4.9 Comparison between the two acceleration techniques, the Backward Ion Acceleration (BIA) and Target Normal Sheath Acceleration TNSA. . . . 93

4.10 Ablation Yield as a function of the laser pulse energy for different target, from Ref. [99]. 94
4.11 Crater profile for different target obtained at low intensity and high intensity laser, a) and b) respectively. 95
4.12 General scheme for time of flight technique. 97
4.13 TOF spectrum obtained irradiating a Carbon based target at low a) or high b) laser intensity. 99
4.14 Possible Fit of the experimental data using CBS function. 101
4.15 Detailed view of photopeak and possible deconvolution of hot and cold electrons. 102
4.16 Yields of the ion production as a function of the charge state. 102
4.17 Experimental set up at IPPLM laboratory and diagnostic equipment. . . . 103
4.18 TOF spectra acquired with Silicon detector a), SiC AZ 25 b), SiC AZ 80 c), Diamond detector d) using a large (left) and short (right) time scale. . 104
4.19 Operating principle of an Ion Collector. 106
4.20 Emission yield of secondary electron as a function of proton energy (left) or electron (right) for different materials. 107
4.21 Possible schemes of an Ion collector consisting in: 1 collector - 2 entrance grid - 3 control grid - 4 grounded housing - R_{load} load resistance - U bias potential. 107
4.22 Typical IC spectrum a) and possible deconvolution of ions using CBS distribution. 109
4.23 SiC a) and IC b) TOF spectra acquired at the same experimental conditions.110
4.24 Scheme of a Ion Energy Analyser. 111
4.25 Typical IEA spectrum. 112
4.26 Ion energy distribution obtained from IEA measurements and deconvolution performed with CBS distribution. 112
4.27 a) chemical formula for PVT, b) PVT plastic scintillator and c) PVT luminescence efficiency as a function of the particle energy for different ion beams. 114
4.28 Luminescence yield as a function of the the 24 and 62 MeV proton stopping power [80]. 115
4.29 (a) Geometric characteristics of the unit expressed in mm, (b) the anode radiant sensitivity as a function of the wavelength and PMT gain (c). . . . 115
4.30 Experimental PVT spectrum a) and deconvolution of the three peaks α-source. 116
4.31 TOF spectra obtained with thick PVT and irradiating PE, Al, Cu and Ta target a) and angular distribution of the emitted particles b). 117
4.32 SiC-TOF spectra acquired at CELIA facility in forward direction irradiating Carbon and Nickel based targets. 119
4.33 SiC-TOF spectra acquired at CELIA facility in forward direction irradiating Au target. 120
4.34 SiC-TOF spectra acquired at IPPLM laboratory in forward direction irradiating Al target. 121
4.35 Cross-section as a function of the projectile energy for deutons, tritium, helium-3, and protons (a) and the corresponding reaction rate vs. the plasma temperature. 122

4.36 Experimental set up at PALS laboratories and in the inset view from the SiC detector in forward direction at 30° angle. 123
4.37 SiC TOF spectrum in forward direction. 123
4.38 SiC TOF spectrum in forward direction. 124
4.39 Typical photopeak obtained irradiating bulk material at low laser intensity (Nd:YAG at UniME). 125
4.40 Dependence of X-rays emission on the atomic number of the target. 126
4.41 Dependence of X-rays emission on the thickness of the target. 127
4.42 Angular distribution of X-rays emission. 127
4.43 Dependence of X-rays emission on the laser energy. 128
4.44 Dependence of X-rays emission on focal position of the laser. 129
4.45 Dependence of X-rays emission on the laser pulse duration. 129
4.46 Schematic of the extraction chamber a), the acceleration region b) and experimental set up using a IEA c). 130
4.47 Ti ions energy distribution obtained with IEA at +30 kV of post acceleration a) and typical RBS spectra of the implanted target. 131
4.48 TOF spectra of plasma ions acquired at $V_{P.A.} = 0, 10, 20$ kV and at a fixed bias of detector $V_{BIAS} = -25$ V. 132
4.49 TOF spectra of plasma ions acquired at a post-acceleration voltage of 0 kV (a), 10 kV (b), 30 kV (c), for different values of detector bias and yield of TOF spectra of plasma ions as a function of detector bias for different values of post-acceleration voltage (d). 133
4.50 Yield of TOF spectra of Al ions as a function of acceleration voltage for different values of detector bias for the damaged detector of the first campaign a) and for the new SIC IAZ 4 detector of the second campaign b). 134
4.51 Yield of ions (a) and electron (b) as a function of acceleration voltage for PVT + PMT system. 135
4.52 Typical TOF spectrum obtained with SiC AZ 25 irradiating Carbon Glass a) and Aluminum b) target at different voltage of post acceleration. 136
4.53 a) Yield of Aluminum ions as a function of the post acceleration voltage at a fixed values of detector bias voltage; b) yield of Aluminum ions as a function of the post acceleration voltage at a fixed value of detector bias voltage. 136
4.54 Yield of proton (a) and Carbon (b) ions as a function of the bias voltage of the detector for fixed values of post acceleration 137
4.55 DLTS spectra of 4H-SiC irradiated with 1.0 MeV Si^+ (a) and 7.0 MeV C^+ (b), [41, 61]. 138
4.56 Intensity of the main levels detected in the DLTS spectra (a) and leakage current (b) at -100 V as a function of ion fluence, [41]. 139
4.57 Intensity of the main levels detected in the DLTS spectra (a) and leakage current (b) at -100 V as a function of ion fluence. 140
4.58 Optical microscope photos of the SiC AZ 80 surfaces exposed to plasma at PALS about 400 times (a), 300 times (b), 150 times (c) and 20 times (d) and of the SiC IAZ 4 surface before exposition to plasma at UniME (a') and after 50 shots (b'). 142
4.59 Procedure for the identification of size distribution of cluster. 142
4.60 SEM photos of typical debris deposited on the SiC surface with a dimension of tens microns (a) and of about 1 micron (b). 143

4.61 Photos of TENCOR profilometer a) and scan of a damaged detector surface. 143
4.62 Thee peaks alpha spectra detected with a SiC with an exposed active surface of 100% (a), 53.18% (b) and 24.84% (c) and peak yield (counts at the peak) vs. exposed area (d). 144
4.63 Logo of the SiCILIA project and prototype of an ion detection wall in SiC. 145
4.64 Prototypes of Schotthy and p-n diode for the realization of ΔE and stop detector. 146
4.65 First attempt to realize a pixel detector, from Ref. [28]. 149

A.1 Comparison between three types of X-Rays detector for the Silver K spectra (a). Definition of energy resolution (b). 151
A.2 Equivalent circuit connected to the detector. 152
A.3 (a) Hypothetical current pulse output. Signal voltage on the external circuit when $RC \ll t_c$ (b) panel or when $RC \gg t_c$ (c) panel. 153
A.4 Solid angle subtended by detector. 154

B.1 The splitting of a degenerate state into a band of allowed energies a) and formation of energy bands for a silicon crystal. 156
B.2 Energy band structure for silicon a) and for gallium arsenide b), examples of indirect and direct semiconductor material, respectively 157
B.3 Determination of carrier density in the conduction and valence band, [105]. 159
B.4 Intrinsic carrier concentrations of germanium, silicon, gallium arsenide, indium nitride, silicon carbide, gallium nitride, aluminum nitride as a function of reciprocal temperature, [42]. 161
B.5 Schematic band diagram, Density of states, Fermi distribution function, Carrier concentration for intrinsic, n-Type and p-Type semiconductor. . . 164

C.1 Graphic representation of solutions in k-space. 167

List of Tables

1.1 Ionization energy for common gasses. 6

2.1 Barrier height from I-V methods and Ideality factor of 4H-SiC n-type Schottky contact for various metal measured at 300 K. 36
2.2 Comparison of the most common physical property for materials of interest. 43

3.1 Characteristics of the transmitted α-particles. 65
3.2 Energy resolution for Si, SiCs and Diamond detectors 68
3.3 Energy resolution for Silicon and SiC detectors. 76

4.1 Ionization energy of Carbon from NIST Atomic Spectra Database [46]. . . 101
4.2 Main physical characteristics of the PVT [55]. 114

List of symbols

C_f	Feedback capacitance
D	Diffusion constant
$\left(\frac{d\sigma}{d\Omega}\right)_R$	Differential scattering Rutherford cross section
E_g	Energy band gap in semiconductors
E_H	Hydrogen ionisation energy = 13.6 eV
E_{ionz}	Mean energy to produce a electron ion pair in gas detector
$E_{e.h}$	Energy needed to produce an electron-hole pair in semiconductor
E_{pair}	Energy needed to produce a carrier information
$F(E)$	Fermi-Dirac distribution function
G_{pre}	Gain of preamplifier
h	Plank's constant = 1.0551×10^{-34} J s
I_k	Ionization energy for the k-th sub-shell
k_B	Boltzmann constant = $1.3806488 \times 10^{-23}$ J K^{-1}
k_{BT}	Plasma Temperature
k_{ib}	Inverse Bremsstrahlung coefficient
k_n	Principal quantum number
k_{RBS}	Kinematic Backscattering factor
$N(E)$	Density states per unit volume per unit energy
N_A	Acceptor concentration
N_A^-	Ionized concentration for acceptors
N_C	Density of states for electron in the conduction band
N_C^*	Effective density of states in the conduction band
N_D	Donor concentration
N_D^+	Ionized concentration for donors

$N_{i.e}$	Number of electron ion pairs in gas detectors
N_Q	Number of generated charges from a radiation in a material
N_V	Density of states for holes in the valence band
N_V^*	Effective density of states in the valence band
P_M	Shockwave pressure
Q_d	Charge deposited by an event in the detector
q	Elementary charge = $1.6021766208(98) \times 10^{-19}$C
$q\phi_n$	Energy difference between the lower limit of the conduction band and the Fermi level
R_f	Feedback resistance
U_P	Ponderomotive energy
V_0	Equivalent accelerating voltage
v_c	Coulombian velocity
v_k	Adiabatic velocity
v_{os}	Electron velocity induced by laser
V_{pre}	Output amplitude of preamplifier
v_{th}	Thermal velocity
W_r	Spectrally integrated recombination intensities
W_B	Spectrally integrated Bremsstrhlung intensities

γ	Adiabatic Coefficient (1.67 monoatomic species)
$\Delta\phi_n$	Image charge barrier lowering
ε_0	Vacuum permittivity = $8.854187817 \times 10^{-12}$ F m^{-1}
ε_r	Relative permittivity
λ_{DB}	De Broglie wavelength
λ	Laser wavelength
λ_D	Debye wavelength
σ	Electrical conductivity
σ_{ION}	Total ionization cross section
σ_k	Cross section for electron
σ_{RPS}	Areal mass of target in RPA regime
ϕ_0	Energy differences between valence band and interface states

ϕ_B	Schottky barrier height
ϕ_m	Metal work function
ϕ_s	Semiconductor work function
χ	Electron affinity
χ_{ION}	Ionization parameter
τ_{pre}	Decay constant of signal in the preamplifier
ω_L	Angular frequency of the laser
ω_P	Plasma frequency

Introduction

This thesis is the result of the three years of research carried out mainly at Plasma Physics laboratories at the University of Messina, but also in National and European laboratories. The main research topic concerned the study and development of semiconductor devices, and in particular Silicon Carbide based devices. Silicon Carbide, more commonly called SiC, is a material that thanks to its excellent mechanical properties and high hardness is widely used in a wide class of applications, such as ballistic protection, in the automotive industry, in the field of brake systems, in the production of particulate filters, in the nuclear physics branch such as coating of nuclear fuel elements, in medicine for imaging applications and in many other fields.
Also in the field of Microelectromechanical systems (MEMS) there are very promising results [22] in the production of pressure sensors, accelerometers, resonant structures, motors, wear resistant devices, chemical sensor, field effect gas sensor devices, microhotplates, optical devices and light emitted diodes. In recent years, however, research has been intensified in the field of power electronic devices. Driven by the progress made in the crystal grow technique, SiC-based technology is what seems to show greater prospects for large-scale production and trade. Currently, SiC is used to produce power inverters and is already produced by several companies world leader in semiconductor solutions such as, Infineon Technologies AG, SEMIKRON or STMicroelectronics, that has been producing this type of SiC-based devices since 2008. These diodes thanks to the physical and chemical properties offered by this materials, have excellent qualities such as optimum switching performance and need a lower thickness to support the same breakdown voltage compared to conventional diodes. Nowadays STMicroelectronics produces SiC devices for:

- Charging station;
- ATX power supply;
- AC/DC power management unit, high voltage, and other topologies;
- Desktop and PC power supply;
- Server power supply;
- Uninterruptible power supply;

- Photovoltaic string and central inverter architecture;
- Photovoltaic power optimizer architecture;
- Photovoltaic microinverter grid-connected architecture;
- Photovoltaic off-grid architecture;
- Telecom power.

Closely related to this area of development there is the innovative research, carried out even in our laboratories, which is devoted to demonstrate the possible usage of this device also as radiations detectors. In this contest the benefits of SiC can be summarized in: high charge collection speed, high resistance to radiation-induced damage, high thermal conductivity and high saturation current speed. Moreover, considering the wide band gap of the material, it is possible to use the detectors at room temperature, since even under such conditions there is a very low dark current density that ranges from 10^{-10} A cm^{-2} at a bias voltage of 200 V up to 10^{-8} A cm^{-2} for a voltage of 700 V. Another consequence of the high band gap is the fact that these devices are blind to visible radiation and to soft UV, allowing the possibility of increasing sensitivity to the detection of heavier ions and protons even in a strongly compromised electromagnetic environment. But one of the most attractive properties of this material is the high resistance to radiation-induced damage due to higher bonding energy and greater displacement energy than traditional semiconductors. These features make the SiC detectors one of the most valuable silicon alternatives in all those experimental situations characterized by a harsh environment, i.e. high doses, high fluency and high radiation-induced damage. There are already promising results in literature on the detection of neutrons, X- and γ- rays and charged particles, but the most interesting application of SiCs concerns the monitoring of radiations emitted by laser generated plasma. Plasma offers infinite applications in many fields such as medicine, industry, but especially in the field of nuclear physics and so. Among the unique features that plasmas offer there is the very high brightness of the ion, electron or photon beam that can be sent in short-duration pulses and the extreme compactness of the source. It should It should be noted that in this field the energy spectrum of the radiations emitted by the plasma is extremely broad as well as the type of particles emitted and therefore extremely versatile devices are required. SiC detectors are very useful in these particular physical conditions in fact technological advances have made it possible to produce diodes with different geometries and characteristics, giving the possibility to choose the best device based on the experimental condition investigated. On the one hand there are SiC devices with a deep sensitive region, suitable for very energetic ions or X radiation, on the other hand there are also detectors with very thin metals and small regions sensitive to less penetrating radiations such as electrons, light ions and UV radiation. Moreover by combining the results of these detectors with devices such as Faraday cup, Ion Energy Analyzer or other diagnostic techniques, it is possible to give a complete characterization of plasma in terms of angular, velocity

and energy distribution of radiation emitted and of temperature and plasma density. It should be noted, however, that SiC is not the only wide bandgap material that can be used for such applications. The diamond, for example, or Gallium Arsenide, are the main competitors of Silicon Carbide. However, it should be noted that for these materials, development processes are not yet optimized and are very costly. The thesis is therefore entirely focused on the comparison of detectors based on SiC and other semiconductor materials, mainly Silicon and Diamond. This comparison will be carried out not only at low fluence where a spectroscopic electronic chain can be used, but above all in the high fluxes regime where a time of flight (TOF) technique is needed. The thesis is made up of the following chapters:

- the first chapter gives an overview of the major particle detection systems by classifying them in on-line and off-line detector, in order to show the main difference with respect semiconductor based detector;
- in the second chapter attention is focused only on semiconductor devices. For this reason some notions on the Schottky metal-semiconductor junction are given, which is the basis of the operating principle of the devices used in this work. Next, the characteristics of these SiC devices and a diamond detector used for comparison are shown illustrating preliminary characterization and simulation performed;
- the third chapter is entirely focused on the detection of ions, electrons and photons using a spectroscopic electronic chain. In fact, when the particle flow is low, it is possible to couple with the detector an electronics to process, amplify, and record the signal. The basic elements of the chain are in fact the preamplifier, coupling the impedance between the detector and the next electronic chain, the amplifier, which allows to modify the signal shape in order to optimize the pulse recording that occurs in a multichannel. The measurements compare the performance of the SiC detectors and the diamond device with that of a traditional Silicon detector, enabling the definition and verification of the energy resolution and response linearity of these devices in a large energy scale. In fact measurements are obtained by detecting both MeV ions emitted by a radioactive source and keV ions generated by an ion implanter. Finally, the preliminary data relating to the detection of electrons and X-rays are shown;
- finally, the last chapter represents the main contribution to this thesis since the results achieved with SiC detectors in monitoring radiations emitted by plasma are exposed. This chapter is introduced from a first theoretical part in which the main features of the plasmas are exposed. Particular attention is therefore directed to non-equilibrium plasmas generated by laser showing possible experimental configurations that lead to different acceleration regimes (BIA, TNSA, RPA). Obviously,

in such conditions it is not possible to use a proportional electronic chain such as that showed in the previous chapter, but it is necessary to employ the time of flight technique, which is then illustrated below. In the following paragraphs, a series of time of fight spectra are shown with the aim of highlighting the common aspects and differences between the low intensity laser spectra (@ UniME) or the high-intensity laser (@ PALS, @ CELIA and @IPPLM) spectra. In fact, these ion spectra were analyzed and fitted using the so called Coulomb Boltzmann Shifted distribution, which allows to estimate some of the most important plasma properties such as the average plasma temperature or the acceleration potential to which particles are subjected. Very often SiC devices are coupled with other types of detectors and for this reason part of the chapter shows how it is possible to combine and possibly confirm the information obtained through SiC, Faraday Cup, IEA and scintillators. To better understand the importance of SiCs in the plasma characterization, a small review of innovative plasma applications is also shown: Laser Ion Source, nuclear reactions and compact X-ray sources. Finally, in the last section of the chapter are reported the characterization measurements done to test the radiation hardness of the material that is one of the major strengths of SiC in this kind of applications.

In the realization of this thesis, the wide series of experimental measurements performed in different national and European laboratories has been enriched with an intense bibliography work to highlight the state of the art on such devices.

Chapter 1

Radiations detection

In general, it is possible to classify all radiations detectors in online devices (ionization chamber, semiconductors, etc ...), which provide direct measurement information, and offline detectors (track detectors, gafchromic films, etc...), which instead require data development and an analysis that takes place after the observation of the process. It is possible to find some common features between them such as the energy resolution or the efficiency as shown in the Appendix A. In this chapter the operating principle of the main types of radiations detector will be described, with the aim of showing strengths and weaknesses with respect to semiconductor detectors.

1.1 Online radiations detectors

Although the semiconductor devices is a relatively new area of interest, it has a enormous impact in the everyday life. In the field of radiation detectors this technology is gradually replacing other detection technique. In the following sections will be presented the state of art of the alternative to the semiconductors based detectors for online detection of radiations, and in particular the attention will be focused on ionization chamber, scintillator and photomultiplier.

1.1.1 Ionization chamber

An ionization chamber is an instruments in which an electric field is applied through a gas-filled volume. The charged particles moving through the gas, as a result of their interaction, ionize the gas producing positive ions and electrons. The presence of the electric field moves the positive ions and electrons in opposite directions along the field

lines, producing a ionization current. Under standard conditions, the speed of the electrons is of the order of $\approx 10^6$ cm/s, while the ions velocity is many orders of magnitude smaller. The average energy for the single ionization does not depend on the energy of the incident radiation, nor by the type of radiation, but only by the gas. It is possible to represent an ionization chamber such as a parallel plate capacitor filled with gas, and suppose that α-particles with a kinetic energy E lose all of their energy in the gas. If E_{ionz} is the average energy of ionization of the gas, each α-particles will produce a number of electron-ion pairs N_{ie} given by:

$$N_{ie} = \frac{E}{E_{ionz}} \tag{1.1}$$

This charge will be collected from the electrodes producing an electrical pulse.

Actually the E_{ionz} is defined as an average energy lost by the incident particles and does not directly corresponds to the First Ionization Potential.

TABLE 1.1: Ionization energy for common gasses.

Gas	First Ionization Potential (eV)	E_{ionz}(eV/ion pair)	
		Electrons	Alpha Particles
Ar	15.7	26.4	26.3
He	24.5	41.3	42.7
H_2	15.6	36.5	36.4
N_2	15.5	34.8	36.4
Air		33.8	35.1
O_2	12.5	30.8	32.2
CH_4	14.5	27.3	29.1

In fact due to the competing mechanism of the energy loss and recombination E_{ionz} results always greater than the Ionization Potential as can be seen in Tab. 1.1, reporting typical values for common gases [43].

By changing the voltage between the plates, it can be obtained for the charge collection the typical trend shown in Fig. 1.1. In the first region the collected charge increases with the applied voltage because at this low values the recombination process leads to a partial neutralization of the produced ions. When the electric field is sufficiently high, the recombination can not occur and the charge collection remains constant (Ion saturation). This is the typical region of operation of the ionization chamber. The number of ions produced by the particle for length unit is a function of gas density. When photons have to be detected, especially if the radiation energy is high, it is necessary to use a high gas pressure inside the chamber: in this case the mean free path results smaller than chamber dimension.

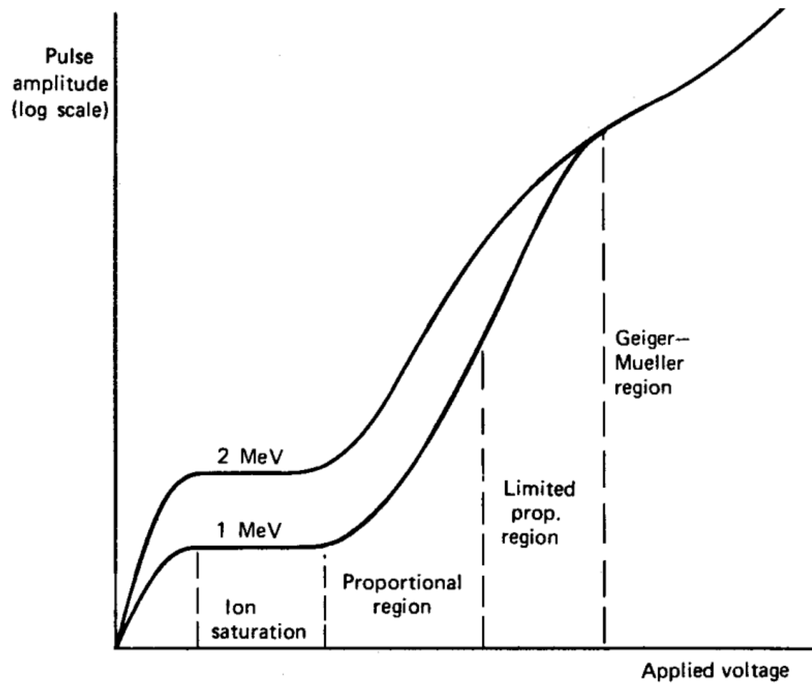

FIGURE 1.1: Variation of ion pair charge with applied voltage.

If the plates of the capacitor which constitutes the ionization chamber are isolated, their difference potential vary as shown in Fig. 1.2, when a total charge q is collected.

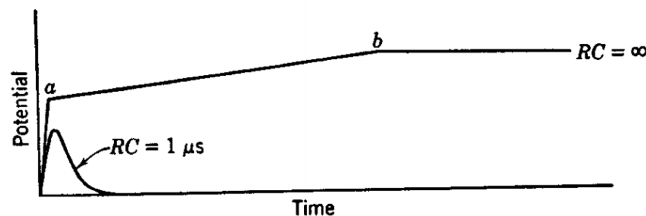

FIGURE 1.2: Behaviour of potential

At first the faster electrons (a), and then ions (b), are attracted by the plates of opposite charge. This fact changes the total charge of the capacitor. Instead if the ionization chamber is held at a constant potential, through an external power supply, it is possible to read the current pulse to ground with a resistance as described in Fig. 1.3. Here the capacity (which often coincides with the capacity of the same chamber) has the function of integrating the current pulses in the time giving or an average current (proportional to the intensity of the radiation) or separated pulses according to the RC constant value. In this second case, the ionization chamber operates as a differential counter or simple counter. In fact one incident particle, depositing all of its energy in the gas, gives rise to a current pulse whose area (charge) is proportional to the energy of the particle. To eliminate the pile-up phenomenon of the signal it is differentiated before being analysed.

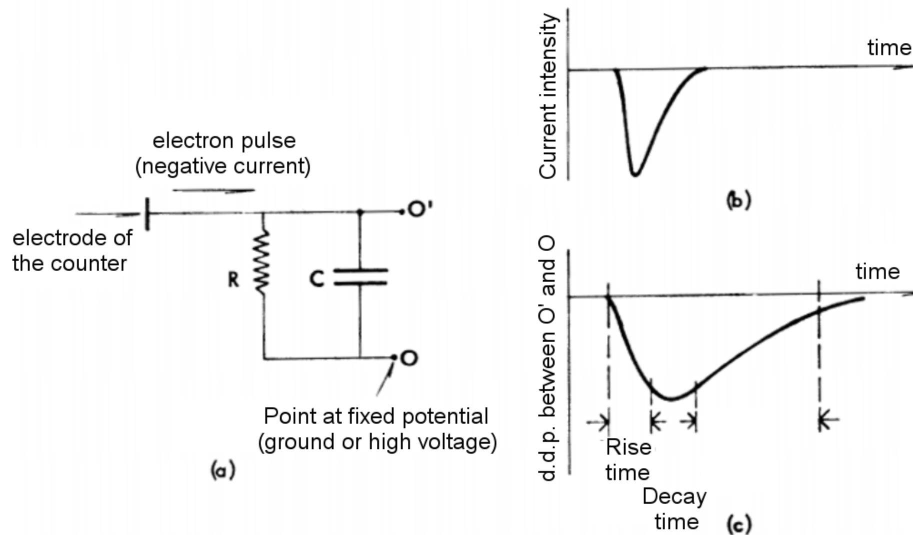

FIGURE 1.3: (a) Electrical circuit representation of a ionzation chamber; behaviour of the current (b) and of the voltage (b) as a function of the time.

The usage of the ionization chamber as a differential counter is limited both at low particles energies, where the noise of electronics (equivalent to approximately $7 \div 8\,\mathrm{keV}$) can degrade the signal, and also at high energy when the range of particles becomes larger than the size of the room. Nowadays there are many modern versions of a gas detectors, based on the same principles described above, and used in the detection of particles in nuclear physics experiments: the multiwire chamber (Multi Wire Proportional Chamber MWPC), the drift chamber and TPC room Drift (Time Projection Chamber). These detectors will be described in the next paragraph after a more detailed explanation of the proportional region and of the Geiger-Muller counter.

Proportional counter

When the value of the electric field in a gas counter is increased beyond the saturation potential, the so called proportional region is achieve. In such conditions increasing the applied voltage between the electrodes the output pulse from the detector starts to increase, remaining proportional to the initial kinetic energy of the revealed particles. The great advantage of this detector is that it also allows the detection of a very low initial ionization, even a single electron ion pair. For a counter with cylindrical geometry the electric field, at a distance r from the axis, is given by:

$$E(r) = \frac{V_0}{r \cdot \ln(b/a)} \tag{1.2}$$

where a and b are the inner and outer electrode radius, respectively. The inner electrode is usually an extremely thin wire ($a \approx 0.01\,\mathrm{cm}$), so that r ($a < r < b$) can be very small and consequently $E(r)$ is very high. Because of the electric field near the anode increases very quickly, electrons gain a kinetic energy sufficient to produce with collisions ions and secondary electrons. These secondary electrons are also accelerated and became able to ionize the gas again. Photons are also generated that produce electrons by photoelectric effect on the walls of the chamber or in the gas volume. If n is the number of electrons produced in the primary ionization by the incident radiation, each of them has a probability P to generate secondary electrons m: the average number of the generated secondary electrons will be:

$$k = m \cdot P \tag{1.3}$$

The total number of electrons N generated after the avalanche multiplication process is then:

$$N = n + nPm + (nPm)Pm + n(Pm)^2Pm + ... \tag{1.4}$$

that can be written as:

$$N = n(1 + k + k^2 + k^3 + ...) \tag{1.5}$$

If $k = mP << 1$ it can be written:

$$N = n\frac{1}{1 - mP} = n\frac{1}{1 - k} \tag{1.6}$$

As can be seen from previous expression, for $k = 0$ there is not any multiplication and N is proportional to n. As much k tends to unity the greater is the multiplication factor M:

$$M = \frac{N}{n} \tag{1.7}$$

The multiplication factor, that can reach a value of 10^2 as can be seen in the example of Fig. 1.4 from Staub et al.[74], is a function of the type of the filling gas, the pressure and the applied voltage. The filling gas is usually a noble gas (such as argon) with addition of small amounts (10%) of organic complex molecules that can absorb photons without ionization process. With an argon-methane mixture can be reached multiplication factors up to 10^4. To use proportional counters for X-rays or photons detection is necessary to have a high-pressure gas. Instead to reveal alpha particles or low beta energy it is necessary to have very thin windows. In some cases there is no input windows and the gas is flushed between the electrodes.

In this case the voltage stability is more important with respect to the ionization chamber because of its variation affects the value of M, and then the response function of the detector. The pulse formation technique is the same of a ionization chamber: also in this case the signal is differentiated by an RC circuit.

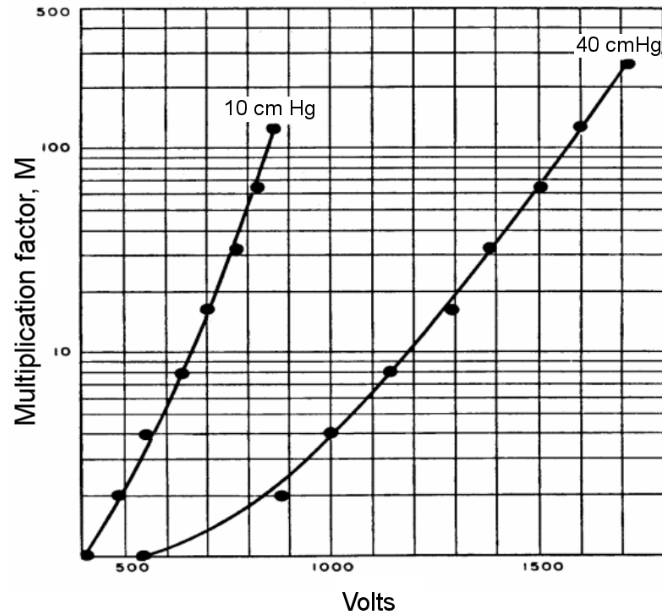

FIGURE 1.4: Multiplication factor, M, as a function of applied voltage for argon at pressures of 10 and 40 cm Hg, radius of center wire $a = 0.013\,\mathrm{cm}$, radius of outer electrode $b = 1.105\,\mathrm{cm}$.

Geiger-Muller counter

When the bias voltage increases up to a certain value in which the product $mP \approx 1$ it can be obtained a discharge, propagating along the axis of the cylindrical counter: the Townsend avalanche phenomenon. The generated electrical signal is large (thus easily legible), but lost the proportionality with the primary ionization (see last areas of Fig. 1.1). The Geiger counter therefore can not be used for spectroscopy, but only for intensity measurements of radiation fields. The discharge propagates along the wire anode at a speed of $10^7\,\mathrm{cm/s}$ and the electrons are collected in a very short time ($\approx 10^{-9}\,\mathrm{s}$). The slower positive ions that remain around the wire, giving rise to a space charge which decreases the electric field, interrupt the discharge. The effect of "quenching" (cooling, extinction) is obtained by mixing the noble gas argon (90%) with polyatomic gas, typically ethyl alcohol (10%). These molecules are able to absorb energy (especially energy of the produced photons) without be ionized. Even if the output pulse is very fast, the Geiger counter has a dead time of the order of $10 \div 100\,\mu\mathrm{s}$ due to the "quenching" effect and it should therefore be used with caution in presence of high counting speed.

Multi Wire Proportional Chamber

The multiwire rooms consist of two or more floors of parallel wires, each of them is biased and read by a independent electronic circuits. When a particle ionizes the gas filling,

Fig. 1.5, only the closest wires collect the electrical signal: in this way the wire that produces the electrical signal identifies a coordinate of the particle.

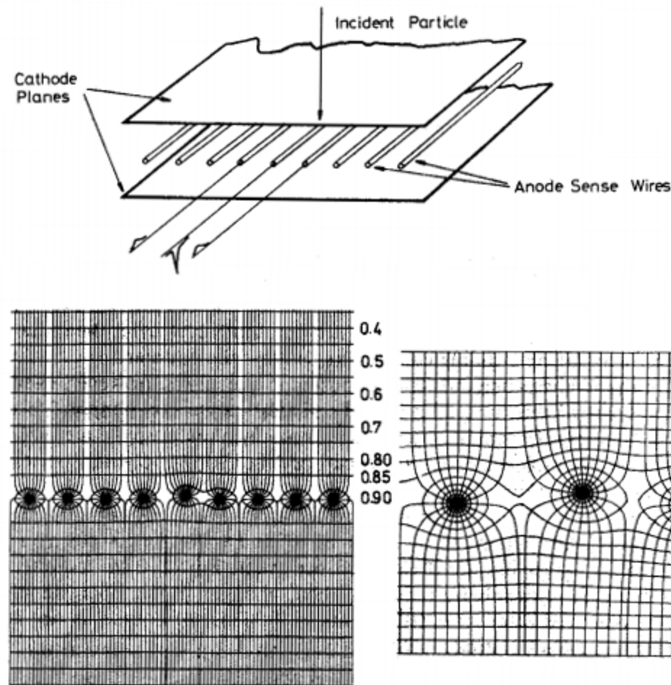

FIGURE 1.5: Schematic of a MWPC and distribution of the electric field lines around wire [20].

In Fig. 1.5 are also shown the electric fields, the potential and the effect of a slight wire displacement on the field lines as reported by Charpak et al. in [20].

If the wires of two independent planes are perpendicular to each of them they are able to measure the X and Y coordinates of the position of the particle. And if there are several levels of wires, like in Fig. 1.6, it can be obtained the tracking of the trajectory of the particle inside the detector. The interactions with vertices can be reconstructed, and if the MWPC are immersed in a magnetic field, by measuring the radius of the curvature of the trajectories, it can be calculated the momentum of the particles.

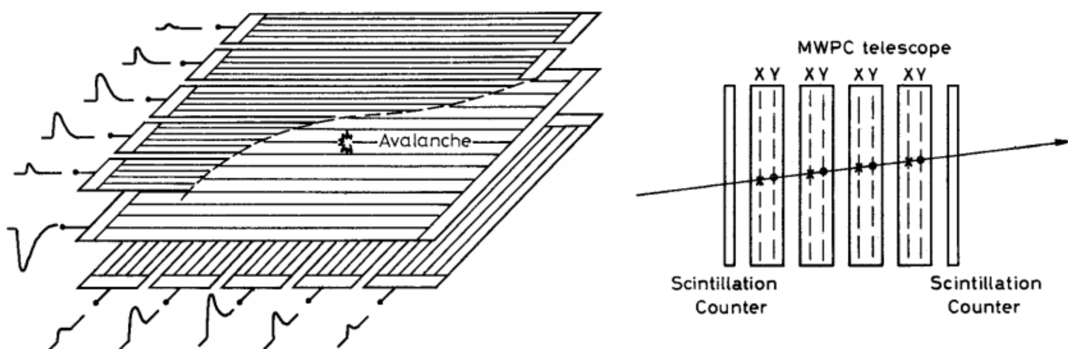

FIGURE 1.6: Track reconstruction through a multi-layer MWPC.

Drift chamber

In this detector the spatial information is obtained by measuring the drift time of electrons produced by the ionization of the incident radiation. Heaving a trigger for a precise time reference, and knowing the drift velocity of electrons in the gas, v_d, the distance between the collecting wire and the origin of the electrons can be calculated by the relation:

$$\int_{t_0}^{t_1} v_d \, dt \tag{1.8}$$

in which t_0, the time of arrival of the particle, represents the trigger signal and is given by a scintillation counter, while t_1 is the instant in which the pulse appears at the anode.

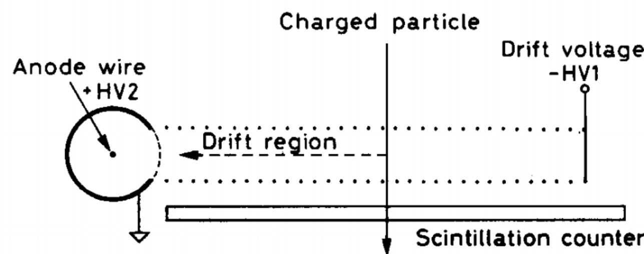

FIGURE 1.7: Principle of operation of a drift chamber.

The uniformity of the electric field in the drift zone, necessary to have a constant drift velocity and therefore a linear response of the instrument, is guaranteed by many equi-spaced wires with a suitable potential difference between them. Since the typical drift velocity of electrons is of the order of $5\,\mathrm{cm}\,/\,\mu\mathrm{S}$ and the dimensions of the drift region are of the order of 5 to 10 cm, the drift times are of the order of $1 \div 2\,\mu$s.

Time Projection Chamber

A Time Projection Chamber works simultaneously as MWPC and as drift chambers. The detector consists in a large cylinder (diameter and length can reach two meters) with a thin plane maintained at high voltage in the centre. The ends of the cylinder are covered with a matrix of wires operating in a regime of proportionality arranged as shown in Fig. 1.8a. Parallel to each wire there is a rectangular cathode. In this configuration the vertex of the interaction is located inside the cylindrical volume. The particles produced in the interaction pass through the volume of the cylinder, producing ionization electrons that under the action of the electric field migrate toward the ends of the cylinder where they are detected by the wire chambers. The radial and azimuthal coordinates are obtained from the position of the wire that produces the electric signal and from the signal induced on the line of cathodes. It has to be observed that the induction signals on

various cathodes will have a certain distribution of amplitudes decreasing with distance from the point of collection.

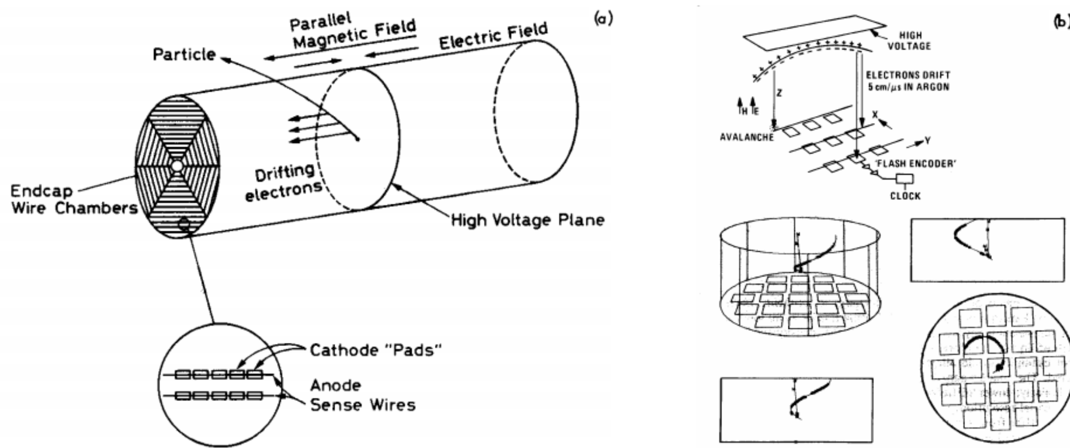

FIGURE 1.8: Scheme of a TPC (a) and reconstruction of a particle trajectory (b).

For this reason with a method for electronic analysis is used to obtain the centre of this distribution. The third coordinate, along the cylinder axis, is given by the electron drift time. The axial magnetic field serves to minimize the lateral spread of the electrons which, for a good response of the detector, should move along parallel trajectories to the axis. In fact electrons produced by ionization, being of low energy, easily can spiralize around the magnetic field lines parallel to the axis of the detector without radial components as shown in Fig. 1.8b.

1.1.2 Scintillation detector

The scintillation detectors are widely employed as particle detectors in nuclear physics. They are based on the property of some materials to emit light when excited or ionized by the incident radiation. The scintillators are always coupled to an amplification system of this light, a photomultiplier, as summarized in Fig. 1.9. In fact the light, generated by the scintillators is transmitted to the photomultiplier, where it is converted into a weak photoelectrons current that contains the information on the measured radiation. This photocurrent is then further amplified by an electron multiplication system and finally it is analysed by the acquisition electronics.

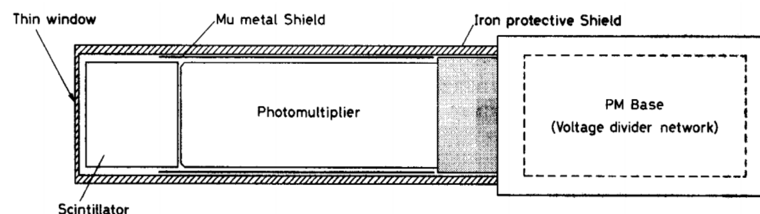

FIGURE 1.9: Scheme of a scintillators detector with a coupled photomultiplier.

Several materials have scintillation properties. The most important among them can be separated into organic and inorganic scintillators.

Organic scintillators

The organic scintillators are mainly aromatic hydrocarbons. Their best characteristic is the rapid decay time (few nanoseconds), which makes them excellent for the generation of pulses for timing. The scintillation light in these compounds is due to energy transitions of covalent electrons of the "π-molecular" orbital. A typical energy diagram is shown in Fig. 1.10.

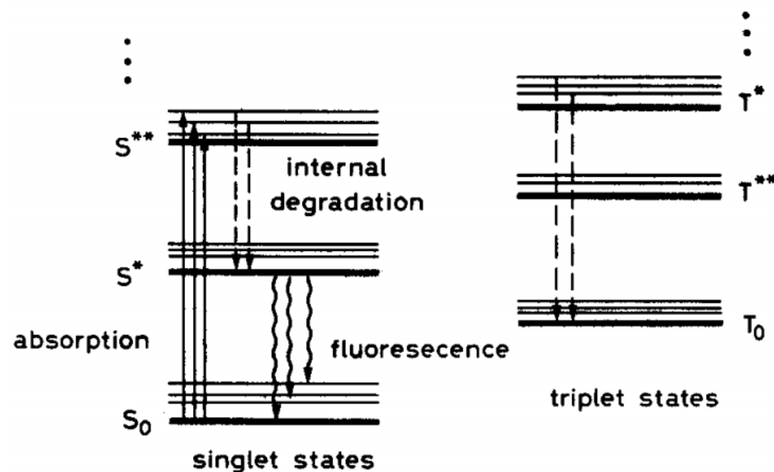

FIGURE 1.10: Energy levels in organic scintillators.

There are distinct states of singlet and triplet. The ground state S_0 is a singlet state. Above it there are the singlet excited levels S^*, S^{**}. There are also triplet states: T_0, T^*, T^{**}, and so. For each electronic level there is a fine structure that corresponds to modes of vibrational excitation. The energy spacing between the various levels of bands is of the order of eV, while that between the vibrational levels is of the order of 0.1 eV. The incident radiation excites the levels as shown by the arrows in Fig. 1.10. Singlet excitations typically decay in some picosecond by S^{**} band to S^* band without emission of radiation. Conversely, the probability of radiative decay from S^* to S_0 is very high and the characteristic time of this process is of some nanosecond. Moreover, the fact that S^* decays to vibrational excited states of S_0 implies that the energy of light radiation is less than that necessary for the transition $S_0 \rightarrow S^*$ and consequently the scintillator is transparent to its own radiation. The triplet states instead decay by internal degradation to the T_0 state without emitting any radiation. The T_0 state cannot directly decay to S_0 because of selection rules. The slower de-excitation mechanism, can takes place through

the interaction with another T_0 state as summarized below:

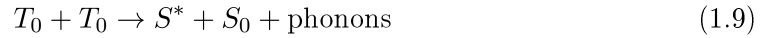

$$T_0 + T_0 \rightarrow S^* + S_0 + \text{phonons} \tag{1.9}$$

and then the S^* state decays as described before. This process contributes to the so-called slow or delayed component the scintillation light. Among the organic scintillators there are anthracene ($C_{14}H_{10}$), stilbene ($C_{14}H_{12}$) and many plastics. Some organic scintillators may be in the liquid state: in this case are used for the detection of very low energy beta particles (^{3}H, ^{14}C). The radioactive sample is dissolved inside of the scintillator, and this avoids any dead thickness between source and detector, maximizing the solid angle that is 4π. The organic scintillators produce extremely fast signals, some nanoseconds, which makes them particularly suitable for timing applications. Another advantage is their low cost and simplicity. The major limitation is undoubtedly the poor energy resolution (due to a low yield of light). Moreover, considering the low value of Z, these devices are not suitable for the detection of photons, but the abundance of hydrogen favors the neutrons detection.

Inorganic scintillators

The inorganic scintillators are generally alkali halide crystals with the addition of small "activators" percentages that are indicated in parentheses. The most common materials include NaI(Tl), CsI(Tl), KI(Tl), LiI(Eu), CsF_2 and $LaBr_3$(Ce). Among the non-alkaline materials there are also $Bi_4Ge_3O_{12}$, the BaF_2 and ZnS(Ag). The luminescence mechanism is completely different from what happens in organic scintillators. In this case the emission of light is not a molecular phenomenon but is connected to the band structure of the crystals, described in more detailed in the following sections. In a pure crystal the passage of an ionizing particle may cause the transition of an electron from the valence band to the conduction band. However the return of the electron to the valence band with the emission of a photon is an inefficient process, and the emitted photons belong to the ultraviolet domain, which is a region of poor efficiency for photocathodes of photomultipliers. To increase the probability of emission of optical photons in the de-excitation mechanism, the structure of the bands is modified by the introduction of appropriate impurities, see Fig. 1.11. The presence of impurities, the activators centers, introduces energy levels within the band gap. An ionizing particle can transfer sufficient energy to an electron, promoting it in the conduction band. But, due to the presence of these levels introduced by the impurities, another process can occur. When the energy transferred to the electron is not sufficient to bring it into the conduction band, it can remain electrostatically bound to the hole. This state weakly bound is called "exciton".

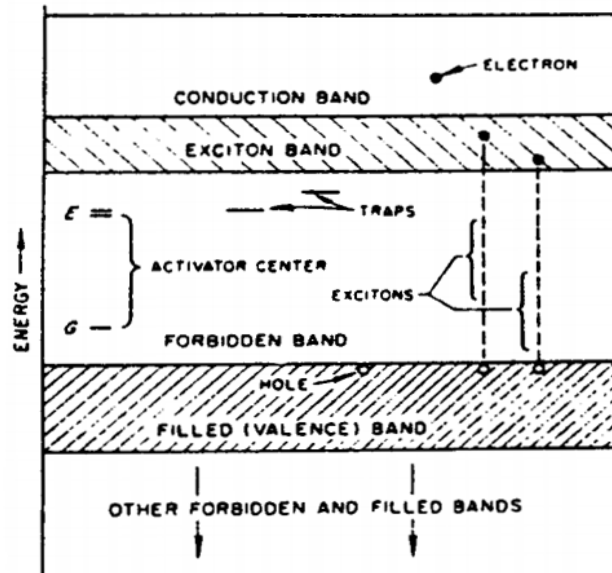

FIGURE 1.11: Energy levels for inorganic scintillators

The exciton can move through the whole crystal but it does not contribute to the conduction. There are a whole series of exciton energy levels in the band gap immediately below the conduction band of the crystal. For example in NaI(Tl) the width of the band gap is of the order of 6 to 8 eV while the band due to the excitons state is $\approx$1 eV. The exciton during its diffusion through the crystal can be captured by an activator center. The subsequent decay of this state occurs with a radiative transition that brings the system in the ground state. This fact is extremely advantageous because first of all in this way the crystal results transparent to the light signal; moreover the emitted light spectrum is not ultraviolet but is in the visible region, where the response of photomultiplier is much better. The inorganic scintillators, compared to organic ones, at the same energy deposited by incident radiation, emit more light (almost an order of magnitude), and then present a better resolution. Another advantage, especially for the detection of photons, is their relatively high atomic number which makes them much more efficient. All scintillators, both organic and inorganic, must be coupled to a photomultiplier, and the set PM-detector must be completely isolated from ambient light, through a sealed vessel. To obtain also the maximum collection of photons, all of the detector walls, are coated with a highly reflective material.

1.1.3 Photomultiplier

In the scheme of Fig. 1.12 are reported the main elements that constitute a photomultiplier: photocathode, focusing and collection optics, multiplication phase.

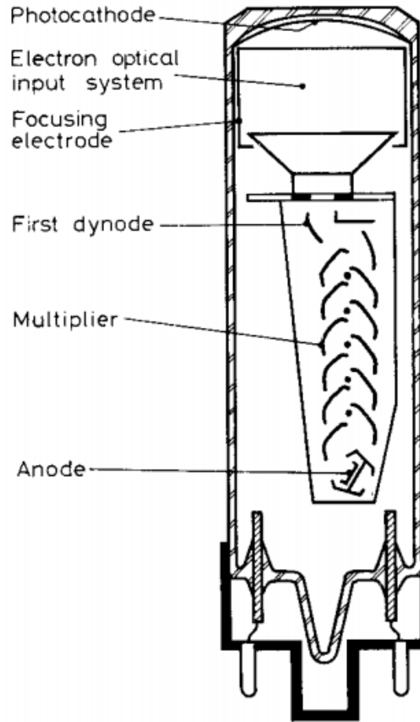

FIGURE 1.12: Scheme of a photomultiplier.

Photocathode

It consists in a layer of photosensitive material that has the function of converting, for photoelectric effect, the optical photons into electrons.

This process can be expressed in terms of probability and the quantum efficiency $\eta(\nu)$, i.e. the ratio between the incoming photons and the outgoing electrons, is given by:

$$\eta(\nu) = (1 - R)\frac{P_\nu}{k}\left(\frac{1}{1 + 1/kL}\right) P_S \tag{1.10}$$

where R is the reflection coefficient, k is the full absorption coefficient of photon, P_ν represents the probability that light absorption may excite electrons to a level greater than the vacuum level, L is the mean escape lenght of excited electrons, P_S is the probability that electrons that reach the surface of the photocathode may be released into the vacuum and ν is the frequency of light. The light pulse duration coming from the scintillator is of the order of some nanosecond, because of the photocathode collects photons emitted isotropically from the interaction point that may undergo reflections on the walls of that enclose the detector. For this reason the emitted electrons have also a temporal distribution of the order of nanoseconds. Since the number of these electrons is in general very low, their overall electric charge is too small to be measured directly, and it is necessary a subsequent multiplication system.

Focusing and collection optics

In order to collect efficiently the photoelectrons, but also to minimize the transit time of electrons,it is necessary to configure and optimize the arrangement of the first dynode. It can be done intervening on the shape and the position of the photocathode or by changing the applied voltage applied on the electrode. It can be defined an efficiency of collection of the first dynode as the ratio between the number of emitted secondary electrons and the number of the incident photoelectrons. This efficiency is generally comprised between 60 % and 90% according to some data sheets taken by literature Ref.[38].

Electron multiplication: dynode section

The photoelectrons emitted from the photocathode are then conducted by a suitable electrostatic filed in the dynode section where, thanks to the mechanism of secondary emission, are multiplied with an amplification of the current between 10-10^8 times. Only at the end of the section these electrons are focused and collected by the last electrode, the anode, that can be realized in the form of rod, plate or mesh electrode. The materials with a higher secondary emission used for the dynodes are alkali antimonide, beryllium oxide (BeO), magnesium oxide (MgO), gallium phospide (GaP) and gallium phosphide (GaAsP) as shown in Fig. 1.13, reporting the secondary emission ratio δ as a function of the accelerating voltage.

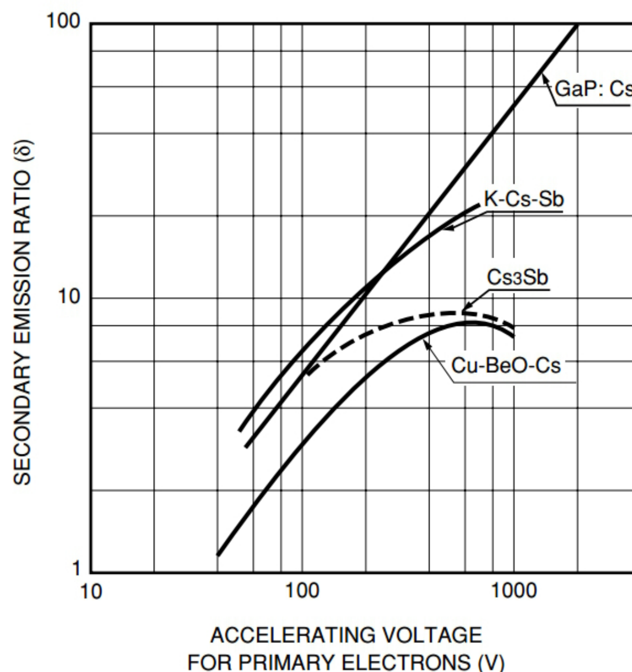

FIGURE 1.13: Secondary emission ratio from Ref. [38].

The amplification of a photomultiplier is strictly connected to δ that in a first approximation, is proportional to the voltage V_d between the dynodes. The dynodes are maintained at a positive accelerating potential, and in this way each dynode attract the electrons coming from the preceding one. This is obtained trough a voltage divider, as shown schematically in Fig. 1.14.

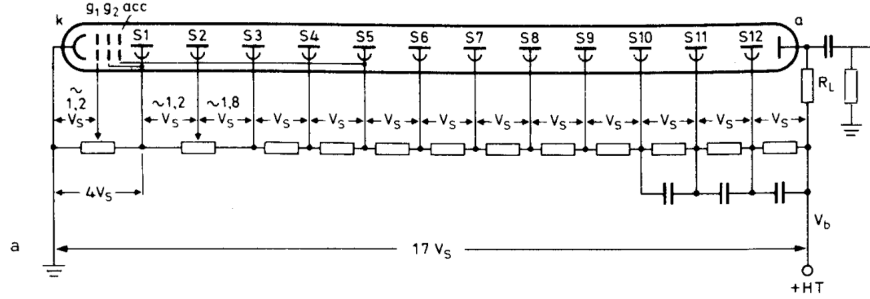

FIGURE 1.14: Scheme of a voltage divider.

It is has to be stressed that being the amplification linear along the dynode section, the final charge remains proportional to the initial one. Therefore the output signal, proportional to the light emitted in scintillations, will be also proportional to the energy deposited by radiation. Under this assumption, i.e. that V_d remains constant along the entire photomultiplier, δ can be written:

$$\delta = kV_d \tag{1.11}$$

and then the gain G of the photomultiplier, ie the ratio of electrons collected at the anode and those emitted from the photocathode, is given by:

$$G = \delta^N = k^N V_d^N \tag{1.12}$$

and also:

$$\frac{dG}{G} = N\frac{dV_d}{V_d} \tag{1.13}$$

The last relation evidences how critical is the stabilization voltage of the dynodes: if for example N = 15, a variation of 0.1% on the dynodes voltage results in a variation of 1.5% on the gain and therefore in a worsening of resolution of the detector. The problem of the voltage stabilization of the dynodes is solved using specific power supplies, and by ensuring that the supply current of the divider is much greater than the electron current along the dynodes (flowing in parallel) so that it can be neglected. Very schematically, the number of optical photons produced by the incident radiation is given by:

$$P_\nu = \frac{E}{h\nu}\varepsilon_\nu \tag{1.14}$$

where E is the energy deposited in the scintillator, $h\nu$ the energy of the optical photons and ε_ν is the scintillation efficiency, and generally it is very low (8% for NaI). The photons follow a typical temporal distribution connected with the de-excitation of the scintillator:

$$P(t) = A \cdot \exp\left(-\frac{t}{\tau}\right) = \frac{P_\nu}{\tau}\exp\left(-\frac{t}{\tau}\right) \tag{1.15}$$

in which τ is of the order of 10 ns for plastic scintillators or 250 ns for NaI.
The number of photoelectrons produced at the photocathode is then:

$$P_e = \varepsilon_L \varepsilon_C P_\nu \tag{1.16}$$

where ε_L is the optical efficiency (generally around 90%), ε_C represents the conversion efficiency of the photocathode (generally around 10%∼20%). Taking into account the last equations P_e can be written:

$$P_e = \varepsilon_L \varepsilon_C \varepsilon_\nu \frac{E}{h\nu} \tag{1.17}$$

and then the total charge Q collected at the anode after the multiplication in the dynodes sections is:

$$Q = P_e \delta^N = \varepsilon_L \varepsilon_C \varepsilon \nu \frac{E}{h\nu} \delta^N \tag{1.18}$$

For example if the first dynode receives about ten electrons, the total charge deposited on the anode corresponds to some picocoulomb.

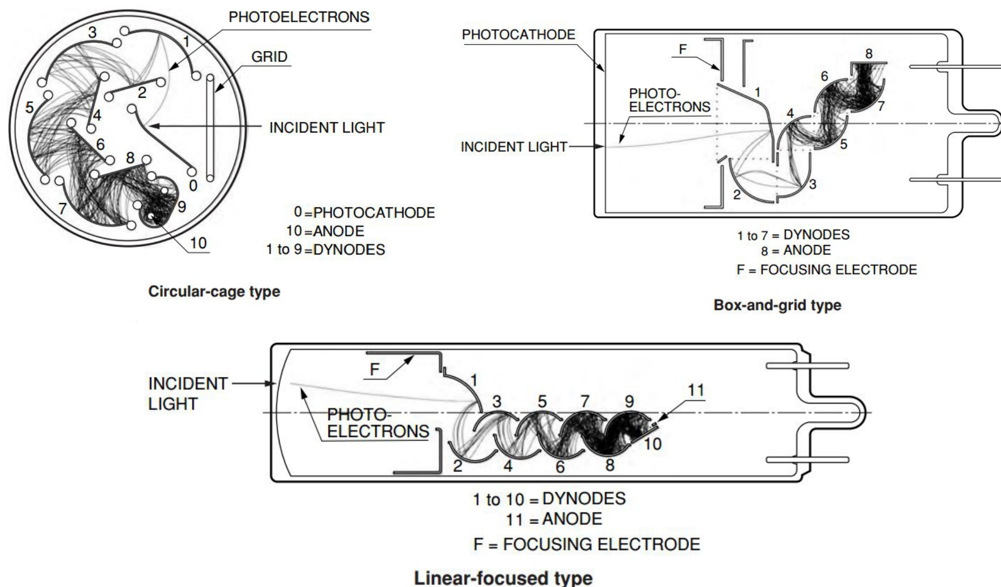

FIGURE 1.15: Different typologies of dynode section from Ref. [38].

It should be observed that the gain factor G may vary slightly from the value previously reported, because it depends also on the geometry of the dynodes section. Today there is

a wide variety of configurations of dynodes and their response time, linearity, collection efficiency, uniformity and transit time can be different. For this reason the position of each dynode is studied by using Monte Carlo simulations, giving the possibility to optimize the electron trajectory inside the tube. Fig. 1.15 shows some examples of dynode structure.

1.1.4 Semiconductor detector

From a theoretical point of view the operating principle of a semiconductor [1] detector is similar to that for ionization chamber: when a radiation impinges on a crystal, along the particle trajectory produces electron-holes pair (analogous to the electron ion pairs) in a time of the order of few picoseconds. These charges are successively collected through an appropriate electric field. The number of the generated charges, $N_{couples}$, depends on the energy E of the incoming particle through the relation:

$$N_{couples} = \frac{E}{E_{pair}} \tag{1.19}$$

where E_{pair} is the necessary energy necessary to produce a carrier information, an electron-hole pair for semiconductors or an electron-ion pair for a ionization chamber (note the similarity with eq. 1.1). The advantage of semiconductor based detectors is precisely this ionization energy, $E_{e.h}$ that is around 3 eV for silicon, very low if compared with 30 eV for a typical gas detector or with 100 eV needed for the creation of an information carrier in a scintillators. For this reason for the same energy of the incoming radiation in semiconductor, being lower the ionization energy, a greater number of pairs will be generated (about 10 times greater), contributing to improve the statistical measure. This energy $E_{e.h}$ is almost completely independent both from the incident energy and on the type of particle, but depends on the temperature: when temperature decreases it increases.
Moreover because of electrons and holes travel faster in semiconductors with respect other detection systems also the time resolution, and time response are very good. Finally comparing the density of a gaseous ionization detectors with that for a semiconductor device, it is evident that in the last case more energetic radiations can be detected in a lower thickness of sensible active region.

For the collection of the charges produced by the incident radiation, however, it is not sufficient to apply two electrodes on the extremity of the semiconductor material since the presence of free carriers would lead to an immediate recombination of electron-hole pairs. Consider for example the relationship between free carriers and generated charge

[1] A detailed description of the physic of semiconductor is reported in Appendix B

in silicon. The density of free carriers[2] in silicon is about $N_i = 1.5 \times 10^{10}\,\mathrm{cm}^{-3}$. In a silicon volume with a surface of $1\,\mathrm{cm}^2$ which extends for about $300\,\mu\mathrm{m}$ there will be a number of free carrier:

$$N_i = (300\,\mu\mathrm{m} \cdot 1\,\mathrm{cm}^2) \cdot 1.5 \times 10^{10}\mathrm{cm}^{-3} \approx 4.5 \times 10^8 \tag{1.20}$$

On the other hand, if for example a 3 MeV alpha particle impinges on the intrinsic silicon volume, the total number of electron-hole pairs produced inside the material, assuming an average energy production of about $E_{e.h} = 3\,\mathrm{eV}$ is:

$$N_{couples}\frac{3\,\mathrm{MeV}}{3\,\mathrm{eV}} = 1 \times 10^6 \tag{1.21}$$

It is evident that N_i and $N_{couples}$ are quite comparable with a consequent loss of information due to the recombination process. Therefore non ohmic contact should be employed such as p-n or Schottky junctions (semiconductor-metal), in which a layer, without free carrier, can be generated, the so called "Depletion layer".
For simplicity consider the situation in which a p-type and a n-type semiconductor material are put in contact. As a result of the different majority carrier concentration, holes and electron diffuse towards n-type and p-type region, respectively, where are eliminated because of recombination. The departures of a majority carrier leaves in the lattice a fixed ion with opposite charge, generating an electric field along the barrier. This electrostatic field will tend to balance the diffusion motion until a dynamic equilibrium condition is reached, when the drift contribution is comparable with the diffusion one. In Fig. 1.16 a typical representation of the depletion layer is reported. The net current density, j_p for holes or j_n for electron, is given by:

$$j_p = \sigma\mathbf{E} - \mathbf{D}\nabla qp \tag{1.22}$$

$$j_n = \sigma\mathbf{E} - \mathbf{D}\nabla qn \tag{1.23}$$

in which σ is the electrical conductivity, $\mathbf{E}$ is the barrier electrical field, $\mathbf{D}$ is the diffusion constant, q the elementary charge and p or n are the number of holes or electron per unit volume. At the dynamic equilibrium the two contributions are the same, that means that no net current will flow in the depletion layer. When an ionizing radiation passes inside the depletion layer some electron holes pairs are generated. These charges, as a result of the barrier electric field, migrate towards the electrodes. According to the Shockley–Ramo theorem the motion of the charges inside the semiconductor induces a current in the electrode caused by instantaneous change of electrostatic flux lines.

[2]For more detaliled information see Chapter 2 focused about semiconductor properties.

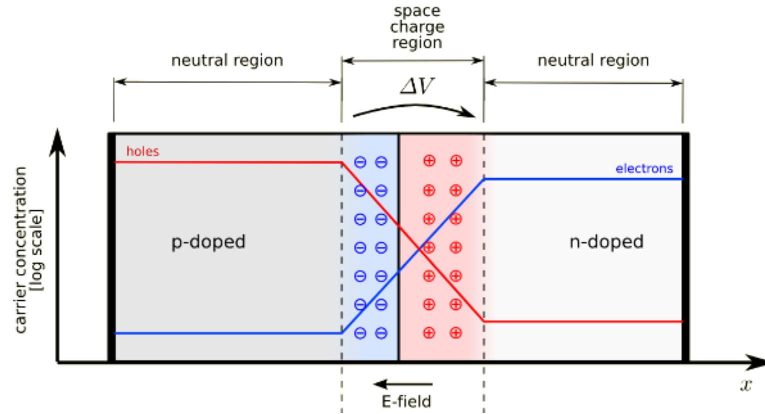

FIGURE 1.16: Schematic representation of a typical p-n junction.

In particular the theorem states that the induced current, i, is:

$$i = E_v q v \tag{1.24}$$

where v is the instantaneous velocity of the moving charge, q is the particle charge and E_v is the component of the electric field in the same direction of v considering an electrode at unit potential while other electrodes grounded.
Note that the electric field, generated naturally along the junction, is not enough to ensure the complete collection of the charges produced by the passage of the radiation. Furthermore, if the thickness of the depletion region is very small the probability of interaction of the radiation inside is limited. For these reasons the junction is reverse biased: it means that an external electric field is added to concordant barrier electric field with a consequent widening of the depletion region and a higher collection efficiency of the produced charges. By increasing the applied voltage, the internal electric field becomes more and more uniform. However there is a threshold, depending on the semiconductor material, that can not be overcome in order to avoid the destruction of the device due to the so-called break-down phenomenon.

1.2 Offline detection system

The above detectors can give an immediate information about the detected radiations and for this reason are also called on-line detector, but there is another typology of devices, the off-line detector, that after the exposition to radiations need a special treatment in order to extract the required informations.

1.2.1 Photographic emulsion

A photographic emulsion consists of a gelatin layer in which are suspended grains of silver bromide (AgBr). Gelatin is deposited on one or on both faces of a support which is usually of cellulose acetate or polyester film. The average size of the grains vary depending on the sensitivity of the emulsion (from 0.5 μm for nuclear emulsion to 2-3 μM for common emulsions). The thickness of the plates varies from few μm to 0.5 mm for the nuclear emulsion, while it is of the order of tens μm for common emulsions. In a silver bromide grain, when it received a sufficient amount of energy, some metal agglomerates of Silver can be formed (Fig. 1.17a), which differ from the electrical point of view from the positive ions Ag^+ of the emulsion grain. The energy to produce this agglomeration of metallic silver is typically of the order of $2 \div 3$ eV. The presence in a grain of one or more agglomerates of silver atoms favors gradually the "reduction" to metallic silver of all other Ag ion of the grain, once this is immersed in the bath of development (Fig. 1.17b). The amplification of the number of metal ions in the development process, respect to the number of those originally produced by radiation is of the order of $10^{10} \div 10^{12}$.

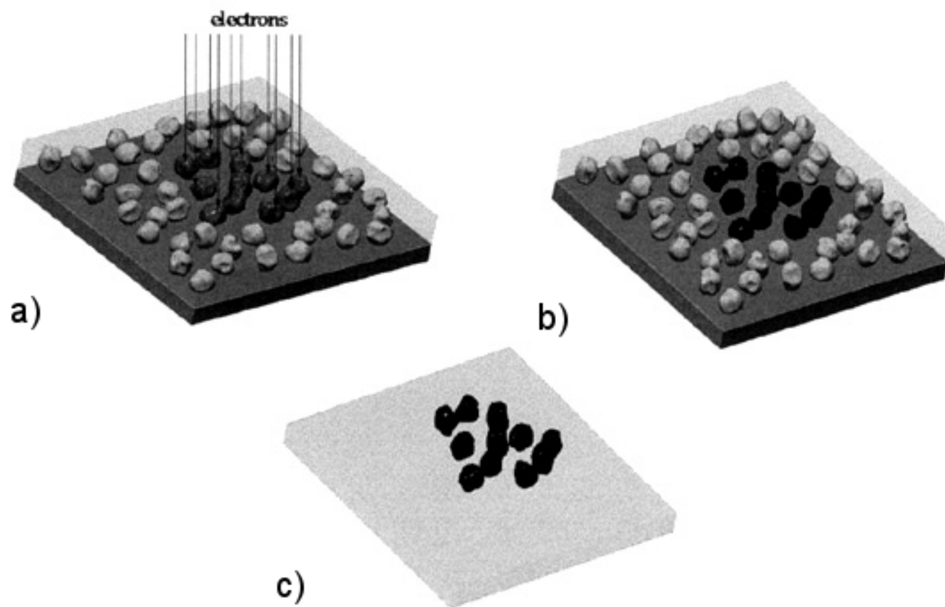

FIGURE 1.17: Processing a Photographic emulsion.

The fixative removes the unexposed, underdeveloped silver bromide grain and subsequent washing removes the excess fixative, obtaining a negative image of the impinging radiations (Fig. 1.17c). Sending on the developed photographic plate a light beam of intensity I_0, by measuring the intensity I that passes through the sheet, the number of the developed grains can be found and consequently the energy lost by the radiation. The "optical density" is the logarithm of the ratio between incident and transmitted

intensity:

$$d = \log_{10}\left(\frac{I_0}{I}\right) \tag{1.25}$$

when $d = 3 \rightarrow I = \frac{I_0}{1000}$ the plate appears almost black. The main property of a photographic emulsion are:

- the "sensitivity" is the inverse of the flow of energy that produces a predetermined optical density. The greater is the sensitivity, the lower is the flow energy necessary to produce a given blackening of the emulsion.
- the "contrast", that is the increase of optical density when the flow of energy is increased by a factor of 10.

The sensitivity of a photographic emulsion depends on the energy of the radiation and has a maximum between 20 and 60 keV, because in this range prevails the photoelectric effect in the silver bromide which has a high Z (Br: $Z = 25$, Ag: $Z = 47$). To increase sensitivity of an emulsion, the films are put in contact with the so-called "intensifying screens", that consists in a material that has fluorescence properties under the action of X-rays: so the sensitivity can be increased by a factor of 50. The photographic emulsions are now mainly used in medical diagnostics and how personal dosimeters for measurement of environmental radiation. In the past they were used extensively as a nuclear track detectors. By making use of a microscope is possible to follow the trajectory of a particle in an emulsion: the higher is the energy of the particle, the longer is the track. Furthermore, if that emulsion is placed in a magnetic field, from the curvature of the particle trajectory can be calculated its momentum and from the length its kinetic energy. A simultaneous measurement of momentum and kinetic energy finally provides the mass of the particle.

1.2.2 Thermoluminescent Dosimeters TLD

Thermoluminescent dosimeters are based on the opposite approach of an inorganic scintillation materials in fact instead to work with the fast fluorescence emission of light due to the quick recombination of eletron-hole pairs, in TLD is strongly favoured the capture of carriers in trapping centres inside the band gap. If the difference in energy between the trapping level and the conduction band is sufficiently large, there is a small probability that the electron, excited from radiation, will escape from the trap in the de-excitation process. Similar considerations are valid also for holes, consequently a TLD works as an integrating detector in which the number of trapped electron and holes is a measure of the number of electron-holes pairs formed by the radiation exposure. After exposition

to radiation, a TLD has to be read through a thermal process in which temperature is progressively increased.

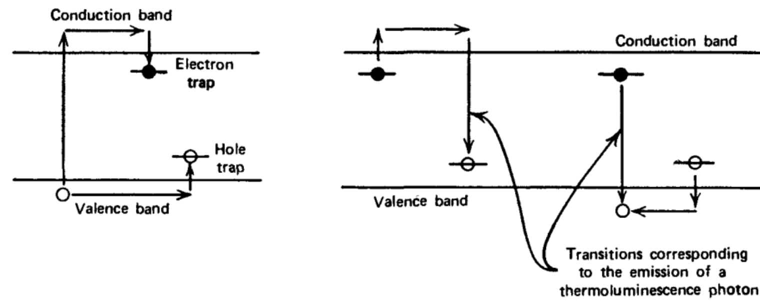

FIGURE 1.18: Formation of an electron-hole pair (a), and illustration of the two possible modes of recombination (b).

There are two different de-excitation process that can occur, according to the height of trap levels: in the first, when the temperature is increased, the trapped electrons can pick up enough thermal energy to be promoted in the conduction band. This temperature will be lower than that required to free the trapped holes, and so the electrons just promoted in the conduction band will migrate and recombine with trapped holes, with the emission of a photon. Instead the second process occurs when the release of a holes is at a lower temperature. Also this process leads to an emission of a radiated photon due to the recombination between the released hole and a trapped electron. Since, ideally, one such photon is emitted per trapped carrier in a TLD system the signal due to the radiation exposition is related with the total number of emitted photon.

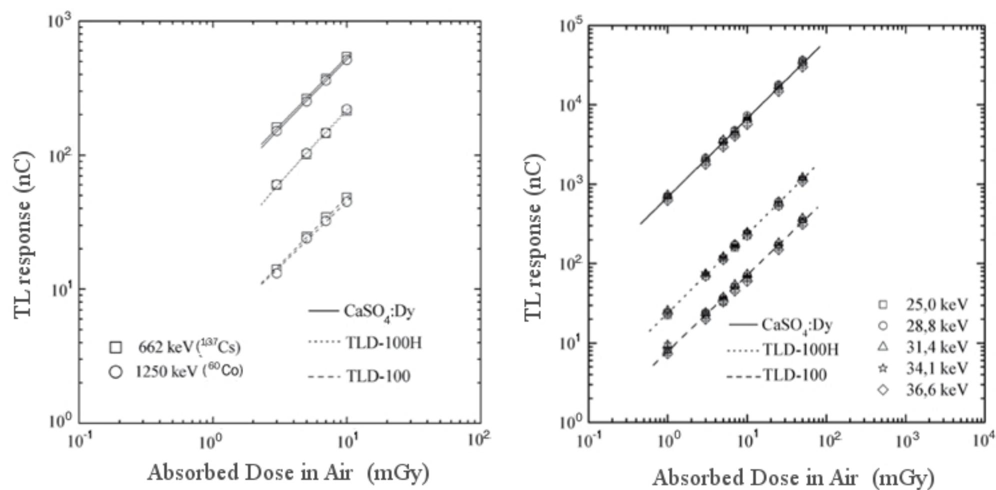

FIGURE 1.19: Thermoluminescent response as a function of absorbed dose in air for different X-rays radiations.

An advantage of this kind of device is the recyclability, because when temperature is sufficiently high, all traps are depleted and the material lost all traces of radiations exposition. Among all the materials that can be employed in a TLD, the most popular is

LiF, with different kind of activators (Mg, Cu, P, Ti) that give the possibility to obtain an emitted light spectrum with a good match with standard photomultiplier.

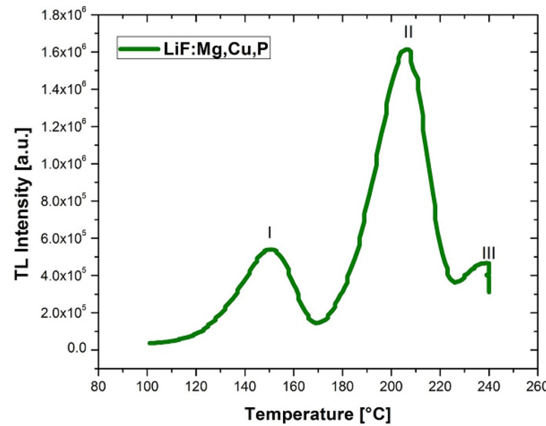

FIGURE 1.20: Glow curve at a dose of 14.6 mGy for LiF:Mg,Cu,P

The main advantage of this material is the close match between the atomic numbers of its constituents and those of soft tissue. For this reason it has come into widespread use as personnel dosimeters. It should be noted that the TL response is strongly influenced by temperature and of course depends by the absorbed dose. Fig. 1.19 reports typical examples of calibration curves [58] for a CaSO4:Dy samples, LiF:Mg,Ti (TLD-100) and LiF:Mg,Cu,P (TLD-100H) devices obtained for different X radiation energies. Instead Fig. 1.20 presents the TL response of a LiF:Mg,Cu,P device as a function of temperature [31]. Moreover thanks to the presence of ^{6}Li, they can also be used as neutron detector using the (n,α) reaction.

1.2.3 Image Plates

An image plate is a position-sensitive radiation detector and as for TLD, the operating principle of an Image Plates is based on the recording of the emitted light due to recombination of electron-holes generated by radiation. However in this case instead of heating the material, a strong light source adds the energy to the trapped charges causing the de-excitation through luminescence states in the so called optically stimulated luminescence. In the simplest approach the excitation source consists in a laser that illuminates for several seconds the sample, and the total excitation light, that has a different wavelength with respect to the laser, is recorded as a function of time as can be seen in Fig. 1.21. In fact using a suitable optical filter the photomultiplier can be shield from the excitation light. Alternatively pulsed light source can be employed. The detector could have a large area (up to 40 cm) and it generally consists in a layer of phosphor.

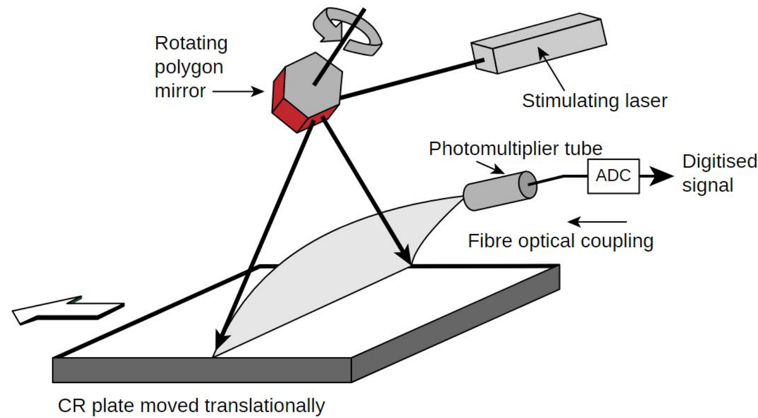

FIGURE 1.21: Typical readout system.

When an incoming radiation interact within the phosphor, it produces storage charges in the near site of interaction. In order to conserve the information about position the readout process is realized with a laser scanning and the emitted photon due to the carrier de trapping is conducted via optical fibers to a photomultiplier. By plotting the intensity of light as a function of the position, finally, it is obtained a digital image, which corresponds to the original pattern of the incident radiation. It should be observed that the spatial resolution is limited by the scattering and diffusion of the laser light inside the thickness of the phosphor layer: but although smaller thickness imply better spatial resolution, a good compromise has to be found for the efficiency of the detector that instead increases with the thickness. Typically commercial image plates have a spatial resolution in the range 100-200 μm with an efficiency that is 100% for X-rays energies up to about 20 keV. Although the image plate is used mainly for X-rays, there are in literature many works showing its applicability for other kind of radiations.

1.2.4 Track-etch detectors

In such material, when a ionizing particle passes, as result of the interaction, some molecules can be damaged along the particle trajectory. This track can be made visible through an etching in a strong acid or base solution. In fact along the paths of damage left by radiation interaction the concentration of damage allows the chemical agent to attack the sample more rapidly than it does in the bulk, revealing the paths of the charged particle ion tracks. The resulting etched sample contains a permanent record of not only the location of the radiation on the plastic but also can gives spectroscopic information about the source, in fact the size and shape of these tracks yield information about the mass, charge, energy, and direction of motion of the particles. Then with a conventional optical microscope it is possible to see the final result.

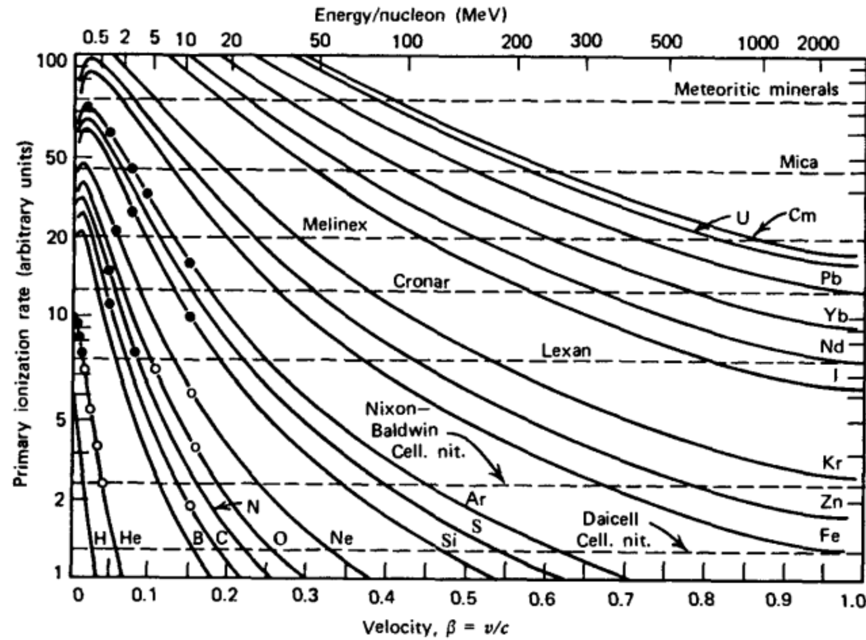

FIGURE 1.22: Relative ionization rate as a function of the energy per nucleon or velocity.

Note that these detector have an intrinsic threshold, since for every particle there is a minimum value of the specific energy loss before the damage is enough to cause an etchable track. This fact defines a specific energy range for every particles, as can be seen in Fig. 1.22. In particular the figure reports the relative ionization rate as a function of the energy and the dashed line indicates the minimum damage rate required for 100% registration of tracks for traditional track-recording materials. The great diffusion of the trach-etch detector is due to the fact that, as for other passive detector, they offer the advantages of simplicity and low cost.

CR-39 track detector

Among the track-etch detector , the most widely used material is the polyallydiglycolcarbonate, also called simply as CR-39, whose structure model is reported in Fig. 1.23. After the radiation exposition it is generally etched with a NaOH solution with concentrations ranging from 2-10 N. To determine the LET[3] value it is need a calibration curve that generally is performed with α-particles or heavily ion. In fact in this way it is possible to found a correlation between the LET value and the etch ratio V, defined as the ratio between the track etching rate and the bulk etching rate. After the scanning of the CR39 surface, once the V-spectrum is obtained and corrected for the angle detection, it can

[3]Linear energy transfer (LET) describes how much energy an ionizing particle transfers to the material traversed per unit distance, and depends not only on the nature of the radiation but also on the material traversed.

be transformed in LET spectra according to the calibration curve of which an example, taken by literature, is reported in Fig. 1.23.

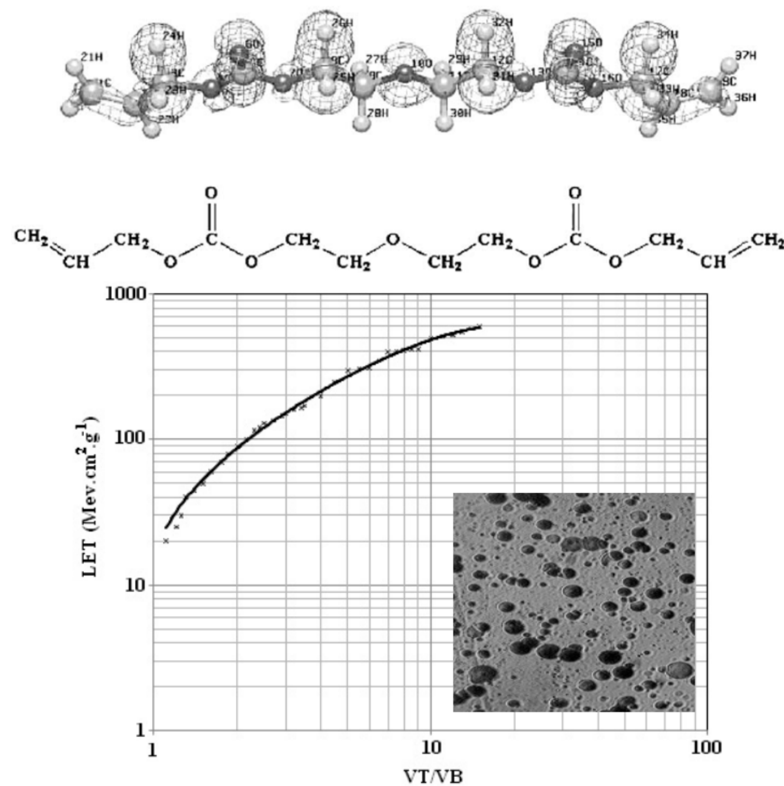

FIGURE 1.23: On the top molecular structure model for the monomer of CR-39, while in the bottom an example of calibration curve, from Ref. [34], obtained from irradiations of ^{12}C (in the inset some typical etched tracks).

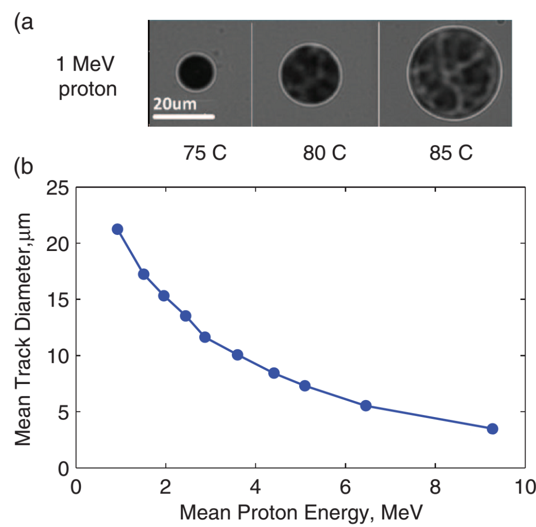

FIGURE 1.24: (a) typical microscope images of 1 MeV proton tracks on CR-39; (b) proton track diameter as a function of incident mean energy for CR-39 etched for 6h in an 80°C solution of 6 N NaOH.

Higher is the particle energy lower is the diameter of the tracks as shown in the literature example [71] of Fig. 1.24. The picture illustrates also the non-uniformity of the track with increasing etchant temperature.

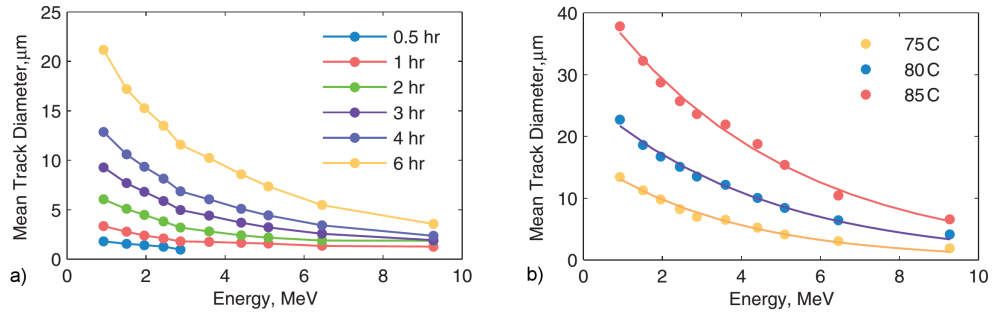

FIGURE 1.25: Proton track diameter as a function of incident mean energy for various etch time (a) and etchant temperature (b).

Besides the etchant temperature the track diameter depends also on the etch time as shown in the two graphs of Fig. 1.25.

1.2.5 GAFchromic films

Ionization chambers and semiconductor materials do not provide an appropriate spatial resolution for many measurements required for treatment planning in radiation therapy. Thermoluminescent dosimetry, even with small dimensions, presents unique dosimetric difficulties and is time consuming. Radiochromic film provides dose measurement at high spatial resolution and has become an important tool to verify dose distributions in highly conformal radiation therapy such as Intensity Modulated Radiation Therapy (IMRT) Recently, a new generation of these films, EBT3, has become available and thanks to its structure (shown in Fig. 1.26) and composition is particularly useful for dose range from 0.2 to 10 Gy, making it suitable for many applications VMAT and brachytherapy.

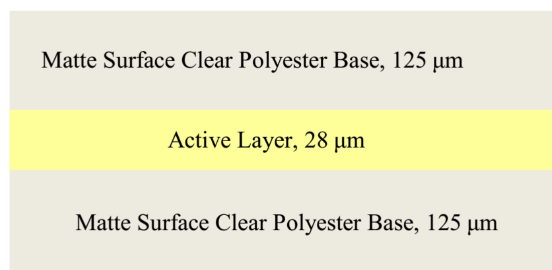

FIGURE 1.26: Structure of a GAFChromic EBT3 film.

The film is comprised of an active layer, nominally 28 μm thick, sandwiched between two 125 μm matte-polyester substrates [15]. The active layer that contains also a marker dye,

stabilizers and other components giving the film its near energy independent response, when it is exposed to radiation reacts to form a blue colored polymer with absorption maxima at approximately 633 nm. The advantage of this film are:

- Develops in real time without post-exposure treatment;
- Minimal response difference from 100 keV into the MV range;
- Near tissue equivalent;
- High spatial resolution with the possibility to resolve features down to 25 μm, or less

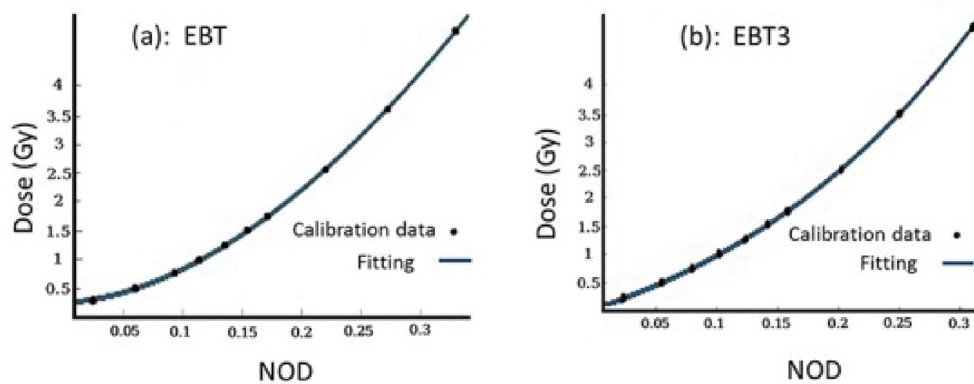

FIGURE 1.27: Calibration curve for EBT (a) and EBT3 (b) films.

An example of calibration curve taken by literature [78] is shown in Fig. 1.27. The fitting formula for dose in Gy as a function of the film's net optical density (NOD), for EBT film follows the equation:

$$D = 33.45\text{NOD}^{1.765} + 0.2389 \tag{1.26}$$

while for EBT3 film is given by

$$D = 75.57\exp(2.609\text{NOD}) - 75.54\exp()2.513\text{NOD}) \tag{1.27}$$

Chapter 2

Semiconductor based detector

In this chapter there will be presented the main important aspects concerning the Schottky barrier junction at the basis of the operating principle of the devices employed in this work. Such devices will then be described, showing the characterization performed on them in terms of leakage current and detection efficiency as a function of energy for the various forms of radiation.

2.1 Theory about Schottky junction

As suggested in the section 1.1.4 of the last chapter, at the base of operation of a semiconductor device, there is the formation of a depleted region without free carrier in which the interaction occurs between the radiation and the material with the consequent formation of the signal. This can be achieved not only at the interface of two types of semiconductor material differently doped (p-n junction), but can be also realized at a metal-semiconductor interface (Schottky or Ohmic junction) or through a metal-insulator-semiconductor.

Certainly the theory of p-n junction is of great importance because these devices are widely used in all modern electronic applications but for the realization of this thesis have been used semiconductors detectors based on Schottky junction and for this reason in the next section there will be shown the main features of this kind of junction.

2.1.1 Schottky Barrier Height

When a metal and a semiconductor are placed sufficiently in contact in such way that they can form a junction two different situations can occur: the formation of a ohmic or

a Schottky junction.

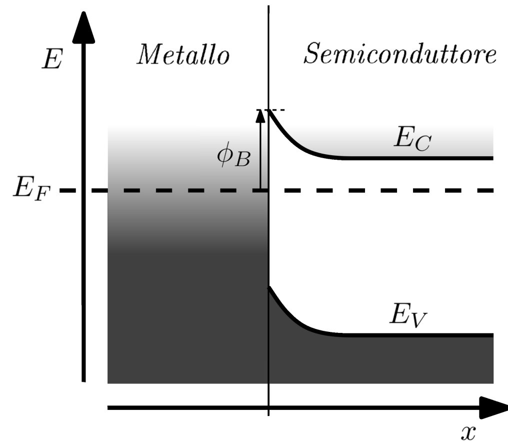

FIGURE 2.1: Representation of the band structure near the metal-semiconductor junction.

To determine if the metal-semiconductor junction belongs to one or the other class is the height of the Schottky barrier with respect to the thermal energy k_BT. The formation of this barrier is essentially due to the deformation of the band structure caused by the alignment of the Fermi levels in the proximity of the junction. Its intensity, ϕ_B, determines the rectifying or ohmic behaviour of the device: for sufficiently large values of ϕ_B, ie when it is significantly higher than the thermal energy k_BT, the semiconductor is depleted near the metal and it behaves as a Schottky barrier; if the height of the barrier takes smaller values, the semiconductor forms an ohmic contact. The rectifying property of a Schottky type junction depends on the extraction work function of the metal, the amplitude of the bandgap and on the type and concentration of dopants in the semiconductor.

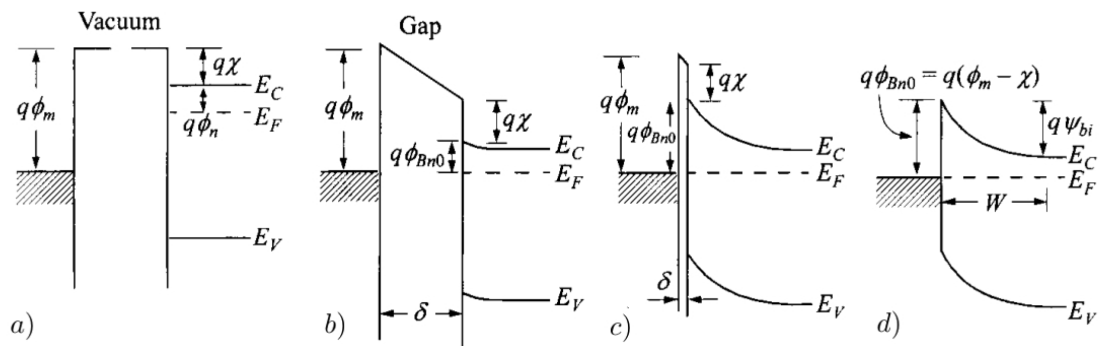

FIGURE 2.2: Deduction of the Schottky-Mott model.

According to the Schottky-Mott theory it is possible to evaluate the energy barrier, ie the product $q\phi_B$ knowing the work function of the metal and the semiconductor, ϕ_m and ϕ_s respectively. The deduction of this model can be explained with the thought experiment

of bringing together a metal and a semiconductor in vacuum, starting from the situation (a) of Fig. 2.2, in which the metal and the n-type semiconductor are initially placed at a certain distance δ. For simplicity consider the ideal case in which no surface state or other anomalies are present. When the two media are put in contact a certain charge will flow from the semiconductor to the metal in order to align the two Fermi levels. With respect to the metal, in the semiconductor the Fermi level is lower of a quantity equal to the difference of the two work function. Note that the work function of a semiconductor is given by the sum:

$$q(\chi + \phi_n) \tag{2.1}$$

where χ is the electron affinity, while $q\phi_n$ is the energy difference between the lower limit of the conduction band and the Fermi level. The potential difference between the two work function:

$$\phi_m - (\chi + \phi_n) \tag{2.2}$$

is defined contact potential. When the parameter δ decreases the electric field between the two materials increases and the surface of metal accumulates a negative charge, while an opposite charge there will be in the depletion region of semiconductor. In the limit $\delta \to 0$, which means when δ becomes comparable with the interatomic distance, the gap becomes transparent to electrons reaching the situation (d) in which:

$$q\phi_B \approx q(\phi_m - \chi). \tag{2.3}$$

Consequently in the contact region between a metal and an n-type semiconductor:

- if $\phi_m > \phi_s$, a rectifying contact is generated with the formation of a barrier in the propagation of electrons in both directions. In particular, the barrier to the movement of electrons from the semiconductor to the metal is equal to the difference $\phi_m - \phi_s$, while the barrier for the opposite current, from the metal to the semiconductor, is equal to $\phi_B = \phi_m - \chi$.

- $\phi_m < \phi_s$ there is no barrier in the conduction band and consequently the nature of the contact is ohmic.

Although there is a certain correspondence because for higher values of the work function correspond higher values of barrier, the Schottky-Mott model is not effectively support from all the experimental results. In fact in many of these, Schottky barrier heights seems to be influenced by the preparation of the metal-semiconductor interface. Generally, the discrepancy between theory and experimental data is justified through the so-called Fermi level pinning phenomenon, which makes the height of the Schottky barrier almost insensitive to the work function of the metal. Cowley and Sze introduced this

phenomenon, [25], that is due to the presence of interface state located between the metal and the semiconductor. The interface state create strong quantum dipoles and absorb a certain amount of charges coming from the metal and this leads to the shielding of the semiconductor. Taking into account these consideration, the barrier height for n-type semiconductor-metal contact can be written:

$$\phi_B = \gamma(\phi_m - \chi) + (1 - \gamma)(E_g - \phi_0) - \Delta\phi_n \tag{2.4}$$

where ϕ_0 is the energy below which the surface state must be filled for charge neutrality at the semiconductor surface, $\Delta\phi_n$ is the image charge barrier lowering[1] and γ is a weight factor which depends on the surface state density and the thickness of the interface layer. Are interesting the two limit case in which $\gamma = 0, 1$. In the first case:

$$\phi_B \approx (E_g - \phi_0) - \Delta\phi_n \tag{2.5}$$

the Fermi level at the interface is pinned by the surface states at the value ϕ_0 above the valence band. The barrier height is independent of the metal work function, and is determined entirely by the doping and surface properties of the semiconductor. In the second case:

$$\phi_B \approx (\phi_m - \chi) - \Delta\phi_n \tag{2.6}$$

when the surface effects are neglected the Schottky-Mott model is obtained. By means of energy minimization processes it is possible to derive profiles interface, taking into account the presence of these states, justifying a whole series of systematic experiments.

TABLE 2.1: Barrier height from I-V methods and Ideality factor of 4H-SiC n-type Schottky contact for various metal measured at 300 K.

Face	Metal	Barrier Height (eV)	Ideality factor
C-	Ti	1.16	1.02
Si-	Ti	0.8	1.15
Si-	Ti/Au/Pt/Ti	1.17	1.09
Si-	TiW	1.22	1.05
Si-	Ni_2Si	1.4	1.1
Si-	Cu	1.6	1.1
Si-	Au	1.73	1.02
C-	Au	1.8	1.02
Si-	Ni	1.3	1.21
C-	Ni	1.6	1.02
Si-	Pt	1.39	1.01

[1] This effect of reduction of the barrier height is due to the fact that when an electron approaches a dielectric medium, induces a positive charge on the interface which acts like an image charge within the layer.

A list of Schottky barrier height and the ideality factor of 4H-SiC n-type Schottky contact with different metals, from studies reported in literature [110], are shown in Tab. 2.1. These data were evaluated by studying the changes of the diode current as a function of the applied voltage, using the so called I-V methods. Note that there are differences in the barrier heights between Si- and C-faces, and the barrier heights for C-faces are in general 0.1 to 0.3 eV larger than those for Si-face.

2.1.2 Depletion Layer

As a consequence of the passage of electrons from the doped semiconductor to the metal, a charge space region is created, completely emptied of mobile charges. For this reason the charge density in that region is due to the ionized donors that equals the donor density N_D in full ionization condition. Assuming that the semiconductor is neutral outside the depletion layer, and adopting the full depletion approximation, the charge density ρ can be written:

$$\rho(x) = qN_D \qquad 0 < x < x_d$$

$$\rho(x) = 0 \qquad x_d < x$$

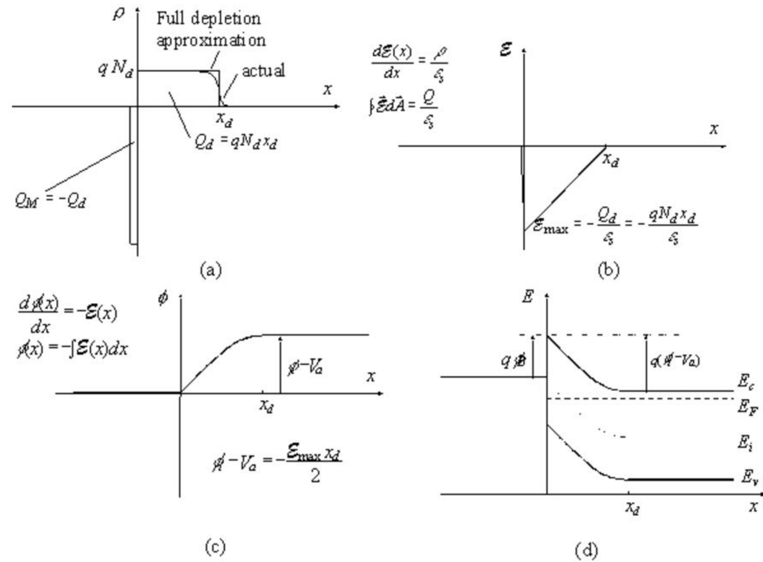

FIGURE 2.3: Behaviour of charge density (a) , electric field (b), potential (c) and energy (d) across the junction.

To obtain the electric field across the junction, the Gauss's law can be employed giving:

$$E(x) = -\frac{qN_d}{\varepsilon_s}(x_d - x) \qquad 0 < x < x_d$$

$$E(x) = 0 \qquad x_d \leq x$$

Obviously only inside the depletion region can exist an electric field, because outside a non-zero filed would case the mobile carriers to redistribute until there is no field. As reported in the maximum value of the electric field Fig. 2.3 is achieved in the interface where:

$$E(x=0) = -\frac{qN_D x_d}{\varepsilon_s} = -\frac{Q_d}{\varepsilon_s} \tag{2.7}$$

where Q_d is the total charge per unit area in the depletion layer. By integrating the last expression the potential across the junction $\phi(x)$ obtained:

$$\phi(x) = 0 \qquad x \leq 0$$

$$\phi(x) = \frac{qN_d}{2\varepsilon_s}[x_d^2 - (x_d - x)^2] \qquad 0 < x < x_d$$

$$\phi(x) = \frac{qN_d x_d^2}{2\varepsilon_s} \qquad x_d \leq x$$

Even if the total amount in charge is the same in metals and in the semiconductor, the thickness of the charge layer is very thin in metal because the density of free carriers is very high with respect to semiconductor and consequently the potential across the metal can be neglected. At the interface the potential $\phi(x=0)$ will be the sum of the built-in potential ϕ_i and the applied voltage V_a:

$$\phi_i - V_a = -\phi(x=0) = \frac{qN_d x_d^2}{2\varepsilon_s} \tag{2.8}$$

and finally solving for x_d :

$$x_d = \sqrt{\frac{2\varepsilon_s}{qN_d}(\phi_i - V_a)} \tag{2.9}$$

So the depth of this region, generally called depletion layer, is essentially determined by

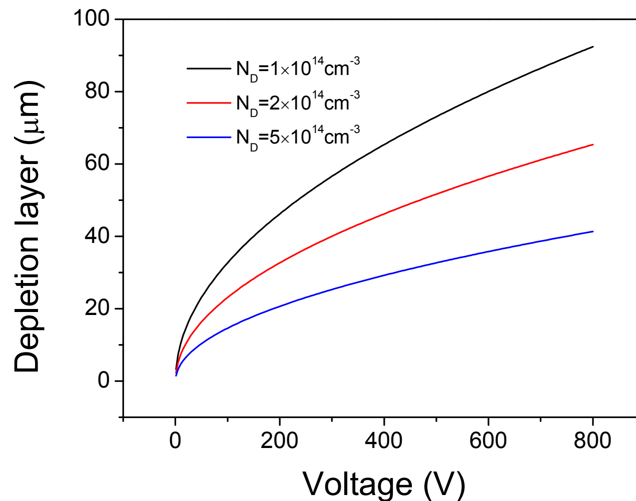

FIGURE 2.4: Depletion layer thickness as a function of the reverse bias voltage.

the doping concentration of the semiconductor N_D and the reverse voltage V_0 applied to the contact of the detector. It is an essential features of a detector because the depletion region represents the active volume in which a radiation can be detected. In Fig. 2.4 are reported the prevision for the behaviour of the thickness of the depletion layer as a function of the reverse bias voltage applied to the detector for three different values of doping concentration.

2.1.3 Capacitance and Resistance in the depletion region

It is also possible to evaluate the capacitance of the junction through the derivative of the charge with the applied voltage:

$$C = \left| \frac{dQ_d}{dV_a} \right| = \sqrt{\frac{q\varepsilon_s N_d}{2(\phi_i - V_a)}} = \frac{\varepsilon}{x_d} \tag{2.10}$$

From last equation it is possible to see that the devices can be modelled as a parallel plate capacitor.

As concerns the resistance, directly from the second Ohm's law:

$$R = \rho \frac{x_d}{S} \tag{2.11}$$

where S represents the diode surface and ρ is the resistivity of the material that for a doped semiconductor is given by:

$$\rho = \frac{1}{q\mu N_D} \tag{2.12}$$

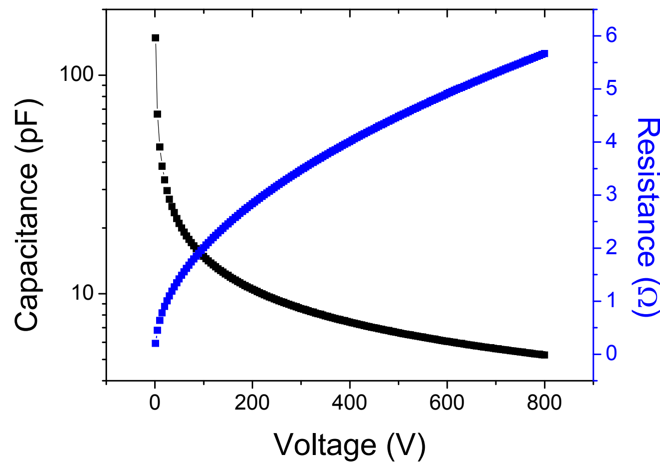

FIGURE 2.5: Estimates of resistance and capacitance as a function of the reverse bias voltage.

As an example in Fig. 2.5 are reported the theoretical resistance and capacitance as a function of the reverse bias voltage, considering:

- doping concentration of $N_d = 2 \times 10^{14}\,\mathrm{cm}^{-3}$;

- electron mobility $\mu = 900\,\mathrm{cm}^2/\mathrm{V\ s}$;

- diode surface $S = 0.04\ \mathrm{cm}^2$;

- relative dielectric constant ε_{SiC}=9.66;

- barrier height $\phi_B = 1.5$ eV.

2.1.4 Schottky diode current

There are three distinctly processes that determine the current flow across a metal-semiconductor junction: the diffusion current, the thermionic emission and the tunneling effect. Assuming that the depletion layer is larger than the mean free path, the current density due to the diffusion of carriers from the semiconductor into the metal can be written:

$$J_n = \frac{q^2 D_n N_c}{V_t}\sqrt{\frac{2q(\phi_i - V_a)N_d}{\varepsilon_s}}\exp\left(-\frac{\phi_B}{V_t}\right)\left[\exp\left(\frac{V_a}{V_t}\right) - 1\right] \tag{2.13}$$

where, ϕ_i is the built-in potential, ϕ_B is the barrier height, and D_n is the diffusion constant and is related with V_t:

$$D_n = \mu_n \frac{k_B T}{q} = \mu V_t \tag{2.14}$$

According to the thermionic emission, electrons that move towards the barrier with an energy equals to or larger than the top barrier can cross it, contributing to the current flow. In this case, ignoring the actual shape of the barrier this current can be expressed as:

$$J_n = A^* T^2 \exp\left(-\frac{\phi_B}{V_t}\right)\left[\exp\left(\frac{V_a}{V_t}\right) - 1\right] \tag{2.15}$$

where A^* is the Richardson constant:

$$A^* = \frac{4\pi q m^* k^2}{h^3} \tag{2.16}$$

Finally the third contribution that is the tunneling current that can be written:

$$J_n = q v_R n \Theta \tag{2.17}$$

where n is the density of available electrons, v_R is the Richardson velocity, ie an average velocity at which electrons approach the metal-semiconductor interface and is given by:

$$v_R = \sqrt{\frac{k_B T}{2\pi m}} \tag{2.18}$$

and Θ represents the tunneling probability that is proportional to $\phi_B^{3/2}$. In Fig. 2.6 are summarized a set of experimental data reported in literature [13] comparing the current densities of several semiconductor materials.

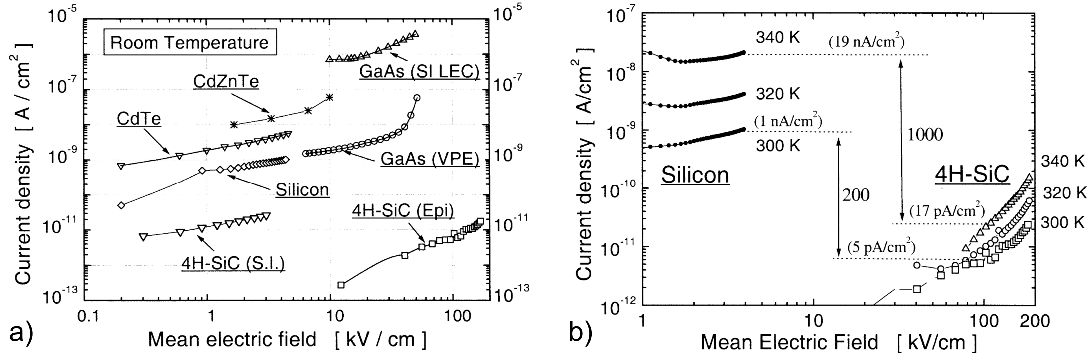

FIGURE 2.6: Current density at room temperature (a) and comparison between current densities of 4H-SiC and Silicon at different temperatures (b).

From this comparison are evident the advantages of Silicon Carbide based detector. In particular, in Fig. 2.6a, were taken into account the leakage current densities at room temperature for Silicon, GaAs grown for the Vapor Phase Epitaxy (GaAs VPE), GaAs Semi-Insulanting grown for the Liquid Encapsulated Czochralski (GaAs SI-LEC), Cadmium Telluride (CdTe), Cadmium Zinc Telluride (CdZnTe), semi-insulating silicon carbide (4H-SiC S.I.), and epitaxial Silicon Carbide (4H-SiC epi). Is very interesting the fact that the 4H-SiC epitaxial detector shows current densities, at room temperature, more than two orders of magnitude lower than those of the other detectors. This is verified although the SiC detector operates at the highest electric fields, up to 170 kV/cm. The ultralow current density is an important aspect since it can yield a very low current noise even in large-area detectors. This feature can fully compensate the lower signal delivered by SiC detectors. In addition, the possibility to apply such high electric fields without junction breakdown and with low current is advantageous for reducing the charge drift time, so having fast signals and low probability of the charge trapping, that significantly affects the performance of most compound semiconductor detectors. In Fig. 2.6b are compared the current density versus the junction internal electric field characteristics measured at 300, 320, and 340 K for SiC and Silicon detector. The SiC current density at 100 kV/cm, varies from 5 pA/cm at 300 K to 17 pA/cm at 340 K, while for the silicon device, the measured values at 3.5 kV/cm vary from about 1 nA/cm at 300 K to 19 nA/cm at 340 K. The ratio between the current densities in Si and SiC diodes changes from 200 to 1000 as the temperature increases from 300 to 340 K.

2.2 Silicon Carbide based detectors

Nowadays there is considerable evidence of the importance of semiconductors technology because in many fields, from engineering to medicine, it plays a very important rule.

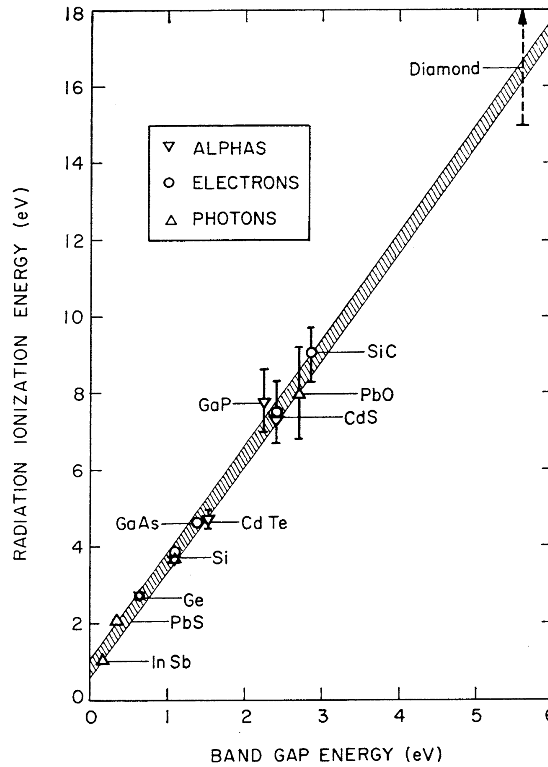

FIGURE 2.7: Ionization energy and bandgap for various semiconductor detector.

Certainly silicon is the most developed and employed material, with a very high level of competitiveness and a wide standardization of the industrial processing. In Fig. 2.7, are reported for comparison the correspondence between the energy bandgap and the radiation ionization energy for a wide class of semiconductor materials. However Silicon imposes several limits in applications which include high temperatures and high doses encouraging the development of devices with wide band gap. Between these, the most promising is 4H-SiC that has been long identified as a radiation hard and physically rugged material with superior electronic properties which are appropriate for nuclear radiation detection purpose and plasma monitoring. Due to the high energy gap (3.26 eV) with respect to Silicon (1.12 eV), SiC does not detect the high visible intensity radiation emitted from plasmas but it detects very well UV, X-rays, electrons and ions with high signal-to-noise ratio also at room temperature thanks to its very low leakage current in the order of pA. Moreover 4H-SiC has a higher value of breakdown electric field (3 MV/cm) and thermal conductivity (4 W/cm°C) with respect to Silicon (0.25 MV/cm and 1.5 W/cm°C, respectively), giving the possibility to employ SiC as high power and

high voltage devices. Another important aspect is the fact that the bonding Silicon-Carbon are stronger than Silicon-Silicon ones, consequently the displacement energy in SiC (25 eV) is higher respect to silicon (16.5 eV). For this reason SiC devices have a greater resistance to damage due to radiation detection. In addition SiC operates at high temperatures (up to 1240 C°) and it has an high response velocity and a fast collection time thanks to high electrons ($\sim$ 900 cm^2/V s) and holes ($\sim$107 cm^2/V s) mobility. However the mean energy necessary to produce an electron-holes pair is lower in Silicon (3.63 eV) respect to 4H-SiC (7.78 eV) so by sending the same radiation to the two devices, in the silicon detector a greater number of electron-holes pairs will be produced with respect to SiC ones. A comparison between the main physical property for different material of interest is reported in table 2.2.

TABLE 2.2: Comparison of the most common physical property for materials of interest.

Physical property	**4H-SiC**	**Silicon**	**GaAs**	**Diamond**
Crystal structure	Hexagonal	Diamond	Zinc-blende	Diamond
Band gap [eV]	3.26	1.12	1.43	5.45
Density [g/cm^3]	3.21	2.33	5.32	3.52
Electron mobility [cm^2/Vs]	800-1000	1450-1500	8500	1800-2200
Holes mobility [cm^2/Vs]	100-115	450-600	400	1200-1600
Breakdown electric field [MV/cm]	2.2 – 4.0	0.2 – 0.3	0.3 – 0.6	10
Mean e-h pair energy [eV]	7.78	3.63	4.21	13
Thermal conductivity [W/cm °C]	3.0 – 5.0	1.5	0.5	20
Max working temperature [°C]	1240	300	460	1100
Effective atomic number	12.54	14	32.06	6
Displacement energy [eV]	25	13-20	15.5	43

2.2.1 Typical structure of a SiC Schottky barrier detector

In Fig. 2.8 is reported a schematic view of a simplified diode structure. It consists in a first metallization layer with a thickness that can range from 20 to 200 nm.

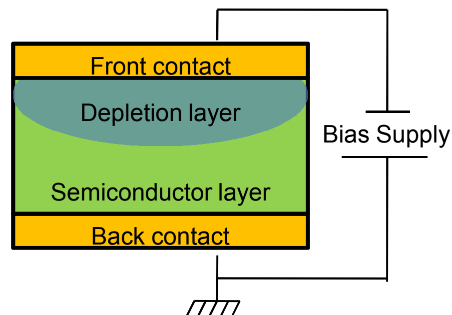

FIGURE 2.8: Simplified structure of a silicon carbide detector.

It generates the metal-semiconductor interface and on it is applied the reverse bias voltage to increase and to make uniform the depletion layer that extends in the lower lightly doped silicon carbide layer ($N_D \sim 10^{14}\,\mathrm{cm}^{-3}$). This n^- SiC layer is grown by epitaxy on a second highly n^+ doped SiC substrate ($N_D \sim 10^{18}\,\mathrm{cm}^{-3}$). Finally an Ohmic contact is formed on the backside of the diode to electrically connect the device to ground. The thickness of the top metallization and the width of the depleted region are essential parameters that define a specific windows in the detectable particle energy. On the one hand if a particle does not reach the depleted region, losing all of its initial energy in the top metallization layer, it will not produce any electron-hole pair. On the other hand if the particle has too energy, it will cross the entire region, losing just one fraction of the total energy. Considering the case of proton impinging on an imaginary detector that has a superficial metallization of 600 nm and an active SiC region of 4 μm on a SiC substrate layer. Proton of 150 keV, as can be seen in Fig. 2.9, lost all of their energy almost entirely in the metallization as confirmed by the Bragg curve reported on the left. If protons have too energy, 850 keV, they are able to overcome the sensible region, losing in it only the 30 %.

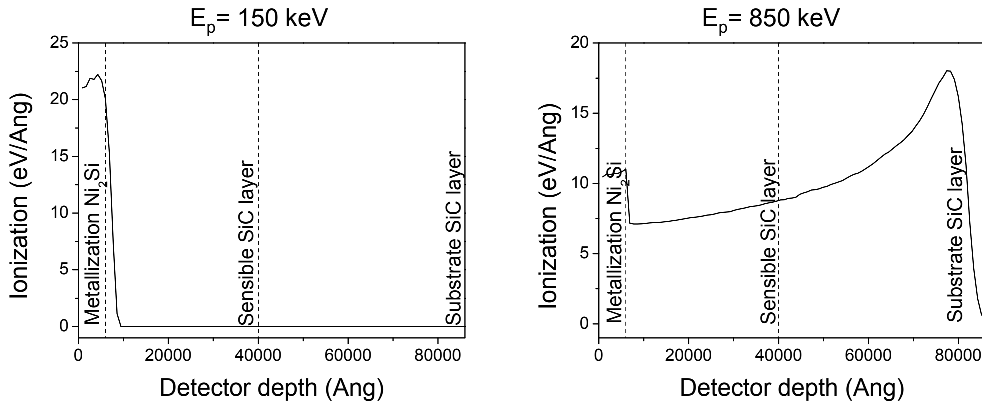

FIGURE 2.9: Simulation of the Bragg peak for proton of 150 keV and 850 keV, respectively into a silicon carbide detector.

Taking into account that the different mechanism through which particles lose energy, according to the nature of the particle, there will be different detectable energy range for each kind of particle. For this purpose there are many simulation codes, software or web databases [11, 40, 112], that allows to recreate the same conditions helping in the definition of this detectable energy. In particular in this thesis have been employed:

- CXRO for photons, [1];
- eSTAR web databases for electrons, [2];
- SRIM2013 for protons and heavier atoms, [3].

The obtained results are logically dependent from the simulated diode structure and for this reason are reported in the next section where SiC detector are discussed.

2.2.2 SiC AZ 80

Many types of SiC detectors have been employed in the preparation of this work. The first one, called SiC AZ 80, has a very thick metallization of nickel silicide (Ni_2Si), about 200 nm in the input contact. The active region of n^- type 4H-SiC has a depth of about 80 μm, Fig. 2.10a. This device has already been widely used and reported in literature [56], for many applications such as the diagnostics of laser plasmas. In this contest it is particularly useful due to its excellent qualities of resistance to damage induced by radiation and for its geometric characteristics, good active surface and thick sensible region. Fig. 2.10b reports a picture of the diode, while in Fig. 2.10c there is a typical I-V characterization that testifies, as expected, a very low leakage current in the reverse bias regime, in the order of nano amperes.

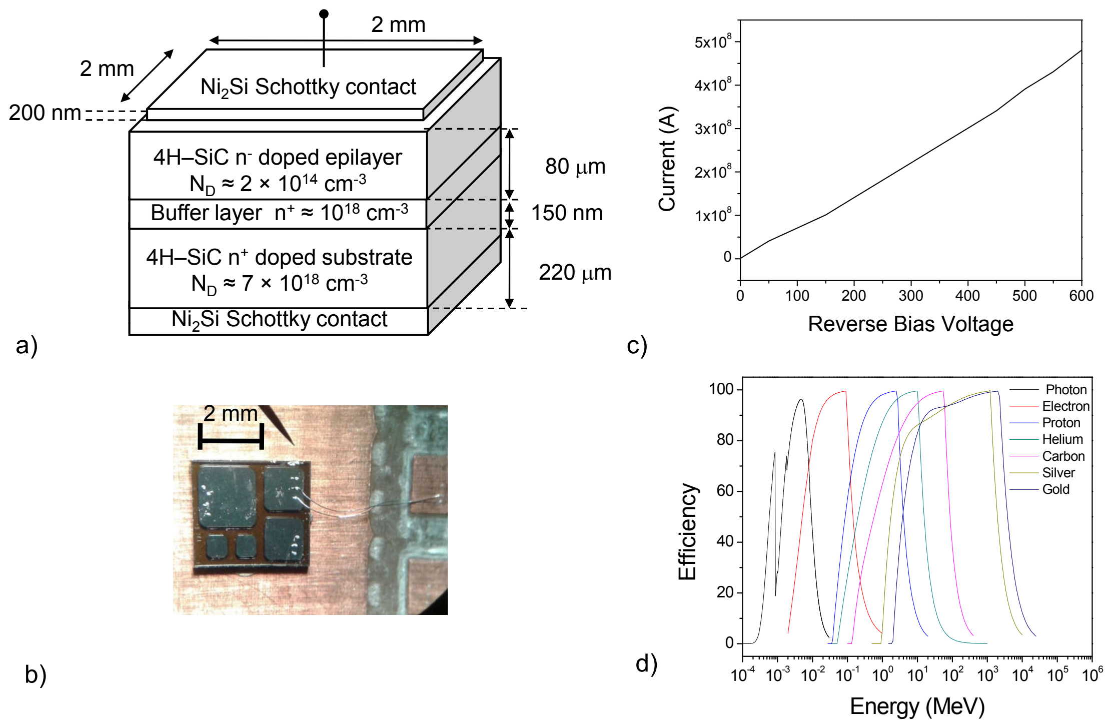

FIGURE 2.10: (a) Schematic of the geometry for the SiC AZ 80 diode, (b) picture of the device, (c) I-V curve characterization and (d) simulated efficiency curves for photons and protons.

In addition it was investigated the response curve of the detector as a function of the energy of the incident radiation, and in Fig. 2.10d there are the results for photons and protons. This analysis was performed with the above mentioned software. In particular for X-rays were combined the transmission and absorption coefficients of the metallization and of the SiC epilayer, respectively. Unfortunately in this detector a very high voltage, ($\sim$ 800 V) has to be applied, in order to fully deplete the active region. This fact limits

the usage of the detector at high vacuum condition. Moreover the thickness of the metallization layer reduce efficiency of lower energetic ions.

2.2.3 SiC AZ 25

In the second SiC device, called SiC AZ 25, the thickness of the metallization was reduced about 20 nm (Fig. 2.11a). Moreover because the SiC epilayer in this case is 25 μm also the reverse bias voltage that has to be applied to the detector is reduced, about -100 V. How can be seen from the efficiency curves reported in A disadvantage of this detector is the very little active surface ($\sim 1\,\text{mm}^2$), as can be seen from Fig. 2.11b. However this problem can be solved if more diode are put in parallel in the readout electronics, leading to an increase of the total active surface also because the leakage current of each diode is very low, Fig. 2.11c. Finally the specific geometry allows to stop and correctly detect proton up to 2.5 MeV, Fig. 2.11d.

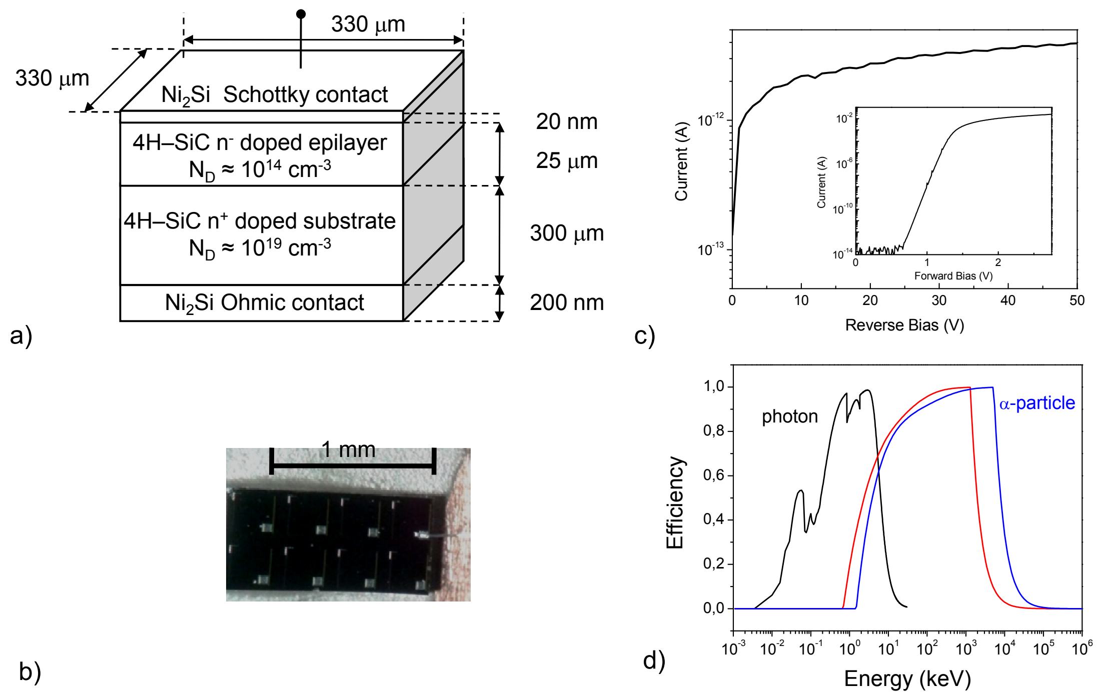

FIGURE 2.11: (a) Schematic of the geometry for the SiC AZ 25 diode, (b) picture of the device, (c) I-V curve characterization and (d) simulated efficiency curves for photons and protons.

2.2.4 SiC IAZ 4

However it should be noted that in order to detect very low energy ions, electrons and UV, the only solution is the partially removal of the top metallization. This was done in

the third device called, SiC IAZ 4, because presents a particular interdigited geometry of contact, explained in Fig. 2.12a and Fig. 2.12b. This fact allows to leave a part of the surface directly exposed to radiation (about 70 %). The strips were realized with a particular photolithographic systems. The I-V curve, in Fig. 2.12c shows again a very low value of leakage current and the simulated efficiency curves indicating a maximum proton energy of about 500 keV because the thickness of the depletion layer is only 4 microns. The disadvantage of this device is the non-uniform metallization that produces an inevitable enlargement of the energy in the spectra of the detected ions with with a inevitable worsening of the energy resolution of the detector.

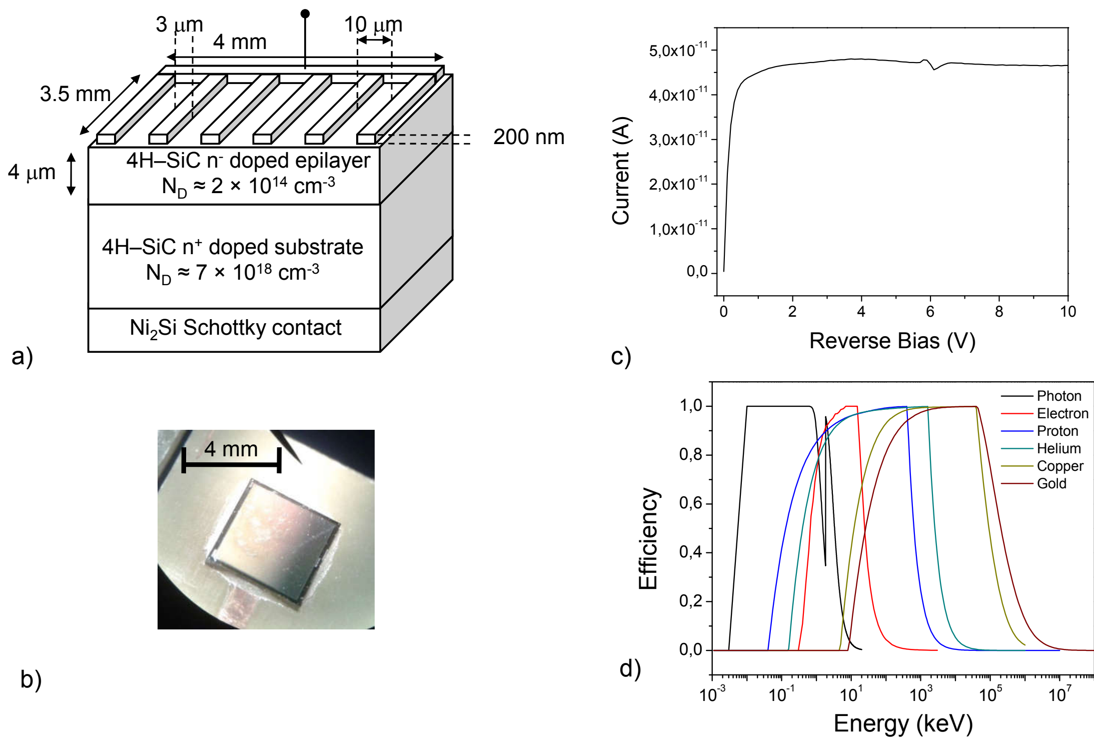

FIGURE 2.12: (a) Schematic of the geometry for the SiC IAZ 4 diode, (b) picture of the device, (c) I-V curve characterization and (d) simulated efficiency curves for photons and protons.

2.2.5 Production of the silicon carbide detectors

In order to enhance the sensitivity at short wavelengths, Schottky diodes are preferred to p-i-n diodes, as the carrier generation occurs in the space-charge region, i.e., at the semiconductor surface, with high built-in electric field. Moreover Schottky diodes are majority carrier devices, thus allowing a faster response than p-n junctions. Finally, Schottky diodes involve simpler fabrication processes than p-i-n structures. The Schottky-type diodes were fabricated at the STMicroelectronics (Catania-Italy) clean room facilities using 4" diameter 4H-SiC epitaxial wafers produced by E.T.C grown onto a heavily

doped substrate. In particular SiC epitaxial layers were grown using a chemical vapor deposition technique [45], which is the most promising method in obtaining thick films. This process is carried out by heating single crystalline SiC substrate wafers in a horizontal hot wall reactor (ACiS M8 by LPE) with flowing of silicon and carbon containing gas precursors that decompose and deposit on the wafer substrate allowing the growth of an ordered single crystal layer. The process is carried out using a temperatures of 1600°, pressure of about 1 bar and silane (SiH_4) and ethylene (C_2H_4) as gas precursors. Moreover in order to reach a very high growth rate, HCl is added to the gas precursors, avoiding the homogeneous silicon nucleation. The growth of very thick layers is an important point in the realization of radiation detectors at least for X-rays and high energy ions; however, the performance of the detectors depends mainly on the epilayer crystalline quality. The process has been improved with the optimization of all the growth parameters, such as temperature, C/Si ratio and Cl/Si ratio, in order to improve the quality of the epilayers and to minimize the defect concentration. The realization of very high breakdown voltage devices needs low dopant concentration and good uniformity. In the growth of n-type SiC epilayers, nitrogen is the most used atom for n-type doping and its intrinsic concentration is dependent on the C/Si ratio as shown in Fig. 2.13.

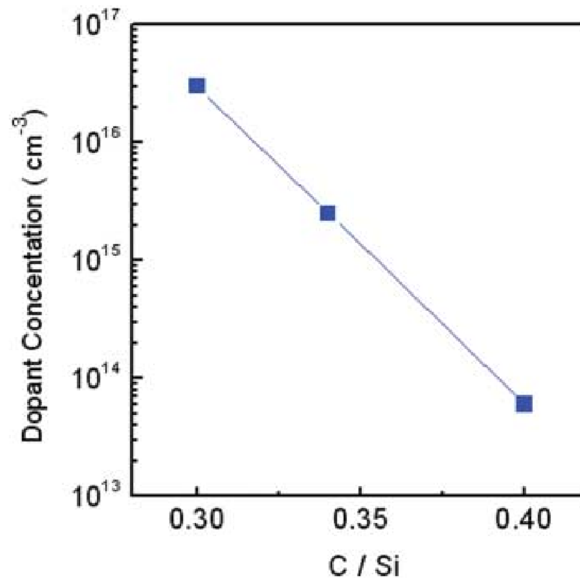

FIGURE 2.13: Intrinsic doping concentration versus the C/Si ratio, [17].

The dopant concentration, for a fixed value of doping precursors flux, depends strongly on the C/Si ratio because of the competition mechanism between n-type doping and carbon vacancy, as the nitrogen atom occupies the carbon site being its electro-negativity and tetrahedral radius close to that of carbon. Using this process it is possible to obtain SiC epilayer more than 100 μm thick, low doped ($<10^{14}$ cm^{-3}) and of excellent crystalline

quality (almost defect free), by using the optimized growth parameters such as Cl/Si ratio of 2.0 and C/Si ratio around 0.4.

After the epilayer growth, the main step to carry out is the formation of ohmic (back of the wafer) and Schottky contacts (wafer front). The ohmic contact on the sample rear, used to carry electrical current ideally without any parasitic resistance, is obtained by depositing 100 nm of Ni in a ultra-high vacuum (UHV) chamber followed by rapid thermal annealing at 950 °C. During thermal treatment, a 200 nm thick nickel silicide (Ni_2Si) is formed and the measured ohmic resistivity result is $10^{-5}\,\Omega$cm [63].

The most important parameters of the top metal–semiconductor Schottky contact are the Schottky barrier height (SBH), the ideality factor and the breakdown voltage. The SBH must be high enough to have low leakage current, the ideality factor close to 1.0 and the breakdown voltage as high as possible. The leakage current must be very low, ideally due only to the thermo-generated carrier over the junction barrier. In addition the metal–semiconductor interface must be uniform and without defects as their presence reduces the barrier, increases the leakage current and reduces the reverse breakdown voltage. In order to realize the two different geometries of contact, interdigited or uniform, different techniques are employed. To realize the uniform metallization it is necessary to combine standard optical lithograpy and highly selective metal etch, while in the second case a photolitography technique is employed. The diodes are then annealed at 600 °C, in a rapid thermal processing, for the formation of Ni_2Si, to improve the Schottky barrier properties and the uniformity of the Schottky barrier with respect to that of pure Ni. It should be observed that in general the leakage current is related not only to the barrier characteristic, but also to the crystallographic quality of the epitaxial layer. In fact the defects act as recombination centers for the e–h pairs and as scattering centers for the charge carriers, causing a decrease in the detector efficiency.

In order to reach high breakdown voltage with the lowest current an edge termination technique is also employed.

Edge terminations, as illustrated in Fig. 2.14, are realized by using highly resistive crystalline layers formed by B^+ implantation and subsequent annealing. Under forward bias condition, there was no significant difference, in terms of SBH and ideality factor, between the devices with and without edge terminations. In reverse bias condition, the leakage current in the device without terminations was higher, due to the electrical field concentration at the edge of the device, and the breakdown occurs at 500 V. Instead, the devices with edge terminations show a lower leakage current (about three orders of magnitude) and the breakdown occurs at 1100 V.

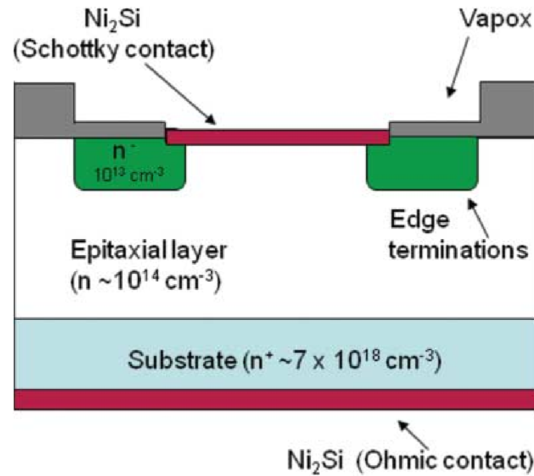

FIGURE 2.14: Schematic structure of a typical SiC Schottky diode.

2.3 Diamond detector

Monocrystalline diamonds are gaining considerations as radiation detectors thanks to their physical and electronic properties allowing the production of high power and frequencies devices. Such as for silicon carbide detector, diamonds are grown through chemical vapor deposition (CVD) technique, giving the opportunity to obtain low defects and low concentration of impurities. As reported in Tab. 2.2, diamond exhibits peculiar physical properties such as the high hardness with a displacement energy of (43 eV), high atomic density (3.51 g/cm^3) high band gap (5.45 eV), high energy to produce e-h pair (13 eV), high thermal conductivity (20 W/cmK), very high breakdown electric field (10 MV/cm), high electron mobility ($\sim$ 1800 cm^2/Vs), high hole mobility ($\sim$ 1200 cm^2/Vs), and high radiation hardness, crystallinity and chemical inertness. The doping of diamond is generally done with boron, that introduces energy levels in the bandgap. The boron-doped diamond (BDD) allows to obtain an interesting device with low dark current, high sensitivity to the charges produced in the active volume, high chemical stability also under extreme environmental conditions, high optically transparence to the visible light, high mechanical resistance and high biocompatibility. Thanks to its excellent qualities diamonds device have been used for many applications, such as for detectors of soft and hard X-rays, for neutrons, for detectors of electrons and ions, as water equivalent dosimeters in radiotherapy, for plasma diagnostics in laser-matter interaction, for radiation detectors working in harsh environments (high temperature, high radiation doses, high chemical reactivity, ...). As can be see from the structure in Fig. 2.15a, the high B-concentration doping ($\sim$10^{19}/cm^3) is employed to improve the ohmic contact of the diamond layers near to the electric contact, while the B-doping at low concentration ($<$ 10^{15} atoms/cm^3) is needed for the formation of the Schottky metal-semiconductor barrier. Usually, the diamond detectors is covered with two conductive films to realize

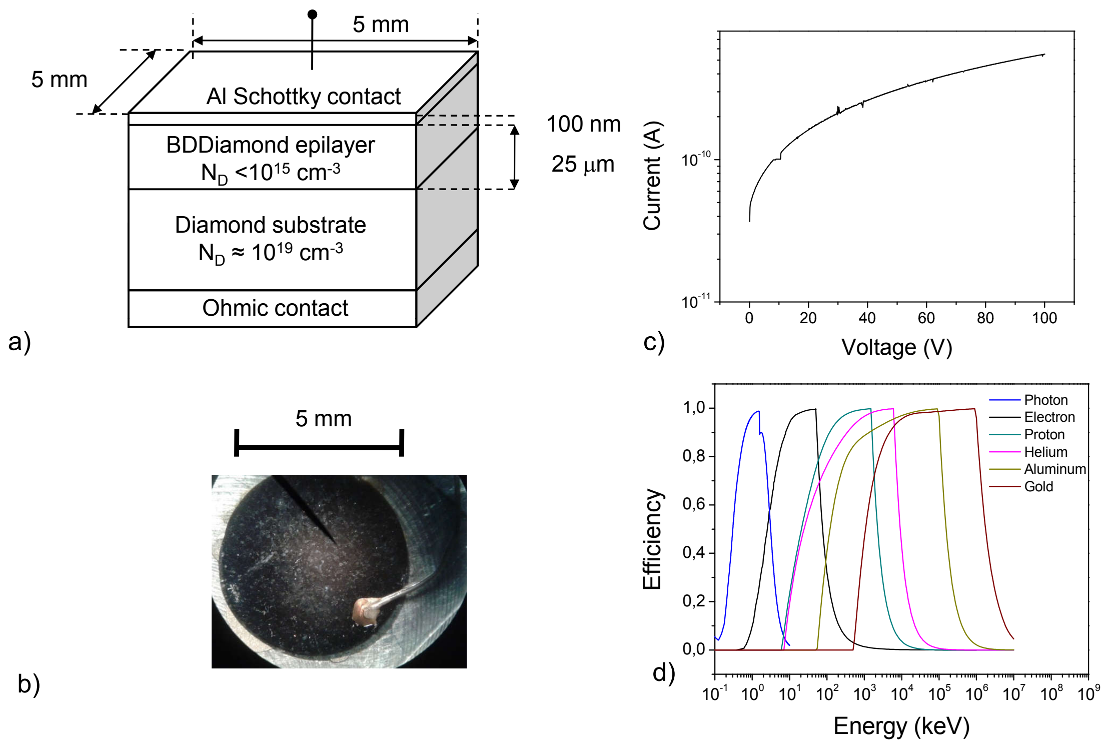

FIGURE 2.15: (a) Schematic of the geometry for the SiC IAZ4 diode, (b) picture of the device, (c) I-V curve characterization and (d) simulated efficiency curves for photons and protons.

contact (aluminum, copper, gold,...). The back face is bonded to a thick metal, while the front face has a thin coverage film to permit the entrance also of low energetic radiations, such as alpha particles. The two faces of the detector are polarized with a voltage of the order of 10-100 V, depending on the electric field value desired for the device control. In Fig. 2.15b is reported a picture taken from the top face of the device. On the Diamond detector was also performed a typical I-V characterization, (Fig. Fig. 2.15c) that testifies the low leakage current at room temperature and was studied the efficiency detection reporting some of these results in Fig. 2.15d.

2.4 Gallium arsenide detector

There are other materials with a high resistance to the damage due to neutrons and γ-radiation. One of these is the SI (semi-insulating) GaAs. In literature are reported some interesting results by Ryc et al. concerning applications in neutron and gamma detection and also in plasma monitoring [65, 66]. In this field for example SI GaAs detector could guarantee a longer operating life with respect conventional Silicon drift detectors. As an example in Fig. 2.16 is reported a I-V characterization performed by the Ryc's group on a prototype of their device based on SI GaAs.

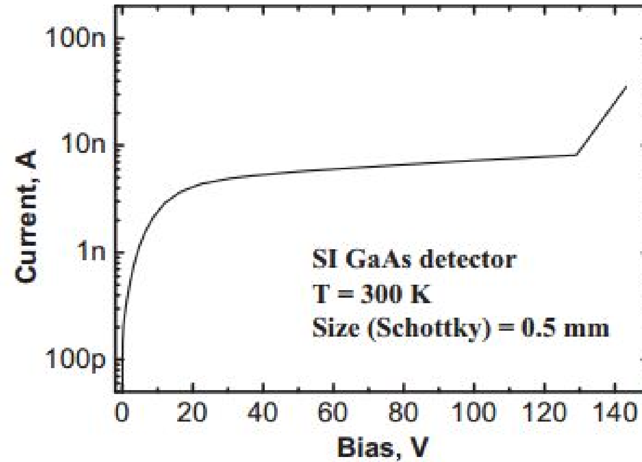

FIGURE 2.16: Current-Voltage characteristics of Ryc's device presented in Ref.[108]

In particular this device presents on the top side a Schottky electrodes of Ti/Pt/Au (10/40/70ṅm) with 0.5 mm size and 2 mm pitch realized with photolithografy mask, an active base of 130 μm width and on the backside it has a quasi-ohmic electrode formed by evaporation of AuGeNi/Au (50/70 nm). Results are very promising as can be seen in the spectrum reported in Fig. 2.17.

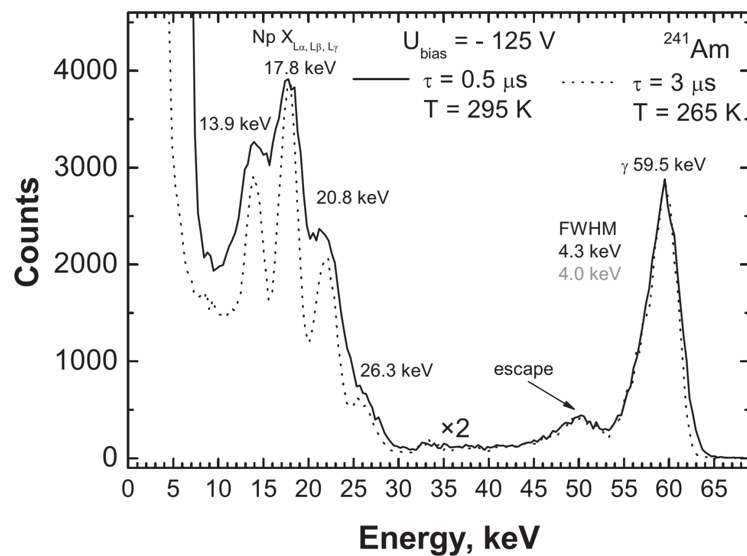

FIGURE 2.17: Spectra of ^{241}Am radioisotope acquired at 295 K and 265 K.

The developed system, GaAs detector and read-out electronics, was applied to detection of X- and γ-rays from the ^{241}Am radioisotope. Spectra were acquired at a bias voltage of -125 V and temperature of 295 K and 265 K. The lowest detectable energy of about 7 keV and 4 keV was observed at 295 K and 265 K, respectively. Calculated energy resolution for 59.5 keV and 17.8 keV peaks is 4.3 keV and 3.6 keV at RT and 4.0 keV and 3.0 keV at 265 K, respectively.

Chapter 3

Application of detector in spectroscopic regime

Low radiation fluence

3.1 Introduction

At low fluence condition it is possible to use a typical electronic chain for alpha particles detection: generally it is called spectroscopic regime. In this scheme we have a proportionality between the output signal of detector and the energy released by radiation in the active layer. With this electronic can be obtained important informations about detector, such as the energy resolution, or the evaluation of efficiency detecting hundred keV and MeV ions. However when the number of event becomes too high, the overall chain, because of the inevitable presence of inductances and capacities, is not able to process independently each one. Consequently, to avoid pile up effects or overlapping of signal, a time of flight technique must be employed. Using this electronic chain, the energies of a particle is calculated by measuring its time of flight of a known distance. These two techniques will be described more in details in this and in the following chapter. The limit between these two approach is about 2×10^6 particles per second.

3.2 Description of the electronic chain

In the simplest electronic chain, employed for example for alpha particle spectroscopy, the output signal of the detector (in charge or in current) is sent to a preamplifier, in which is converted in a voltage signal. Note that the length of the cable, connecting the detector to the preamplifier, must be as short as possible, because this will not only minimize the preamplifier noise (due to the capacitive loading of the cable) but will also

maintain the stability of the preamplifier. The function of the preamplifier is to couple the impedance and to improve the signal to noise ratio. Through the preamplifier can be also given the bias to the detector connecting it to a bias supply, and finally it can be also connected to a pulse generator that is very important for the calibration of the overall chain.
After this first stage of amplification the signal is processed by an amplifier that gives the possibility of modifying the shape. Finally, after the necessary digital-to-analog signal conversion it is stored in a multichannel analyzer where the pulses are counted based on amplitude: in this way as a final result a histogram of frequency against pulse amplitude is obtained. Along the overall chain the signal can be monitored using an oscilloscope connected in parallel.

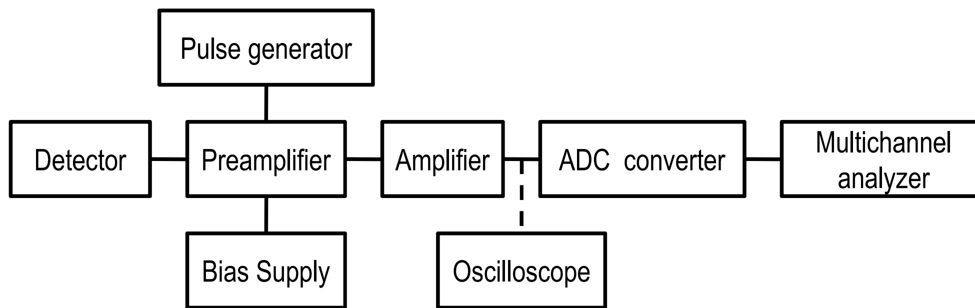

FIGURE 3.1: Electronic chain used in spectroscopic regime.

3.2.1 Preamplifier

There are different kinds of preamplifier depending on the characteristics of the connected detector and on the researched information: charge sensitive, transistor reset, current sensitive, parasitic capacitance. However for the development of this work only the charge sensitive type was employed, because it is the better solution when the pulse generated by the detector (Semiconductor detector, Proportional Chamber) is very small and the attention is focused on the energy of the detected particles. If Q_d is the charge generated by the events on the detector and consequently accumulated in the feedback capacitor C_f of the preamplifier, the amplitude of output signal V_{pre} of the preamplifier is:

$$V_{pre} = \frac{Q_d}{C_f} \tag{3.1}$$

Moreover, considering the feedback resistance R_f, the decay constant τ_{pre} of the signal is:

$$\tau_{pre} = R_f C_f \tag{3.2}$$

Another important parameter is the sensitivity of the preamplifier, connected with the gain G_{pre}:

$$G_{pre} = \frac{V_0}{E} = \frac{q}{C_f E_{pair}} 10^6 \tag{3.3}$$

where E is the energy in MeV deposited by radiations and E_{pair} is the energy necessary for the production of a carrier information. For example considering a feedback capacitor of about 1 pF the corresponding gain will be approximately 50 mV/MeV.
The used preamplifier is a commercial device produced by EG&G ORTEC. In particular the 142A Model was employed because it is designed for use with room-temperature-operated silicon surface-barrier detector with a input capacitance range from 0 to 100 pF. In Fig. 3.2 is reported a schematic of the circuitry of the preamplifier.

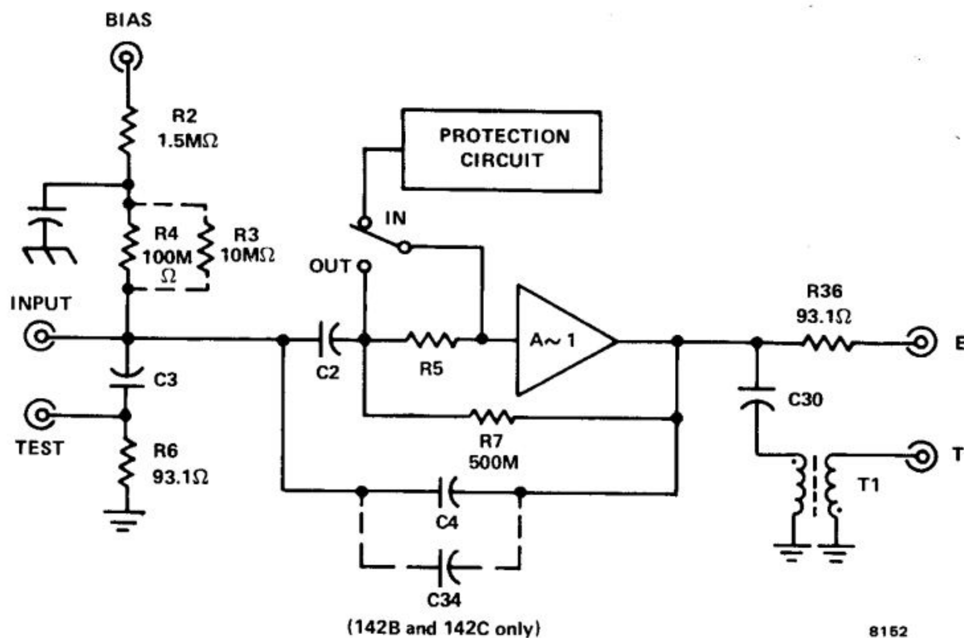

FIGURE 3.2: Simplified block diagram of the circuitry in ORTEC 142 series.

As can be seen in the simplified electrical scheme of Fig. 3.2, the charge-sensitive loop is essentially an operational amplifier with capacitive feedback, C_4, that is 1 pF. The conversion gain is nominally 45 mV/MeV. This conversion gain can be increased by decreasing the value of the feedback capacity but a subsequent increase in rise time will occur. The upper limit is the stray capacity (0.1 - 0.2 pF) with C_4 completely removed. Two simultaneous outputs are provided:

- the output marked E is used for energy measurements. The output signal is taken through a resistance of about 93 Ω, and its polarity is opposite with respect the input pulse polarity.

- the output indicated with T has been designed for timing applications and is essentially a transformer-coupled differentiated timing output.

A bias circuit is included to accept the operating voltage required by the detector. The bias accepted through the SHV Bias connector is furnished through R_2 and R_4 with a total resistance of about 100 MΩ. This circuit serves to protect electronics: in fact any leakage current flow through this high resistor. However it should be noted that for a high-leakage detector there will be a considerable voltage drop, so it is important to check the detector properties and correct the bias voltage. Power for the preamplifier is supplied through the captive power cord and 9-pin Amphenol connector that can be attached to the mating power connector on any ORTEC main ampifier. A voltage test pulse for energy calibration can be send through the Test input connector. Logically during the calibration procedure the detector with the bias applied has to be connected (or its equivalent capacitance).

3.2.2 Spectroscopy linear amplifier

The next important step is the amplifier that provides the pulse-shaping controls needed to optimize the performance of the analog electronics. In fact its primary purpose is to magnify the amplitude of the preamplifier output pulse from the millivolt range into the 0.1 to 10 V range facilitating an accurate pulse amplitude measurements with analog-to-digital converters. In addition the modification of the pulse shape allows to improve and optimize the energy resolution. However it should be noted that if on the one hand achieving the optimum energy resolution requires long pulse widths, on the other hand, short pulse widths are essential for high counting rates. So in each condition a compromise pulse width must be selected which optimizes the quality of information collected during the measurement.

The ORTEC Model 672 energy spectroscopy amplifier was chosen because it presents several advantages. The total gain is the product of two contributions a coarse gain and a fine gain and consequently cab be continuously adjustable from 2.5 to 1500. In particular the coarse gain is firstly used to find the crude range and then the fine gain is altered to find the accurate value to produce the optimum peak height. The most important characteristic of this ORTEC module is the high automation of all the critical adjustments: automatic baseline restorer, noise discrimination, Pole-Zero adjustment and pile-up rejector. This automation simplifies the usage of the device and allows to obtain high-performance with all types of detector.

The simplest concept for pulse shaping is the use of a CR high-pass filter followed by an RC low-pass filter as showed in Fig. 3.3. The signal coming from the preamplifier first passes through a CR, high-pass filter. This improves the signal-to-noise ratio by attenuating the low frequencies, which contain a lot of noise and very little signal.

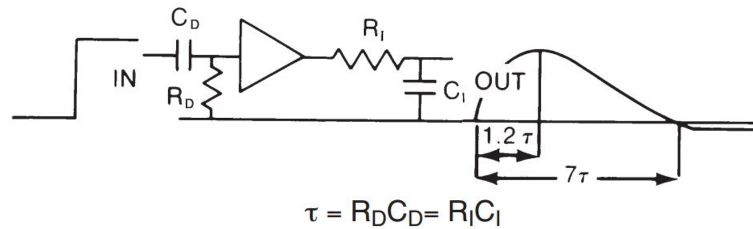

FIGURE 3.3: CR-RC pulse shaping for unipolar output.

The decay time of the pulse is also shortened by this filter. For that reason, it is often referred to as a "CR differentiator." Just before the pulse reaches the output of the amplifier, it passes through an RC low-pass filter. This improves the signal-to-noise ratio by attenuating high frequencies, which contain excessive noise. The rise time of the pulse is lengthened by this filter. Although this filter does not perform an exact mathematical integration, it is frequently called an "RC integrator." Typically, the differentiation time constant $\tau_D = C_D R_D$ is set equal to the integration time constant $\tau_I = R_I C_I$, i.e. the amplifier shaping time constant $\tau = \tau_D = \tau_I$. In order to minimize the noise contribution, affecting the energy resolution of the detector, it is very important the choice of the appropriate amplifier shaping time constant. At short shaping time constants, the series noise component of the preamplifier is dominant. This noise is typically caused by thermal noise in the channel of the field-effect transistor, which is the first amplifying stage in the preamplifier. At long shaping time constants the parallel noise component at the preamplifier input dominates. This component arises from noise sources that are effectively in parallel with the detector at the preamplifier input (e.g., detector leakage current, gate leakage current in the field-effect transistor, and thermal noise in the preamplifier feedback resistor). The total noise at any shaping time constant is the square root of the sum of the squares of the series and parallel noise contributions. However the choice of the proper shaping time is more in general a compromise between operating at a shorter time constant for accommodation of high counting rates and operating with a longer time constant for a better signal-to-noise ratio. In the ORTEC 672 model the shaping time can be modified on the front panel of the device and can be chosen between 0.5, 1, 2, 3, 6, and 10 μs.

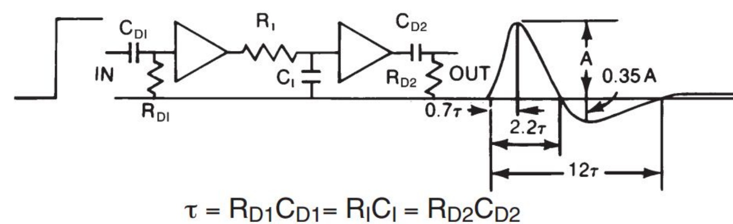

FIGURE 3.4: Doubly-Differentiated CR-RC-CR Shaping for bipolar output.

Although the unipolar output pulse is normally the better choice for energy spectroscopy measurements, there is also the possibility of a bipolar output. Fig. 3.4 shows the bipolar output pulse obtained when a second differentiator is inserted just before the amplifier output. Double differentiation produces a bipolar pulse with equal area in its positive and negative lobes. It is useful in minimizing baseline shift with varying counting rates when the electronic circuits following the amplifier are ac-coupled. The drawbacks of double differentiation relative to single CR differentiation are a longer pulse duration and a worse signal-to-noise ratio

Logically the internal circuit of the amplifier is not so simple in order to improve the capability of the amplifier. In particular the simple RC integrator is replaced with a more complicated active integrator network (Fig. 3.5), with the aim of increasing the signal-to-noise ratio of the pulse-shaping amplifier. This is important for semiconductor detectors, whose energy resolution at low energies and short shaping time constants is limited by the signal-to-noise ratio. For this reason a semi-Gaussian pulse shaping is generally adopted. The advantage of using this solution is the reduction of the output pulse width and a reduction in the amplifier dead time per pulse. Another important component regards the Pole-Zero cancellation. Pole Zero cancellation The benefit of Pole-Zero cancellation is the improvement of the peak shapes and resolution in the energy spectrum at high counting rates. Fig. 3.5 illustrates the Pole-Zero cancellation network, consisting in a resistor R_2 added in parallel with capacitor C_D, and adjusted to cancel the undesired undershoot. The result is an output pulse exhibiting a simple exponential decay to baseline with the desired differentiator time constant.

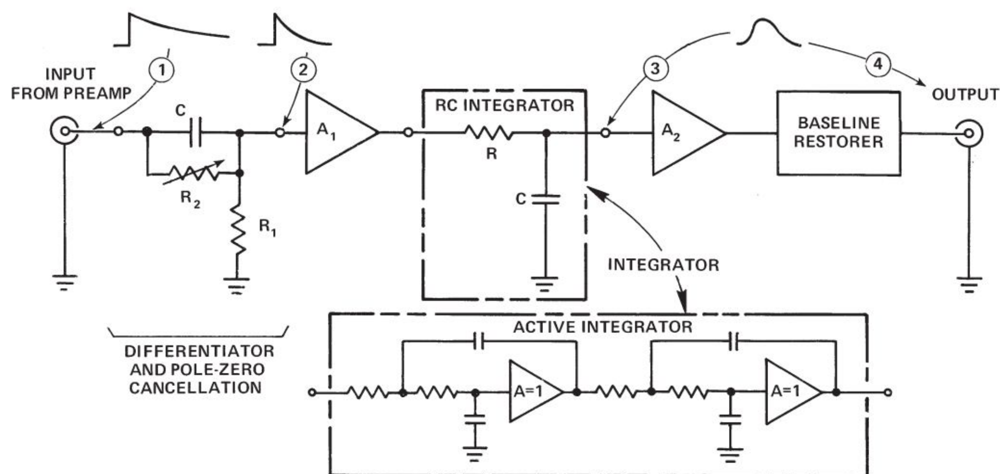

FIGURE 3.5: Pole-Zero cancellation network.

To ensure good energy resolution and peak position stability, the ORTEC 672 amplifier is equipped with an automatic baseline restorer and pile-up rejection. The baseline restorer behaves just like a CR differentiator, in which the baseline between pulses is returned to

ground potential by resistor R_{BLR} (Fig. 3.6). In order not to degrade the signal-to-noise ratio of the pulse-shaping amplifier, the C_{BLR} R_{BLR} time constant must be at least 50 times the shaping time constant employed in the amplifier. The circuit presents a switch S_1 that is opened for the duration of the amplifier pulse, and closed otherwise, so that the CR differentiator function is active only on the baseline between pulses.

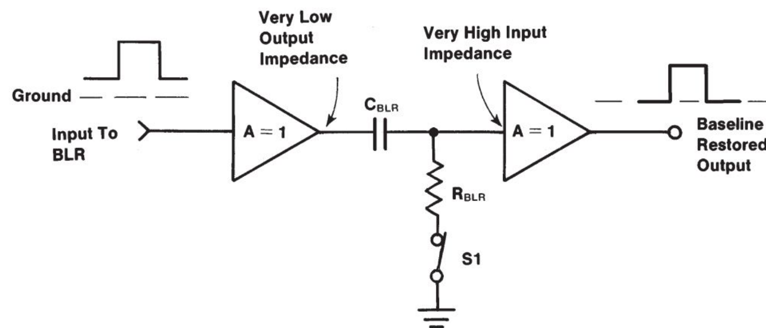

FIGURE 3.6: The diagram of the baseline restorer.

The pile-up rejector is implemented by adding a "fast" pulse shaping amplifier with a very short shaping time constant in parallel with the "slow" spectroscopy amplifier. In the fast amplifier, the signal-to-noise ratio is compromised in favor of improved pulse pair resolving time. A fast discriminator output triggers an inspection interval T_{INS} (Fig. 3.7) that covers the width T_W of the slow amplifier pulse.

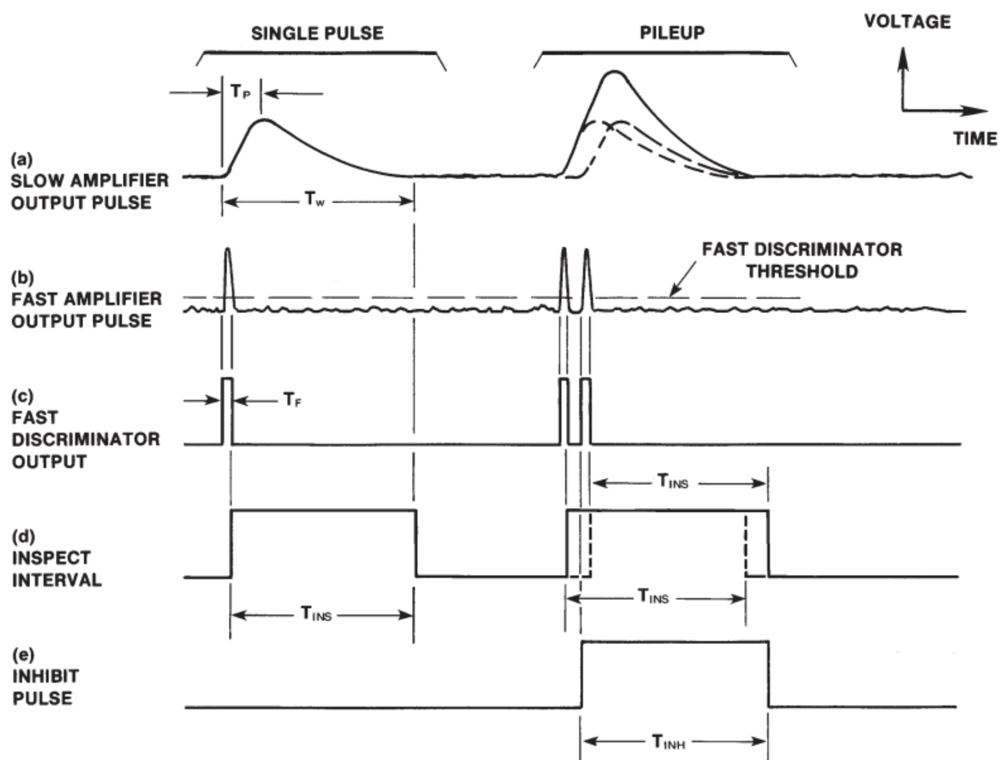

FIGURE 3.7: Schematic of the Pile-Up Rejector.

If a second fast discriminator pulse from a pile-up pulse arrives during the inspection interval, an inhibit pulse is generated. The inhibit pulse can be used in the associated ADC or multichannel analyzer to prevent analysis of the piled-up event. The pulse shape from the spectroscopy amplifier contributes to the dead time of the spectrometry system. As can be seen in Fig. 3.7 the dead time attributable to the amplifier pulse shape T_D is equal to the sum of the effective amplifier pulse width, T_W, and the time-to-peak of the amplifier output pulse T_P :

$$T_D = T_P + T_W \tag{3.4}$$

and the unpiled-up output rate r_0 for the amplifier is related to the input counting rate r_i from the detector by the throughput equation:

$$r_0 = r_i \exp[-r_i(T_D)] = r_i \exp[-r_i(T_P + T_W)] \tag{3.5}$$

Graphically this equation is reported in Fig. 3.8 for amplifier shaping time constants ranging from 0.5 to 10 μs. The amplifier output counting rate reaches its maximum when

$$r_i = \frac{1}{T_D} \tag{3.6}$$

higher counting rates require shorter shaping time constants.

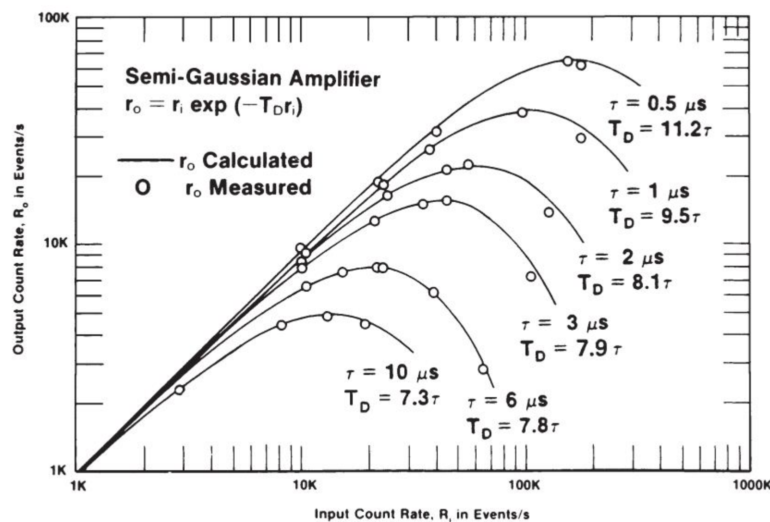

FIGURE 3.8: Unpiled-Up Amplifier Output Rate as a Function of the Input Rate for different values of shaping time constants.

3.2.3 Amptek MCA-8000D

The last step is represented by the Amptek's MCA-8000D a compact, high performance, digital MultiChannel Analyzer (MCA). Superior performance is obtained from a high speed ADC, a 100 MHz 16 bit ADC. The MCA-8000D does not implement digital pulse

shaping, but digitizes the input signal (the output of an analog shaping amplifier) to measure the pulse height and obtain the pulse height spectrum. The high speed ADC, with a 10 ns conversion time, reduces dead time increasing throughput. The digital circuitry yields high accuracy and stability. The analog input accepts positive unipolar or bipolar semi-gaussian type pulses of shaping time constants $\geq$200 ns or peaking time $\geq$500 ns and a minimum pulse height of 5 mV. The dynamic range is 0 to +1 V or 0 to +10 V, software selectable. Input impedance is 100 kΩ (MCA-8000D Option PA). The input has overload protection up to $\pm$20 V.

The MCA-8000D uses a USB 2.0 full speed to be interfaced with a laptop computer through the DPPMCA software package as Amptek's digital signal processors. This software offers spectral analysis features include energy calibration, setting regions of interest (ROI), computing ROI information (centroid, total area, net area, FWHM), spectrum smoothing, summing of spectra, subtraction and scaling of background spectra.

3.3 Detection of MeV α-particles

In order to test the effective response of SiC devices, adopting the spectroscopic regime, were employed different type of radiations source. The first analysis was carried out on the MeV α-particles emitted by radioactive source. From these measurements it is possible to carried out many useful informations: it can be measured the energy resolution, the linearity between particles energy and output signal can be tested, an estimate about the detector and electronics velocity can be given, and so on.

3.3.1 Radioactive source

The employed radioactive source is a three peak alpha source which contains ^{239}Pu (τ = 24.1 y), ^{241}Am (τ = 433.1 y) and ^{244}Cm (τ = 17.8 y). From the certificate of measurements of alpha emitting radioactive reference source we know that the measured ratios of the activities of Am/Cm/Pu is 1/1.075/1.301. The certificate is dated 17 June 1983 where there was an initial activity of 1.65×10^5 alpha particles per minute. According to this information we estimate a current activity of about: $A_{Pu}(t) = 1058.80$ Bq, $A_{Am}(t) = 774.40$ Bq and $A_{Cm}(t) = 255.88$ Bq. Fig. 3.9 reports the decay scheme of the three elements, showing the different branching ratios.

The measurements were performed in vacuum and the source was placed in front of the detector at a distance of 1.5 cm, as showed in Fig. 3.10.

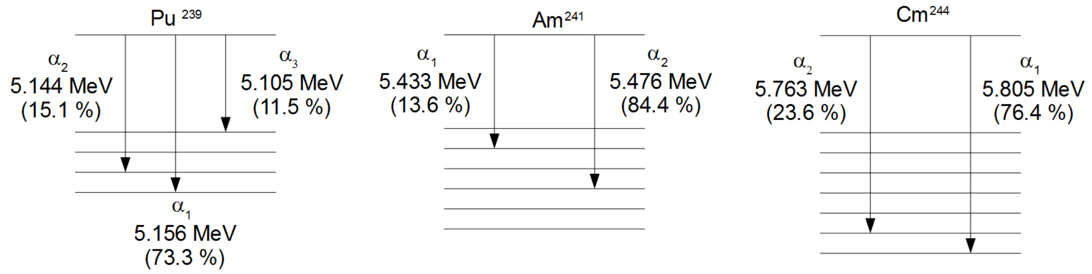

FIGURE 3.9: Decay scheme and branching ratios of the multi-peaks alpha source.

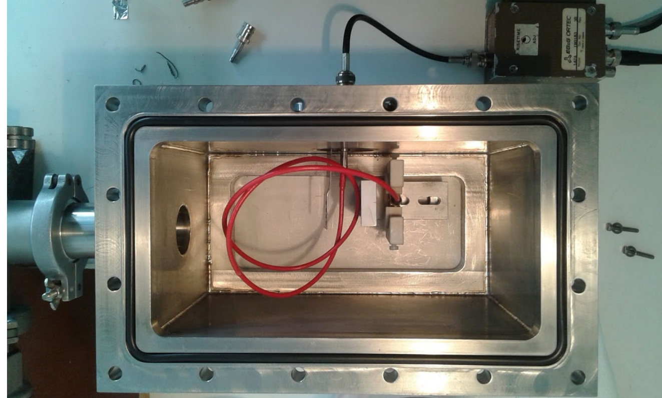

FIGURE 3.10: Photo of the vacuum chamber.

3.3.2 Results with radioactive α-source

The four spectra of Fig. 3.11 represent the different response of Silicon, SiC and Diamond detectors, to the same multi-peaks α source described in section 3.3.1. The measurements were performed with the same experimental conditions in order to compare directly the behaviour of the detectors. The detector-source distance was maintained fixed at 1.5 cm and all measurements were done in vacuum condition at about 10^{-4} mbar. The same read-out electronic has been employed, described in section 3.2, using the same parameters configuration: coarse gain 20, fine gain 9.40, unipolar input (positive for Si and Diamond detector, negative for SiC devices). These spectra show both the vantage and disadvantages of the employed detectors. In the case of Silicon and SiC AZ 25, spectra a) and b) respectively, thanks to the very thin metallization, an excellent energy resolution has been obtained, how can be seen from the similar shape of the two spectra. The good energy resolution allows the discrimination of the smaller peaks due to less probable decay process. However, due to the little active region of the SiC AZ 25 (less than 1 mm^2), a low statistic of events has been achieved and consequently a lower number of counts with respect others detectors. In this sense is very interesting the comparison with SiC AZ 80 of spectrum c). Thanks to the high active surface a high number of counts has been obtained, but the presence of the thick metallization (200 nm of Ni_2Si) worsens the energy resolution.

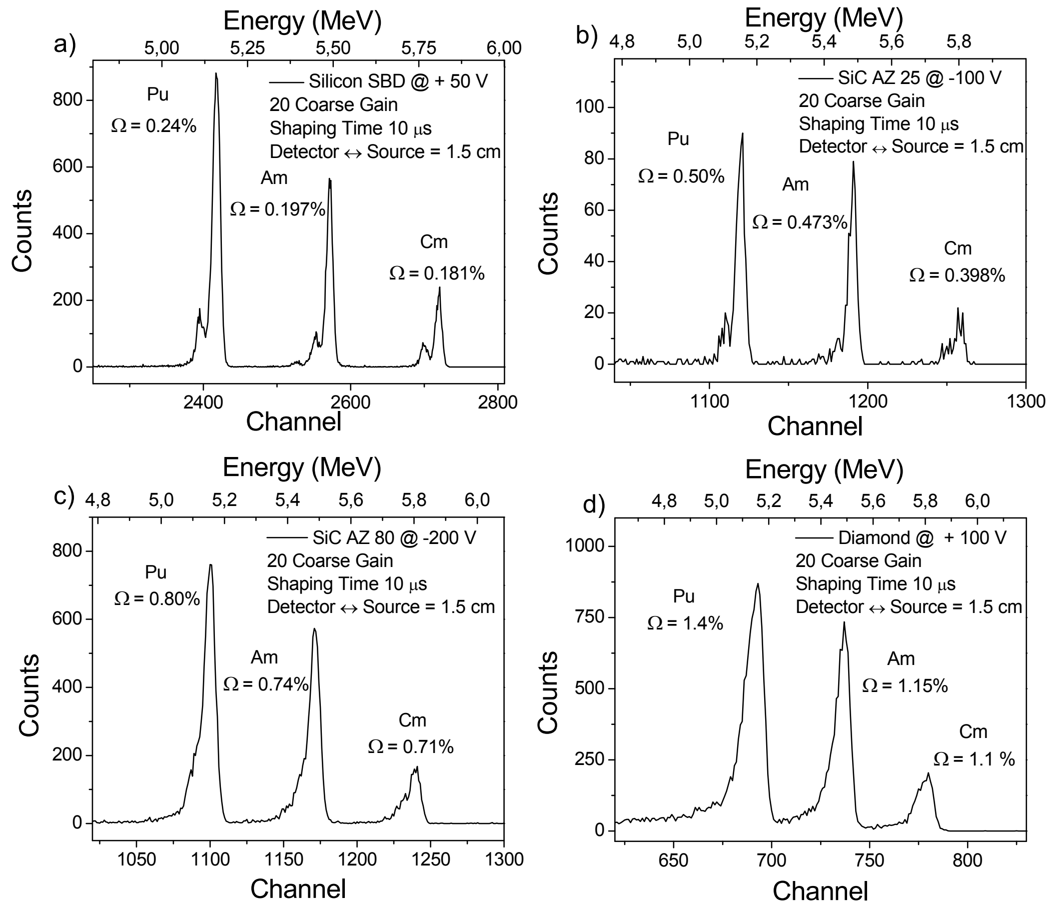

FIGURE 3.11: The four α spectra acquired with: a) traditional Silicon Surface Barrier Detector; (b Silicon Carbide detector AZ 25; c) Silicon Carbide AZ 80; (d Diamond detector.

Similar considerations could be done with the last spectrum obtained with the Diamond detector that has a greater active region than SiC AZ 80 that permits to detect more α-particles. However the energy necessary for the production of an electron-hole pair in Diamond is higher than SiC and so the three peaks result widen than the other detectors. In the SiC AZ 80, even if the little peaks are connected with the main peaks it is possible to individuate them in the little edge at lower energy, while in the case of Diamond are completely included in one peak without any possibility to distinguish them.

3.3.3 Effects of Mylar absorbers

For explore a widen energy range, thin absorbers of Mylar (6, 12, 18 μm thick) were placed between the multi-peak source and the detector. The detector source was maintained the same during the measurements, and the presence of the absorber placed in front of the detector has the double effect of reducing the α-particles peak energy producing a shift of the spectrum toward lower channel, but also a widening of the energy distribution

of the radiations as can be see in Fig. 3.12 for Silicon b), SiC AZ 80 c) and Diamond detector d).

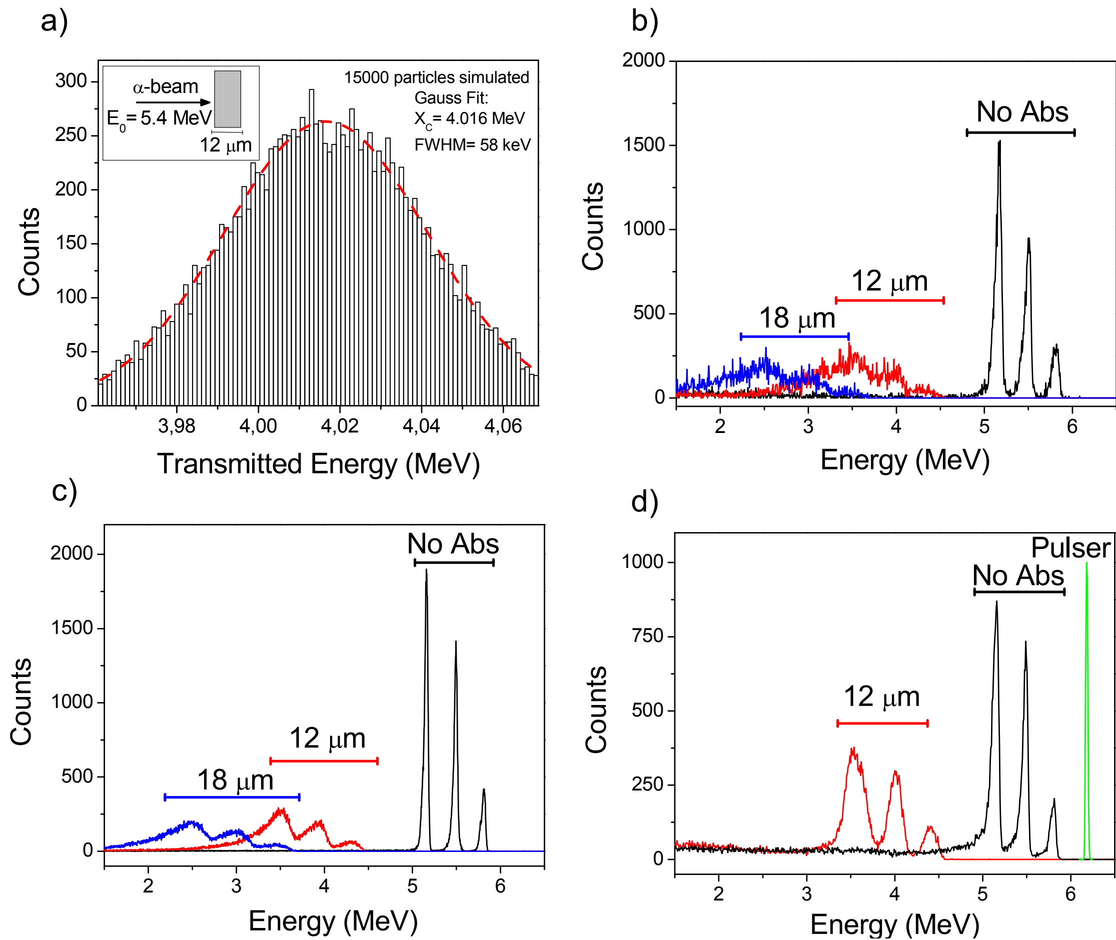

FIGURE 3.12: a) Simulated transmitted energy of 15000 α-particles after 12 μm Mylar absorber; α spectra acquired with: b) traditional Silicon Surface Barrier Detector, (c Silicon Carbide detector AZ 80 and (d Diamond detector using 12, 18 μm Mylar absorbers.

These aspects can be taken into account through computer simulation using the SRIM software (The Stopping and Range of Ions in Matter)[112]. Through a SRIM simulation is possible to know the characteristics of the transmitted α-beam after the Mylar layer in terms of the transmitted energy distribution. Then using conventional software, these simulation data can be analysed and fitted through a Gaussian function in order to evaluate the new peak position and the FWHM representing the new α energy peak and the straggling due to Mylar absorber, respectively. As an example in Fig. 3.12a is reported a simulated energy distribution of α-particles crossing a Mylar layer 12 μm thick, with the parameters of the fitting Gaussian function. The results obtained repeating the same procedure for the three peaks of the α-source and for the different Mylar thickness are summarized in Tab 3.1.

TABLE 3.1: Characteristics of the transmitted α-particles.

Peak Position (MeV) X_C	Energy Straggling (keV) FWHM	Mylar Thickness (μm)
2.534	84.451	18
3.035	81.377	
3.499	86.498	
3.603	63,884	12
4.016	58,742	
4.410	61,445	

3.3.4 Calibration process

In the Diamond spectrum Fig. 3.12d is reported a typical peak obtained using the pulse generator. This device plays an important role both in the determination of the noise due only to the read-out electronic but especially in the calibration of the MCA system. The pulse generator was connected to the test input of the preamplifier (Fig. 3.1) and the generated signal was compared with that coming from the α-particles detection. Then through an oscilloscope connected in parallel to the MCA system a calibration curve was determine for each detector, finding a correspondence between the height of signal in the oscilloscope (in mV), the channel of the MCA system and then the corresponding value of energy. The four calibration curves, used for the energy scale reported in the top x-axis of Fig. 3.11, are:

- For Silicon detector:

$$E[\text{MeV}] = -0.0389 + 0.00215\frac{[\text{MeV}]}{\text{Channel}} \cdot X[\text{Channel}] \tag{3.7}$$

- For SiC AZ 25:

$$E[\text{MeV}] = -0.11077 + 0.0047\frac{[\text{MeV}]}{\text{Channel}} \cdot X[\text{Channel}] \tag{3.8}$$

- For SiC AZ 80:

$$E[\text{MeV}] = 0.03951 + 0.00465\frac{[\text{MeV}]}{\text{Channel}} \cdot X[\text{Channel}] \tag{3.9}$$

- For Diamond detector:

$$E[\text{MeV}] = -0.0457 + 0.00751\frac{[\text{MeV}]}{\text{Channel}} \cdot X[\text{Channel}] \tag{3.10}$$

3.3.5 Effects of the detector bias voltage

To be sure to collect all charges generated by the arrival of the radiation, the variation of the spectrum in function of the dielectric polarization voltage has been studied, and the results are shown in Fig. 3.13.

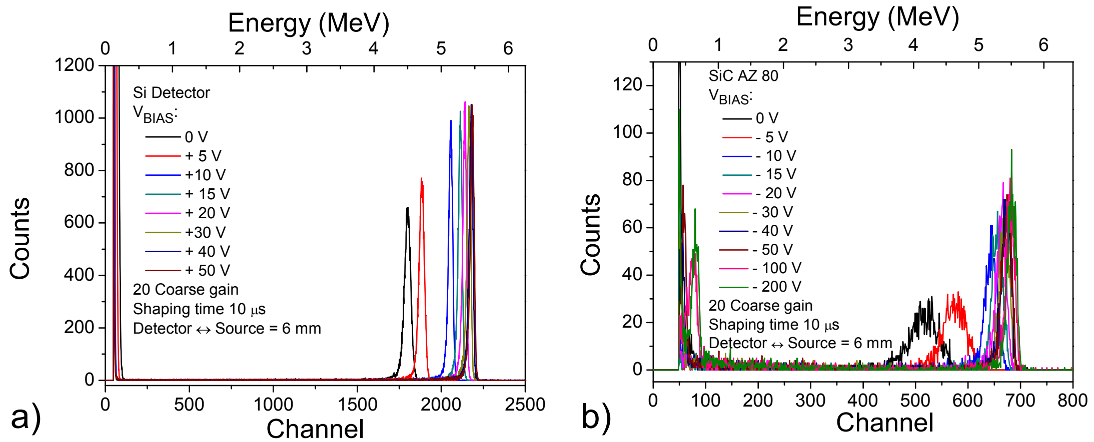

FIGURE 3.13: Detection of α-particles emitted by a single peak Am source through Silicon (a) and SiC AZ 80 (b) detector at different bias voltage.

The spectra were obtained using a monochromatic source of alpha particles (Am^{241}) through the SiC AZ 80 and for comparison also by means of the Silicon Detector. When the bias voltage increases, it also increases the depletion region and therefore the depth of the active region. In this way, a greater number of charges, produced along the track of the incident particle, are collected leading to a shift of the spectrum to higher channels and to an increase in signal output with an improvement in peak resolution. Once the polarization voltage reaches the saturation value, there are no evident variations of the spectrum in terms of peak and width position. This condition is achieved when the depth of the depletion layer is greater than the particle penetration range within the detector. In this case, thanks to SRIM simulation it was evaluated a value of about 18.2 μm for 5.48 MeV alpha particles within the SiC, as shown in Fig. 3.14a. In accordance with eq. 2.9, which describes the depth of the depletion layer as a function of the bias voltage applied to the various detectors, this condition is reached at + 40 V for Silicon, -100 V for SiC AZ 80, - 30 V for SiC AZ 25 and + 100 V for the Diamond detector, as shown in Fig. 3.14 Once this saturation condition is reached eventually, a small increase in yield can be observed because increasing the bias voltage actually increases the electrical junction field. Charges are then collected more quickly by overcoming recombination processes problems.

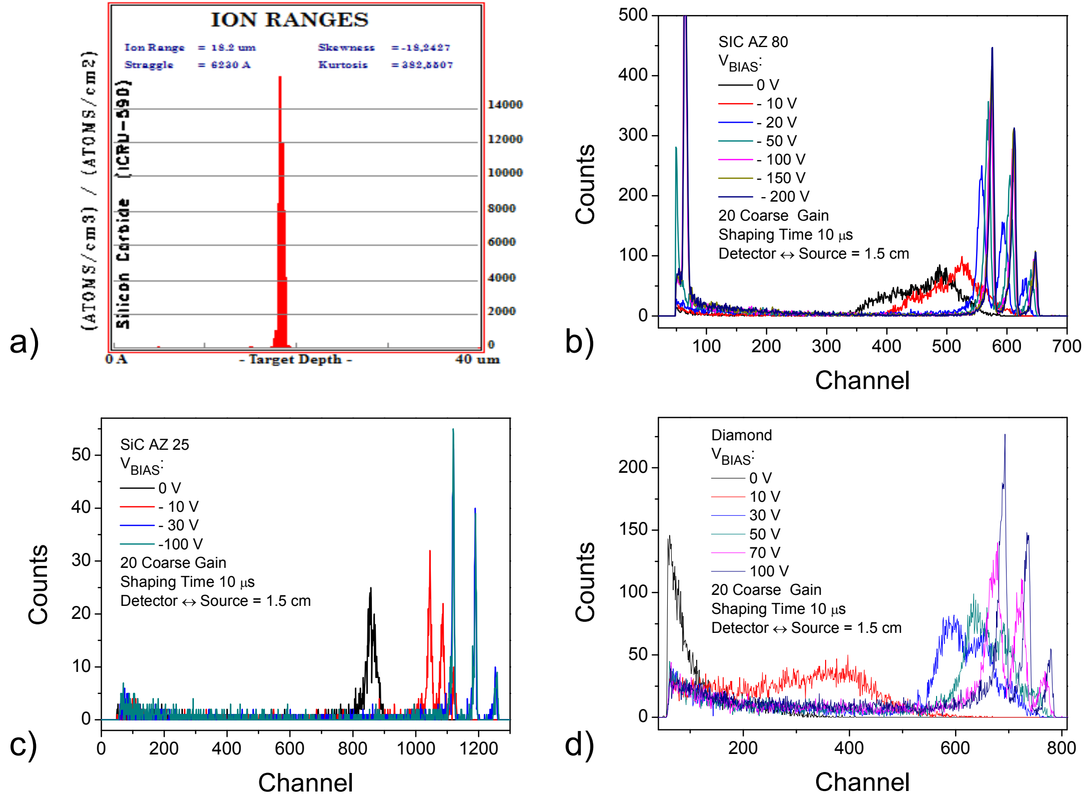

FIGURE 3.14: Ion range of 5.46 MeV α particles in SiC and detection of α-particles emitted by the three peak α-source through SiC AZ 80 (b), SiC AZ 25 (c) and Diamond (d) detector at different bias voltage.

3.3.6 Energy resolution

After the calibration procedure, it was possible to evaluate the energy resolution of the detectors in the energy range between 2.5 and 6 MeV. As described in section A the energy resolution is given by the quadrature sum rule (eq. A.3) and for this reason the experimental energy spreads of the peaks Ω_{Exp}, reported in Fig.3.11, have to be rescaled taking into account the broadening due to the readout electronic (Ω^2_{Elec}) and to the geometrical factors of the experimental set-up such as the metallization layer (Ω_{Metal}) and absorbers (Ω_{abs}). The energy straggling in the dead layers of the detectors was evaluated using the same procedure employed for the straggling due to the Mylar absorber. Thanks to SRIM simulation code was found a value of 4.9 keV, 17.89 keV and 7.238 keV for SiC AZ 25, SiC AZ 80 and Diamond detector respectively while for the Silicon device, considering a metallization of 20 nm of Au, was obtained a value of about 10 keV. In order to evaluate the contribution due to the electronic noise a spectrum reporting only the peaks due to the pulse generator was firstly acquired. Then using the specific calibration curve, the FWHM of the generated peaks was converted in the corresponding energy spread. In this way was measured an electronic noise of 9 keV for the Silicon detector, 14 keV for the two Silicon Carbide devices and 28 keV for the

Diamond detector. The resolution values Ω_{Intr}, obtained from the eq. A.3, are reported in Tab. 3.2

TABLE 3.2: Energy resolution for Si, SiCs and Diamond detectors

Energy (MeV)	Resolution (%)			
	Silicon	SiC AZ 25	SiC AZ 80	Diamond
2,534	0,956	-	1,802	-
3,035	0,749	-	1,473	-
3,499	0,602	-	1,28	-
3,603	0,51	-	1,18	7,42308
4,016	0,45	-	1,02	5,16194
4,41	0,39	-	0,85	4,13689
5,155	0,16468	0,40891	0,66496	1,28268
5,484	0,10898	0,38804	0,61213	1,02196
5,806	0,09345	0,30518	0,5982	0,98076

As expected from the discussion following the spectra of Fig. 3.11, the better energy resolution was obtained with Silicon Surface Barrier detector, followed by SiC AZ 25 and SiC AZ 80 and then Diamond.

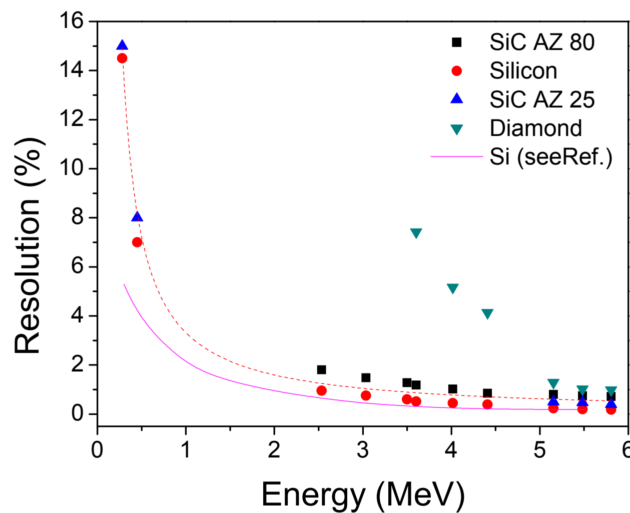

FIGURE 3.15: Energy resolution for Silicon, SiC AZ 25, SiC AZ 80 and Diamond detector in the energy range between 200 keV and 6 MeV, compared with literature results of Ref. [109].

Combining these resolution values with other data coming from other experiments at lower energy (see section 3.4.2) it is possible to realize Fig. 3.15. These results demonstrate that with SiC detectors it is possible to obtain energy resolution values very close to Silicon devices as put in evidence by the red dotted line inserted to guide eyes. Moreover the experimental results showed in this section are in good agreement with resolution values reported in literature for Silicon detector (violet line) in the considered energy range.

3.3.7 ΔE measurements

The Silicon Carbide detector labelled SiC IAZ 4, can not be directly compared with the above detectors, because of the MeV α-particles can not be stopped within the 4 μm of the active region.

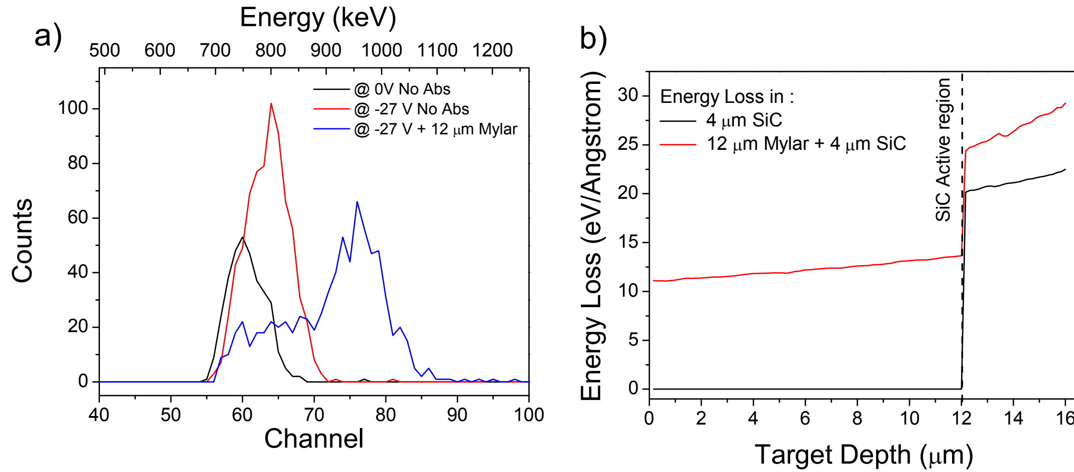

FIGURE 3.16: Response of the SiC IAZ 4 to a single peak α-source (^{241}Am), changing the bias voltage and using a Mylar Absorber (12 μm thick).

For this analysis was used a single peak α-source of ^{241}Am emitting at 5.484 MeV, because the presence of other peaks (Pu or Cm) would determine only a broadening of the peaks being a ΔE measurements. The range of 5.484 MeV α-particle in SiC, as confirmed by SRIM simulation, is about 18μm, losing an energy of $\sim$ 205 keV/μm. The response of the SiC IAZ 4, reported in Fig. 3.16, is related only to the small fraction of energy released in the 4 μm thick SiC epilayer, and not to the total incident energy. The detector is able to detect α-particles also when no bias voltage is applied, because the metal-semiconductor potential is able to partially deplete the 4H-SiC epilayer. Actually by changing the bias voltage the energy loss spectrum remains approximately the same, because the depletion layer remains 4 μm. When is applied a voltage the shape of the active region changes, but not the thickness as can be seen in Fig. 3.17. The Schottky barrier develops ellipsoidal active zones under the strips, separated from each other, with a thickness of about 4 μm. So when the voltage is increased the separation between these active regions is reduced. This leads to an increase of the volume of the overall active region that however maintains a maximum depth of 4 μm. On the one hand, the higher the active volume the higher the number of particles that are collected from the detector, with a consequent increase of counts number. On the other hand, the peak's position remains almost the same, since the energy loss is similar in the 4 μm depletion layer.

As expected, after the calibration process, the peak is centered at about 800 keV, close to the value calculated by SRIM of the energy loss (831 keV), both at 0 V and at -27 V.

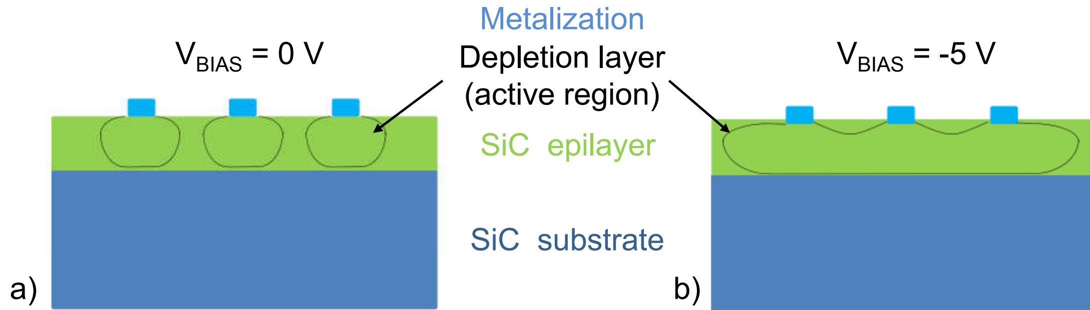

FIGURE 3.17: Profile of the depletion layer at 0 V and (a) and -5 V (b).

In this case the energy resolution of the peak relative to the 5.48 MeV α-particles cannot be evaluated accurately. However taking into account its width of about 80 keV at 800 keV the corresponding energy resolution is approximately 10% in agreement with literature [86]. When a thin Mylar absorber is placed in front of the detector another interesting result is obtained. The peak position shifts towards higher channel. This can be explained with the fact that lower energy α-particles lose more energy in the 4 μm SiC. Again SRIM simulations permits to verify this result. In fact, as can be seen in Fig. 3.16b, the total energy loss in the active region can be calculated through the integral of the two ionization distributions. Without any absorber, the energy that particles lose in the active region is 831 keV, as said before, while considering a 12 μm Mylar layer in front of the detector, this energy increases to 1.056 MeV. In fact in the experimental spectrum, the peak obtained with the Mylar absorber is centered at about 1 MeV. The importance of this measurements is the possibility to realize telescope ion detector. These devices are realized combining a thick detector (such as the SiC AZ 80) to measure the total ion energy and a thin detector (such as the SiC IAZ 4) to determine the stopping power and the ion energy loss. Using the Bethe-Bloch formula and the data coming from the two detectors it is possible to distinguish different detected ion species.

3.4 Detection of sub-MeV He ions

In order to investigate the detector energy resolution at lower ion energy were detected hundred keV ions coming from the 300 kV ion implanter of the Physics Department of Catania University.

3.4.1 Ion Implanter

The ion implanter was employed to accelerate helium ions from 100 keV up to 600 keV using both He^{+} and He^{++}, with an ion current ranging between 100 pA and 1 μA. A

schematic of the facility is reported in Fig. 3.18.

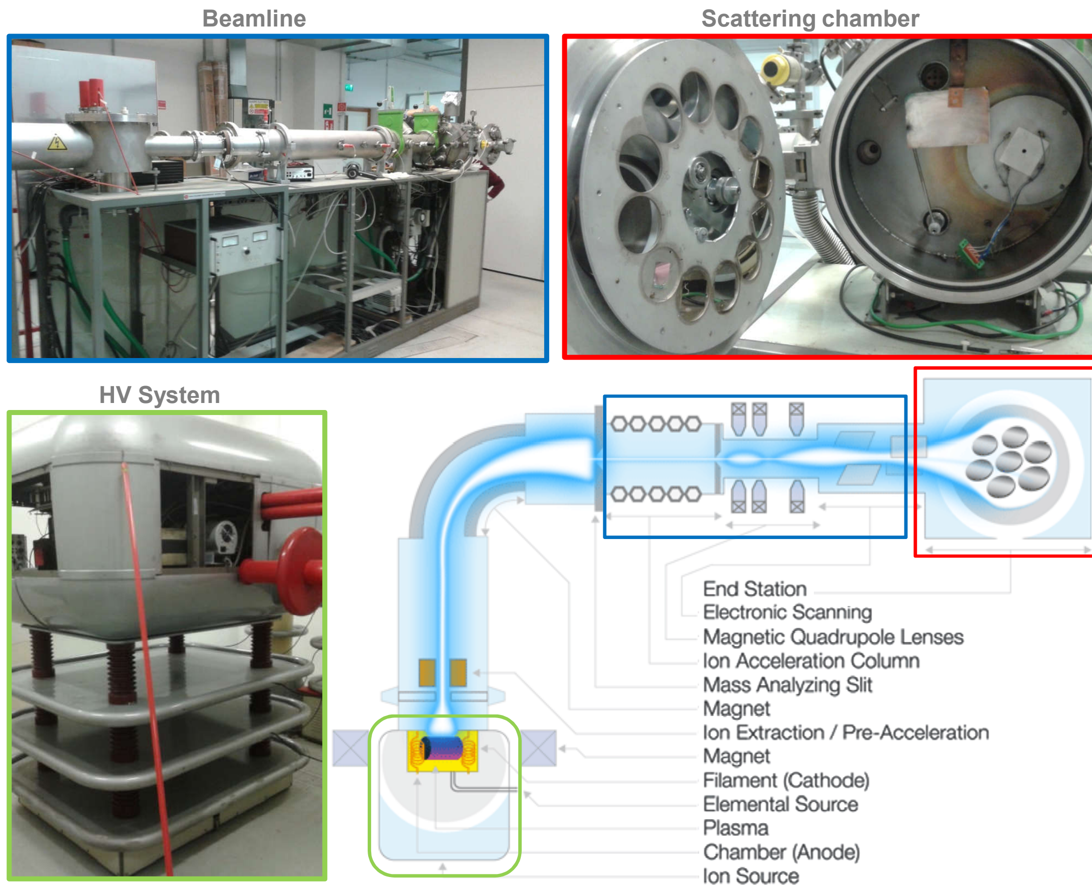

FIGURE 3.18: Structure of the Ion Implanter in the Department of Physics of the University of Catania with photos of the Chamber ion source, of the electromagnetic deflecting system and of the End station.

The first stage is represented by the source chamber in which the He gas is ionized through the impact with electrons. Once are generated ions cross the magnet region where are analysed and selected based on their charge and mass. After this phase of analysis, the ions entering the acceleration column in which are accelerated by electric fields. And finally, before reaching the end station, the beam is further focused and through an electronic scanning it is possible to define exactly the x-y position.

However because of the ion current was still very high causing pile up effects if the detector was placed on the main helium beam, it was necessary to adopt a Rutherford Backscattering Spectroscopy (RBS) configuration. The detectors collect He ions backscattered at 165° by the target as showed in Fig. 3.19. In this investigation were used not only bulk material, thick target of Al, Si, Cu, Ag or Au, but also multilayer targets deposited by PVD (physical vapour deposition) technique on Si substrate.

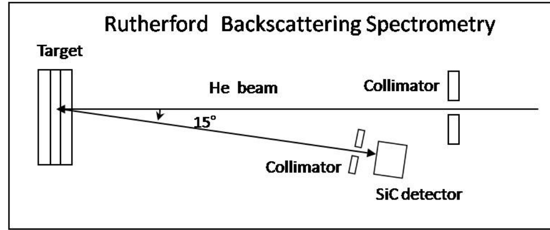

FIGURE 3.19: Rutherford Backscattering Spectrometry.

The detection geometry was different for the three detectors: the detector-target distance was 11.5 cm for I-SiC, which corresponds to a solid angle of 0.45 msr; the detector-target distance was 12 cm for M-SiC, which corresponds to a solid angle of 0.07 msr; the detector-target distance was 8 cm for Si detector, collimated by an aluminium hole of 6 mm^2 surface, which corresponds to a solid angle of about 1 msr. The low detection solid angles used in the experiment avoids any pile-up effect in the acquired spectra.
In the analysis of the experimental data two important aspects have to be taken into account when a RBS approach is adopted. The first is the kinematic backscattering factor k_{RBS}, depending on the energy of the backscattered particle E_{bks} with respect to that of the incident one E_0, according to the following relation [52]:

$$k_{RBS} = \frac{E_{bks}}{E_0} \left(\frac{m\cos\theta + \sqrt{M^2 - m^2\sin^2\theta}}{m + M} \right)^2 \tag{3.11}$$

where m and M are the masses of the incoming ion and of the target atom, respectively, and θ is the backscattering angle. For helium beams at 165° angle k assumes the value of 0.5556, 0.5688 0.7803, 0.8642 and 0.9232 for Al, Si, Cu, Ag and Au, respectively. The second important aspect is the differential scattering Rutherford cross sections in the laboratory system $(\frac{d\sigma}{d\Omega})_R$, depending on [52]:

$$\left(\frac{d\sigma}{d\Omega}\right)_R = \left(\frac{Z_1 Z_2 e^2}{2E\sin^2\theta}\right) \frac{\left[\cos\theta + \sqrt{1 - \left(\frac{m}{M}\sin\theta\right)^2}\right]^2}{\sqrt{1 - \left(\frac{m}{M}\sin\theta\right)^2}} \tag{3.12}$$

where Z_1 and Z_2 are the atomic numbers of the projectile and the target atoms, respectively, and E is the energy of the projectile immediately before the scattering process.

3.4.2 Experimental results

In order to test the linearity and efficiency to lower energy radiations we employed these devices in the detection of sub-MeV He ions accelerated by the 300 keV ion implanter of the Department of Physics in the Catania University, described in section 3.4.1. In this

case the low current 600-keV Helium beam, backscattered by target, is revealed at an angle of 165°.

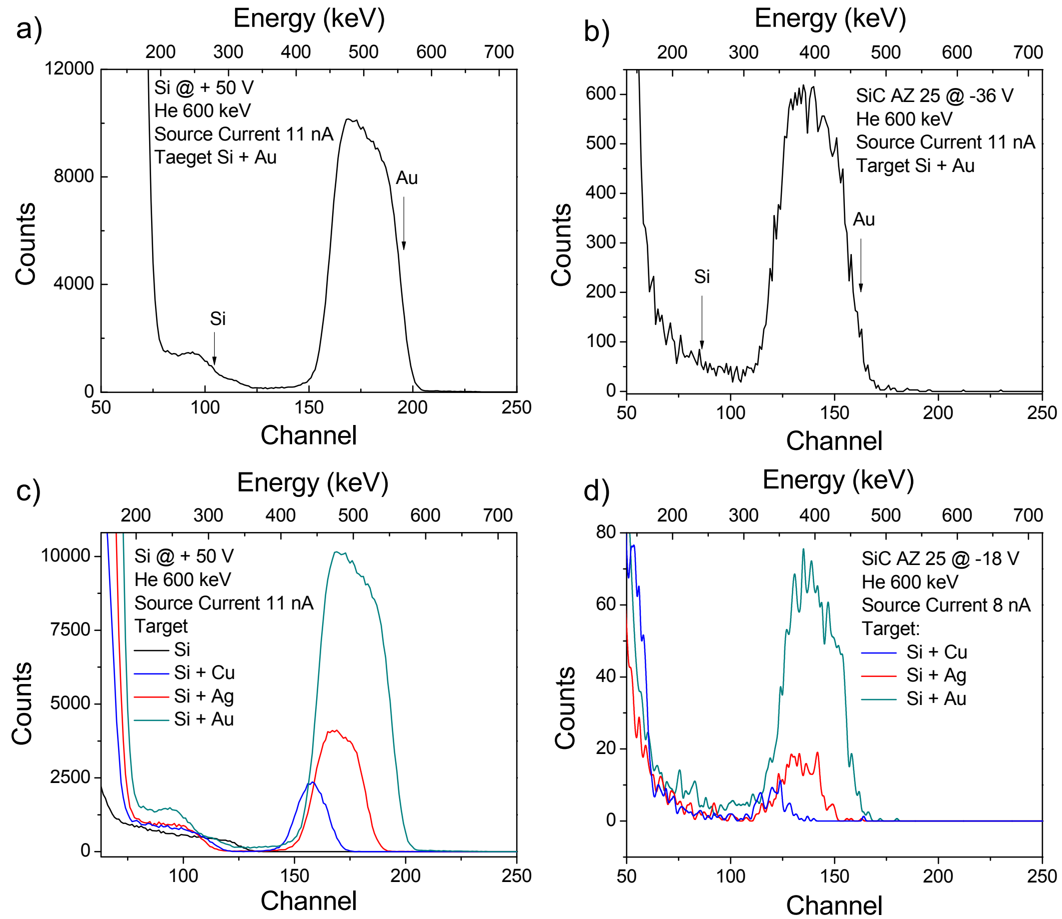

FIGURE 3.20: Silicon a), c) and SiC IAZ25 b), d) spectra detecting Helium beam backscattered by Silicon, Au on Silicon, Ag on Silicon and Cu on Silicon target.

All measurements presented in this section were performed using the electronics reported in section 3.2 using a coarse gain of 50, a fine gain of 9.46 and 2 μs of shaping time. The results are presented in Fig. 3.20. Fig. 3.20a shows a typical spectrum obtained with the Silicon device detecting the He^{++} beam, with an initial energy of 600 keV, backscattered by target consisting in a thin layer of Au deposited on Silicon. The spectrum reveals the presence of a wide peak (channels 150-200) due to the α-particles backscattered from the Au film and a second small peak, around channel 100, that is not completely separated from the background: it is due both to the He ion backscattered by the silicon substrate and to the electronic noise. Also in the second spectrum (panel b), acquired in the same experimental condition with a SiC AZ 25, there is a wide peak (channels 120-170) due to α-particles backscattered by Au, while the peak due to Silicon backscattering is completely included inside noise. The evident difference in the number of counts of the two spectra is mainly due to the geometry factor and in particular in the different solid angle subscribed by the two detectors. In fact the ratio between the two experimental

collection solid angle, i.e. 15, is very close to the ratio of 14.3 between the Silicon yield (maximum number of counts), about 10000 counts, and the SiC yield, about 620 counts. Taking into account eq. 3.11, it is possible to evaluate the energy of the backscattered He ions:

$$E = k_{RBS}E_0 = 0.92 \times 600\,\text{keV} = 552\,\text{keV} \quad (3.13)$$

These backscattered ions have to cross also the metallization layer of the two detector, loosing 112 keV and 10 keV, in SiC AZ 25 and Silicon, respectively. Note that in this experiment the energy loss in the SiC AZ 25 is high because in addition to the 20 nm Ni_2Si metallization there is an absorber of 250 nm in thickness of SiNH a CVP semitransparent passivation film with 2.3 g/cm3 mass density. From these considerations a correlation between channels and ion energy can be found: channels 182, 155 at which the Au surface peak was obtained, correspond to an energy of 544 keV, and 442 keV for Si and SiC detector, respectively. It is clear that one point is not enough for a calibration curve and for this reason were done the same measurements using different target elements: Silicon bulk target, Copper on Silicon, Silver on Silicon and Gold on Silicon. The results were summarized in Fig. 3.20c.d, reporting the comparison between the spectra acquired with Si and SiC AZ 25 device of α-particles backscattered at a fixed incident helium energy of 600 keV and a fixed source current. The maximum alpha energies coming from the surface backscattered layers in the case of Si detector occurs to the channel 194 for Au, 182 for Ag and 166 for Cu, while for SiC detector occurs to the channel 154 for Au, 145 for Ag and 127 for Cu. As done before from eq. 3.11, it is possible to evaluate the energy of the backscattered He ions from Cu (468 keV), Ag (518 keV) and Au (554 keV). In order to take into account the different energy loss in the detector's metallization layer these energies have to be rescaled to 544, 507, 457 keV for Silicon detector and 442, 396, 342 keV for SiC detector. From these correlations between channels and energies was found a calibration with a conversion factor of 2.92 keV/channel for SiC and 3.01 keV/channel for Silicon. In this way was estimated the top x-axis energy scale reported in the four spectra of Fig. 3.20. From these spectra can be also evaluated the thickness ΔX of the film of Au, Ag, Cu deposited on Silicon substrate, using the equation:

$$\Delta X = \frac{\Delta E_{RBS}}{k\left(1\frac{dE}{dx}\right)_{E_0} + \frac{1}{|cos\theta|}\left(\frac{dE}{dx}\right)_{kE_0}} \quad (3.14)$$

in which, ΔE_{RBS} is the energy spread of the peaks, $\frac{dE}{dx}$ is the stopping power and can be evaluated through SRIM simulation and finally k and θ represent the kinematic factor and the backscattered angle, respectively. From the calculations a value of 130, 95, 54 nm for Au, Ag and Cu, respectively, rather close to the values determined during target preparation.

3.4.3 Variation of source energy and current

In order to test the behaviour and the linearity of the detectors the measurements reported in the spectra of Fig. 3.21 were performed, acquiring the detector response by changing the ion energy between 300 keV and 600 keV, and the source current in the range between 2 nA and 15 nA.

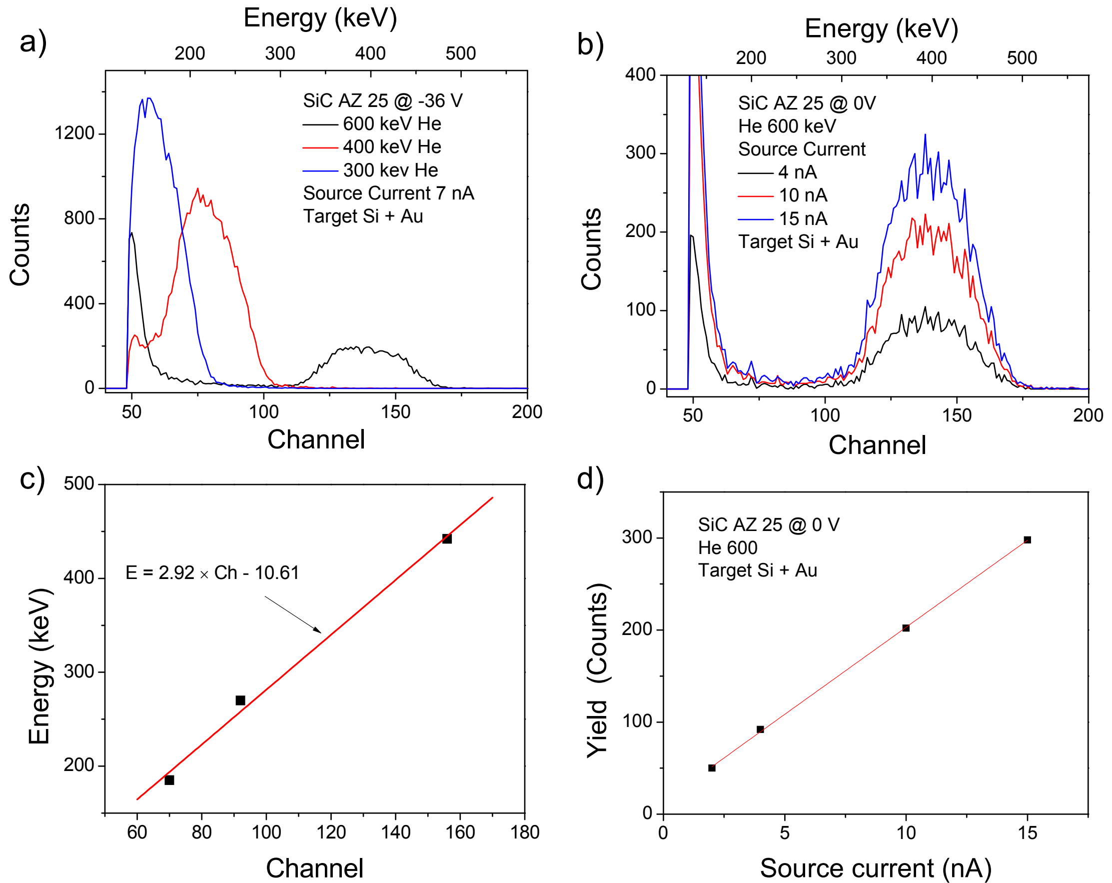

FIGURE 3.21: SiC spectra obtained by changing the source conditions in terms of ions energy and current.

The results were carried out irradiating the same target (Si + Au) and as expected, at lower ion energy, the Au peak shifts to a lower channel number and the detection yield increases. According to the eq. 3.12, the increase in the number of counts obtained decreasing ion energy is related to the increase of the scattering cross section with the square of the ions energy. The experimental values obtained from the net area subtended by each Au peak is very close to the expected ones evaluated from the eq. 3.12. The calibration curve, also reported in Fig. 3.21c, allows to insert the energy scale also in these spectra, and data are in good agreement with the estimated energy values of α-particles penetrating in the SiC device's active layer: 185 keV, 270 keV, and 442 keV for ion beam energies of 300 keV, 400 keV, and 600 keV, respectively. It should be noted that

also these set of data can be used to calibrate the multichannel systems, as described in literature [104]. However the results obtained with the two procedures are exactly the same. Moreover thanks to energy scale presents in the spectrum, from the steepness of Au signal, were extracted the resolution values reported in Tab.3.3.

TABLE 3.3: Energy resolution for Silicon and SiC detectors.

Energy (keV)	Resolution (%)	
	Silicon	SiC AZ 25
280	14.5	15
450	7.9	8

As expected by changing the source current a very good linearity was obtained in the response of the SiC detectors Fig. 3.21b. In the three cases the peak position remains the same, only the area of the peak increases by increasing the current, in fact higher is the current source higher is the number of He particles backscattered and consequently detected form the devices. This behaviour is evidenced when the maximum yield is plotted as a function of the source current like in Fig. 3.21 showing an excellent linearity.

3.4.4 Multilayer target

Further tests on these devices were done using a multilayer target. It consist in a silicon substrate in which were deposited firstly a thin film of Copper (50 nm), then a film of Silver (90 nm) and finally a film of Gold (125 nm).

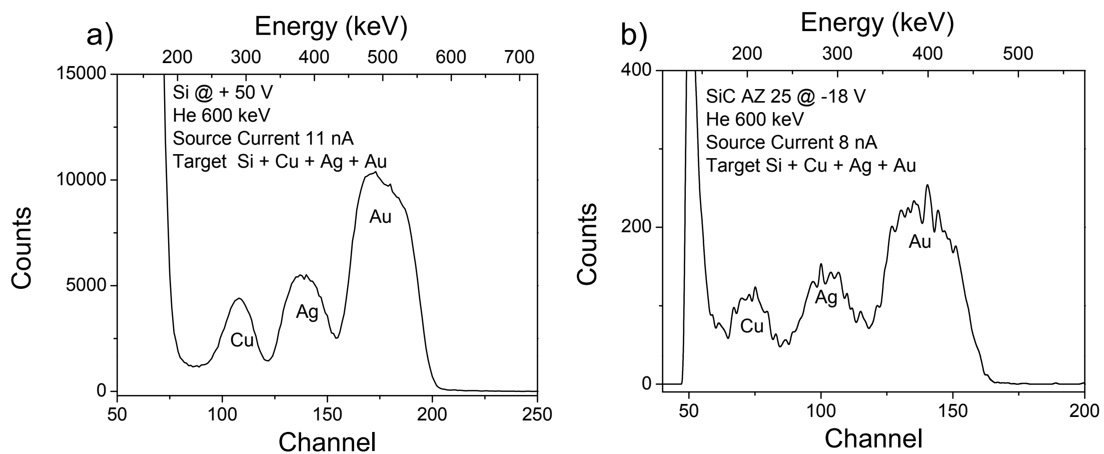

FIGURE 3.22: Silicon (left) and SiC (right) spectra obtained irradiating a multilayer target.

Spectra acquired at fixed helium energy of 600 keV for both detectors, Silicon and SiC AZ 25, are shown in Fig. 3.22. The three peaks due to the different films are well separated in the Silicon detector case, while for SiC they show a small overlapping. Again, using

eq. 3.14 the thickness of the three thin layers can be evaluated: the obtained values 55 nm, 98 nm and 130 nm for the Cu, Ag, and Au layer are in good agreement with values determined during the target preparation.

3.4.5 Measurements with SiC IAZ 4

In these analysis the SiC AZ 80 can not be used because of the presence of the thick metallization does not allow the ion detection. On the other hand also the SiC IAZ 4 shows a poor resolution as can be seen in Fig. 3.23.

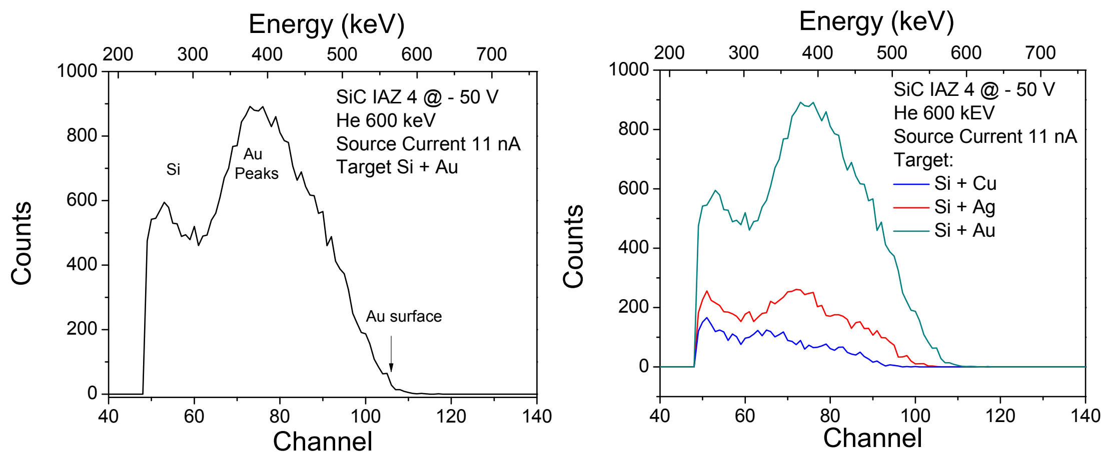

FIGURE 3.23: Response of SiC IAZ 4 to He ions backscatterd from the Si + Au target a) and the multilayer target b).

The spectrum relative to the Si + Au acquired using the SiC IAZ 4 detector, Fig. 3.23a, appears contract, as result of the not-uniform and non-planar detector surface. In fact the spectrum is given by two contributions: the first due to He ions impinging on an directly exposed active area of the detector; the second is due to ions that before reach a depleted region cross the interdigit metallization strip with a consequent energy loss and straggling. Analogously, Fig. 3.23b shows the similar spectrum of the multilayer target. In this case it is not possible to distinguish the three separate film materials.

3.5 X-rays detection

In Fig. 3.24 are illustrated the results of the new investigation performed with X-rays emitted by an Amptek mini X-ray tube and using the same read out electronic shown before. The X-rays tube is provided with a grounded anode, variable current and voltage controlled via USB. Moreover, it has a 50 kV/80 μA power supply, a Silver target and a Beryllium window.

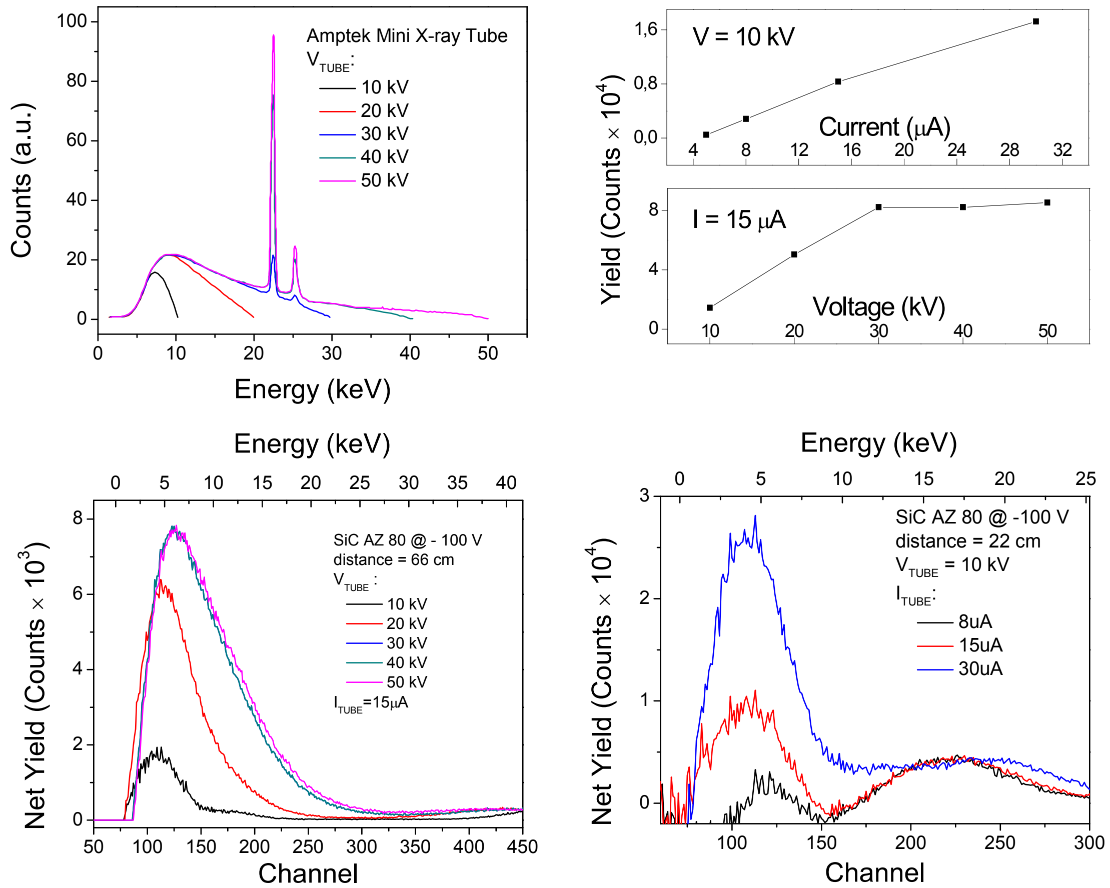

FIGURE 3.24: a) Tabulated spectra given by Amptek site; b) measured yield as a function of current and voltage of tube; experimental spectra obtained by changing voltage c) and current d) of tube.

According to Amptek specifications [4] there is an approximate flux of 10^6 counts per second/mm^2 on the axis at a distance of 30 cm using 50 keV/1μA. The spectra in Fig. 3.24a are directly provided by the Amptek web site. The SiC response was investigated by changing both the voltage and the current of the X-ray tube. As shown by results summarized in Fig. 3.24b, an increment in current corresponds to a linear increase of detection yield (counts), while an increment in voltage produces firstly an increase in the number of counts under the peak until a saturation condition is reached for tube voltage of about 30 kV. Above this value an increment of photon energy determines, practically, the same energy loss in the detector. It should be noted that the increment of the SiC yield obtained in the two cases, is due to different reasons: when the tube current is changed the enhancement is due to the variations of the photon flux, while when the tube voltage is modified the variation is due to the photon energy. Fig. 3.24c reports the SiC net yield, after background subtraction, as a function of the X-ray energy using a fixed current of the X-ray tube (15 μA) and changing the voltage of the tube. Also in this case an accurate calibration has been performed to correlate the MCA channels to the X-ray energy about 1.09 keV/channel). The counts around 40 keV are

mainly due to noise and to the difference between acquired spectrum and background spectrum (X-ray tube switched off). Fig. 3.24d reports the measurements performed at a fixed voltage of the tube (10 kV) by changing the current of the tube. Such behaviour is in agreement with the theoretical curve of efficiency of Fig. 2.10 as confirmed by the energy calibration of the spectrum. Also in this case the difference between the spectrum and the background may give rise to virtual negative peaks. However our attention is given to the main X-rays yield which is proportional to the tube electron current incident on the silver anode. Fig. 3.24d is related to a minor distance with respect to that used in Fig3.24c. This configuration enhance the yield counts and produces pile-up effects.

A new investigations was also performed in order to compare the response to X-ray generated by a 40 kV, 15μA X-ray tube source for the SiC AZ 80 and SiC IAZ 4.

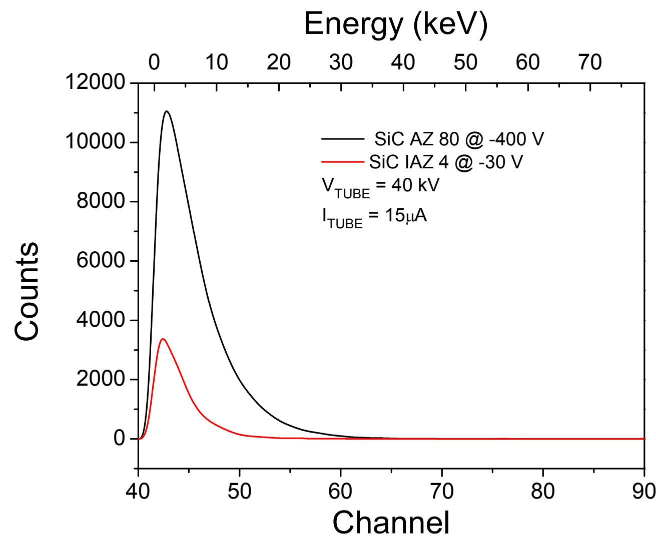

FIGURE 3.25: Response of M-SiC and I-SiC detectors to an x-ray source at 40 kV.

The corresponding spectra are shown in Fig. 3.25. The yield detected by SiC AZ 80 decreases considerably at the energy of 20 keV, while, for the I-SiC at 12 keV, in agreement with the simulated efficiency of the two detectors. As expected, the thicker detector shows a higher yield and detects higher X-ray energies, while the thin detector shows a lower yield and is most suitable for lower X-ray energy detection. The obtained spectra do not show the characteristic peaks but only a continuum spectrum because both the detectors have insufficient thickness to completely absorb the incident X-ray photons.

It should be noted that these spectra are preliminary results and many efforts has to be done in order to optimize the read-out electronics and in particular the coupling between detector and preamplifier. In literature, [12]-[48], are present very promising results obtained with radioactive X-ray source. As an example of the possibility of 4H-SiC device on the top of Fig. 3.26 is reported a spectrum of a ^{241}Am radioactive source,

acquired at two different temperature and on the bottom Fig. 3.26 are shown the energy resolution values for X-rays for two SiC detectors.

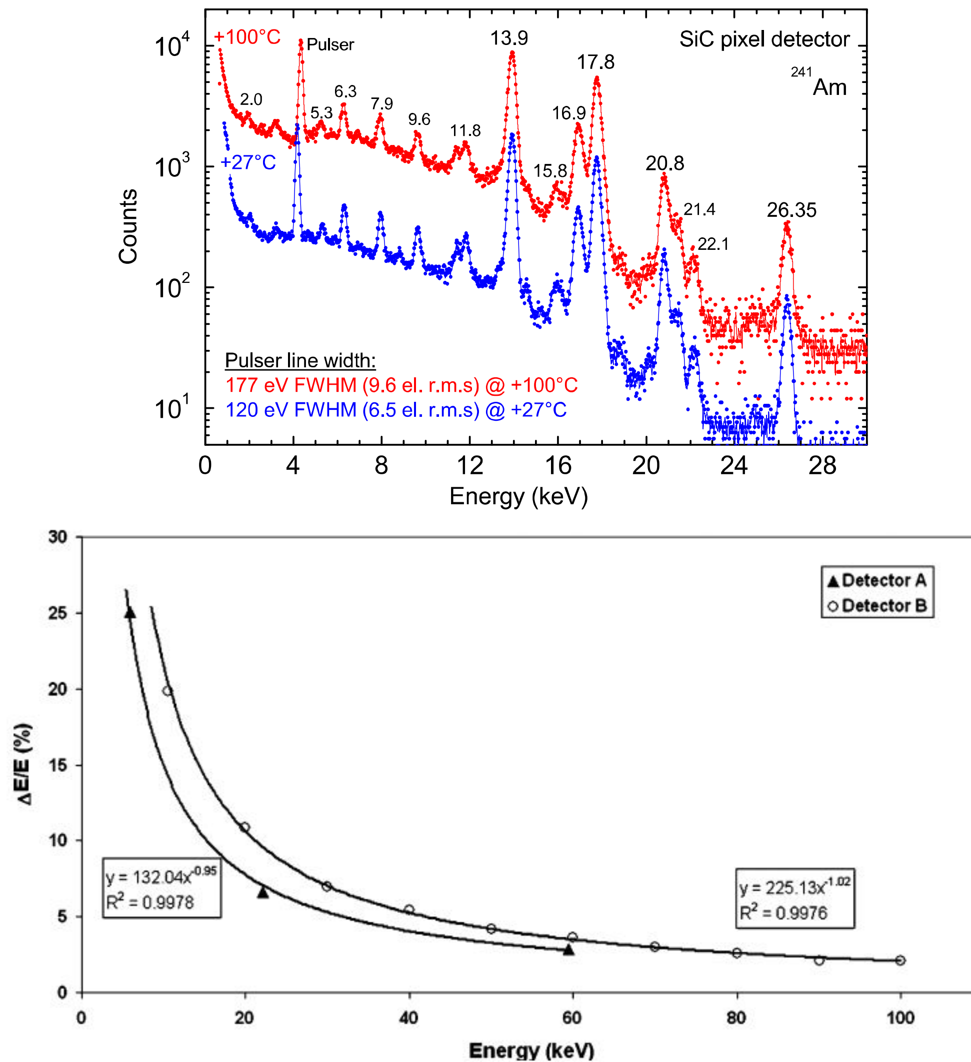

FIGURE 3.26: On the top spectra of ^{241}Am acquired at +27° and +100°C [12]; on the bottom energy resolution for two SiC detectors as a function of energy [48].

The properties of SiC allow also to adopt these detectors as dosimeter for ionizing radiations. They could represent an alternatives to silicon and diamond semiconductor detectors recently employed in radiotherapy offering comparable properties of e–h pair production. For such dosimeter measurements it is not required a spectroscopic electronic chain but, the detector reverse current after and during the detection of radiations is monitored by a Keythley picoamperometer (mod. 6485 picoammeter) inserted in the bias electrical circuit. Fig. 3.27 shows two sets of preliminary measurements obtained using the SiC AZ 80 detector placed near to a FAG dosimeter in air. The SiC was covered with 10 μm polyethylene to be in the electronic equilibrium during the detection. Both detectors were irradiated, separately, with a 20 kV X-ray tube and with 1.3 MeV gamma rays emitted from a ^{60}Co radioisotope. The SiC was monitored through the

reverse current with the Keythley picoamperometer, which was correlated to the dose rates measured with the FAG dosimeter. The two set of measurements show that the reverse current ranges from the leakage value of about 10 pA, maintained at low dose rates, to a maximum value of about 1–2 nA obtained at high dose rates. The higher dose rates were obtained with the gamma exposition.

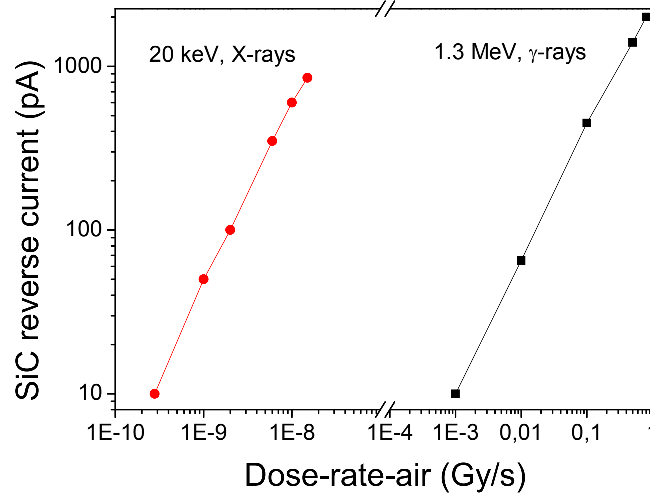

FIGURE 3.27: SiC reverse current monitored as a function of the dose rate for exposition to a 20 kV X-ray tube and to 1.3 MeV γ-rays from the 60Co source.

The increment is linear with the dose rate using both X-rays and gamma rays in the investigated ranges of dose rates, in agreement with the literature [16].

3.6 Characterization with β^- emitted from a radioactive source and electron gun

The SiC AZ 80 was also tested with β^- emitted by ^{90}Sr-^{90}Y source and from a low energy electron gun. In the first case we used a composed source of ^{90}Sr-^{90}Y.

As can be seen from Fig. 3.28, the Sr-betas have a mean energy of 195.8 keV and end-point energy of 546.0 keV, while Y-betas have a mean energy of 933.7 keV and end-point energy of 2280 keV, as reported in the inset of Fig. 3.29a. The fluence of the source on the detector was estimated to be $\sim 10^4$ β-particles of 1 MeV per second. Fig. 3.29a shows the SiC net yield as a function of the β energy emitted from the Sr-Y source at different distances in vacuum, after the background subtraction. The spectrum shape is due to the continuum β-energy distribution from about 100 keV up to 2.3 MeV and to the curve of electron efficiency reported in Fig. 2.10. The β emitter source was employed to study the SiC response to high electron energy (100 keV-1 MeV), and to evaluate the real detection efficiency at high electron energy.

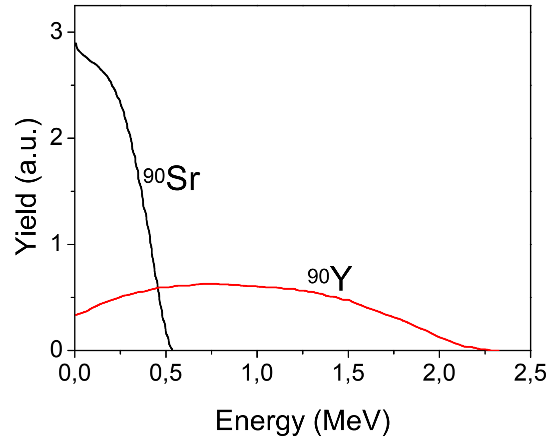

FIGURE 3.28: Characteristics of the ^{90}Sr-^{90}Y β-source.

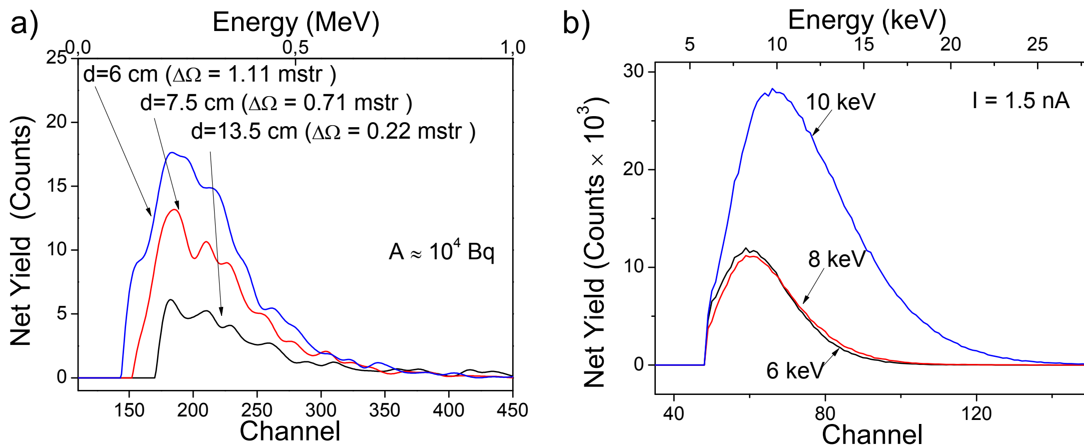

FIGURE 3.29: a) spectrum obtained from the ^{90}Sr-^{90}Y source or detecting electrons coming from an electron gun system b).

In order to characterize SiC detector also at low electron energy it was used an electron gun producing electron beam accelerated from 1 keV to 10 keV by a Kimball Physics Electron Gun Systems EGG-3101 Model. Fig. 3.29b shows the SiC net Yield as a function of electron energy emitted from the electron gun operating at 1.5 nA and different voltages from 5 kV to 10 kV. Also in this case, being in the threshold of the detector efficiency the shape of the spectrum is strongly influenced from the electron energy deposition in the active layer of the detector. In fact for electron energy of about 6 keV the detection efficiency decreases quickly to zero and the detector response is not linear as can be seen from the spectra at 8 keV and 10 keV of Fig. 3.29b. The curve of electron efficiency shows a fast decay at low electron energy with a cut-off at energy below 2 keV. The detection efficiency at 6 keV and 8 keV is 0.60 and 0.68 respectively, giving rise to their ratio of 1.13, comparable with the experimental spectra yield ratio of 1.0.

Chapter 4

SiC detectors for plasma-laser diagnostic

High radiation fluence

4.1 Introduction

Thanks to the physical property of Silicon Carbide, described in section 2.2, the most favorable applications of SiC-based detectors is represented by the diagnostic of plasma generated by laser. In fact this experimental situation is characterized by a harsh environment i.e. high temperature operability and high radiation conditions. In these last few years this subject, the non-equilibrium plasma generated by laser, is becoming more and more one of the major research topics for new and important applications [82] ranging from nuclear physics to chemistry, from microelectronics to engineering, from medicine to biology and from cultural heritage to environmental analysis. In particular one of the most attractive features is the possibility to obtain very compact ion, electron, neutron or X-rays sources with high time and space resolution for laser ion sources [32], nuclear reactions occurring in hot plasmas [90], multi-energetic ion implantation from plasma emission [6], proton therapy [23], laser ablation developing plasma for archaeological and environmental applications [87]. For these reasons since few years it has been becoming important an accurate study of all the physical properties of plasma and the characterization of the emitted radiations.

4.1.1 Plasma

Plasma can be considered the fourth state of matter in addition to solid, liquid and gas. Although in the universe the plasma state constitutes more than 95% of the known

material, it is extremely rare to find it in the Earth. To observe a gas-plasma transition, it is necessary to bring the system temperature to an extremely high value. Under these conditions, the gas molecules divide into the ionic component positively charged, and electronic one. In order to take into account the fraction of gas that is ionized it is useful to define the parameter χ_{ION}:

$$\chi_{ION} = \frac{1}{1 + \frac{n_a}{n_i}} \tag{4.1}$$

where n_a is the density of neutral atoms while n_i represents the density of atoms in the i-th state of ionization. The ionization states of an element is also related to the temperature and pressure though the Saha ionization equation [67]:

$$\frac{n_{i+1} n_e}{n_i} = \frac{2}{\lambda_{DB}^3} \frac{g_{i+1}}{g_i} \exp\left[-\frac{\varepsilon_{i+1} - \varepsilon_i}{k_B T}\right] \tag{4.2}$$

where g_i is the degeneracy of states for the i-ions, ε_i is the energy to obtain an i-ionized atom, n_e is the electron density, T is the temperature of gas and λ is the thermal de Broglie wavelength of electron given by:

$$\lambda_{DB} = \sqrt{\frac{h^2}{2\pi m_e k_B T}} \tag{4.3}$$

in which m_e is the electron mass. The Saha equation can be also expressed in terms of the ionization energy I and the initial gas density n_0:

$$\frac{n_i}{n_0} \approx 2.4 \times 10^{15} \frac{T^{3/2}}{n_i} \exp\left(-\frac{I}{k_B T}\right), \tag{4.4}$$

As can be seen in Fig. 4.1 higher is the density n_0 higher will be the plasma temperature to reach the same ionization state.

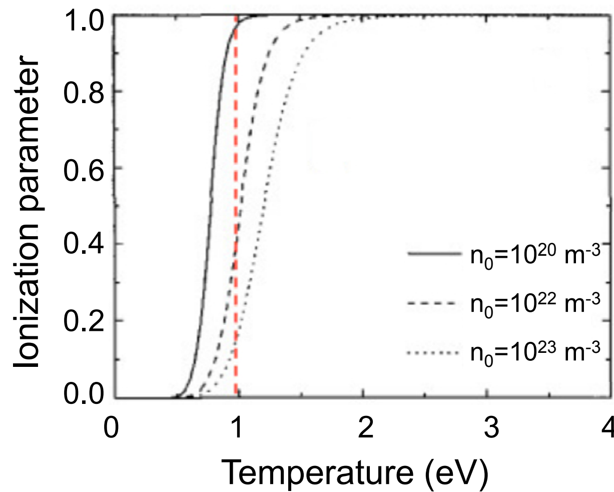

FIGURE 4.1: Ionization parameter as a function of the plasma temperature.

An important aspect that differentiates plasma from any ionized gas is the so-called quasi-neutrality condition. Considering a generic charge within the plasma, in principle it would be free to interact with all the other charged particles through Coulombian interactions. In fact that potential decreases very slowly with distance, being proportional to $1/r$. However, since the charges are free to move, the negative charges will tend to concentrate around each positive ones. This leads to the shielding of the positive charge from the predominantly negative charge region causing the annulment of the potential at a certain distance. Indicate with $Q(r)$ the amount of charge contained within the radius sphere r centered on the positive charge then the quasi neutrality condition can be expressed:

$$Q(r_s) \approx 0 \tag{4.5}$$

where r_s represents the distance to which the screen action becomes important. It is useful to define the so called Debye length, λ_D:

$$\lambda_D = \sqrt{\frac{k_B T}{4\pi n_0 e^2}} \tag{4.6}$$

It is possible to demonstrate that the charge contained in the sphere with radius r is proportional to:

$$Q(r) \propto \left(1 + \frac{r}{\lambda_D}\right) \exp\left(\frac{-r}{\lambda_D}\right) \tag{4.7}$$

and consequently $Q \to 0$ when $r \to \lambda_D$

4.1.2 Non-equilibrium plasma generated by laser

One of the possible ways to generate a plasma is the interaction between matter and high power laser pulses, as shown in Fig. 4.2 obtained irradiating in vacuum a Cu bulk target with a ns laser pulse with an intensity $I = 10^{10}\mathrm{W/cm^{-2}}$.

FIGURE 4.2: CCD image of a Cu plasma generated by a Nd:YAG laser.

The process leading to the generation of a plasma can be synthesized in three distinct phases.

1 laser-target interaction;

2 laser-plasma interaction;

3 supersonic adiabatic expansion along the normal to the target surface.

In the first phase, when a laser pulse is focused on a target, the material is rapidly ionized. In this phase dominate the photosionization and sputtering processes that lead to the removal of electrons, atoms, molecules and clusters from the irradiated target. These processes depend heavily on the intensity and fluency of the laser and in fact there is a particular ablation threshold value below which substantially fluorescence and heating effect is induced. For example as can be seen in Fig. 4.3 for Cu target irradiated at infrared region 1064 nm, the ablation threshold is 6.8 J/cm^2, but at 532 nm is 6 J/cm^2 and at 308 nm is 3 J/cm^2.

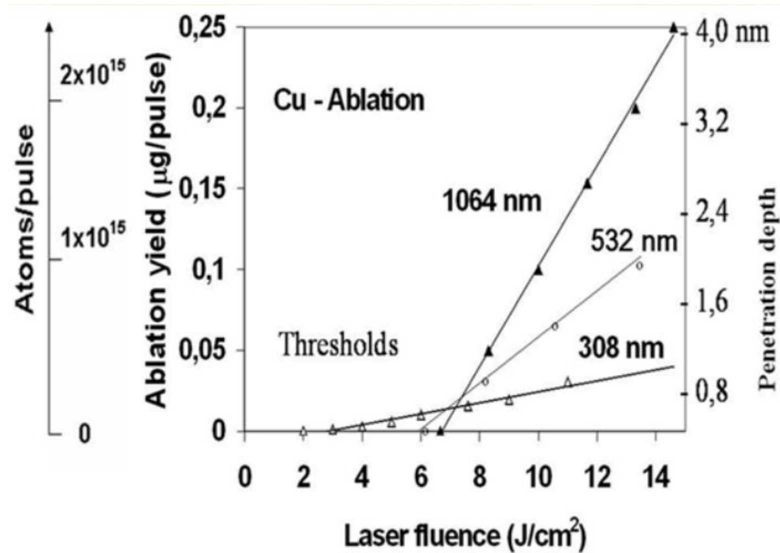

FIGURE 4.3: Ablation yield as a functioon of the laser fluence [102].

One of the main effects responsible of the energy transfer from the laser to the target is the ponderomotive force.

Considering the example of Fig. 4.4, the force that a charged particle experiences in an inhomogeneous oscillating electromagnetic field $\mathbf{E} = E_0 \cos(\omega t - \mathbf{k} \cdot \mathbf{x})$ is:

$$\frac{dv_x(t)}{dt} = \frac{eE_0}{m_e} \cos(\omega t - kz) \tag{4.8}$$

$$\frac{dv_z(t)}{dt} = v_x \frac{eB_0}{m_e} \cos(\omega t - kz) \tag{4.9}$$

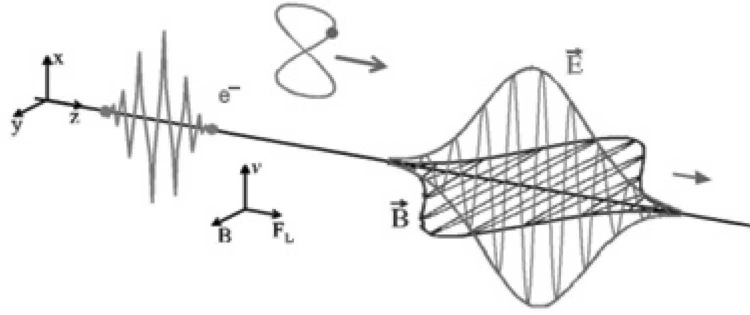

FIGURE 4.4: Description of the ponderomotive force.

The integral of the electron equation of motion gives:

$$v_x = v_{osc}\sin(\omega t - kz_0) \tag{4.10}$$
$$x(t) = -\frac{V_{osc}}{\omega}\cos(\omega t - kz_0) \tag{4.11}$$

where the quantity v_{osc} is the the electron quiver velocity and is given by:

$$v_{osc} = \frac{eE_0}{m_e\omega} \tag{4.12}$$

The maximum displacement along the x direction is given by:

$$d = \frac{eE_0}{m_e\omega^2} \tag{4.13}$$

From this consideration it is possible to define the ponderomotive energy U_P, that represents the acceleration of the ionized electron in the laser field in the following way:

$$U_P = \frac{e^2E_0^2}{4m_e\omega^2} = \frac{e^2E_0^2\lambda^2}{16\pi^2 m_e c^2} = 9.33\cdot 10^{-14}(I\lambda^2)\,\mathrm{eV} \tag{4.14}$$

where λ (μm) is the laser wavelength and I (W/cm^{-2}) is the laser intensity. So in conclusion the absorption mechanism is related to the $I\lambda^2$ factor. This factor, as it will be later, actually plays a very important role in the definition of many plasma characteristics.

In the second phase the interaction between the laser and the generated plasma occurs. In Fig. 4.5, as a sort of snapshot of this moment, are reported typical profiles of density, temperature and expansion velocity of the plasma. The laser light propagation within the plasma follows the dispersion relation:

$$\omega_L^2 = \omega_P^2 + k^2c^2 \tag{4.15}$$

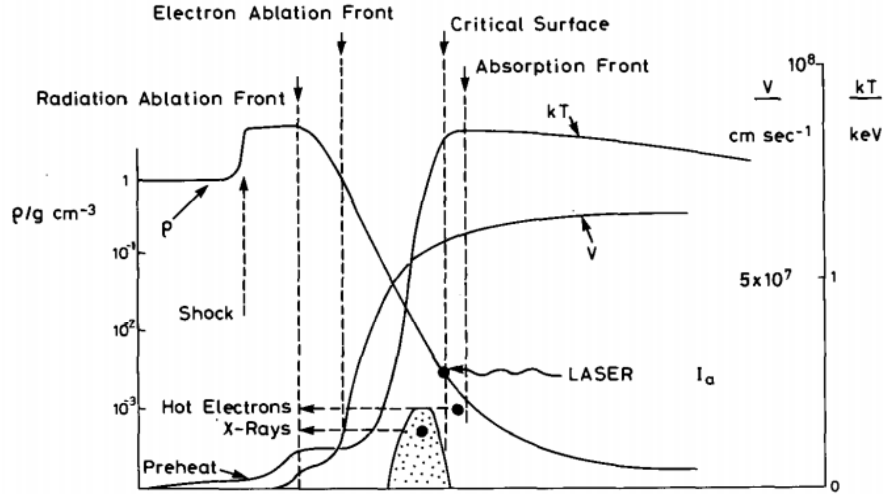

FIGURE 4.5: Typical temperature, density and expansion velocity profiles of a plasma generated by irradiation of a solid target by a nanosecond laser pulse focused on target at an irradiance of 10^{14}W/cm^2 [64].

where ω_L and k are the angular frequency and the wave number of the laser light and ω_P is the plasma frequency given by:

$$\omega_P = \sqrt{\frac{4\pi n_e e^2}{m}} \tag{4.16}$$

where e and m are the charge and the mass of the electron, respectively and n_e is the plasma electron density. Another useful parameter is the the group velocity v_g:

$$v_g = c\sqrt{1 - \frac{\omega_P^2}{\omega_L^2}} \tag{4.17}$$

it decreases as the electron density increases, reaching the limit value $v_g = 0$, at the critical density n_c defined as:

$$n_c = \frac{m\omega_L^2}{4\pi e^2} = 1.1 \times 10^{21}\lambda^{-2}(\mu\text{m})\ \text{cm}^{-3} \tag{4.18}$$

Laser light cannot propagate at densities $n_e > n_c$ (overdense region) and consequently the main interaction develops in the underdense plasma.

At this step the main absorption mechanisms such as the inverse Bremsstrahlung effect, ion turbulence and resonance absorption, are due to the presence of electrical field within the plasma and lead to momentum and energy transfer. Concerning the inverse Bremsstrahlung effects [36], the oscillations of electrons under the action of the laser electric field cause their collision with ions giving rise to transfer of electromagnetic energy to the plasma. After a certain distance L the fraction of absorbed laser energy in

an uniform plasma is given by:

$$\alpha_{abs} = 1 - \exp(-k_{ib}L) \tag{4.19}$$

where

$$k_{ib} = 3.1 \times 10^{-7} Z n_e^2 \ln\Lambda \omega_L^{-2} \left[1 - \left(\frac{\omega_P}{\omega_L}\right)^2\right]^{-1/2} (T_e(\text{eV}))^{-3/2}\ \text{cm}^{-1} \tag{4.20}$$

is the inverse Bremsstrahlung coefficient, i.e. the imaginary part of the laser wave vector k, $\ln\Lambda$ is the Coulomb logarithm for electron-ion collisions.

Finally the third step concerns the supersonic expansion of plasma in vacuum. The electron and ions velocity results dependent on three main factors and can be represented as:

$$v = v_{th} + v_k + v_c \tag{4.21}$$

in which:

$$v_{th} = \sqrt{\frac{3k_BT}{m}} \tag{4.22}$$

$$v_k = \sqrt{\frac{\gamma k_BT}{m}} \tag{4.23}$$

$$v_c = \sqrt{\frac{2ZeV_0}{m}} \tag{4.24}$$

The first v_{th} is due to the thermal agitation of particles and gives rise to a typical Boltzmann distribution. It depends on the mass of the ion m and of temperature T. The second is an adiabatic term v_k which takes into account the fact that the expansion occurs in vacuum. It this factor is present γ i.e. the adiabatic coefficient (1.67 for monoatomic species). The addition of the adiabatic term involves the modification of the velocity distribution function which becomes a Maxwell-Boltzmann shifted function. Finally, in order to consider the influence of the charge, the third term v_c, called Coulombian velocity, is added to the velocity distribution. This additional component is due to acceleration that charged particles acquire because of the potential difference produced by the spacing between fast electrons and slow ions that is of the order of the Debye length. In fact this term is given by the ion charge Ze and the equivalent voltage developed in the non-equilibrium plasma V_0. Consequently the overall distribution function is the so called Coulomb Boltzmann Shifted function (CBS)[83], and can be written in the following way:

$$F(v) = A\left(\frac{m}{2\pi k_BT}\right)^{3/2} v^3 \exp\left[-\frac{m}{2k_BT}(v - v_k - v_c)^2\right] \tag{4.25}$$

where A is a normalization constant, m the ion mass and T, the temperature. Concerning the ions yield, some estimations can be given through the semi empirical law according to the Lotz's theory [49, 50] that allows to calculated the ionization cross sections through the electron–atom and electron–ion impact. In particular the total ionization cross section σ_{ION} is the sum of the various cross section σ_k due to every single electron contained in the k-th sub-shell:

$$\sigma_{ION} = \sum_{k=1}^{N} \sigma_k = \frac{4.5 \cdot 10^{-14}}{E_e} \sum_{k=1}^{N} \frac{n_k}{I_k} \ln \frac{E_e}{I_k} \tag{4.26}$$

where N is the total number of sub-shell of the considered atom, n_k is the number of electrons in the k-th sub-shell, I_k is the ionization energy for the k-th sub-shell and E_e is the energy of the incident electrons. In Fig. 4.6 is shown the behaviour of the Lotz cross section as a function of the ratio between electron energy and ionization energy.

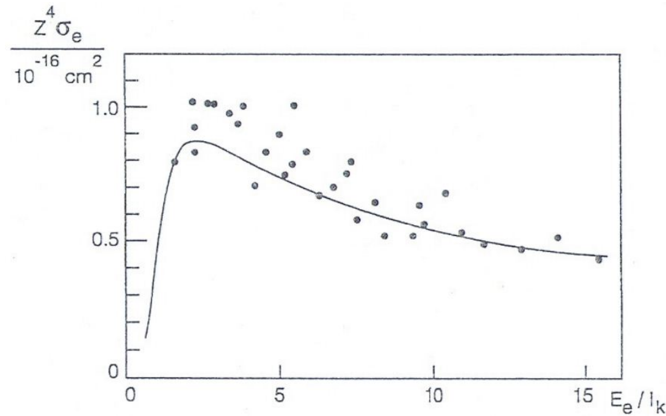

FIGURE 4.6: Cross section dependence on the ratio between electron energy and ionization energy

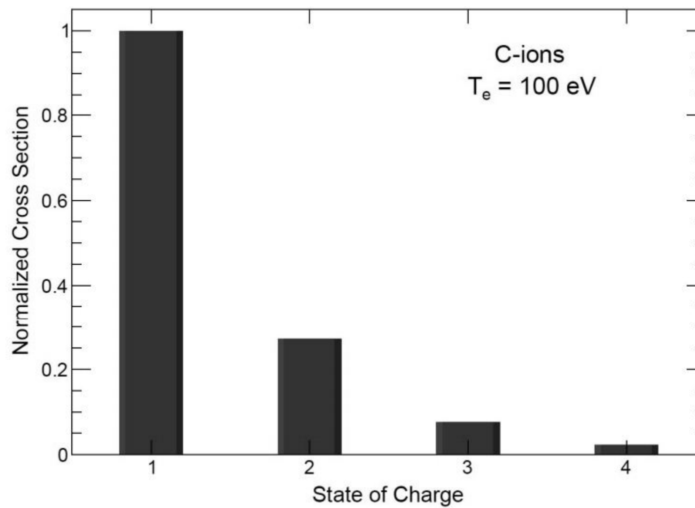

FIGURE 4.7: Calculated cross section for C ions.

From the eq. 4.26 it is possible to calculate the expected yields for the different charge states of Carbon ion, considering an incident monochromatic beam of electron with an energy of 100 eV, that represents a typical energy obtainable using a low laser intensity. The obtained values, normalized with respect the charge state 1+ are showed in Fig. 4.7

It should be noted that in plasma, beside the ionization due to electron impact, also the photon ionization occurs. However the electron impact ionization represents the most probable ionization process since its cross section is some order of magnitude higher than the cross section for the photon ionization.

Concerning photon emission, there are three fundamental emission processes. In the first case, the emission occurs in the continuum spectrum and is due to the interaction between free electrons and the Coulomb potential of ions, the so called Bremsstrahlung effect. The second process is due to the recombination, i.e. when a free electron pass from a free state to a bound state. The third mechanism produces a line spectrum because of the transition between discrete energy levels [37]. The ratio in which Bremmstrahlung or recombination phenomena occurs is strongly influenced by the atomic number of the target. In particular, considering the ratio of the spectrally integrated recombination and Bremsstrahlung intensities:

$$\frac{W_r}{W_B} \approx 2.4 \frac{Z^2 E_H}{k_B T_e} \tag{4.27}$$

in which $E_H = 13.6\,\mathrm{eV}$ is the Hydrogen ionisation energy. For low Z and/or high temperature plasmas Bremsstrahlung emission overcomes recombination emission and viceversa. The overall X-rays pulse duration is comparable with the laser pulse but changes according to the considered spectral range: the higher is the energy of the considered photon the shorter is the duration of the emission. Finally the peak of X-ray emissivity is located in the plasma region which combines both high temperature and high electron density, typically just beyond the critical density surface as can be seen in Fig. 4.5. So the main photon characteristics are actually influenced by the electron properties that, as described in the eq. 4.14 depend on the $I\lambda^2$ factor. The electron velocity induced by laser is:

$$v_{os} \approx 25\lambda(\mu\mathrm{m})\sqrt{I(\mathrm{W\ cm^{-2})}}\mathrm{cm/s} \tag{4.28}$$

Moreover from the observation of the X-ray spectrum comes out the presence of a superthermal electron component. They are generally called hot electrons, to differentiate them from the thermal maxwellian component (cold eectrons). The population of the hot components n_h is much lower than the thermal one n_{th} about $n_{th}/n_h \approx 100$. Also the hot electrons can be modelled with a Maxwellian distribution but with a much higher

temperature T_{hot}:

$$kT_{hot} = \left(\sqrt{1 + \frac{I\lambda^2}{2.8 \times 10^{18} W\mu^2/\mathrm{cm}^2 - 1}} \right) \cdot 511\,\mathrm{keV} \tag{4.29}$$

that however depends on the $I\lambda^2$ factor. Many other plasma parameters depend on this factor, such as the shockwave pressure:

$$P_M = 12.3 \left(\frac{I_L}{10^{14}} \right)^{2/3} \lambda^{-2/3} \left(\frac{A}{2Z} \right)^{1/3} \tag{4.30}$$

the ion temperature:

$$k_B T_i \text{ (eV)} = 2 \cdot 10^{-5} \sqrt{I_L (\mathrm{W\,cm^{-2}}) \lambda^2 (\mu\mathrm{m}^2)} \tag{4.31}$$

the emitted ion current:

$$j_s \approx 74 \sqrt{\frac{sz}{A}} \lambda^{-1} \sqrt{I} \tag{4.32}$$

the electric field generated as a result of charge separation effects:

$$E = 9.75 \cdot 10^{-5} \sqrt{I_L \left(\frac{\mathrm{W}}{\mathrm{cm}^2} \right) \lambda (\mu\mathrm{m})^2} \tag{4.33}$$

and consequently the equivalent accelerating voltage:

$$V_0(\mathrm{V}) = 2.6 \cdot 10^{-4} \sqrt{I_L \left(\frac{\mathrm{W}}{\mathrm{cm}^2} \right) \lambda^2 (\mu\mathrm{m})^2} \tag{4.34}$$

In fact Fig. 4.8 by I. Spencer et al. [72], shows a good proportionality between the $I\lambda^2$ factor and the experimental data of the maximum proton energy obtained by Tan et al. [77], Beg et al. [10] and Clark et al. [24].

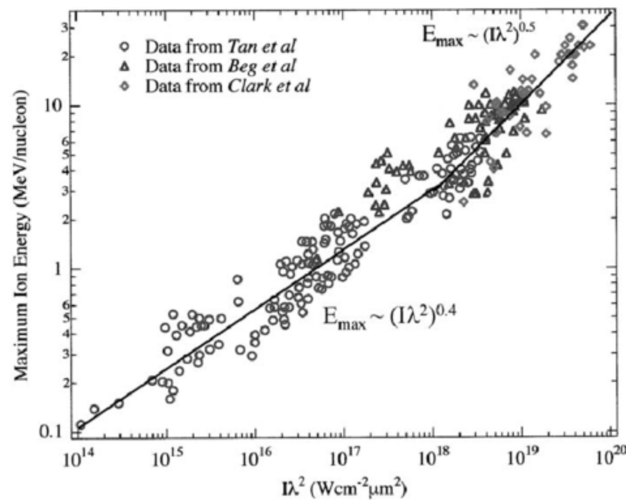

FIGURE 4.8: Maximum proton energy plotted as a function of $I\lambda^2$, experimental.

4.1.3 Backward Ion Acceleration, Target Normal Sheath Acceleration and Radiation Pressure Acceleration

The phenomena occurring in the laser-matter interaction depend not only on the laser's properties, but also on the target configuration and geometry. When a thick target is used ($> 20\,\mu$m), since the plasma emission occurs in the same half-plane where the laser hits, this experimental situation is usually called Backwards Ions Acceleration (BIA). As seen in Fig. 4.9 when the laser pulse interacts with a target, the first particles emitted in the same laser incidence plane, are electrons. Then the ions are also emitted, following the electron cloud. In this way a very high accelerating electrical field is developed due to the space separation between ions and the electronic cloud, of the order of the Debye length.

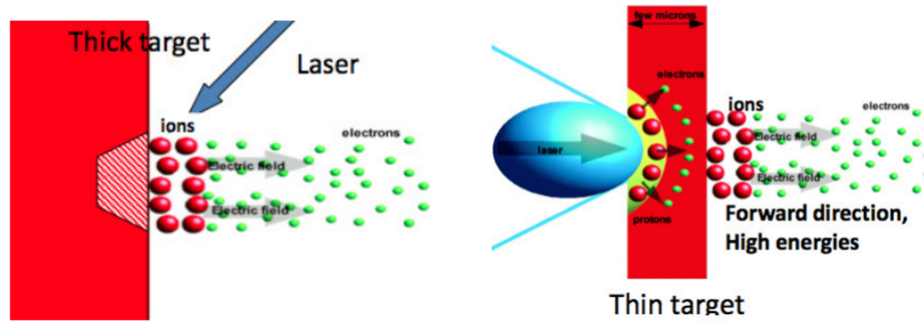

FIGURE 4.9: Comparison between the two acceleration techniques, the Backward Ion Acceleration (BIA) and Target Normal Sheath Acceleration TNSA.

If the target is very thin, of the order of some μm, the electron diffusion length may be greater than the same thickness of the irradiated material. Consequently, there are electron diffusive motions both in the forward and in the backward direction. This experimental condition, showed in Fig. 4.9, is generally referred as Target Normal Sheath Acceleration (TNSA). Again the charge separation generates an intense electric field responsible for ion acceleration, especially in the target's back surface, even if it is not irradiated from the laser. The BIA regime in general leads to a high ion current, with accelerations up to few MeV/Z, while with TNSA technique, although the ion current is lower, higher values of ion energy can be obtained, about 10 MeV/Z. However in the last cases very thin targets have to be adopted and high intensity laser, ranging between $10^{15}\,\mathrm{W/cm^2}$-$10^{18}\,\mathrm{W/cm^2}$, is required. However it should be noted that thanks to the technological improvements of laser in the last years, very high intensity has been reaching, beyond $10^{20}\,\mathrm{W\ cm^{-2}}$. However a new plasma physics is required to describe these new phenomena and the CBS model has to modified. So the new frontier is represented by the so-called Radiation Pressure Acceleration (RPA), in which it will be possible to accelerate ions up to GeV/Z energy, obtaining a highly monoergetic beam and very small divergence about $< 4°$, [62]. Besides the very high laser intensity also

ultra thin foils have to be employed (5-10 nm). Thanks to the attractive electrostatic force with ions, electrons, that at first are accelerated by the ponderomotive potential, give rise to a dense electron layer just beyind the backside of the foil. Then this dense electron layer undergoes a strong acceleration from the high light pressure, that is of the order of Gbar. The advantage of RPA regime is the fact that due to the directly transfer of momentum from laser to the particles that have to be accelerated, the final ion energy should scale as:

$$E_i \propto (I\tau/\sigma_{RPS})^{\alpha} \tag{4.35}$$

where τ is the pulse duration, σ_{RPS} is the areal mass of the target and the exponent α depends on the final velocity of particles (2 when $v_{final} << c$, 1/3 when $v \approx c$). So, even if it has never been demonstrated experimentally, the RPA regime should provide a much favourable intensity scaling than TNSA regime, that instead, as described before, results proportional to:

$$E_i \propto \sqrt{I\lambda^2} \tag{4.36}$$

4.1.4 Estimation of radiations fluence

Clearly, the current of particles emitted by the plasma has a strongly dependence from the laser and target conditions. However, only to have an estimate of the high fluence to which detectors are subjected, for each laser pulse an estimation of the current will be given.

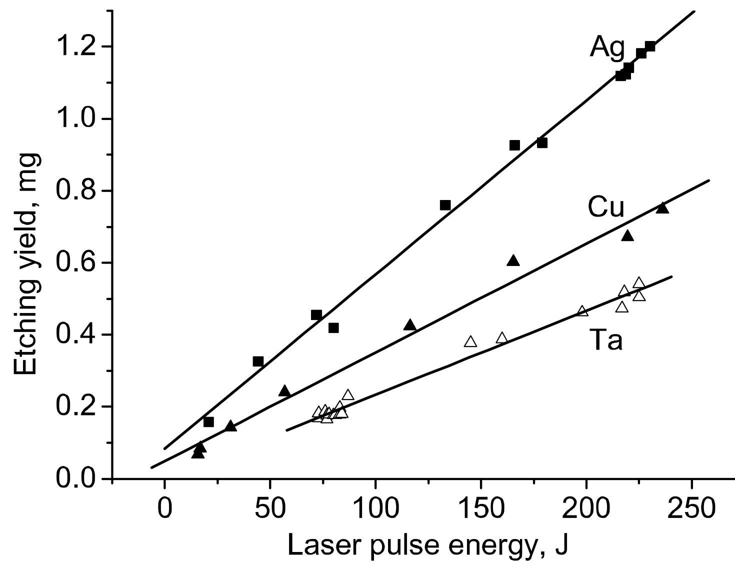

FIGURE 4.10: Ablation Yield as a function of the laser pulse energy for different target, from Ref. [99].

The number of atoms ejected from the target after the laser-matter interaction can be obtained from previous studies already reported in literature, such that illustrated in Fig. 4.3, of Ref. [102], or in Fig. 4.10, of Ref. [99] for low and high intensity laser respectively.

These analysis are performed using a profilometer (TENCOR p-10 model) that scans the crater region and from geometrical considerations the ablated material can be evaluated. Typical profile of the crater obtained using a low and high laser intensity are shown in Fig.4.11.

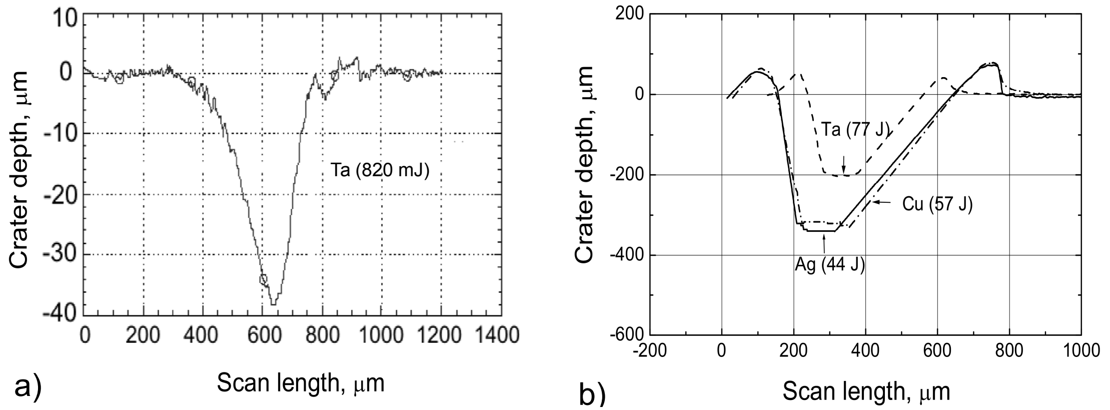

FIGURE 4.11: Crater profile for different target obtained at low intensity and high intensity laser, a) and b) respectively.

At low laser intensities ($\sim 10^{10}$ W/cm^2) the ablation of a thick target has a yield of the order of 1 μg/pulse, the fractional ionization is low ($\sim$10%), the maximum charge state is about 10^+, the ion energy is of the order of 100 eV/charge state, the ion temperature about 100 eV and the maximum electron density of the order of 10^{16}/cm^3, [97]. At medium laser intensities ($\sim 10^{15-16}$ W/cm^2 the ablation yield of thick targets is of the order of 1 mg/pulse, the fractional ionization is about 95%, the ion energy is about 100 keV/charge state, the ion temperature is of the order of 10 keV and the maximum electron density is of the order of 10^{20}/cm^3 [47]. At very high laser intensities ($\sim 10^{19}$ W/cm^2), when the pulse of tens of fs duration is used and the irradiated target is thin (10–100 μm), the ablation yield depends on the laser spot diameter and the target thickness, and generally it is below 1 μg/pulse, while the fractional ionization is 100%, the ion energy in the forward direction is about 1–10 MeV/charge state, the ion temperature is above 10 keV and the maximum electron density is of the order of 10^{22}/cm^3, [24].

Such an example, considering a polyethylene target CH_2, irradiated at PALS facility (I=10^{16} Wcm^{-2}), considering an ablation yield of 1 mg/pulse, the number of atom X

can be determined from the relationship:

$$14 : 6 \cdot 10^{23} = 10^{-3} : X \tag{4.37}$$

and so:

$$X = \frac{6 \cdot 10^{23} \cdot 10^{-3}}{14} \approx 5 \cdot 10^{19}\text{atoms} \tag{4.38}$$

Instead for a low laser intensity a value of three order of magnitude less is in general achieved. Of course these value are refereed to the total number of atoms emitted in every direction from the target. But also considering a very low solid angle, $10\,\mu$str, these number are still very high of the order of 10^{14} and 10^{11}, respectively. Similar considerations can be done also for the number of electron. Imaging to fully ionize the CH_2 atom, the total number of electron should be:

$$8 \times 5 \cdot 10^{19} = 4 \cdot 10^{20} \tag{4.39}$$

that considering the same solid angle becomes $4 \cdot 10^{15}$. The photon yield is also very high, because there are several mechanisms that should be taken into account that lead to the generation of photon such as the atomic emission or the Bremsstrahlung effects. Considering, for example, that only these phenomena occur, both at 1%, the total number of photon is $2 \cdot 10^{18}$ and hence $2 \cdot 10^{13}$ taking into account the solid angle.

More complex is the estimation of radiations current. As expected, the values are extremely high because the huge number of particles reaches the detector in the order of a few hundred ns. The ionic current, using high intensity laser may be greater than 10 A corresponding to a particle flow of 10^{10-8} particles in few nanoseconds, as well as the current of electrons that may be higher than 1 A. In addition to this there is also the emission of neutral particles, and heavier molecules that contribute to the total dose reaching the detector.

4.2 Description of TOF technique

The diagnostic of plasma generated by high intensity laser can not be performed using the spectroscopic chain described in section. 3.2 due to the very high radiation conditions. In such conditions a time of flight technique (TOF) has to be used. In this scheme the energy of radiations is determined by its time needed to cross a know distance i.e. the flight length d. In particular, simultaneously to the laser pulse, a trigger signal is sent to the oscilloscope, starting the acquisition. After laser-target interaction, the particles that are emitted from the plasma, reach the detector at different times according to their velocity and energy. This generates a signal that is recorded by the oscilloscope as the

arrival time i.e. the time of flight t_{TOF}. Knowing the time of flight t_{TOF} and the flight length d, the particle velocity v_i can be evaluated from:

$$v_i = \frac{d}{t_{TOF}} \tag{4.40}$$

and therefore the energy will be given by:

$$E_i(\text{eV}) = \frac{1}{2}\frac{m_i v_i^2}{e} \tag{4.41}$$

From these equations it can be understand that the sensitivity of the measurements is essentially determined from the sampling rate of the oscilloscope that must be very high, about few GS/s, in order to be able to distinguish the different times of flight of particles. The electronic chain is quite simple as can be seen in the scheme of Fig. 4.12.

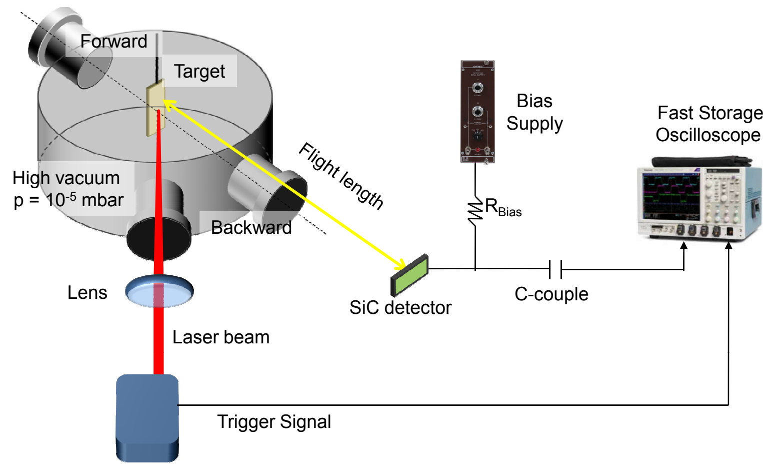

FIGURE 4.12: General scheme for time of flight technique.

The detector presents a typical biasing circuit consisting in a coupling capacitance C with the oscilloscope and a resistance R through which is connected to the bias supply. Choosing the appropriate values for R and C, which determine the decay constant of the electronics, it is possible to put in evidence or the very fast component of the spectrum, essentially due to photon and electron, or the slow component due to ions detection. There are many advantages in the usage of the TOF technique. First of all it gives the possibility to monitor very high particle flux, without any problems concerning pile-up effects. It represents an on-line diagnostic and in short times can gives a summary description of the plasma. Moreover as it will be described in the following sections, from the analysis of a TOF spectrum more informations can be carried out such as the energy distribution of the corresponding ion charge state, their temperatures, the intensity of the accelerating voltage, the electron temperature and so on. Finally this technique can be applied in a wide range of laser intensities and conditions. There will be presented results obtained using:

- Nd:YAG laser: with the fundamental wavelength at 1064 nm and the 2nd harmonic at 532 nm, pulse duration 3 ns, maximum pulse energy 300 mJ, laser intensity 10^9 W/cm^2 @ UniME (IT);

- Nd:YAG laser: with the fundamental wavelength at 1064 nm, the 2nd harmonic at 532 nm and the 3rd harmonic at 355 nm, pulse duration 9 ns, maximum pulse energy 900 mJ, laser intensity 10^{10} W/cm^2 @ INFN-LNS (IT);

- Iodine laser: with the fundamental wavelength at 1315 nm and the 3rd harmonic at 438 nm, pulse duration 300 ps, maximum pulse energy 1 kJ, laser intensity 10^{16} W/cm^2 @ PALS (CZ);

- Ti Sapphire laser: with the fundamental wavelength at 800 nm, pulse duration 39 fs, maximum pulse energy 200 mJ, laser intensity 10^{18} W/cm^2 @ CELIA (FR).;

- Ti Sapphire laser: with the fundamental wavelength at 800 nm, pulse duration 45 fs, maximum pulse energy 370 mJ, laser intensity 10^{19} W/cm^2 @ IPPLM (PL);

On the other hand the disadvantage in the adoption of the TOF technique is the fact that for photon the measure of energy becomes not immediate. In fact if the ions energy can be determined from their times of flight, for photons the same calculation can not be done since they arrive simultaneously to the detector, travelling with a velocity c. However some estimations about the mean energy of photon can be done by using different absorbers in front of the detector, as it will be described in the section .

4.2.1 Typical TOF spectra

The TOF technique, as described before, can be used in a very wide range of laser intensity, from 10^9 up to 10^{18} W cm^{-2}. In this section there will be pointed out the main difference between two typical spectra obtained at low 10^{10} W cm^{-2} and high 10^{16} W cm^{-2} laser irradiation conditions. In Fig. 4.13 are compared typical TOF spectra obtained at INFN-LNS and PALS facility, respectively. Such experimental conditions are very different and the accelerations gained from the particles include very different energy ranges. In fact since in the first case were expected ion energies of the order of some hundred eV, the SiC IAZ 4 has been chosen as detector. Instead at PALS facility, very high energy are generally obtained [56] up to some MeV, and consequently the detector with the deepest depletion layer (SiC AZ 80) have been used. The first spectrum, Fig. 4.13a, was obtained detecting particles emitted after the interaction of laser with a Carbon target, placing the detector at a distance of 48.5 cm along the target surface and in the backward direction with respect the laser incidence.

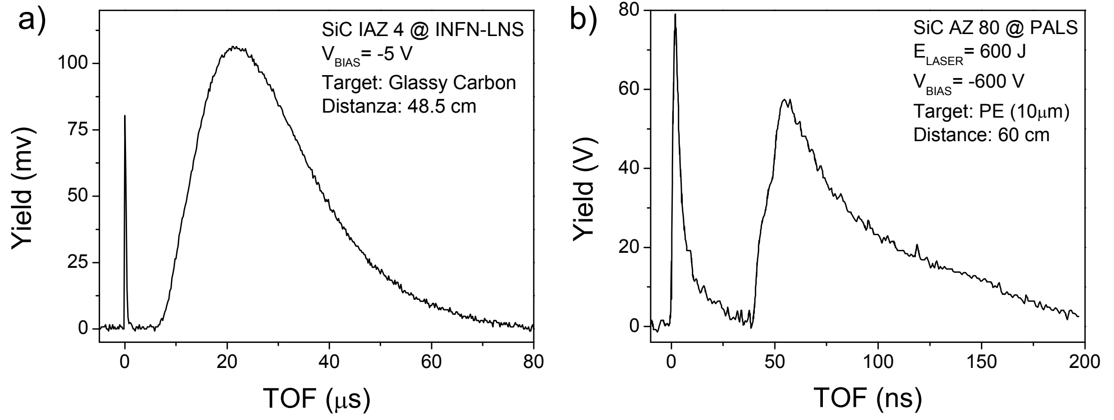

FIGURE 4.13: TOF spectrum obtained irradiating a Carbon based target at low a) or high b) laser intensity.

The very narrow peak at $t = 0$ is mainly due to photon detection, soft X-rays and UV. This peak is generally called photopeak and constitutes the start of the acquisition. Beside the photopeak a wide structure is present for time of flight ranging 6 - 60 μs related to ions detection. In general this structure is quite difficult to analyse because it is constituted by the overlapping of many signals due to the various ion charge state. From a first look of the spectrum a first estimate of the ions energy can be given. A first calculation on proton maximum energy can be done considering a time of flight of 8.7 μs and a flight distance of 48.5 cm. In fact using the eq. 4.40 the proton energy is:

$$v_p(\mathrm{m/s}) = \frac{d}{t_{TOF}} = \frac{0.485\,\mathrm{m}}{8.7 \cdot 10^{-6}\,\mathrm{s}} = 0.56 \cdot 10^5 \mathrm{m/s} \tag{4.42}$$

and hence the energy, from eq. 4.41:

$$E_p(\mathrm{eV}) = \frac{1}{2}\frac{m_p v_p^2}{e} = \frac{1}{2} \cdot \frac{1.67 \cdot 10^{-27}\,\mathrm{kg}\,(0.56 \cdot 10^5\,\mathrm{m/s})^2}{1.60 \cdot 10^{-19}\,C} = 15.95\,\mathrm{eV} \tag{4.43}$$

This result gives an estimation of the energy per charge state. So according to this result the Carbon ion will have an energy proportional to their charge state. For example the C^{3+} should have an energy three times greater than proton, etc .

Also the second spectrum of Fig. 4.13b shows a similar shape: photopeak and ions. However it should be noted that in this case the detector SiC AZ 80, placed at about 60 cm, looks particles emitted in forward direction with respect the laser incidence at about 30°. So, if in the first spectrum a BIA acceleration condition was investigated, in this case was adopted a TNSA configuration. In fact the irradiating target consists in a thin foil of polyethylene about 10 μm thick. The photopeak starts at $t = 0$ but in this case is due not only to the detection of hard X-rays (from a few keV up to a few tens of keV), but also to relativistic electrons, belonging to the hot component. Instead the cold electron are detected in the long tail following the photopeak for times of flight between

10-50 ns. The large peak starting at about 40 ns is due to ions detection and in particular to the very fast proton at the biginning of the peak, then there are the six charge state of carbon followed by more heavier molecules C_xH_y arriving for time of flight greater than 150 ns. Again, using eq. 4.40 and eq. 4.41, a first estimate of proton energy can be given obtaining a maximum proton energy of about 1.2 MeV.

However for both spectra, more detailed information can be obtained once a fit procedure has been performed. In order to distinguish the various contributions due to the different ion charge state the experimental data are deconvolved using the CBS function. In particular the CBS distribution expressed in time appears like:

$$f(t) = A\sqrt{\left(\frac{m}{2\pi k_B T}\right)^3}\frac{d^4}{t^5}\exp\left[-\frac{m}{2k_B T}\left(\frac{d}{t} - \sqrt{\frac{\gamma k_B T}{m}} - \sqrt{\frac{2zeV_0}{m}}\right)^2\right] \tag{4.44}$$

where A is a normalization constant, m and z are the mass and the atomic number of the considered ion, respectively, d is the flight length γ is the adiabatic coefficient that for monoatomic species is 1.67, k_BT is the equivalent plasma temperature while V_0 represents the equivalent acceleration voltage developed in the non-equilibrium plasma. Starting from this expression was written the following fitting function:

$$Y(t) = A_0\sqrt{\left(\frac{A_1}{2\pi A_2}\right)^3}\frac{d}{t^5}\exp\left[-\frac{A_1}{2A_2}\left(\frac{d}{t} - \sqrt{\frac{1.67A_2}{A_1}} - \sqrt{\frac{2A_3A_4}{A_1}}\right)^2\right] \tag{4.45}$$

Actually, once the ion charge state is chosen, the only parameters that play an important role in the deconvolution are:

- the normalization curve A_0 that changes the height of the curve;
- the factor $A_2 = k_BT$ related to the ion temperature which intervenes in the width of the curve;
- the parameter $A_4 = eV_0$ connected to the equivalent accelerating voltage which shift the curves to longer or shorter times of flight.

The possible solutions of the deconvolution process are reported in Fig. 4.14.

In the first spectrum Fig. 4.14a, obtained at low laser condition, the fit was performed using only five curves one to proton and the other for the first four charge state of Carbon. This choice is determined from the fact that, tacking into account the ionization energies data, reported in the NIST Atomic Spectra Database [46] for Carbon, reported in Tab. 4.1.

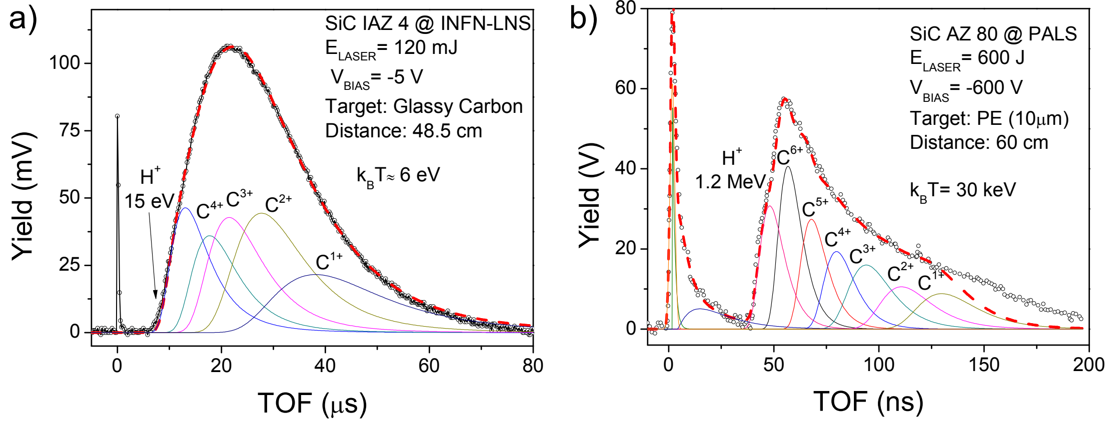

FIGURE 4.14: Possible Fit of the experimental data using CBS function.

TABLE 4.1: Ionization energy of Carbon from NIST Atomic Spectra Database [46].

Ion Charge	Ionization Energy (eV)
+1	11.26
+2	24.38
+3	47.89
+4	64.49
+5	392.09
+6	489.99

The energy for the ionization of the fifth electrons results too high, 392 eV, considering the low laser intensity at INFN-LNS. The four charge state are obtained at 19.13 μs (C^{4+}), 22.09 μs (C^{3+}), 27.06 μs (C^{2+}), 38.26 μs (C^{1+}) and are in good agreement with the expected values for the energy $\sim$ 60, 45, 30 and 15 eV, resulting proportional to the maximum energy for proton calculated before. From the fit parameter A_4, an equivalent temperature of 6 eV was estimated.

The Fig.4.14b presents the possible deconvolution of the PALS spectrum. The faster detected ions are protons detected at 48 ns corresponding to a kinetic energy of 1.2 MeV. The faster carbon ions are detected at 66 ns corresponding to a kinetic energy of about 7 MeV, due to the contribution of C^{6+} ions. In fact for such laser conditions the Carbon ions are surely fully ionized. This value obtained for the Carbon ions energy results compatible with an ion acceleration of about 1.15 MeV per charge state as expected from the energy of proton calculated before and is in good agreement with literature [18]. Note that the energy of 1.2 MeV protons is a little value if compared with results obtainable in TNSA regime at PALS facility, in fact Torrisi et al. demonstrates that, using particular irradiation condition, this energy may reaches a value of about 5 MeV [81, 92]. The deconvolved Boltzmann ion distributions are regularly shifted proportionality to their charge state and show a width corresponding to plasma temperature of 30 keV, in good agreement with literature [98]. Fig. 4.15 shows a more detailed view of the photopeak region with the deconvolution relative to X-rays, relativistic electrons and cold electrons.

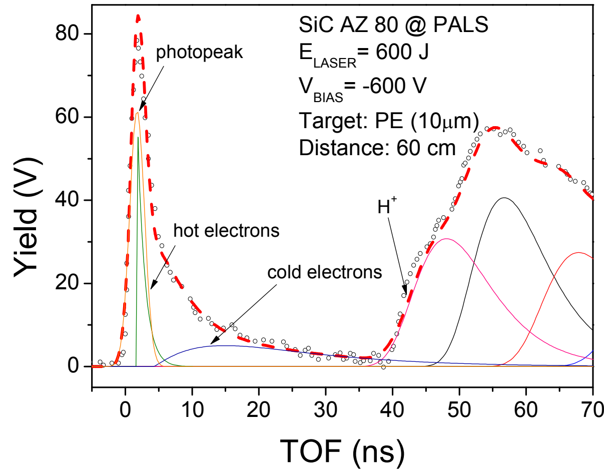

FIGURE 4.15: Detailed view of photopeak and possible deconvolution of hot and cold electrons.

It can be seen that photons and relativistic electrons are detected simultaneously at the laser shot, while cold electrons, with kinetic energy below some tens of keV, constitute a signal separated by the photopeak and occurring before the faster ion peak. The cold component shows a TOF spectrum compatible with a Maxwell-Boltzmann distribution:

$$f(v) = \sqrt{\left(\frac{m}{2\pi k_B T}\right)} 4\pi v^2 \exp - \frac{mv^2}{2k_B T} \tag{4.46}$$

From this fit it is possible to extract a energy windows ranging approximately between 52.8 keV and 0.6 keV and an equivalent temperature of about 9.55 keV.

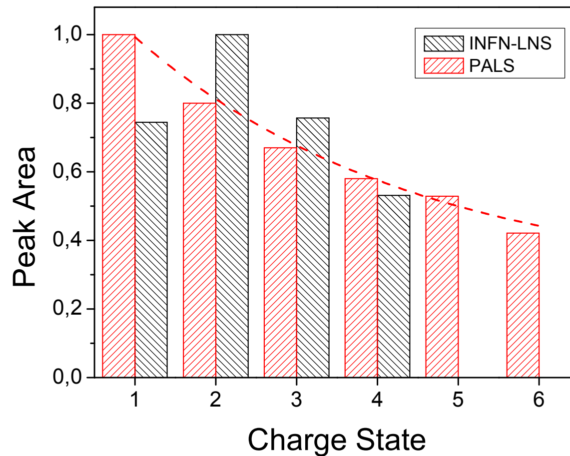

FIGURE 4.16: Yields of the ion production as a function of the charge state.

An important test of the obtained fitting curves for ions comes from the comparison with theoretical prevision of Lotz's equation 4.26. Fig. 4.16 shows a comparison between the yields of the ion production as a function of the charge state, calculated through the integral of the experimental ion charge state distributions, for the two experimental

conditions. Both data were normalized to the charge state C^{1+} and the obtained experimental trend seems to be in good agreement with the theoretical trend obtainable according to the Lotz approach [49].

4.3 Comparison in the response of SiCs, Diamond and Silicon Detector

Recently, an experimental campaign was conducted at Warsaw's IPPLM, where it was possible to compare the response of the different solid state detectors. As can be seen in Fig. 4.17 all detectors were placed in forward direction with respect the laser incidence but at different angles.

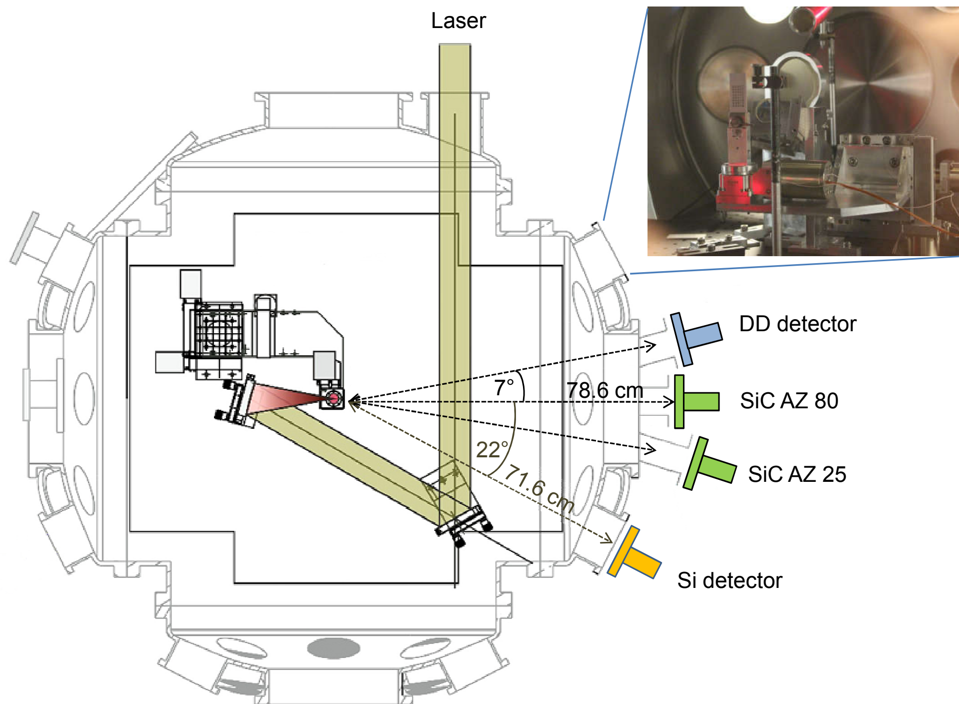

FIGURE 4.17: Experimental set up at IPPLM laboratory and diagnostic equipment.

In fact considering the normal to the target at 0° the Silicon detector was placed at 22° and at a distance of 71.6 cm, the SiC AZ 25 and SiC AZ 80 were placed at 7° and 0°, respectively at a distance of 78.6 cm while the Diamond detector was placed at −7° at a distance of 78.6 cm. The selected shot was performed with a laser energy of 280 mJ, a pulse duration of 51 fs, and a focal position of 0 μm. The target is a thin (6 μm thick) multilayer of Al and Graphene. The obtained spectra are reported in Fig. 4.18.

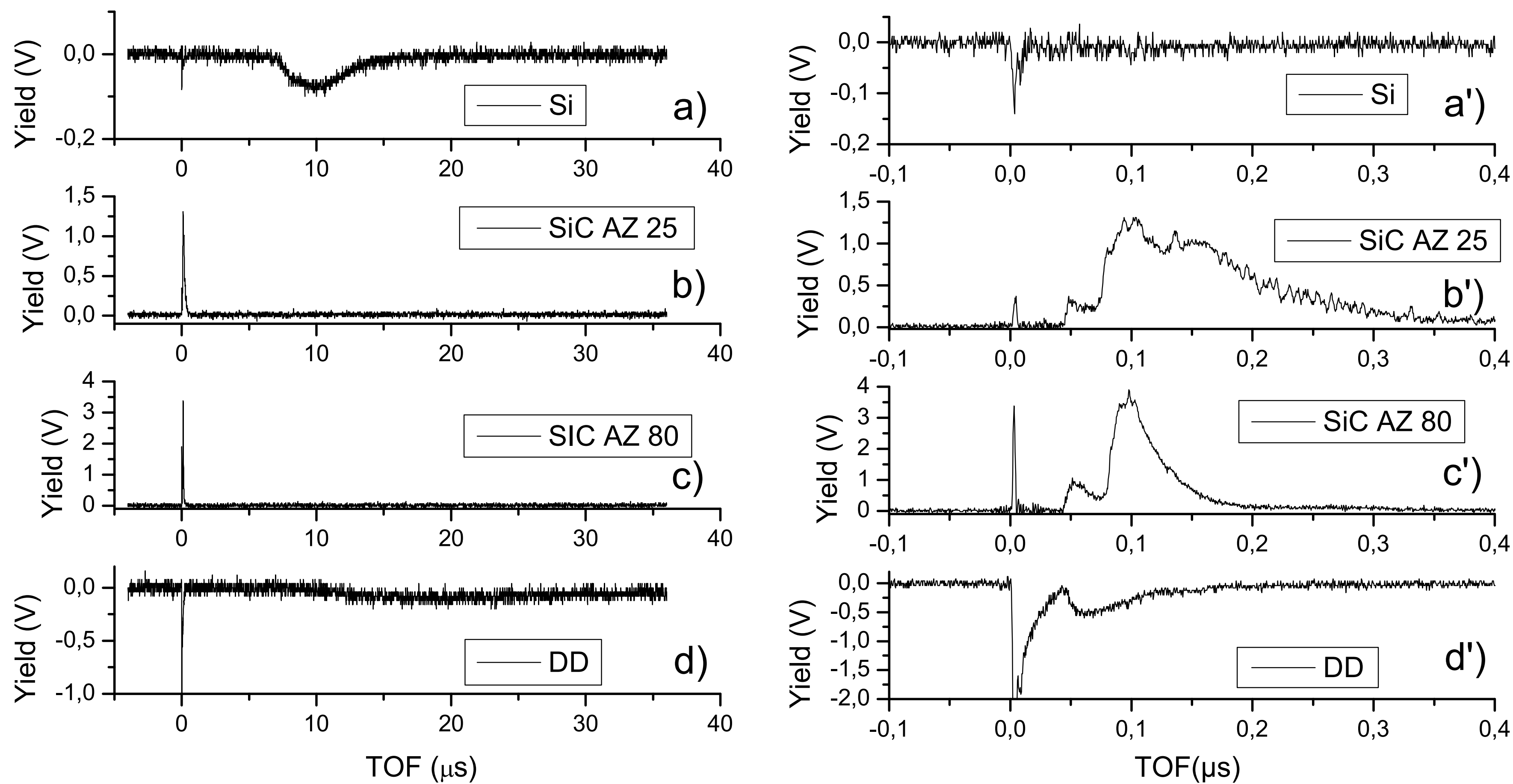

FIGURE 4.18: TOF spectra acquired with Silicon detector a), SiC AZ 25 b), SiC AZ 80 c), Diamond detector d) using a large (left) and short (right) time scale.

At long time scale Fig. 4.18a-d it would seem that only silicon and diamond devices detect something. These detectors having an extremely thin metallization, are able of detecting even low energy radiations (in the order of some tens of eV). However the most interesting result is obtained at shorter time scale, as reported in Fig. 4.18a'-d'. In fact both two SiC detectors reveal a fast proton peak at 50 ns, confirmed also by the Diamond detector. The proton peak is followed by the a widen structure due to Carbon and Aluminum. However due to the thicker metallization layer the SiC AZ 80 spectrum does not present the second structure at higher time of flight representative of slower and heavier ions. Another interesting aspect is the fact that in the DD spectrum the photopeak is followed by a long tail that is generated by electron detection. In the other detector is not so evident so from this result Diamond detector seems to be more efficient in the electron detection with respect SiC and Silicon devices.

4.4 Comparison with other plasma diagnostics

Beside Silicon Carbide detectors many other device can be employed for the diagnostic of laser generated by plasma. Some examples of on-line diagnostics are:

- Langumir probe or the optical spectroscopy that can be used to measure electron density and temperature;
- Mass quadrupole spectrometry that gives information about the abundance of selected elements and their time evolution;
- CCD or Streak camera to study the evolution of plasma selecting particular range of wavelength;
- Optical spectrometry and X-rays detector.

There are also off-line detection system such as the RBS spectroscopy of implanted materials, superficial analysis with profilometer, track detectors, diffractometric interference and so on. Moreover it can be used very complex systems such as the Thomson Parabola Spectrometer, that combine electrical and magnetic deflection for separate ions according to the charge-mass ratio. However remaining within the ambit of time of flight technique also electrostatic probe (such as Ion Collector, Faraday cup, delayer grid) or scintillator coupled with a photomultiplier systems, can be used for a wider description of plasma properties. In this section there will be described the Ion collector, the Ion Energy Analyser and the PVT scintillator, and there will be pointed out the main advantage and disadvantage with respect Silicon Carbide detector.

4.4.1 Ion collector

In general the operating principle of a Ion Collector is quite simple. When a positive ion hits on the Faraday Cup an electron is pulled from the mass, passing through a current meter to neutralize the positive charge of the ion as shown in Fig. 4.19.

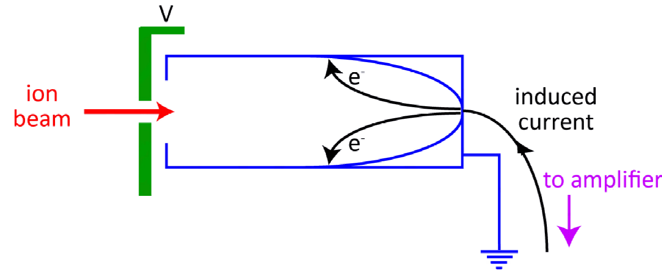

FIGURE 4.19: Operating principle of an Ion Collector.

For a continuous ion beam (each with a single charge):

$$\frac{N_i}{t} = \frac{I}{e}, \tag{4.47}$$

where N_i is the number of the observed ions in the time t, I is the total current and e the elementary charge. Actually experimentally it is not so simple apply this expression because ions penetrating the metal generally have higher energies than the work function of the material of the cup leading to the generation of free electrons known as secondary electrons. When an electron leaves the cup, the charge left will simulate the arrival of an additional ionic charge causing an error in the measurement. The generation of secondary electrons depends on:

- the mass, the charge and the energy of incoming ions;
- incidence angle;
- geometry and the material of the cup.

In fig. 4.20 shows the variations of the yield of secondary electrons emission as a function of radiation energy in different materials [39, 68].

However, there are techniques that can be used to limit the effect of secondary generation of electrons, that can be distinct in passive and active techniques. The passive techniques relate to the choice of material and geometry of the cup. The active techniques allow to limit both the input of secondary electrons produced in the scattering chamber inside the cup and the release of secondary electrons produced within the cup favoring its collection. To do this, magnetic fields can be used to confine the electrons to the cup, or grids can

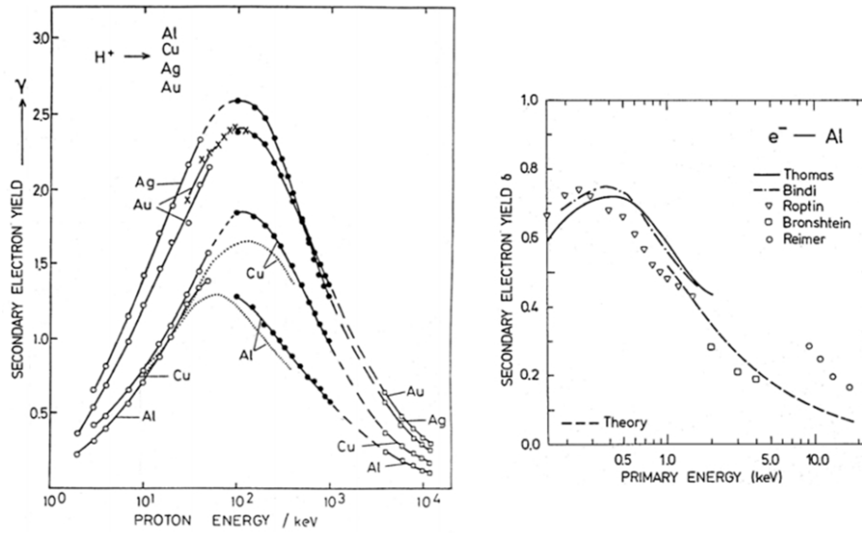

FIGURE 4.20: Emission yield of secondary electron as a function of proton energy (left) or electron (right) for different materials.

be used before the collector metal, which are generally negatively polarized to force the secondary electrons to come back into the cup. By combining magnetic fields and grids, it is possible to reduce the secondary emission of electrons to a few hundred parts per million. Sometimes a second grid positively loaded is placed in front of the negative grid to reflect back the ions that "bounce" in the metal without releasing their charge. In Fig. 4.21 are reported schematic drawing of typical charge collectors used in laser-plasma investigations [107].

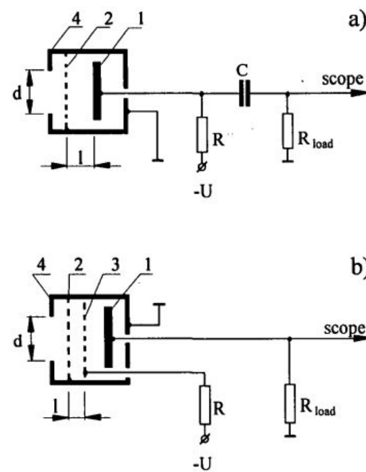

FIGURE 4.21: Possible schemes of an Ion collector consisting in: 1 collector - 2 entrance grid - 3 control grid - 4 grounded housing - R_{load} load resistance - U bias potential.

Starting from the eq. 4.47 and taking into account observations just made regarding the emission of secondary electrons, it is possible to write the output current of collector I_c

as the combination of an ion current I_i and a current due to secondary electron I_e :

$$I_c = I_i + I_e = e\varepsilon vS \left[\sum_{j=0}^{z_{max}} [z_j(t) + \gamma_j(t)] n_{i,j} \right] \tag{4.48}$$

where ε is the transparency of the entrance grid, $S = \pi d^2/4$ is the collector surface, v is the plasma velocity, z_j is the charge state of the j-th ionic species, γ_j is the secondary ion-electron emission coefficient, $n_{i,j}$ is the density of the j-th ionic species. Defining the quantity:

$$n_i = \sum n_{i,j} \quad \bar{\gamma} = \sum_j \gamma_j n_{i,j} / \sum_j n_{i,j} \quad \bar{z} = \sum_j z_j n_{i,j} / \sum_j n_{i,j}$$

it is possible to write eq. 4.48 in the following way:

$$I_c(t) = \varepsilon e v S \bar{z}(t) n_i(t) [1 + \bar{\gamma}(t)/\bar{z}(t)] = \tag{4.49}$$

$$I_c = \varepsilon [1 + \bar{\gamma}(t)/\bar{z}(t)] I_{coll} \tag{4.50}$$

where I_{coll} represents the ion current in the input grid for a given instant of time t. On the other hand, the current I_c will be given by:

$$I_c = \frac{U_c}{R_{load}} = \varepsilon [1 + \bar{\gamma}(t)/\bar{z}(t)] I_{coll} \tag{4.51}$$

where $U_C(t)$ is the bias potential and R_{load} the load resistance. Consequently I_{coll} is given by:

$$I_{coll}(t) = \frac{U_c(t)}{\varepsilon R_{load}[1 + \bar{\gamma}(t)/\bar{z}(t)]} = e\frac{d}{dt}[N(t)\bar{z}(t)] \tag{4.52}$$

where $N(t)$ is the total number of ion reaching the collector. So the ionic charge distribution in time is:

$$dQ/dt = e\frac{d}{dt}[N(t)\bar{z}(t)] = \frac{U_c(t)}{\varepsilon R_{load}[1 + \bar{\gamma}/\bar{z}(t)]} \tag{4.53}$$

From this last equation it can be obtained also the ionic distribution in velocity dQ/dv and in energy dQ/dE; By integrating them, the total charge and the total energy of impinging ions can be calculated.

4.4.1.1 Analysis of a typical IC-TOF spectrum

In Fig. 4.22a is reported a typical spectrum obtained through an Ion Collector. In this case a thick target of PE was irradiated using the low intensity laser Nd:YAG operating at UniME laboratory.

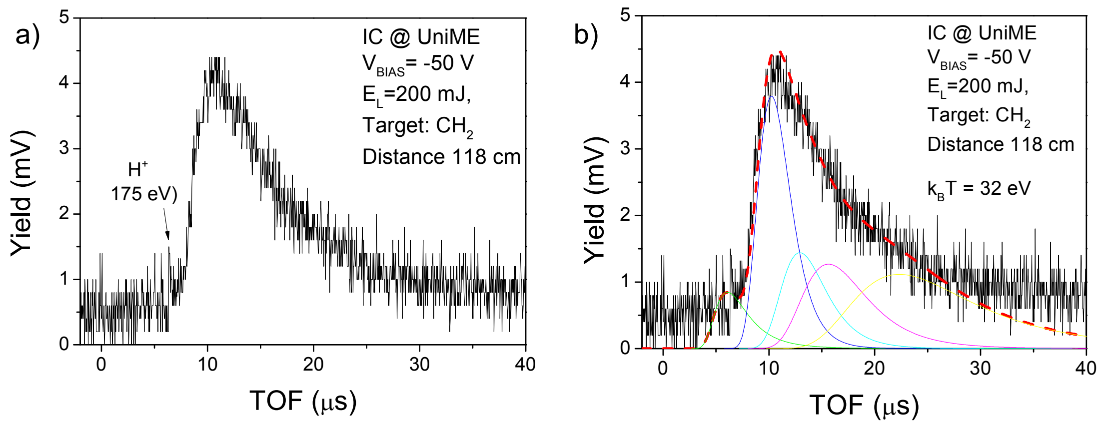

FIGURE 4.22: Typical IC spectrum a) and possible deconvolution of ions using CBS distribution.

The IC was placed at a flight distance of 118 cm along the normal to the target surface. The spectrum shows similar characteristics, compared to typical SiC-TOF spectra. However in this case the photopeak is just above the noise, and it is not possible to detect any electron-induced signal since the grid is negatively polarized. Also in this case is present a large peak, starting from 6 μs that reaches about 30 μs due to protons and carbon ions detection. Using eq. 4.40 and eq. 4.41 was evaluated a mean proton energy of about 175 eV considering the little edge present for time of flight lower than 8 μs. This data seems to be confirmed also from the fitting process and the CBS functions employed for proton and the four charge state of Carbon are compatible with a temperature of 32 eV, as shown in Fig. 4.22b.

4.4.1.2 Comparison in the ion response between SiC and IC

The Fig. 4.23 shows a comparison of two time of flight spectra captured with a SiC and IC detector, respectively, under the same experimental conditions. The target consist in a very thin polymeric foil ($\sim$ 10μm) of PET polyethylenetheraphtalate with gold nanoparticles. In these measurements the detectors are placed at the same distance from the target, about 155 cm. The spectra indicate the presence of a fast photopeack followed by a tail, probably due to the detection of fast electrons and/or a delayed X-ray emission, followed by ions peaks. The difference in the shape of the signal in the ionic part of the SiC and IC spectra is due to the different detection method. On the one hand, if the SiC signals are proportional to the energy deposited by the ions and photons in the sensitive volume of the device, on the other hand the IC signals are due to ionic charge deposited on the surface of the Faraday Cup. As a result, photons and charged particles with low charge but high energy, such as protons, generate high signals in the SiC detector, while ions with high charge induce high signal in the Ion Collector.

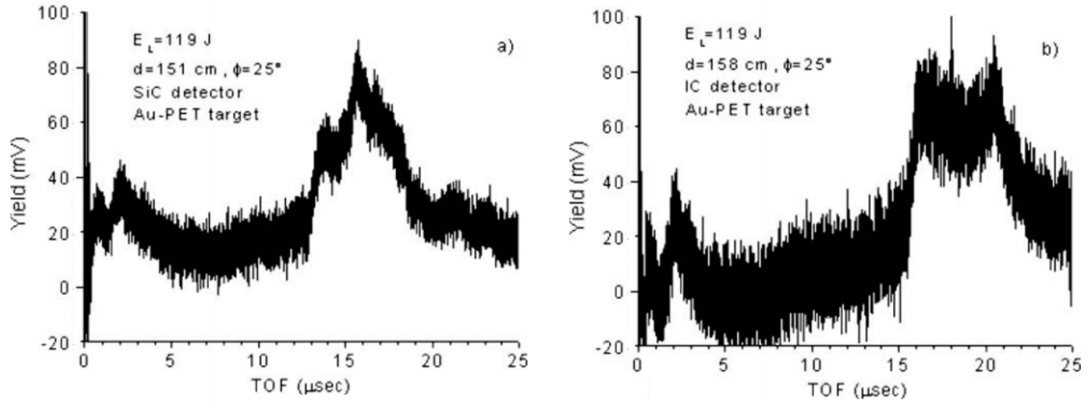

FIGURE 4.23: SiC a) and IC b) TOF spectra acquired at the same experimental conditions.

From these considerations, it is possible to observe that the first peak present in the SiC spectrum (13 μs) is substantially absent in the IC spectrum, proving that it is due to proton with high energy, and therefore well-revealed by SiC, but with a low charge, and therefore not very visible from the IC. On the other hand, however, the ionic tail of Au at high TOF (20-25 μs), not well visible in the SiC spectrum, corresponds to slower ions that have low energy but present high current. Another aspect to point out is that the solid angle subtended by the two detector is very different because although they are placed at the same distance, the active surface of SiC is much smaller than that of the IC:

$$\left(\frac{\Delta\Omega}{\Omega}\right)_{SiC} = 8.8 \times 10^{-7} \tag{4.54}$$

$$\left(\frac{\Delta\Omega}{\Omega}\right)_{IC} = 7 \times 10^{-5} \tag{4.55}$$

However, despite this large solid angle difference (about 80 times), the yield (mV) of the two signals is quite comparable and consequently the sensitivity of the SiC results greater than that of the IC. In fact the response of the two detectors Y_{SiC} and Y_{IC} are given by [95]:

$$Y_{SiC} \propto \varepsilon \frac{\Delta\Omega}{\Omega}\frac{dN}{dt}\langle E\rangle \tag{4.56}$$

$$Y_{IC} \propto \varepsilon \frac{\Delta\Omega}{\Omega}\sum_{i=1}^{Z} i\frac{dN_i}{dt} \tag{4.57}$$

where N is the number of the particles reaching the active region of the detector, ε is the detector efficiency (100%), $\Delta\Omega/\Omega$ is the solid angle subtended by the detector, Z the maximum charge state, N_i is the number of particles with the $i-$th charge state and

$\langle E \rangle$ is the mean energy of particles that is defined as:

$$\langle E \rangle = \frac{\int E\, f(E)\, dE}{\int f(E)\, dE} \tag{4.58}$$

in which $f(E)$ represents the particles energy distribution that in a first approximation can be given by a Boltzmann function.

4.4.2 Ion Energy Analyser

The main part of the IEA is the deflection system, which is made of two coaxial metallic cylinders of radii R_1 (inner plate) and R_2 (outer plate) maintained at potential V_1 and V_2, respectively, [107]. A scheme of the IEA is shown in Fig. 4.24.

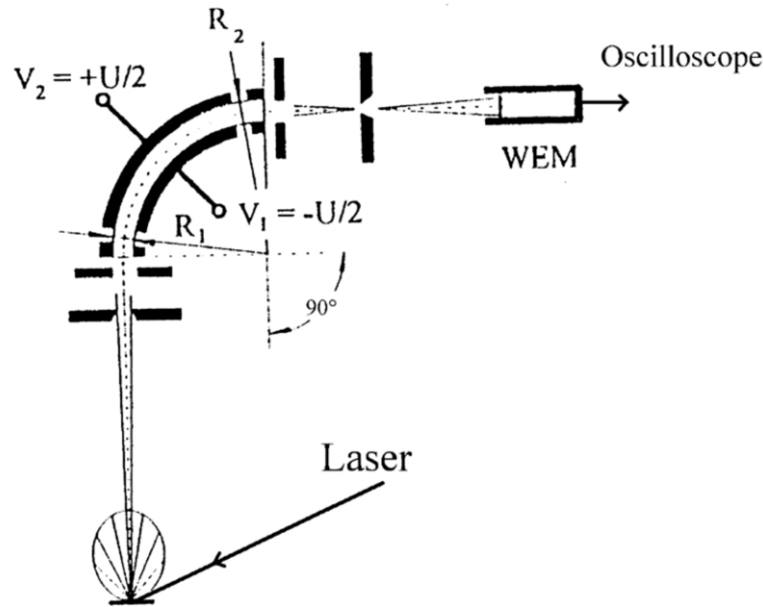

FIGURE 4.24: Scheme of a Ion Energy Analyser.

The particles deflected by the plates can be detected through a WEM connected to a high-frequency digital oscilloscope. Generally the IEA works with a symmetric polarization, at which $V_1 = -V_2 = U/2$. In these conditions, a particle with mass m, velocity v and charge ze is detected only if its kinetic energy E is in agreement with the following relationship:

$$\frac{E}{z} = \frac{eU}{2\ln(R_2/R_1)} = k_{IEA}eU \tag{4.59}$$

where k_{IEA} is a geometrical factor of the IEA. Thus, the IEA operates as a filter, which permits the passage of a given energy-to-charge state ratio E/z. Changing the U voltage it is possible to detect ions with different E/z ratios. Generally, the plate's bias ranges between ± 10 and $\pm 120\,\mathrm{V}$

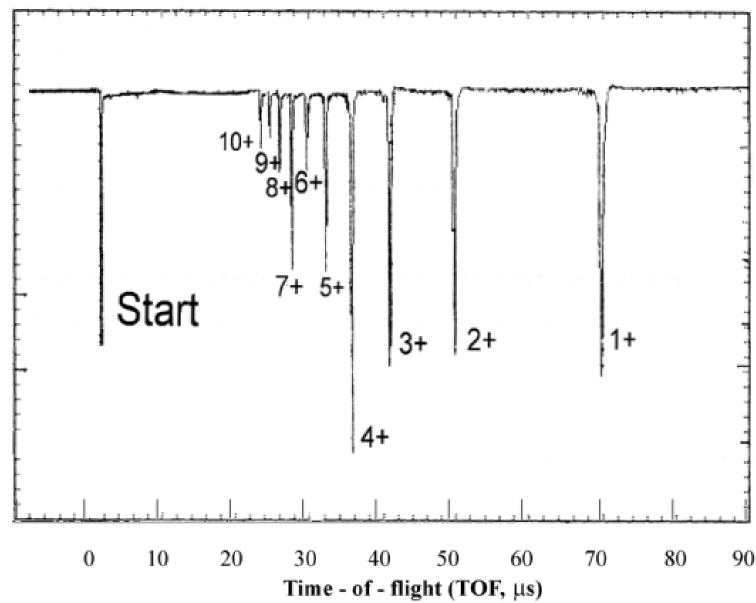

FIGURE 4.25: Typical IEA spectrum.

A typical IEA spectrum obtained irradiating a Gold target (500 μm thick) with the Nd:YAG laser of INFN-LNS is reported in Fig. 4.25. The IEA was placed in the backward direction at 0° with respect the target normal surface that is rotated of 45° with respect the laser incidence. The IEA spectrum, obtained with a fixed bias $U = \pm 80\,\mathrm{V}$ shows different negative peaks representing the same given value of the E/z ratio for different ion charge state. The temporal distance, between the start given by laser and the stop signal collected in the IEA-WEM, permits calculation of the ion velocity and energy, using the same relationship described for SiC-TOF spectra. For examples the velocity of the Au $^{1+}$ ions is $1.85 \times 10^4\,\mathrm{m/s}$ and corresponds to a kinetic velocity of 350 eV.

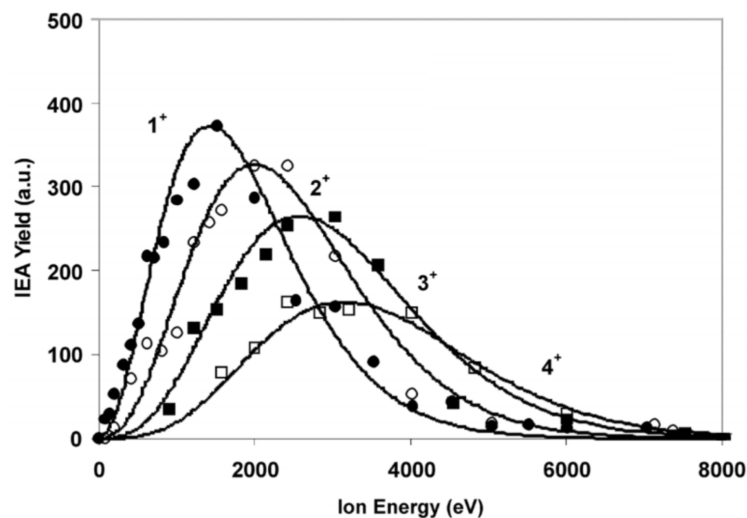

FIGURE 4.26: Ion energy distribution obtained from IEA measurements and deconvolution performed with CBS distribution.

By changing the U bias step by step, from ±10 V to ±120 V, it is possible to detect different E/z ratios and to give the experimental ion energy distributions as a function of the ion charge state as shown in Fig. 4.26. The CBS function was used to fit each ion distribution and it was obtained a value of about 345 eV for the plasma temperature [96]. Certainly the overall procedure with an IEA leads to more accurate values of ion distributions and plasma temperatures if compared with results coming from the analysis of SiC-TOF spectrum. However it should be noted that to obtain a good statistic of experimental points for an IEA spectrum many shots have to be done on the same target. For example to obtain the distributions reported in Fig. 4.26 more than 20 shots have been done. This fact in general represents a disadvantage when target does not offer enough fresh surface. Moreover attention has to be done to maintain unchanged the experimental conditions (chamber temperature, laser-target configuration, laser parameters and so on) during the measurements to avoid the detection of false peaks. Concerning the sensibility of the IEA system, it results higher than SiC detectors, because IEA is able to detect also the single ion. Instead the sensibility of SiC detector is determined by the leakage current that represents the noise that has to be overcome to obtain a detectable signal. The leakage current in general is very low as described in the second chapter, but depends on the damage of the diode hence it increases with the plasma exposition. A detailed description of this phenomenon will be reported in the last section of this chapter. However it should be observed that the experimental conditions impose a certain limit to the maximum voltage that can be applied to the plates of the IEA, and consequently there is a limitation in the deflection and detection of the very fast component of ions and to the high energetic particles. This in general represent a disadvantages in the detection and analysis of the higher charge state that having an high energy are not efficiently deflected. Consequently their statistics is sometimes too poor to be able to fit data with a CBS distribution.

4.4.3 PVT Scintillator coupled to photomultiplier

Also plastic scintillator can be used as detector to monitor radiations emitted by plasma. Among the different material the organic Polyvinyl Toluene (PVT) based scintillators doped with fluors present many advantageous features such as the fast response and low cost production making them a rational choice for use in large detectors [27]. It were used two PVT scintillator: the first, called thick PVT, has a cylindrical shape with a diameter of about 15 mm and a thickness of 12 mm while the second one, thin PVT, is a thin foil of about 200 μm and a square shape of 5×5 mm. PVT is made up of long chain vinyl toluene molecules. Toluene consists of a benzene ring bonded to a methyl (CH3) and a

vinyl group (CH2-CH-). In tab. 4.2 are summarized the main physical characteristics of the Polyvinyl Toluene scintillator.

TABLE 4.2: Main physical characteristics of the PVT [55].

Monomer	C_9H_{10}
Effective mass number	0.542
Density (g/cm^3)	1.032
Maximum light emission (nm)	423
Refraction index	1.58
Attenuation lenght (cm)	250
Specific heat (J/g °C)	1.7
Softening temperature (°C)	70
Decay constant of the main component (ns)	2.4

Fig. 4.27a.b shows the chemical formula of the Polyvinyl Toluene and a photo of the thick PVT scintillator. In the organic medium the molecule itself is the primary agent for the energy conversion. A small fraction of the energy of the incoming beam produces electronic excitation in the benzenic ring and singlet states whose de-excitations is responsible for the fast light emission, typically 2.4 ns. Activators as fluorine can be added to obtain peculiar optical properties, such as wavelength shift, high scintillation efficiency, and a better coupling with detector system.

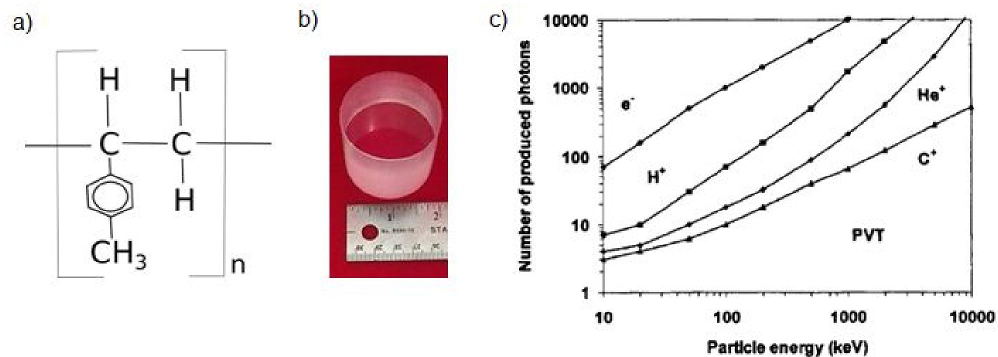

FIGURE 4.27: a) chemical formula for PVT, b) PVT plastic scintillator and c) PVT luminescence efficiency as a function of the particle energy for different ion beams.

In general the PVT luminescence is proportional to the radiation fluence (particles/cm^{2}s) as can be seen in Fig. 4.27c. However high fluency radiations, for example proton of ~ 1 kGy [94], can leads to a luminescence non-linearity with the absorbed dose caused by temporary or permanent molecular damage, as can be seen in Fig. 4.28. Quenching is an example of temporary effect due to the high energy density released along the ion track, responsible of non-radiative de-excitations. Quenching does not represent a permanent damage of the polymer and it is removed in times of the order of 10^{-12} s [79]. Irreversible radiation damage induced in the molecular structure, which suffers scissions and cross-links production along the incident ion track [73] can also occur at relatively high doses, of the order of 10^{13}/cm^2.

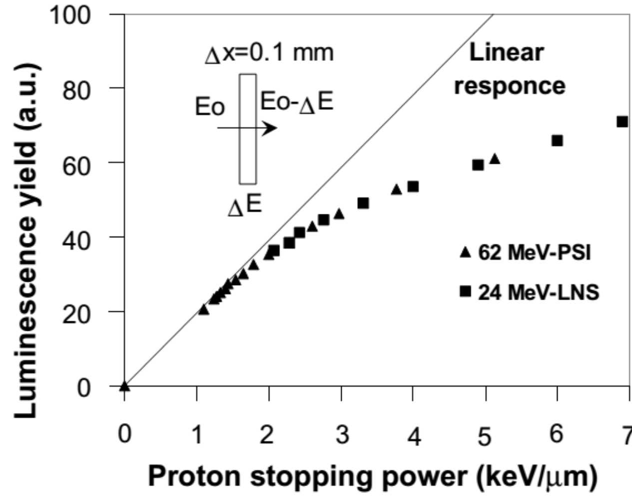

FIGURE 4.28: Luminescence yield as a function of the the 24 and 62 MeV proton stopping power [80].

The reason of this behaviour of the polymer consists in the damage of the polymeric chains containing benzenic rings. The main peaks of the luminescence yield, in facts, are due to de-excitations of the aromatic rings into their surrounding of branched aromatic structure. Consequently, each damage in the molecular structure produces modifications in the luminescence response.

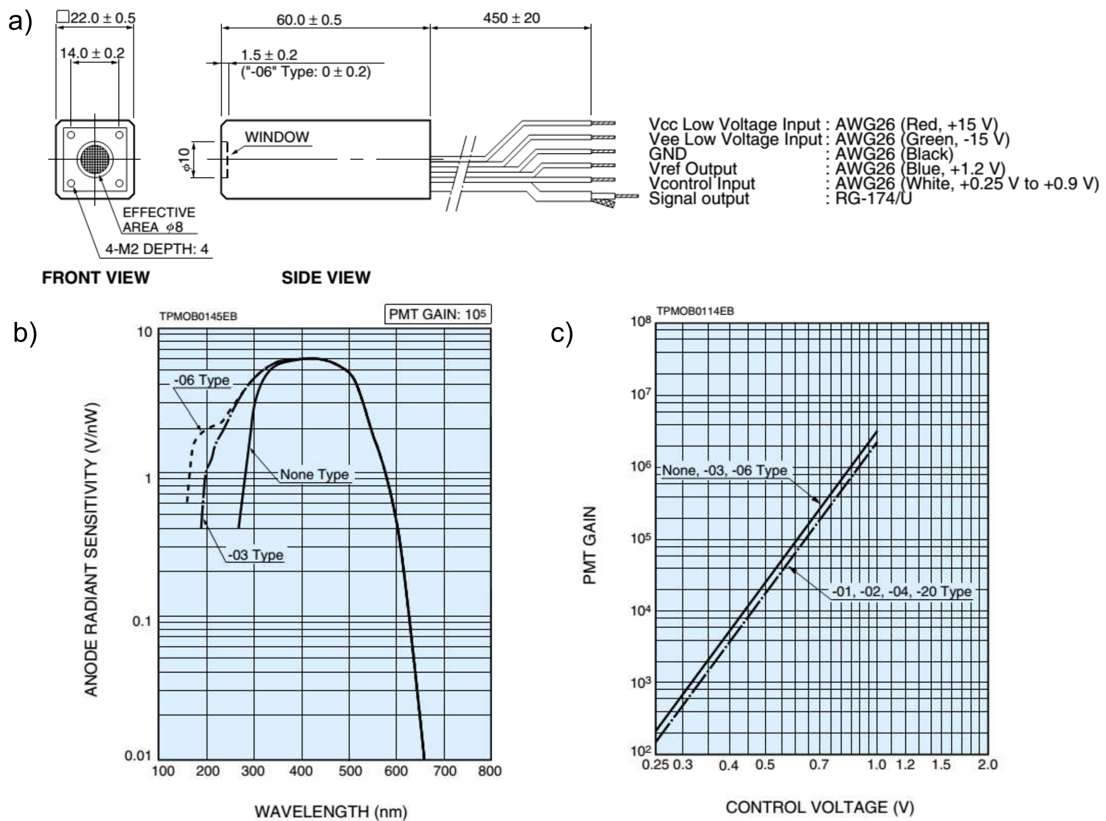

FIGURE 4.29: (a) Geometric characteristics of the unit expressed in mm, (b) the anode radiant sensitivity as a function of the wavelength and PMT gain (c).

PVT scintillators are coupled through an optic fiber with a Hamamatsu Photosensor Module (Type No. H5784) that comprises a metal package photomultiplier tube, a low-power consumption high-voltage power supply and a low noise amplifier. In this device the electrical current from the photomultiplier tube is converted to a voltage by an amplifier installed near the anode output pin of the photomultiplier tube improving the signal processing. The amplifier feedback resistance of 1 MΩ allows a current-to-voltage conversion factor of 1 V/μA, and covers a frequency bandwidth from DC to 20 kHz.

In Fig. 4.29a are reported the geometric characteristics of the unit. Moreover as can be seen from the anode radiant sensitivity reported in Fig. 4.29b, the spectral response is between 300 and 650 nm for general applications in visible range. This curve is calculated for a fixed values of PMT gain (10^5), but adjusting the control voltage (Vcontrol Input) it is possible to change this gain and hence the sensitivity, as reported in Fig. 4.29c.

In order to understand the capability of the overall detection system, consisting of PVT scintillator and PMT, preliminary experiments have been performed at UniME concerning the alpha particles detections (Fig. 4.30) and the diagnostic of ions emitted by laser generated plasma (Fig. 4.31).

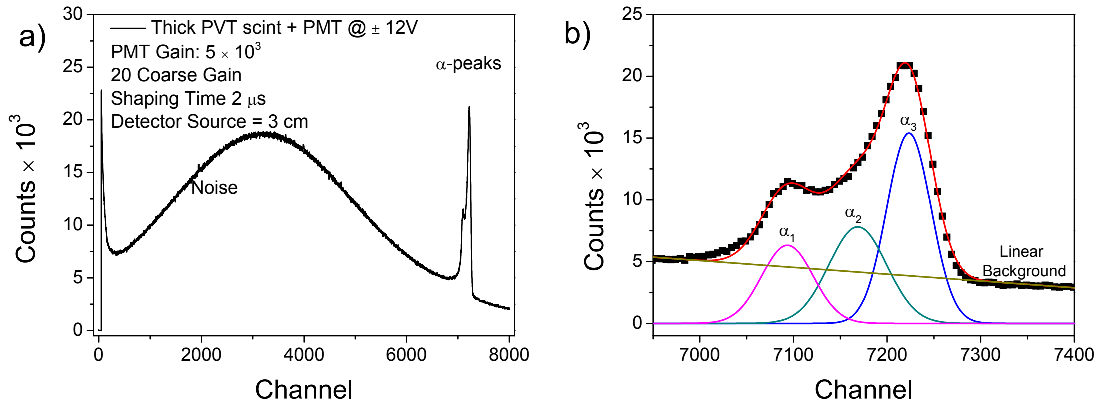

FIGURE 4.30: Experimental PVT spectrum a) and deconvolution of the three peaks α-source.

In the first case the spectroscopic electronic, also used with SiC detectors, has been employed and the α-particles are emitted by the multi-peak α-source described in section 3.3.1, obtaining data showed in Fig. 4.30a. Despite the source was placed in dark inside the chamber at a distance of about 3 cm from the scintillator, there is a strong noise component in the spectrum. Subtracting to this spectrum data obtained without the source inside the chamber, it is possible to identify the three structures of alpha particles emitted by Pu, Am and Cm by performing a Gaussian data fit (Fig. 4.30b). The reason of such unexpected behaviour are under investigation. In Fig. 4.31 are instead reported typical TOF spectra obtained with the thick scintillator placed very near to the

plasma, about 4 cm and irradiating bulk target of Polyethylene, Aluminium, Copper and Tantalum.

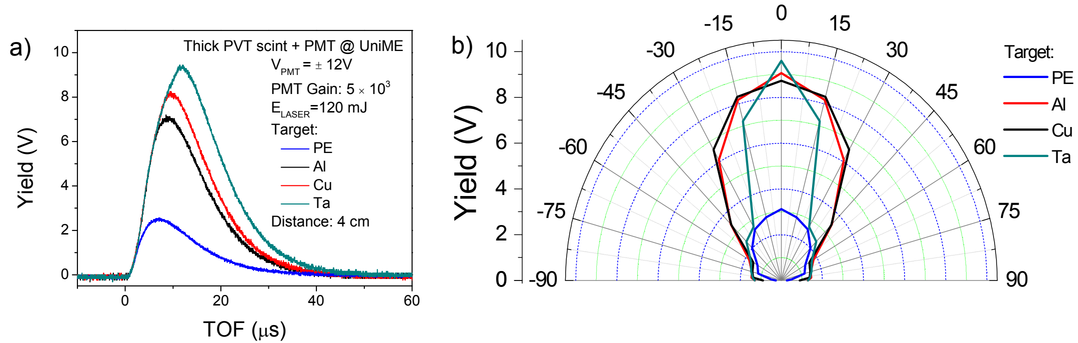

FIGURE 4.31: TOF spectra obtained with thick PVT and irradiating PE, Al, Cu and Ta target a) and angular distribution of the emitted particles b).

From the spectra it is not possible to distinguish the photon detection with respect electron and ions being very close to plasma emission.

The same considerations are still valid for the thin PVT scintillator in which, as expected, it was obtained only a reduction of the total yield.

Thanks to the thick PVT it was evaluated the angular distributions of the emitted radiations at a flight distance of only 4 cm. The results for different targets are summarized in the graph of Fig. 4.31b, showing a good agreement with literature data [84, 89].

In conclusion it can be stated that PVT scintillators could be used as support device in TOF measurements.

The main advantage of these device consist in the very wide active surface that can be achieved. In fact in time of flight technique it would be necessary a long flight distance in order to be able to distinguish from the different ion species. However, with traditional detector can not be used flight distance higher than 1.5 m because due to the very low solid angle subtended by the device, the ion yield is in general too low to be detected. The relatively low price and simplicity of production allow to obtain large PVT scintillators that in theory could be employed at higher flight length.

4.5 Use of SiC detectors in laser-plasma applications

As described before, studies on plasma radiations are opening new scenarios and, of course, for these new applications an accurate monitoring of the main plasma properties is required. In the next sections it will be show some of the advantages of the SiC detectors in the characterization of these experimental conditions. As a first example, it

will be shown how a typical TOF analysis performed with these detectors can be useful for optimizing ionic current or energy for Laser Ion Source applications. Then it will be discussed the possibility of studying the fusion processes in laser generated plasma and how SiC detectors can lead to confirmation of the occurrence of the reaction. Finally, an accurate study on the photopeak for X-ray imaging and analysis of post-accelerated ion beam for implantation applications will be presented.

4.5.1 Laser Ion Source

One of the most promising application of plasma generted by laser is the so called Laser Ion Source (LIS). As reported in literature [100] there are many advantages in using LIS:

- Production of any kind of ions beam;
- High beam current (~ 1 A);
- High directivity ($\pm$ 30°);
- High energy ($\sim$1 MeV/charge state)
- High ion yield ($\sim 10^{19}$ ions/pulse)

These are only representative values because as demonstrated by Torrisi and al. [93], in particular experimental conditions, using new femtosencond laser (I=10^{18} W/cm^2), near monochromatic 20 MeV proton can be also obtained. In this section, the strength of the CBS model will be demonstrated through the deconvolution of different spectra acquired under various experimental conditions. This kind of analysis is fundamental as it helps to understand what are the fundamental steps that have to be done with the goal of getting higher and higher ions energy.

The first set of measurements were done employing the Ti Sapphire Eclipse laser system with a pulse duration of 39 fs and a maximum energy of about 200 mJ using a TNSA configuration.The laser shot presents also a low contrast pedestal (10^{-5}) whit an intensity of 10^{13} W/cm^2. The presence of this pedestal is of great importance, since it has enough energy to create a pre-plasma. The interaction between pre-plasma and the main laser pulse leads to non-linear mechanisms inducing self-focusing or filamentation effect with a consequent enhancement of the laser energy transfer to the plasma. The plasma was monitored by different SiC AZ 80 detectors both in forward and in backward direction. In particular the spectra showed in Fig. 4.32 comes from a SiC detector, with an inverse bias of 600 V and placed along the normal to the target surface in forward direction with respect the laser incidence. The laser focal position onto the target surface was managed

though a CCD camera permitting to measure micrometrically its distance from the target surface.

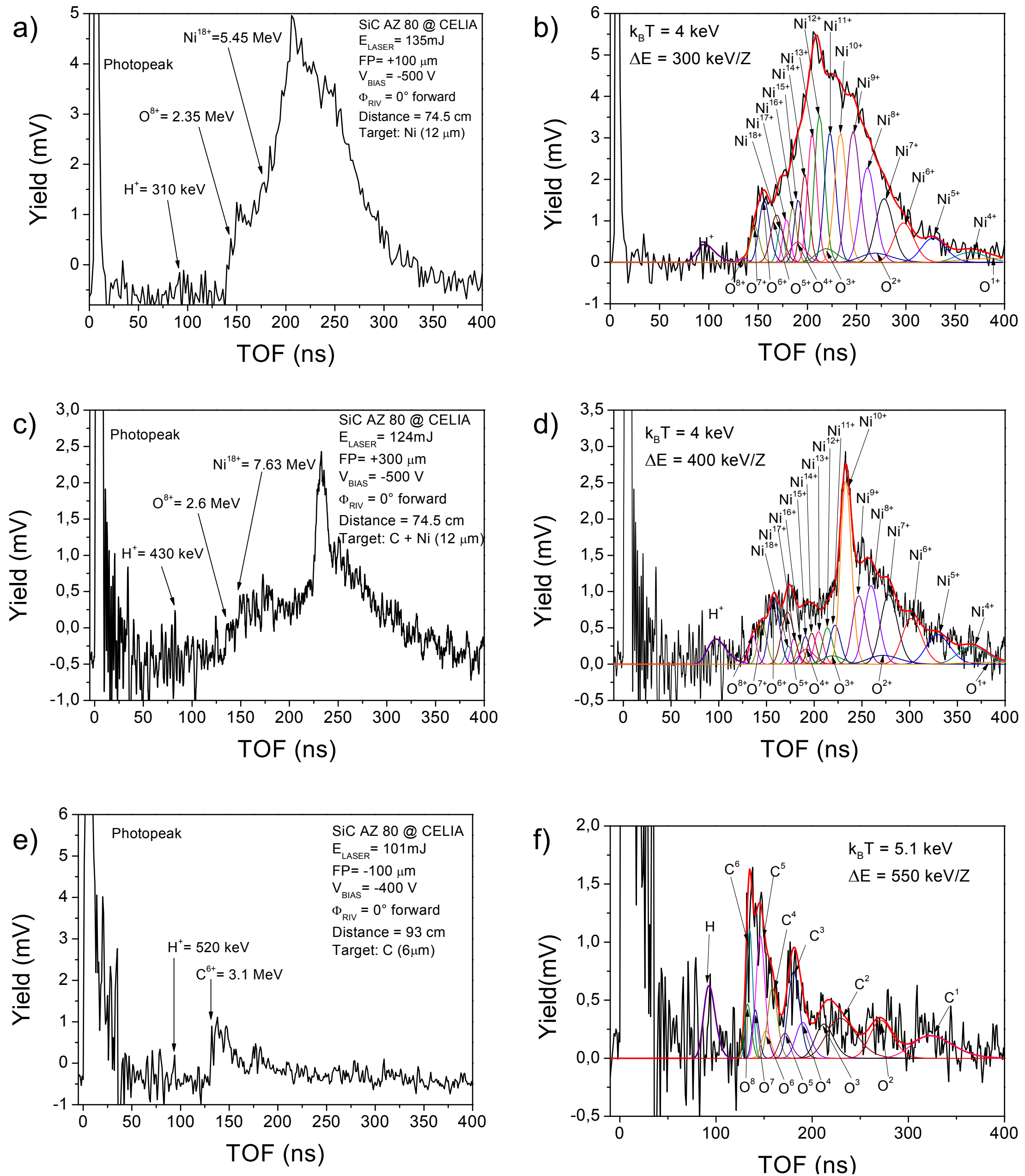

FIGURE 4.32: SiC-TOF spectra acquired at CELIA facility in forward direction irradiating Carbon and Nickel based targets.

The adopted FP condition was varied from 0 μm (i.e., on the target surface) to+100 μm (inside the target surface) and to -100 μm (in front of the target surface) using micrometric step motors. Fig. 4.32a shows the spectrum obtained irradiating a thin foil of Nichel (12 μm) focusing the laser pulse inside beside the target surface (+ 100 μm). It evidences the presence of a first peak due to proton detection completely separated by the widen structure due to Nickel ions starting from 170 ns. Moreover the first edge ($\sim$150 ns) is

compatible with the eighth charge state of Oxygen present in the target as contaminant. In fact the deconvolution of Fig. 4.32b was obtained taking into account both the eighteen charge states of Nickel and the eight charge state of Oxygen. All distribution results proportional to a mean acceleration of about 300 keV/charge state and a ion temperature of about 4 keV. A little increment of ion energy has been obtained in the spectrum reported in Fig. 4.32c through the irradiation of a compound material of Nickel and Graphene. In this case the proton peak has been obtained at about 75 ns corresponding to an energy of 430 keV and the Nickel ions are detecting at about 150 ns corresponding to an energy of 7.63 MeV for the Ni^{18+}. Also in this case it was individuated the presence of Oxygen contaminants. Again the deconvolution (Fig. 4.32d) confirms the presence of these elements and gives a mean ion energy proportional to 400 keV/charge state. However the temperatures does not change with respect the previous case. The causes that lead to very high yield of the Ni^{10+} are still under investigation but are to be found in the internal structure of the target material and in particular of the graphene which may presents some specific direction inside the lattice that favor the acceleration of a specific ionic species. A good energy enhancement has been obtained in the last spectrum of Fig. 4.32e, especially if the laser energy is considered. In fact despite the lowering of the laser energy (101 mJ), the signal of protons seems to start from 90 ns that corresponds to an energy of 520 keV. The enhancement can be explained by two factors: the first reason can be due to the thin target used for this shot, a Graphene layer, 6 μm thick. The second aspect concerns the focal position that has been employed, i.e. -100 μm, that as said before, can lead to non-linear effect. The position of the proton peak is confirmed by the deconvolution showed in Fig. 4.32f, since the carbon ions are shifted in time according to an energy shift proportional to 550 keV/charge state. Moreover the width of the six curves of carbon testified an increase of the ion temperature that is equal to 5.1 keV.

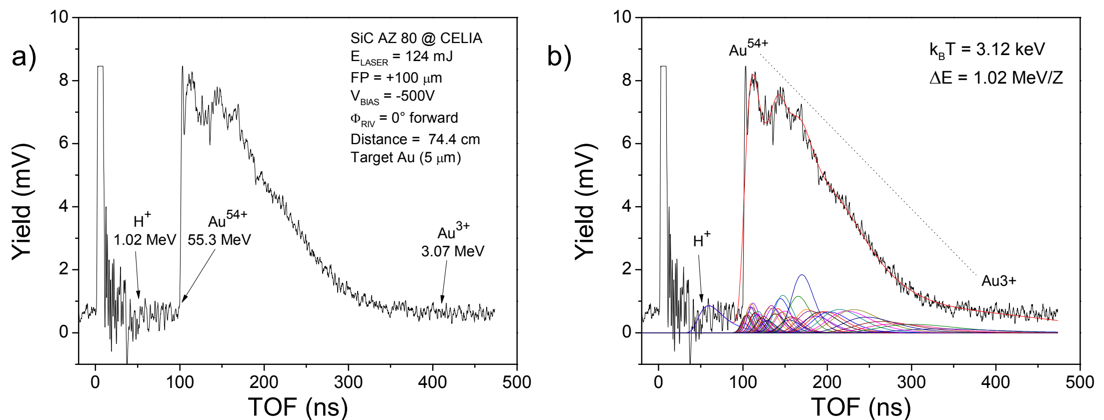

FIGURE 4.33: SiC-TOF spectra acquired at CELIA facility in forward direction irradiating Au target.

The effect due to the metallic nature of the target is evident in the spectrum reported in Fig. 4.33, that according to literature [56] leads to an increment of plasma temperature and ion energy. This spectrum was obtained at CELIA laboratory, using the same

experimental set up discussed before. The difference in this case consists in the irradiated target that is a thin foil of Au (5 μ thick). The proton peak occurs at 53 ns corresponding to a maximum proton energy of 1.02 MeV. The faster Au peak is detected at 101.2 ns and corresponds to an energy of 55.3 MeV. This energy value suggests that it could be due to the detection of Au^{54+}. In Fig. 4.33b the possible deconvolution of the widen structure ranging between 100 ns and 450 ns is reported. Although a relatively low temperature has been obtained (3.12 keV), the fifty-four gold charge states are centered at a proportional energy of 1.02 MeV/Z as suggested by the maximum proton energy.

In the analysis of the last spectrum (Fig. 4.34a) the deconvolution of the data plays an important role because it put in evidence the occurrence of unexpected phenomena. It was obtained irradiating a thin Al target (6 μm thick) by the Ti:Sapphire laser operating at IPPLM laboratories in Warsaw. In this case thanks to the higher laser intensity (10^{19} W/cm^2) with respect the previous one (10^{18} W/cm^2), proton energy, measured at the beginning of the wider peak at 40 ns, reaches the highest value of 1.8 MeV.

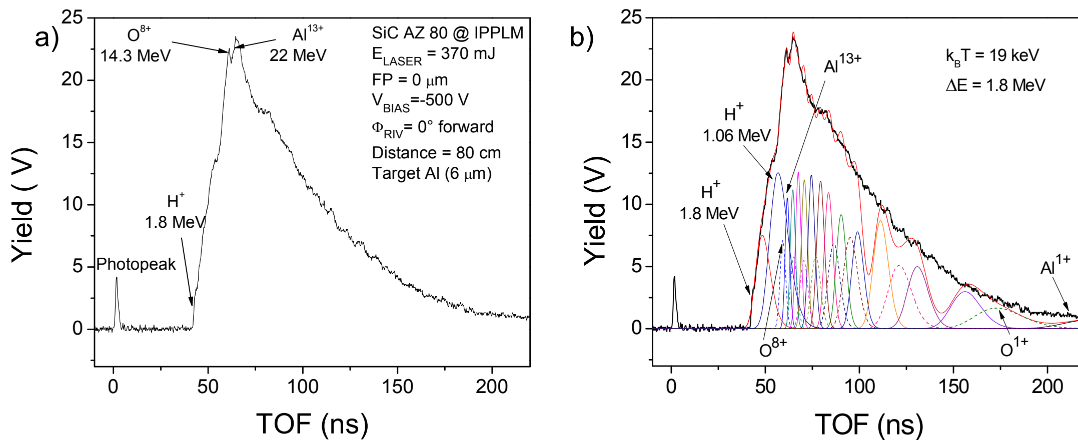

FIGURE 4.34: SiC-TOF spectra acquired at IPPLM laboratory in forward direction irradiating Al target.

At this high laser intensities, the target atoms are completely ionized and in fact it is possible to identify the contributions of the eight charge state of Oxygen with an energy of 14.3 MeV and the thirteenth charge state of Aluminum with an energy of 22 MeV. All charge state have been considered to realize the deconvolution of data showed in Fig. 4.34b. The interesting aspect of this deconvolution lies in the fact that the fit process does not converge until a second proton distribution is added to the software. This peak presents a TOF corresponding to mean proton energy of 1.06 MeV but the explanation for this second peak is still unclear and may be due to the detection of protons coming from the far side of the target or can be due to the subsequent generation of proton caused by recombination effects.

4.5.2 Fusion reaction

Plasma-laser induction of nuclear events has been knowing a growing interest since it develops nuclear energy without generation of dangerous radioactive nucleus. Moreover nuclear reaction induced by plasma laser could represent a valid tools to verify astro-physics theory. Mainly the attention is given to D-D reaction that occurs through two equivalent branches:

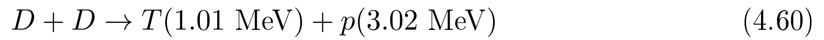

$$D + D \rightarrow T(1.01 \text{ MeV}) + p(3.02 \text{ MeV}) \tag{4.60}$$

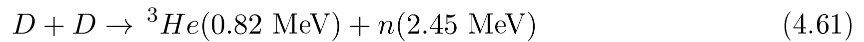

$$D + D \rightarrow {}^{3}He(0.82 \text{ MeV}) + n(2.45 \text{ MeV}) \tag{4.61}$$

Beside the cross section σ, since reactants, produced within plasma, present a distribution of velocity v, it is useful the introduction of the parameter $\langle \sigma v \rangle$, the so called reaction rate, that represents the fusions per volume per time. As can be seen in Fig. 4.35 the maximum cross-section of the D-D fusion, obtainable accelerating deuton and making them react with deuterium atoms contained into an irradiated target, occurs at about 3 MeV at which it assumes a value of about 0.2 barns, while the reaction rate increases from zero at room temperatures up to meaningful magnitudes at temperatures of 10–100 keV.

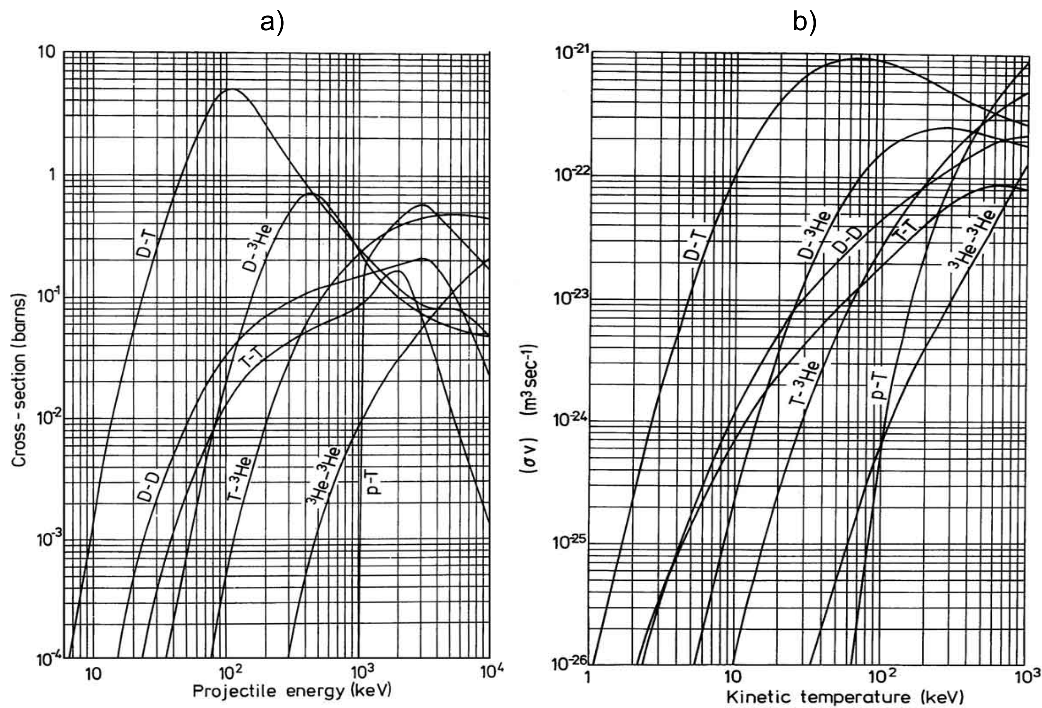

FIGURE 4.35: Cross-section as a function of the projectile energy for deutons, tritium, helium-3, and protons (a) and the corresponding reaction rate vs. the plasma temperature.

Experiments performed at PALS facility irradiating thick (1 mm) and thin (5 μm) CD_2 targets represents the first attempt to reach this goal. The experimental set up is shown

in Fig. 4.36 and SiC detectors were employed in time of flight configuration to monitor radiations emitted by plasma in backward and forward direction and to verify the occurrence of the reaction.

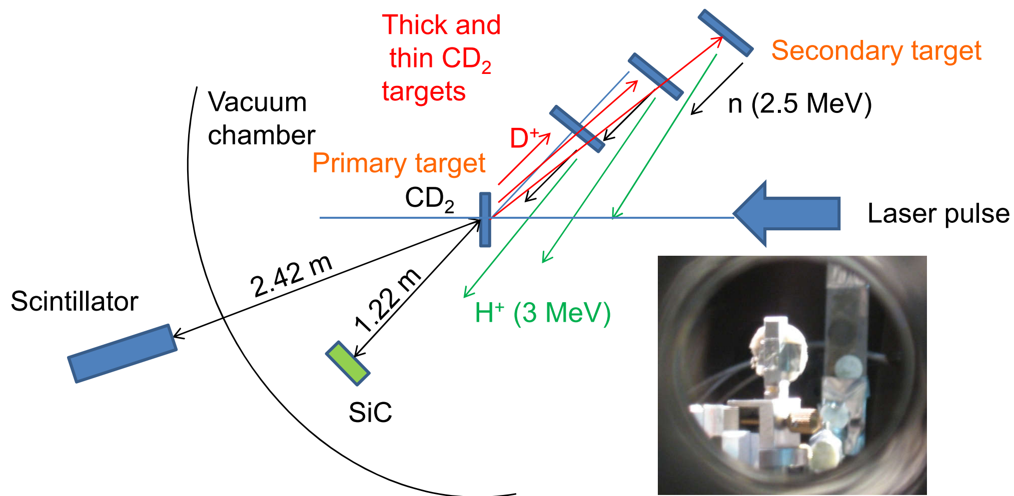

FIGURE 4.36: Experimental set up at PALS laboratories and in the inset view from the SiC detector in forward direction at 30° angle.

The laser irradiation produces non-equilibrium plasma with deutons and carbon ions emission with energy of up to about 4 MeV per charge state. Accelerated deutons may induce high D-D cross section for fusion processes generating 3 MeV protons and 2.5 MeV neutrons. Moreover, in order to increase the mono-energetic proton yield, secondary CD_2 targets were employed to be irradiated by the plasma-accelerated deutons.

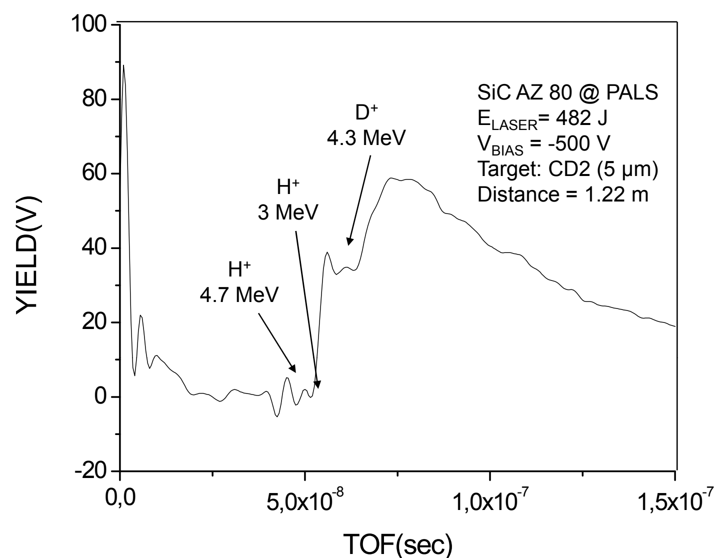

FIGURE 4.37: SiC TOF spectrum in forward direction.

Fig. 4.37 shows an example of TOF-SiC spectrum obtained in forward direction with a target-SiC distance of 122 cm. The spectrum shows a deuton peak at 55 ns corresponding

to a kinetic energy of 4.3 MeV and two proton peaks at 50 ns and 40 ns corresponding to an energy of 3.0 MeV and 4.7 MeV, respectively. These proton contributions may be due to the proton emission from the D-D nuclear fusion occurring inside the primary target or to the proton driven plasma acceleration due to the absorbed hydrogen inside the polymeric matrix. It was measured a maximum deuton energy of about 10 MeV irradiating the thin target of deutered polyethylene.

Measurements performed with a second SiC detector placed in bacward direction demonstrated that the yield of the characteristic proton peak at 3.0 MeV increases detecting radiations emitted at little angles with respect to the normal direction. These results are very interesting because indicate that produced deutons have very high probability to generate D-D fusion if used to irradiate deuterium atoms. The fusion processes can be induced in the same primary target and in the three secondary CD2 targets placed at three different distances from the primary one.

In order to verify the occurrence of the fusion reaction the spectrum of Fig. 4.38 recorded by a SiC detector placed along the normal to the secondary targets in forward direction, has been deconvolved.

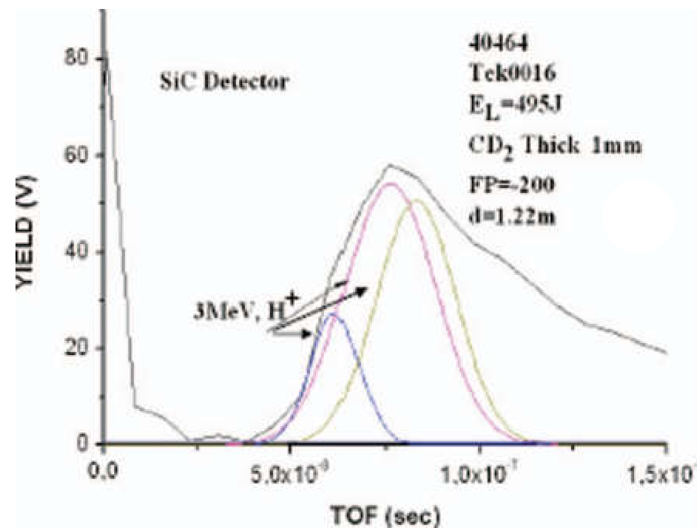

FIGURE 4.38: SiC TOF spectrum in forward direction.

In fact the large peak recorded at about 80 ns represents a convolution of three different proton peaks coming from the three secondary targets. The three curves were obtained by considering the sums of the flight time of the deutons coming from the primary target to arrive to the three secondary targets and the TOF of protons coming from the secondary targets to arrive to the SiC detector. From the fit appears that peaks are experimentally compatible with proton energy of 2.8 MeV, and the large proton peak can be due to the monoenergetic protons coming from the first superficial layers of the secondary targets, demonstrating that the D-D fusion occurred, [90]. Another validation of the occurrence

of the reaction coming from TOF measurements done with scintillators which detects neutron peak compatible with a energy of 2.5 MeV.

4.5.3 Compact X-rays source

Nowadays sources of short-wavelength radiation (Ultraviolet and X-ray spectral regions) [9, 106] are of particular interest. Laser-plasma sources are promising in this region, since they are quite compact and allow operation in wide spectral and intensity ranges. Moreover such technique finds many important applications in wide scientific fields, such as medicine, biology, chemistry, engineering and solid state research, which requires X-ray imaging with high spatial and temporal resolution [14, 76]. An other attracting features concerns the development of next generation semiconductor based on extreme ultraviolet lithography (EUVL) [9] that requires bright and efficient radiation sources. For these applications it is evident that is needed a full characterization of the X-rays spectrum. For these reason taking advantage of SiC properties it was studied and compared the X-ray emission from plasma generated by low ($\sim 10^{10}$ W/cm^2) and high ($\sim 10^{18}$ W/cm^2) intensity laser trying to understand the influence of target and of laser parameters. A TOF spectrum is reported in Fig. 4.39, where it is showed typical photopeaks obtained irradiating C, Al, Cu, Ag, Ta target.

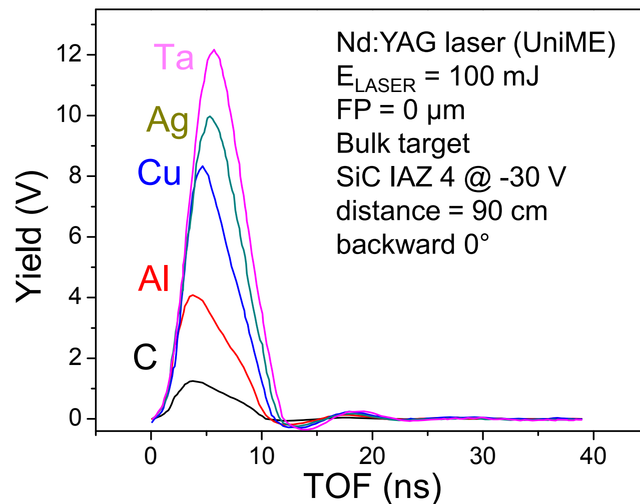

FIGURE 4.39: Typical photopeak obtained irradiating bulk material at low laser intensity (Nd:YAG at UniME).

In particular the figure shows the response of the SiC IAZ 4 detector to photon UV and soft X-rays produced by a plasma generated by 3 ns laser at intensity of 10^9 W/cm^2 (UniME laboratories). Independently of the used target, the photons detection yield presents a duration of about 3–4 ns ($FWHM$), comparable with the laser pulse duration. This means that detectors are very fast and able to operate during the laser shot i.e.

during the formation of the laser-generated plasma. Another interesting aspects, that will be discussed in more details in the next section, concerns the strong dependence of the detection yield with the target atomic number. In fact a linear increase of the yield was obtained in agreement with literature data [103] and due to the increment of the plasma electron density increasing the atomic number of the target element.

4.5.3.1 Target influence

The first analysis concerns the dependence of X-rays emission on the target composition and in particular on the atomic number. In the graphs of Fig. 4.40 are plotted the maximum yield as a function of the atomic number.

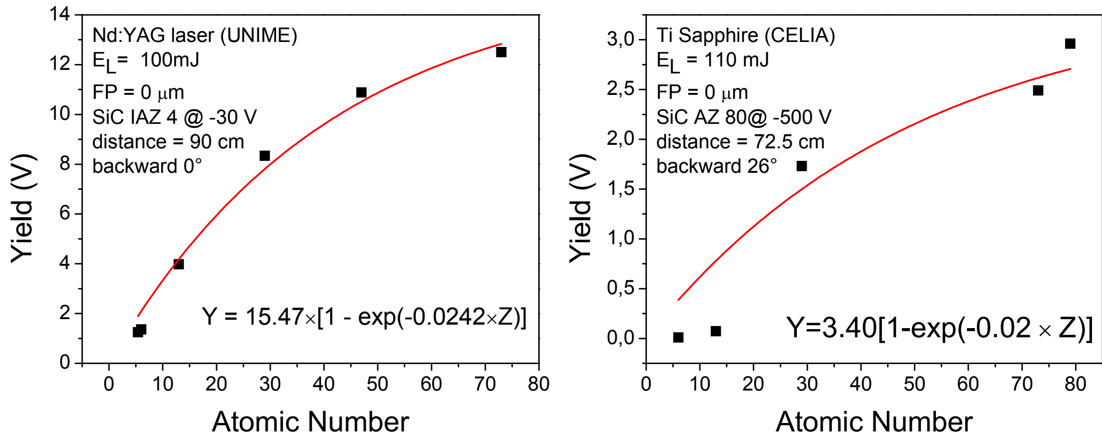

FIGURE 4.40: Dependence of X-rays emission on the atomic number of the target.

The spectra were acquired at low intensity (Nd:YAG laser in Messina) and at high intensity (Ti Sapphire laser at CELIA) using SiC IAZ 4 and SiC AZ 80, respectively both in backward direction. In both situations a similar behaviour was obtained and a similar empirical law was carried out:

$$Y = 15.47 \times [1 - \exp(-0.0242 \times Z)] \tag{4.62}$$

$$Y = 3.40 \times [1 - \exp(-0.02 \times Z)] \tag{4.63}$$

This result can be explained with the fact that increasing the atomic number of the target more electrons are injected into the plasma as a consequence of the ponderomotive force. The higher electron density favours the particles acceleration with a consequent increase of the photon emission and plasma temperature in agreement with literature data [8, 29]. Also the influence of the target thickness was evaluated and the experimental results were reported in Fig. 4.41.In particular these data were obtained at high intensity laser, detecting photons emitted in backward direction form Au targets (2.48, 15, 25 and 50 μm thick) and maintaining all other experimental parameters fixed.

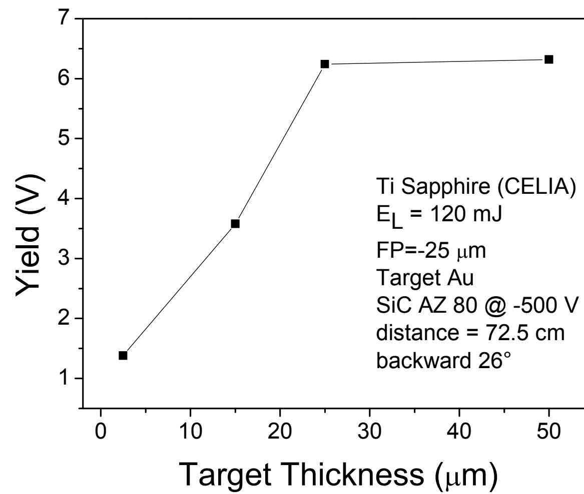

FIGURE 4.41: Dependence of X-rays emission on the thickness of the target.

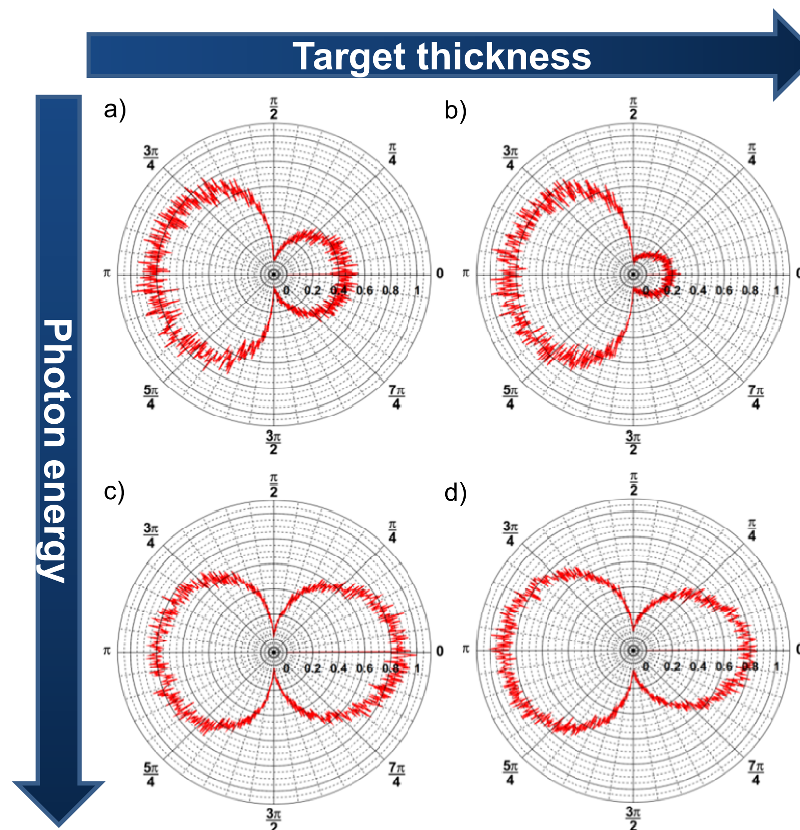

FIGURE 4.42: Angular distribution of X-rays emission.

The graph shows an initial increase tending to saturate. In fact increasing the thickness of the target the amount of material involved in the laser ablation processes also increase until is reached a certain saturation conditions, for thickness of about 30 μm, when the material thickness is higher than the penetration range of the laser-matter interactions within the target. Looking in forward direction the target absorption of X-rays has to

be taken into account, and hence the angular distribution of the outcoming radiation is modulated by target as can be seen in Fig. 4.42. Indeed, as also confirmed by simulations [21], X-ray yield from electrons with lower energy shows no significant deviation from isotropic emission, which remains unchanged as the target thickness varies, as shown in panels a) and b). This behaviour changes gradually for hotter electrons in panels c) and d), where the X-ray emission is weakly peaked along the normal to the target surface. This may be attributed to the facts that the scattering effects of electron are larger at lower energies and the angular divergence is becomes relatively high for the produced photons with low energies, and vice versa.

4.5.3.2 Laser Parameters

As shown in section 4.1.2, many plasma parameters depend on the $I\lambda^2$ factor. In order to test the influence on the X-rays emissivity the laser intensity has been modified changing separately the laser energy (Fig. 4.43), the focal position (Fig. 4.44) and the pulse duration (Fig. 4.45)

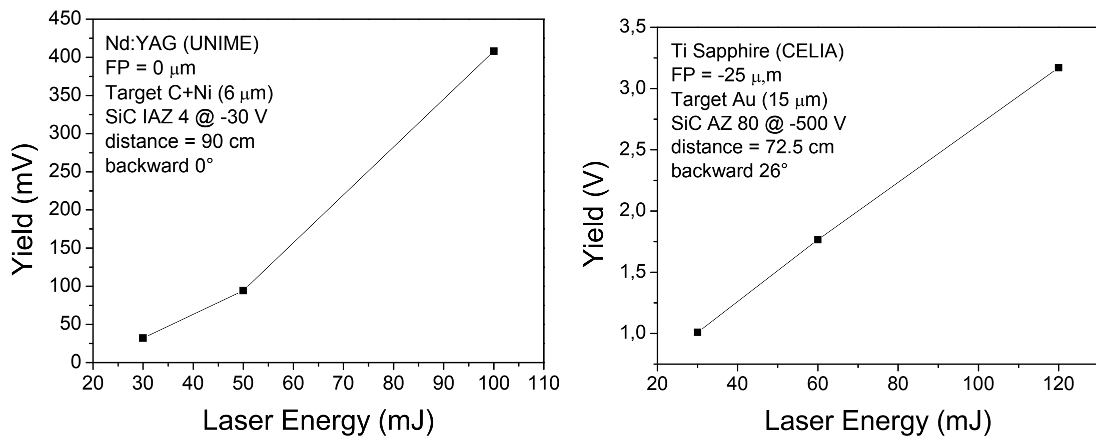

FIGURE 4.43: Dependence of X-rays emission on the laser energy.

The spectra were obtained irradiating, at low laser intensity a multilayer target consisting in Carbon and Nickel, while at high laser intensity a thin target of Gold. In both cases the detectors were placed in backward direction. As expected by increasing laser energy, a linear increase in photons yield is also observed. This is due to the fact that the increase of the laser energy gives the electrons the possibility to gain more energy leading to a greater emission of photons.

The focal position also plays an important role as can be seen in Fig. 4.44. The position in which laser is focused with respect the target surface, not only determines the size of the laser spot but a proper choice of this distance can favour the development of self-focusing effects and non-linear acceleration enhancement.

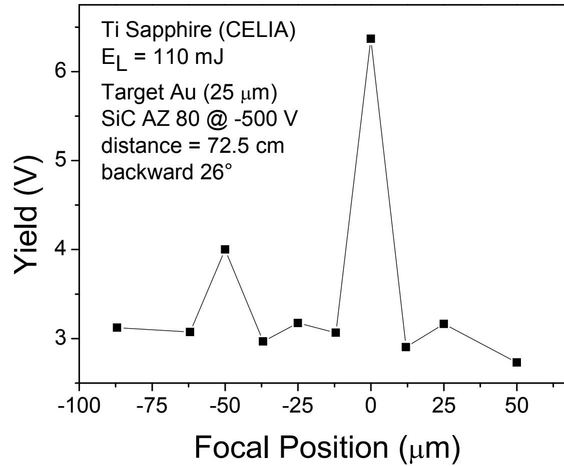

FIGURE 4.44: Dependence of X-rays emission on focal position of the laser.

Thanks to these self-focusing effects it is possible to explain the presence of a second peak for $\mathrm{FP} = -50\,\mu$m, in addition to the maximum obtained for $\mathrm{FP} = 0\,\mu$m. Also ions present similar dependence on this laser parameter showing a very similar shape plotting the ions yield as a function of the focal position as reported in literature [47].

Finally also the effects of pulse duration have been analysed, as shown in Fig. 4.45.

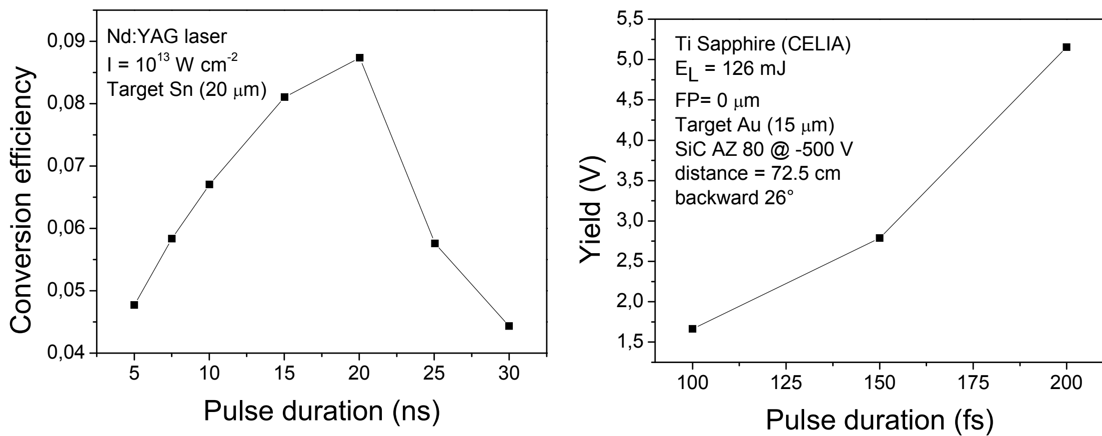

FIGURE 4.45: Dependence of X-rays emission on the laser pulse duration.

For low intensity laser, according to literature [7], at the beginning there is a good growth increasing the pulse duration because electron can interact for longer times with the laser pulse gaining more energy. However when the laser pulse becomes too long the overall laser intensity decrease leading to the reduction of photon emission. For high intensity laser only the first region was investigated due to the constrains imposed by the laser configuration parameters. The lower and the higher pulse duration can not be investigated.

4.5.4 Multi energetic ion implantation

Another possible application of laser generated plasma is the ion implantation. However using a ns laser at 10^{10} W/cm^2, the maximum ion energy is in general below 1 keV/charge state [33, 88], and is not sufficient to employ the obtainable ion beams, except for ion sputtering, deposition thin films and laser ion sources. In order to increase the energy of these ions emitted from laser-generated plasma, can be employed post acceleration systems as shown in literature [35, 101]. In general a voltage of the order of 30–100 kV can be employed to accelerate ions at energies depending on their charge state. The ion beam production from low laser intensities shows the advantage to be economic, of small dimensions, using high repetitive laser pulses (∼10–100 Hz), to be of high reproducibility, thanks to the use of laser repetition rate irradiating roto-translating thick targets to extract a near constant ion current. Moreover due to the multi-atomic species emitted from the target and to the different charge states of the ejected ions, it can be easily obtained a source with a multi-ionic and multi-energetic beam.

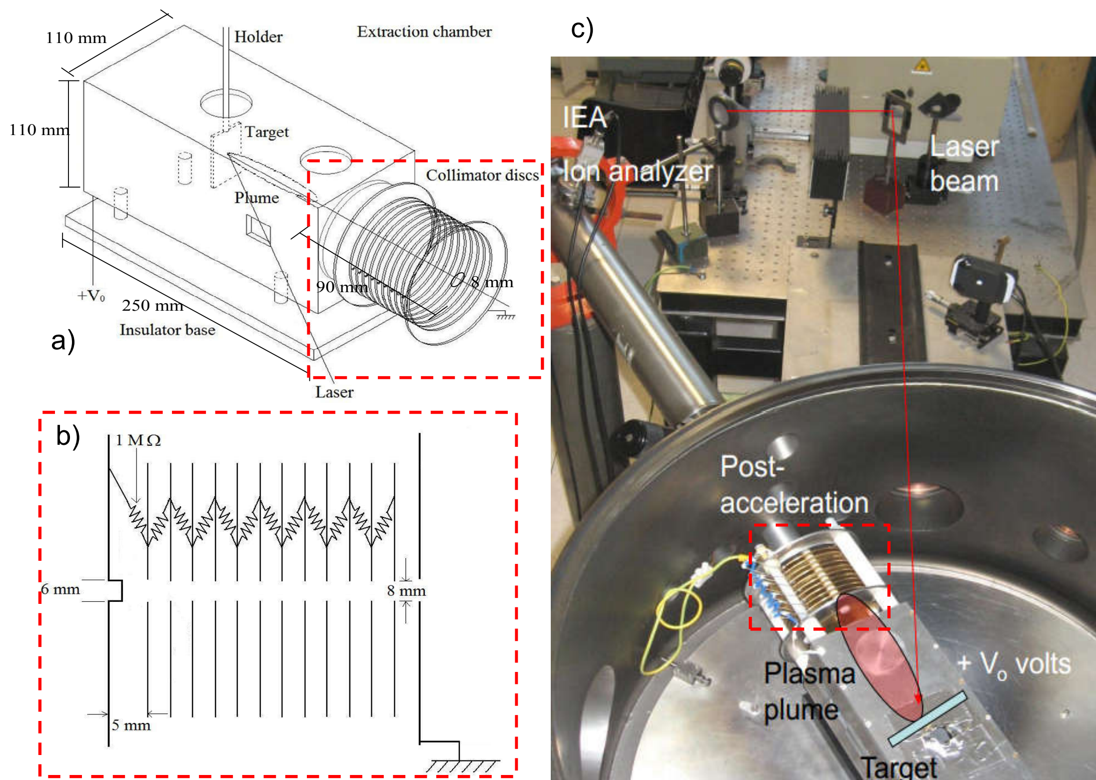

FIGURE 4.46: Schematic of the extraction chamber a), the acceleration region b) and experimental set up using a IEA c).

At INFN-LNS is present a post acceleration systems in which the positive polarization of the laser-irradiated target permits to extract ions from the plasma that under the effects of a high electric field along the emission direction, gain a kinetic energy proportional to their charge state [91]. A schematic of the extraction chamber is shown in Fig. 4.46a.

The target is in the centre of the acceleration chamber and it is at the same electrical potential of the chamber, that can be set between 0 up to +30 kV, by using a high voltage power supply (Yokogawa, 30 kV–200 mA). A lateral hole permitted the laser to enter inside the chamber and to hit the target at an angle of 43° with respect to the normal surface. The acceleration region is represented in Fig. 4.46b and consists in an electrical structure of 12 metallic discs all parallel and aligned along to the chamber longitudinal axis, at a distance of 5 mm from each other, with a central hole of 8 mm in diameter, electrically connected together through 10 MΩ resistors.

Typical characterization measurements are performed using an IEA system, using the experimental set reported in Fig. 4.46c.

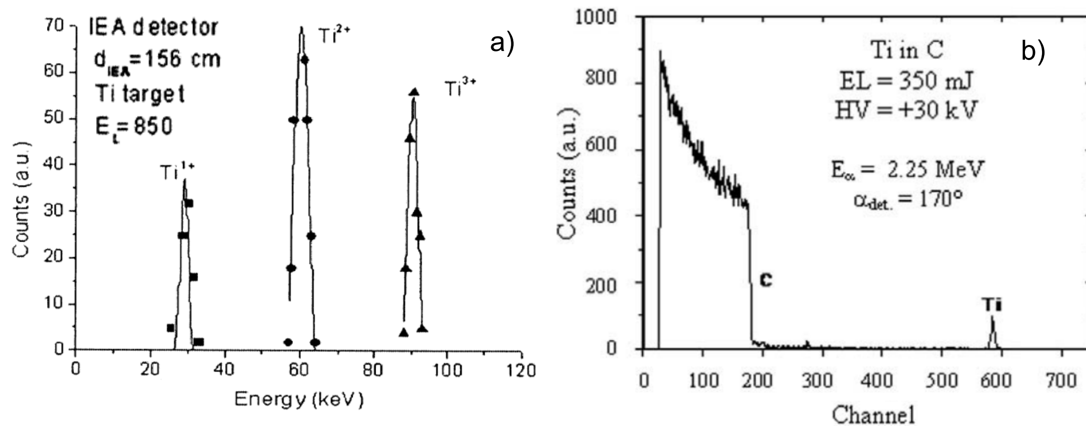

FIGURE 4.47: Ti ions energy distribution obtained with IEA at +30 kV of post acceleration a) and typical RBS spectra of the implanted target.

In Fig. 4.47 is reported a typical ion distribution, obtained at INFN-LNS, irradiating a Ti target with +30 kV of post acceleration. It is obtained a good proportionality in fact the three curves result peaked at about 30, 60, 90 keV for Ti^{1+}, Ti^{2+} and Ti^{3+} respectively. Using a Gaussian distribution to fit the peaks it was evaluated an energy resolution ΔE/E of 10, 8 and 4% for Ti^{1+}, Ti^{2+} and Ti^{3+}, respectively. As confirmed by RBS measurements, reported in Fig. 4.47b, the implantation of Ti ions in C substrates occurs and presents a thickness around 40 nm, corresponding to a Ti energy of about 50 keV as simulated by SRIM code.

A new approach to monitor ion implantation through this post acceleration system has been developing since few years, using the SiC IAZ 4 device [70]. In fact ion energy of 30 keV per charge state is in general too low to be monitored with continuous front electrode detectors. Thanks to the particular design of the SiC IAZ 4, with a direct sensible region exposed to radiation, it is possible to monitor with good sensitivity ions generated in plasma and post-accelerated, with an energy ranging within 1 keV and 30 keV.

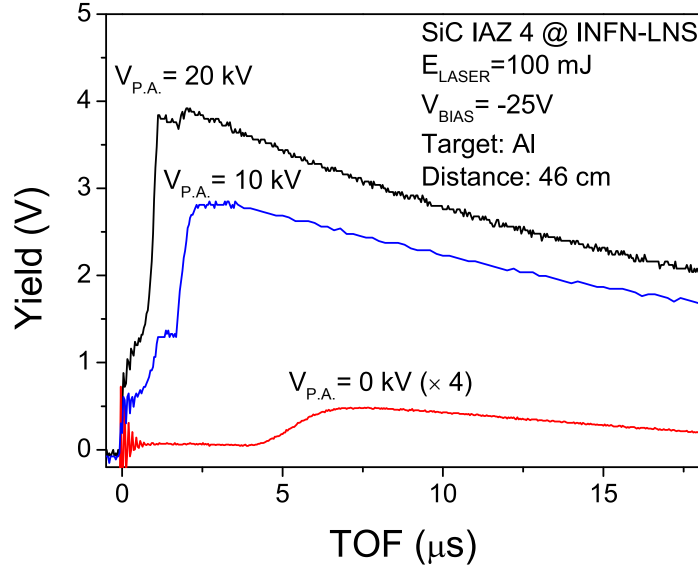

FIGURE 4.48: TOF spectra of plasma ions acquired at $V_{P.A.} = 0, 10, 20\,\text{kV}$ and at a fixed bias of detector $V_{BIAS} = -25\,\text{V}$.

Typical TOF spectra of Al plasma ions without post-acceleration ($V_{P.A.}$) and with post-acceleration voltages of 10 kV and 20 kV, acquired by the SiC IAZ 4 detector at fixed reverse bias (V_{BIAS}) equal to -25 V, are shown in Fig. 4.48. These spectra were obtained with the Nd:YAG laser of INFN-LNS, reducing laser energy to 100 mJ in order to be sure to obtain only a single charge state of Al. SiC detector is placed along the normal to the target surface (direction of maximum acceleration) at a distance of 46 cm (being 10 cm long the path inside the expansion chamber, 6 cm long the post acceleration path and 30 cm the ion free flight path), however the determination of energy is not immediate. Due to the presence of the post acceleration system the TOF can be expressed as:

$$t = t_0 + t_a \tag{4.64}$$

where t_0 is the time lost by ions to escape the expansion chamber (10 cm long) and t_a is the time spent in the post-acceleration path (36 cm long). It should be noted that the time t_0 is always the same, even in presence of the post acceleration, so it can be subtracted to the experimental time t in order to evaluate t_a and calculate the ion energy also when post acceleration is active. From the spectrum without post-acceleration, it was detected a broad peak at about 5.5 μs due to Al^{1+}, resulting in a $t_0 \approx 1.2\,\mu$s. Under the effect of the post acceleration of 10 and 20 kV, this peak shifts to 2.5 μs and 1.8 μs corresponding to an Al energy of 11 and 20 keV, respectively, proving that these are ion Al^{1+}. Another faster signal step is observable in both spectra at a time of about 1.4μs (10 kV) and 1.2 μs (20 kV), which is related to lighter ions, such as protons, coming from hydrogen absorbed in the target surface. These times of flight are compatible with a

proton energy of 10 and 20 keV in agreement with the expected value due to the applied post-acceleration field.

In order to highlight and study the influence of the device bias on the detection performance, the spectra for each post acceleration voltage were acquired at different detector's bias values. The spectra obtained at an acceleration voltage of 0, 10 and 30 kV by changing the reverse detector bias from 0 up to -30 V are reported in Fig. 4.49.

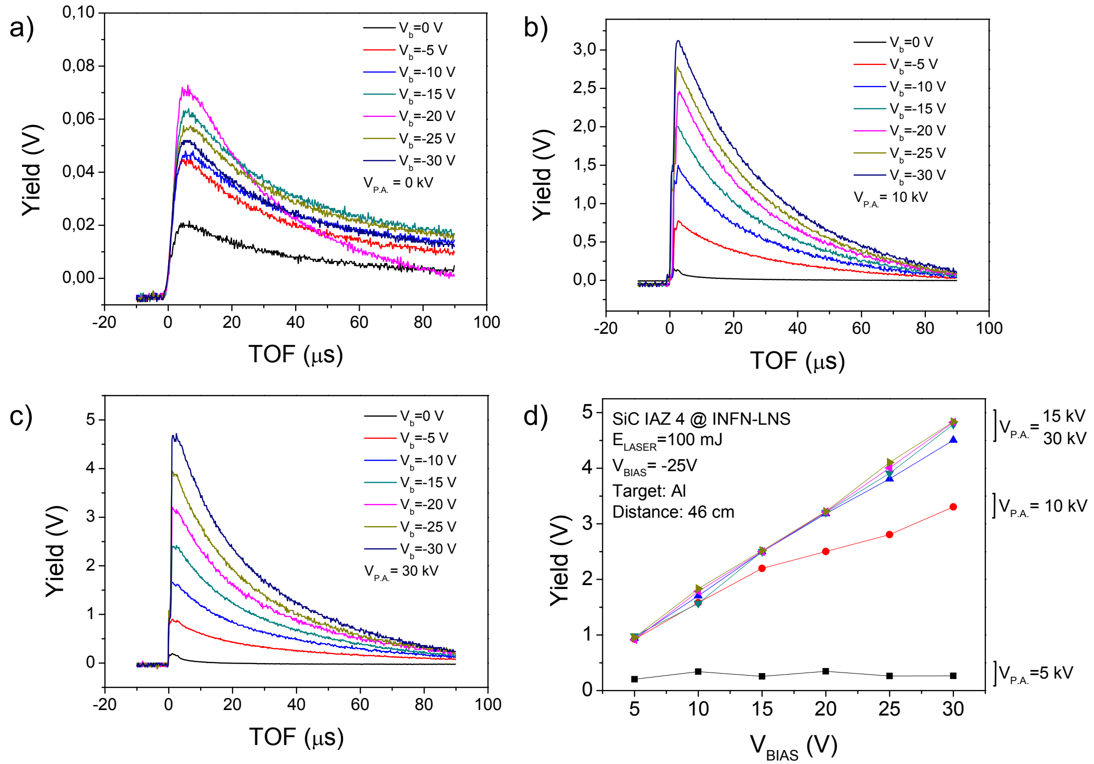

FIGURE 4.49: TOF spectra of plasma ions acquired at a post-acceleration voltage of 0 kV (a), 10 kV (b), 30 kV (c), for different values of detector bias and yield of TOF spectra of plasma ions as a function of detector bias for different values of post-acceleration voltage (d).

The increase of reverse bias of the detector induces a change in the shape spectra and a proportional increase of the spectrum intensity. To put in evidence the difference of the shape, the decay time constant of the spectrum has been evaluated. Considering the spectra obtained using a post acceleration of 10 kV the signal decay time is 6 μs at V_{BIAS}=0 V, increases up to about 20 μs for V_{BIAS}=5 V and does not change significantly with a further increase of detector bias supply. Similar results are obtained for the other values of post acceleration voltage. This behaviour can be explained taking into account the non-uniform distribution of the electric field and hence of the depletion layer. As just described in section 3.3.7, at V_{BIAS} = 0 V a large portion of the device is un-depleted and very low energy ions are lost. For this reason the observed signal is characterized by a weak signal, with short decay time, being the signal due only to the faster (more

energetic, more penetrating in SiC) ion component of the plasma. Increasing the reverse bias, at $V_{BIAS} = -5\,\mathrm{V}$ the epitaxial layer is almost fully depleted (see Fig. 3.16) and a larger portion of ions is detected with a consequent relevant increase of the spectrum intensity. The longer decay time is due to the collection of very low energetic ions that have a very low penetration range but are detected thanks to the enlargement of the active region with respect to the case where $V_{BIAS} = 0\,\mathrm{V}$. To confirm what has just been said, in Fig. 4.49d, the detection yield (the maximum of the TOF spectrum) is plotted as a function of the reverse bias and for different values of post-acceleration voltage. For low values of acceleration voltage (5 kV), the yield is low and independent on the bias voltage. In fact ions with 5 keV energy exhibit a very low penetration depth in SiC implying charges generation in the neutral near surface device region (few nm). An increase of post-acceleration produces an increase in the yield because more carriers are generated by the more energetic ions in a deeper region with a consequent improvement in the collection efficiency.

Other useful information come from Fig. 4.50 that summarizes the complete study of the detection yield trend versus the post acceleration voltage for fixed values of the V_{BIAS}.

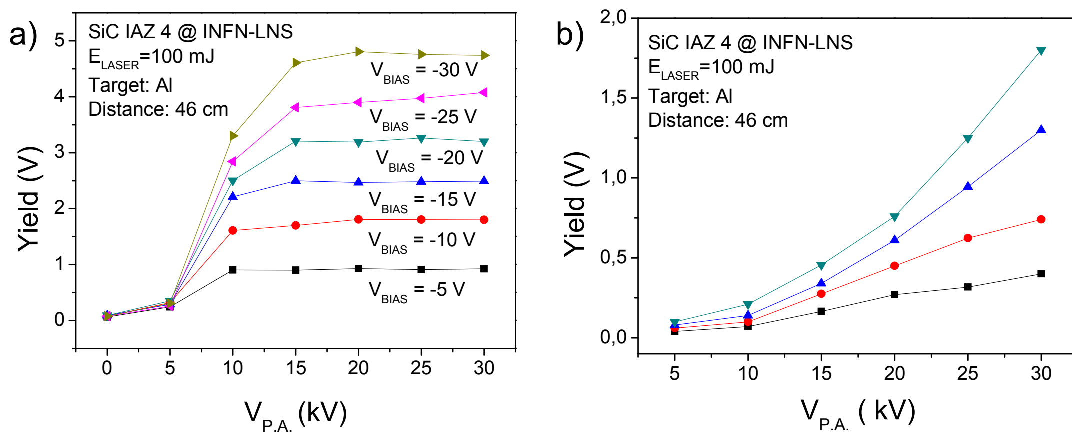

FIGURE 4.50: Yield of TOF spectra of Al ions as a function of acceleration voltage for different values of detector bias for the damaged detector of the first campaign a) and for the new SIC IAZ 4 detector of the second campaign b).

The yield should increase linearly with the ion energy and then with the post-acceleration voltage however from these results a quite complex behaviour was obtained with a saturation of the detection signal at $V_{P.A.}$ of about 15 kV and a saturation level that growths with V_{BIAS} This effect of saturation observed in the detection yield at high post-acceleration voltage could be related to carrier recombination effects due to the presence of defects and/or recombination centers or to a local excess of ions generated e-h pairs. It is well known that defects or impurities in a semiconductor can promote

recombination reducing the carrier lifetime and the collection efficiency of charge generated, in fact carriers can be trapped during their drift to the electrode and do not contribute to the charge signal. A second mechanism that may cause the detection yield saturation is the high local density of e-h pairs. In presence of the plasma, the detector is hit by a very high flux of UV photons, soft X-rays and ions, all contributing to e-h pair generation. However, a second experimental campaign was performed under the same experimental conditions at INFN-LNS, where a new interdigitized detector was employed, with the same characteristics as the previous one, but not yet exposed to any plasma radiations. The data does not show any saturation as can be seen from Fig. 4.50, the analogous of Fig. 4.48b. This result therefore seems to confirm that the saturation is due only to the damage of the detector and not to the excess of e-h pairs.

A similar behaviour has been also obtained using the thin PVT scintillator placed at a distance of 55 cm and coupled through an optical fiber with the Hamamatsu photomultiplier tube (Type No. H5784).

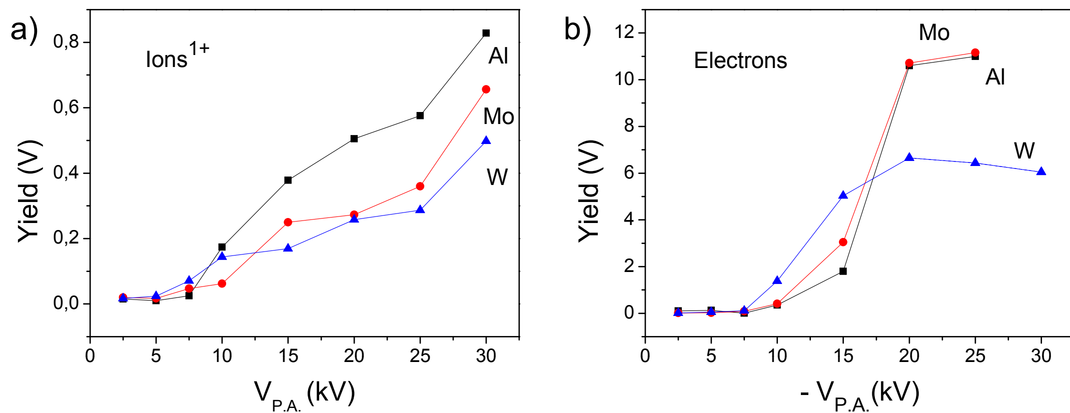

FIGURE 4.51: Yield of ions (a) and electron (b) as a function of acceleration voltage for PVT + PMT system.

Bulk target of Al, Mo and W were irradiated at the same experimental conditions with a low energy in order to obtain only the first charge state. The PMT was set with a gain factor of about 5×10^3 and was polarized at a voltage of $\pm$12 V. A linear increase has been obtained increasing the post acceleration voltage, as can be seen in Fig. 4.51a. In order to evaluate also the electrons behaviour, it was It was also to change the post acceleration polarity has been reversed. For Al and Mo it was reached a quasi-saturation conditions, while for W the saturation occurs at lower post acceleration voltage, about -20 kV. Recently also the SiC AZ 25 detector has been tested, showing good linearity and excellent efficiency also in this low ion energy. In fact as verified by SRIM simulation the thin metallization (20 nm) is soon overcame by ions applying few keV to post acceleration voltage.

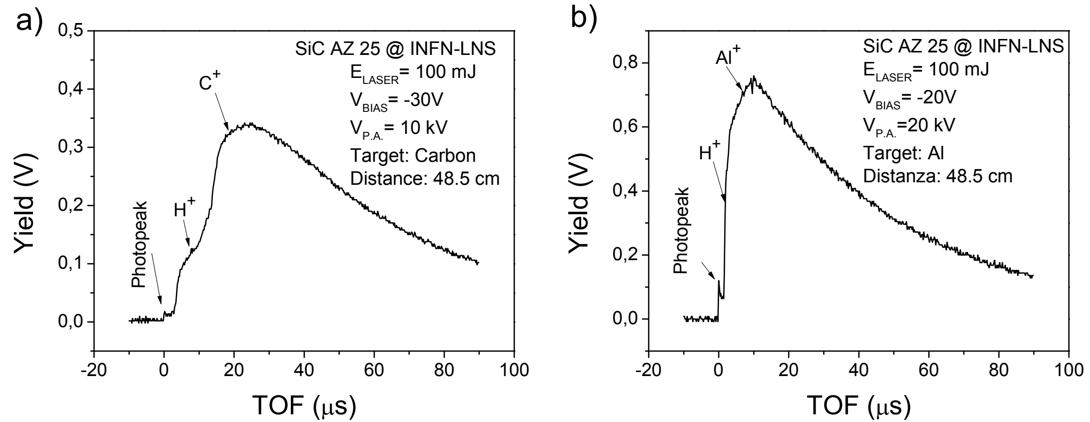

FIGURE 4.52: Typical TOF spectrum obtained with SiC AZ 25 irradiating Carbon Glass a) and Aluminum b) target at different voltage of post acceleration.

Two typical spectra are showed in Fig. 4.52. The first was obtained irradiating a Carbon Glass target and using a post acceleration voltage of 10 kV. This spectrum has a very small photopeak, and present a very clear step at about 7 μs. In this case it is easy to separate the contribution due to protons from that due to ion (C^{1+}). The same thing in general is not valid for the second spectrum obtained irradiating an Al target and using a post acceleration of 20 kV. Also here the intensity of the photopeak is very low and it is possible to see the protons only from the variation of the rising time.

As was done for SiC IAZ 4 and PVT, a series of measurements were also made for various diode polarizations and at various post-acceleration voltages for the SiC AZ 25. The results are shown in Fig. 4.53 for Aluminum and Fig. 4.54 for Carbon.

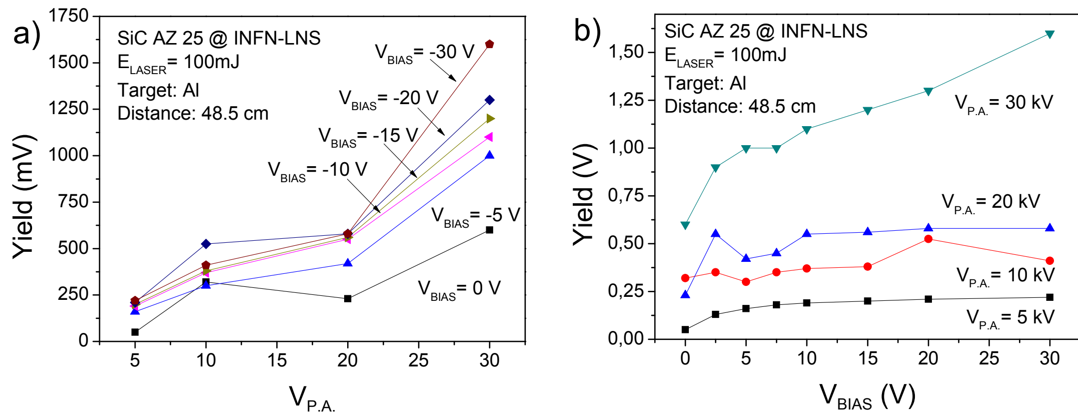

FIGURE 4.53: a) Yield of Aluminum ions as a function of the post acceleration voltage at a fixed values of detector bias voltage; b) yield of Aluminum ions as a function of the post acceleration voltage at a fixed value of detector bias voltage.

On the one hand the increase of the post acceleration voltage again leads to a proportional increase in the yield of Al ions (Fig. 4.53a) due to a better ions extraction from the

acceleration chamber. On the other hand, once it is fixed the post acceleration voltage, an increase of detector bias beyond 10 V does not cause any change in ion yield. As said before, in the case of Carbon target, it is possible to clearly distinguish proton from Carbon ion, so it has performed a separated analysis of the two species, as can be see in Fig. 4.54.

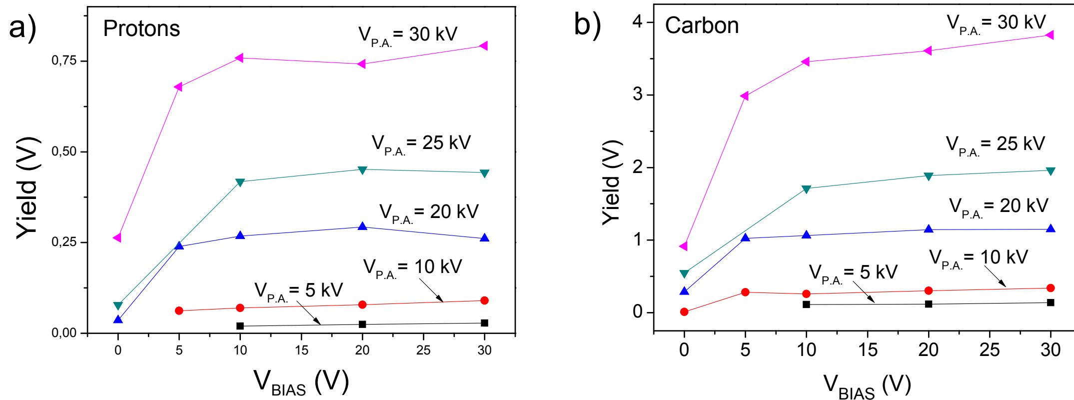

FIGURE 4.54: Yield of proton (a) and Carbon (b) ions as a function of the bias voltage of the detector for fixed values of post acceleration .

However no evident difference has been obtained, and such as for the Al ions, a saturation condition is reached for $V_{BIAS} \approx 10\,\mathrm{V}$

4.6 Radiation hardness

One of the most important features that distinguishes SiC-based detectors from conventional detectors is the high resistance to radiation-induced damage. In fact the displacement energy in Si-Si structure of 15 eV [111] is lower if compared with SiC structure, in which the threshold displacement energy is 19 eV and 38 eV for C and Si, respectively [51], indicating that defects generation threshold in SiC is higher with respect to Si. In this section there will be discussed both some literature data and some of our analysis performed to highlight the excellent qualities of SiC devices when they are employed in the detections of very high ionizing radiations and plasma diagnostic.

4.6.1 Literature data

In literature can be found several studies report on the formation of material defects by ion- or electron-irradiation and their influence on the properties of SiC [19, 30, 57]. In many fields such as the aerospace and the particle detectors, it is essential to know the effects of ion-irradiation on the material properties because the defects modify the

electrical characteristics of devices as diodes. As an example, in the graphs of Fig. 4.55 are reported two studies of literature [41, 61] performed on the defects induced by 1 MeV Si^+ and 7 MeV C^+ ions on 4H-SiC in a large fluence range, respectively. The investigations were done through Deep Level Transient Spectroscopy (DLTS) that allows to follow the evolution of irradiation-induced defects by increasing the ion fluence.

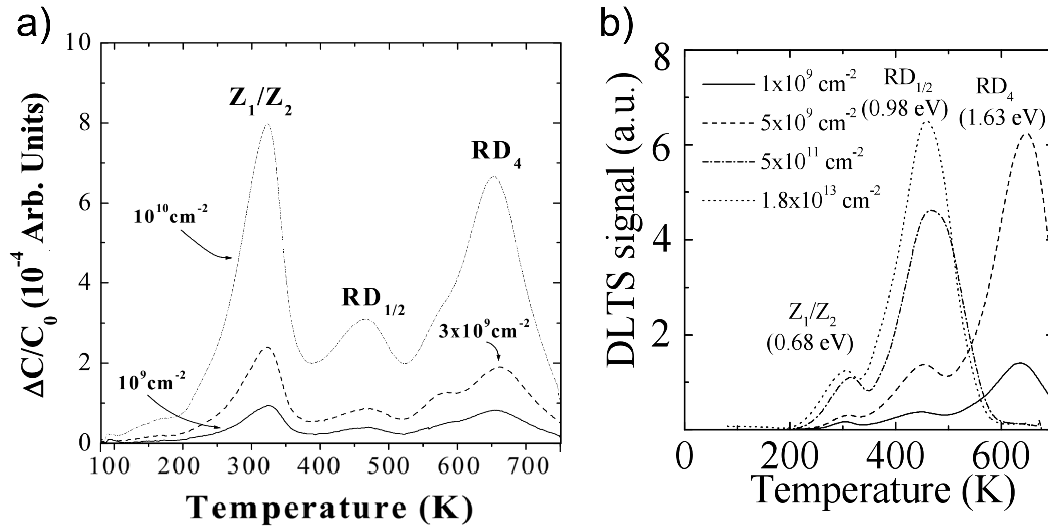

FIGURE 4.55: DLTS spectra of 4H-SiC irradiated with 1.0 MeV Si^+ (a) and 7.0 MeV C^+ (b), [41, 61].

This technique is based on the measurement of differential capacitor transients in the depletion layer of the junctions due to periodic pulse. Actually the time constant of the capacitive transient is measured as a function of temperature. In fact temperature is increased slowly with respect to the pulse repetition frequency allowing to highlight peaks of capacity as a function of temperature. Repeating the measurement with different pulse period and correlating the various results it is possible to deduce the activation energy of traps and the corresponding impurities concentration. Depending on the polarization used for the impulse (reverse or direct), both impurities of majority and minority carriers can be studied.

In the case of Si-ions, Fig. 4.55a, the spectrum evidence three peaks located at 0.68 eV, 0.98 eV and 1.63 eV below the conduction band. After irradiation at the fluence of 5×10^9 ions/cm^2, the trap concentration of these three peaks increase indicating an accumulation of the same kind of defects. Also in the C-ions case, Fig. 4.55b, after irradiation the intensity of the peak at about 300 K increases and the spectra show the formation of two more peaks, located at 480 K and 650 K, respectively. The last peak shows also a shoulder at 550 K. These levels were located at 0.68 eV, 0.98 eV and 1.4 eV below the conduction band edge, respectively and their intensities (trap concentration) increase with increasing the ion fluence.

These behaviours evidences an evolution of the ion-irradiation defects with increasing ion fluence. In fact, as can be seen in Fig. 4.56a, Izzo and al. in [41], individuate three main fluence regions.

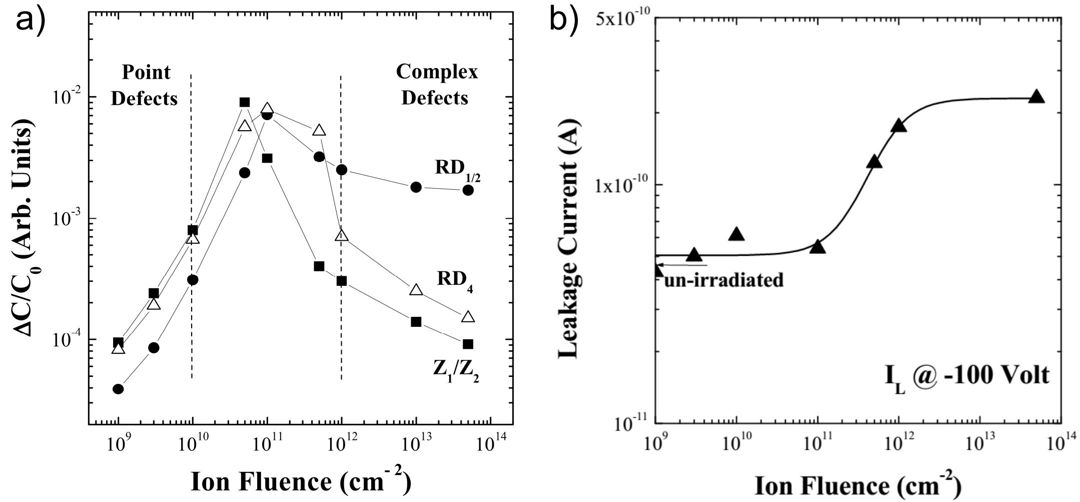

FIGURE 4.56: Intensity of the main levels detected in the DLTS spectra (a) and leakage current (b) at -100 V as a function of ion fluence, [41].

In the range $10^9 - 10^{10}\,\mathrm{cm}^{-2}$ the levels can be related to the point defects produced by ion irradiation and reaction between primary defects is negligible; in the range $10^{10} - 10^{12}\,\mathrm{cm}^{-2}$ recombination and aggregation of point defects occur; at higher fluence the damage is mainly composed by the defect related to the $RD_{1/2}$ level (a complex defects involving a carbon and a silicon vacancy) together to more complex defects. In fact the RD_4 level, associated to a Carbon vacancy, follows the same trend of the Z_1/Z_2 attributed to carbon vacancy or to an antisite, that at high fluence decreases in intensity.

In order to get more information about the influence of defects on the electrical material properties, the inverse I-V characteristics of Schottky diodes were acquired and the leakage current measured at -100 V versus ion fluence is reported in Fig. 4.56b. In this figure the leakage current is low and equal to the value measured in the un-irradiated diodes in the the fluence range $10^9 - 10^{11}\,\mathrm{cm}^{-2}$, where the damage is mainly composed of point or point-like defects. In this fluence range the average vacancy density created by ion beam is between $10^{16} - 10^{18}\,\mathrm{cm}^{-3}$.

At higher fluence, where complex defects are formed, the leakage current increases of about a factor five.

These results put in evidence the radiation hardness of SiC device, because indicate that point or point-like defects created at low fluence do not influence the performances of Schottky diodes in reverse bias.

4.6.2 Plasma induced damage

When SiC detectors are employed in TOF measurements for plasma-laser diagnostic, the damage usually can be distinguished into two different typologies:

1. crystal defects in depth induced by ion energy deposition by ions stopped in the active layers, releasing high energy at the Bragg peak;
2. surface damage due to the partially coverage of the detector surface due to clusters, debris, molecules and atoms generated from plasma and from secondary radiations in the vacuum chamber where plasma is produced.

In depth damage

In order to evaluate the crystal damage induced by ions, various SiC detectors with different plasma expositions at PALS laboratory, have been characterized with I-V measurement. These were performed in high vacuum at different bias, from -100 V up to -600 V using two Keithley instruments (2410 1100V SourceMeter and 2636 SYSTEM SourceMeter) .

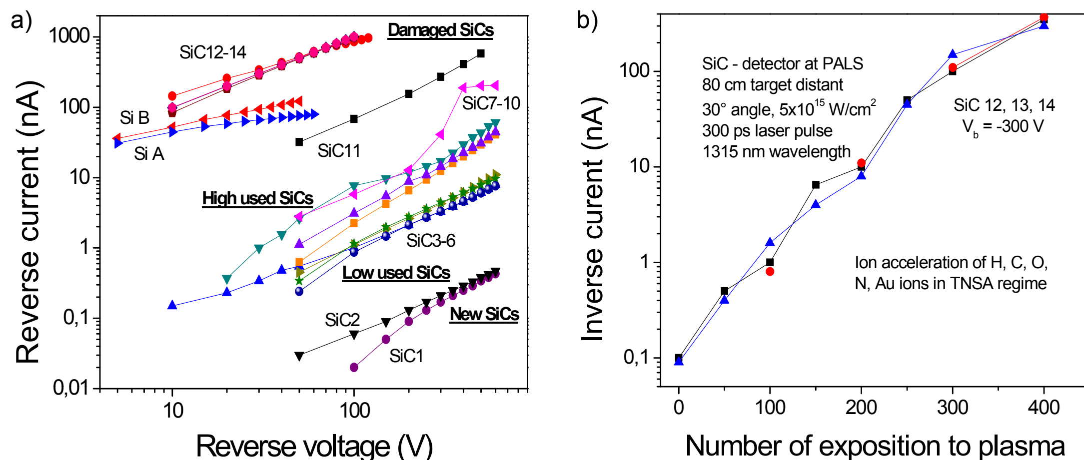

FIGURE 4.57: Intensity of the main levels detected in the DLTS spectra (a) and leakage current (b) at -100 V as a function of ion fluence.

Fig. 4.57a shows the 14 I-V curves obtained polarizing inversely the SiC schottky junction at room temperature (21 °C). It is possible to observe that the inverse current at 100 V reverse bias ranges between about 10 pA for un-exposed detectors (new SiCs) up to about 10 nA for high used SiCs and extending up to about 100-1000 nA for high damaged detectors exposed to many times (about 400) to plasma pulses. In the graph are also reported for comparison the I-V curves of two traditional Silicon Surface Barrier detector

(Si A and Si B). The dependence of the inverse current as a function of the number of expositions to the plasma generated by PALS laser operating in single pulse at an intensity of 5×10^{15} W/cm^2 in a TNSA regime was also studied. The considered detectors were placed at 80 cm from the target and at 30° angle with respect to the target normal forward direction. Through the irradiation of targets containing hydrogenated polymers and metals, overall gold, an ion acceleration higher than 1 MeV per charge state has been obtained. In such conditions, as can be seen in Fig. 4.57b reporting the I-V curves evaluated at -300 V applied bias of three different SiC detectors, the inverse SiC current grows approximately exponentially with the number of plasma expositions. The effect of leakage current increment with the exposition times is due to the defects generated in the active layer by the high LET (linear energy transfer) radiation. Mainly energetic heavy ions, such as gold, having high nuclear stopping power may produce collision cascades with Si and C atoms moving from their equilibrium positions and generating defects, such as vacancies, interstitial and others. Such generated defects reduce the electron-hole mobility enhancing the diode leakage current. It should be noted that it is very difficult to evaluate with accuracy the dose received by the SiC during plasma exposition, since as described in this chapter the properties of radiations emitted by plasma (angular and energy distribution, charge state, temperature, density) are strongly influenced by the experimental conditions (target characteristics, laser parameters, etc..) so it can not be studied exactly the dependence of damage as a function of the implanted doses that changes in each laser shots. However, as reported in literature [26], from RBS (Rutherford backscattering spectrometry) analysis of ion implanted in Si-substrates placed near to the SiC detectors, approximated evaluations indicate that ion doses of the order of 10^{14} ions/cm^2 are absorbed for each laser shot at PALS. Moreover taking into account the CBS energy distribution of ions, the defects should be uniformly distributed in the entire active zone of the detector.

Surface coverage

Plasma expositions produces also a partial surface coverage of the detector due to clusters, molecules and atoms deposition. A first cluster deposition can grows after many plasma exposition producing a thick film, which composition depends on the nature of the laser irradiated target, plasma properties (temperature, density, angular distribution of emitted particles,...) and geometrical position of the SiC detector with respect to the target. Generally the surface coverage is not uniform because nanometric and micrometric clusters are emitted not isotropically from plasma, giving rise to localized debris randomly distributed masking the total area of the exposed detector.

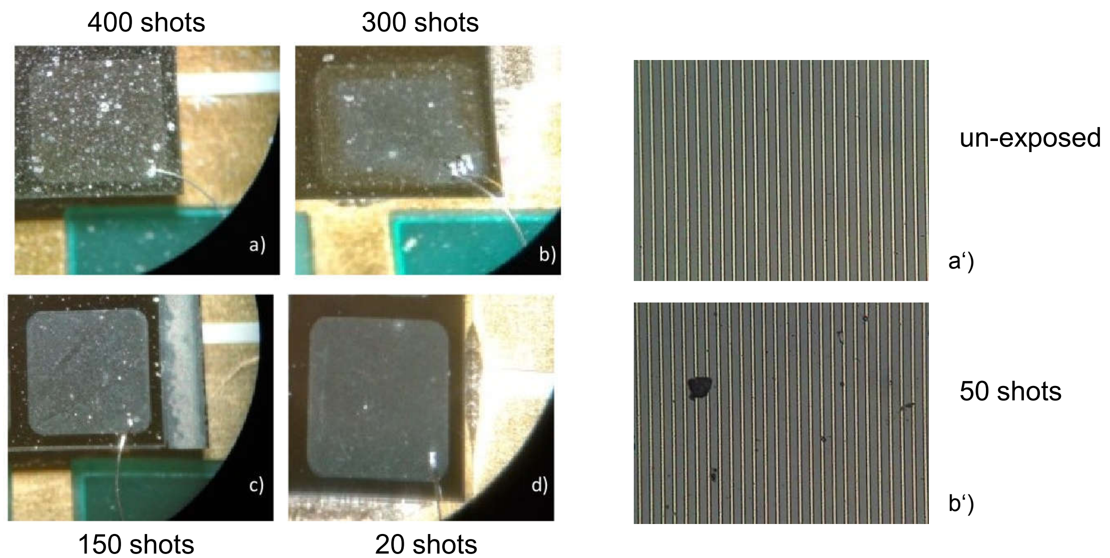

FIGURE 4.58: Optical microscope photos of the SiC AZ 80 surfaces exposed to plasma at PALS about 400 times (a), 300 times (b), 150 times (c) and 20 times (d) and of the SiC IAZ 4 surface before exposition to plasma at UniME (a') and after 50 shots (b').

Fig. 4.58 shows a set of optical microscope images of the SiC AZ 80 and SiC IAZ 4 surfaces exposed for different times to the laser-generated plasma at PALS facility and UniME laboratories, respectively. Images show micrometric debris deposited on the detector surface, together with vapors coming from the laser-generated plasma.

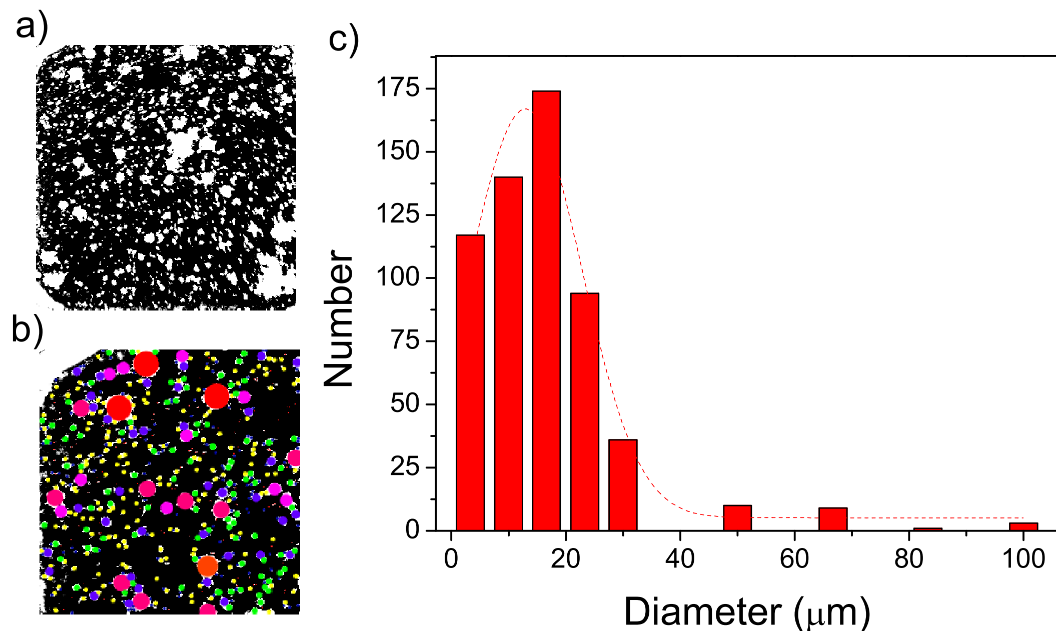

FIGURE 4.59: Procedure for the identification of size distribution of cluster.

As can be seen in Fig. 4.59, thanks to a free software of image manipulation it was possible to put in evidence the debris edge a), classify each debris according to a circular

mask with decreasing diameter b) and plotting the final size distribution c). Optical and electronic (SEM) microscope investigations confirms that the deposited debris have a large size distribution [85], with an average value of about 10-30 μm and show also submicrometric clusters with dimensions from 10 nm up to about 1 μm are present, as reported in the SEM photos of Fig. 4.60a.b, respectively.

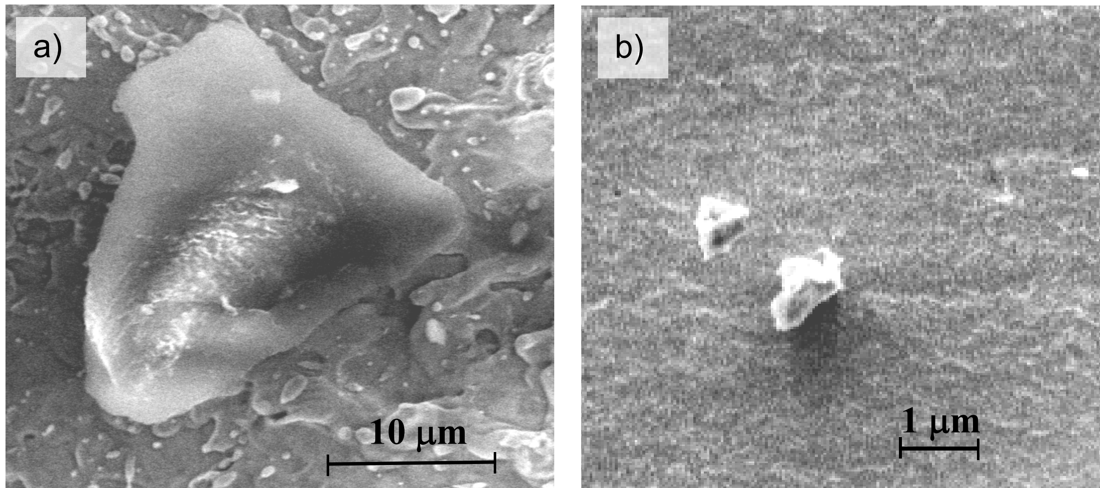

FIGURE 4.60: SEM photos of typical debris deposited on the SiC surface with a dimension of tens microns (a) and of about 1 micron (b).

The cluster deposition was also evaluated studying the surface roughness and topography of a damaged detector surface through a TENCOR p-10 profilometer at INFN-LNS in Catania fig. 4.61a. This device has a vertical resolution of 0.1 nm with an horizzontal scan of 1 mm.

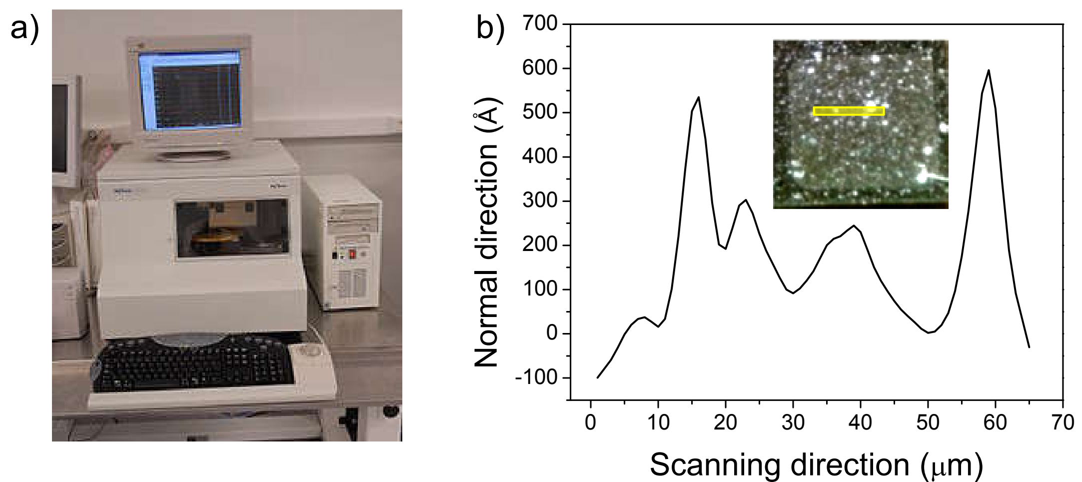

FIGURE 4.61: Photos of TENCOR profilometer a) and scan of a damaged detector surface.

A damaged SiC detector was selected for the analysis of the surface condition of the detector. A typical shape of the morphology is shown in Fig. 4.61b and put in evidence

the presence of complex structures that can reach a thickness of about 600 Å.

In order to study the decrement of SiC efficiency due to micrometric debris deposition it was studied the response to α-particles coming from a radioactive source by changing the free active surface of the detector. The reduction of the exposed area has the effect of reducing the total number of particles reaching the active layer and consequently leads to reduction of the detector signal as can be seen in Fig. 4.62. The three spectra were obtained adopting the spectroscopic electronic chain and using the same experimental parameters, but the adopted detector present a surface totally free form debris (a) or free at 53.6% (b) and 24.8% (c).

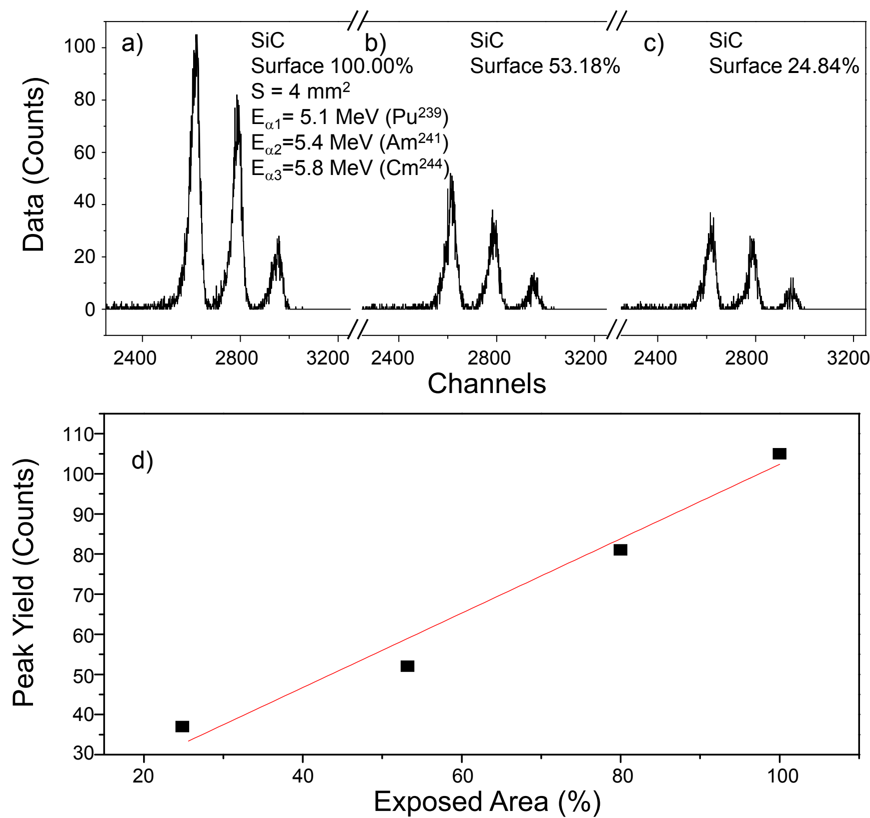

FIGURE 4.62: Thee peaks alpha spectra detected with a SiC with an exposed active surface of 100% (a), 53.18% (b) and 24.84% (c) and peak yield (counts at the peak) vs. exposed area (d).

The data were summarized in Fig. 4.62d and as expected, the α-peak yield (number of counts under the Pu peak), observed in the multichannel analyzer spectrum, shows a linear decrement proportional to the exposed area.

Conclusion and Future challenge

This thesis confirms that Silicon Carbide technology today can offers a valid response to many challenges posed by the physics of detectors, because it gives the possibility to combine the excellent properties of Silicon detectors (resolution, efficiency, linearity, compactness) with greater radiation resistance (up to five orders of magnitude for heavy ions), greater thermal stability and a visible light insensitivity. It is possible to achieve these conclusions by observing the excellent behavior shown by the three different SiC detectors at low fluence using a spectroscopic electronic chain and at high fluence in which a time of flight technique has been employed. The energy resolution has been evaluated in the energy range between few hundred keV and some MeV and results very close to traditional Silicon detector. At 5.48 MeV for example, for Silicon has been obtained an energy resolution of 0.1 % versus 0.3 % for SiC AZ 25, 0.6 % for SiC AZ 80 and 1.0 % for Diamond detector.

The measurements carried out, with proportional electronic chain, with the SiC IAZ 4 detector are also very interesting because represent the first examples of measurements made in ΔE with SiC detectors. It is known that coupling a detector in ΔE with a stop detector it is possible to realize telescopic systems such as CHIMERA, the multi-detector operating at INFN-LNS. Each element of CHIMERA consists of a silicon detector (first stage) followed by a crystal of CsI (Tl) (second stage) by which it is possible to detect and identify charged particles by means of different identification methods (ΔE-E, time of flight TOF, discrimination based on signal shape).

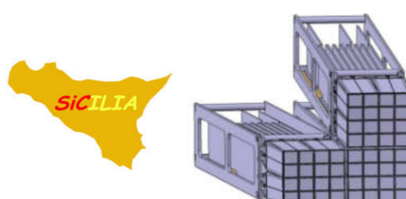

FIGURE 4.63: Logo of the SiCILIA project and prototype of an ion detection wall in SiC.

The importance and innovation of this kind of devices is testified by the launch of several INFN projects such as the experiment called SiCILIA [5]: Silicon Carbide detectors for Intense Luminosity Investigations and Applications The purpose of SiCILIA is to develop innovative processes that allow a massive production of thicker SiC detectors and a larger active area (about 1 cm^2) with a very low level of defects, Fig. 4.63.

In this project, it will test both the traditional approach using Schottky diodes and the new approach using a p-n junction. The prototypes of the ΔE and Stop detector, using the two approach are reported in Fig. 4.64.

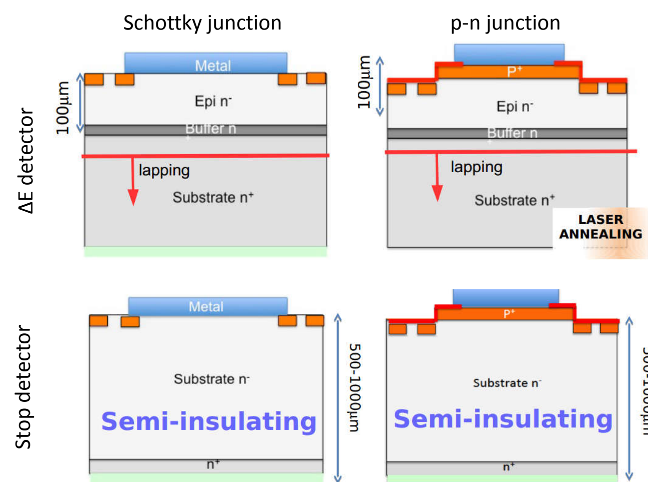

FIGURE 4.64: Prototypes of Schotthy and p-n diode for the realization of ΔE and stop detector.

The measurements carried out at the ionic implanter of the department of physics at the University of Catania have served to demonstrate once again the excellent linearity of the SiC devices response even at lower ions energies. Even in this case, the energy resolution is comparable to that of the Silicon detectors. Another important aspect that comes out from this experimental campaign is that SiC detectors can be successfully used in RBS analysis, showing an excellent linearity with the ion source current and energy. The analysis of SiC RBS spectra leads to a correct interpretation of target composition.

However, for the properties offered by SiC, the most attractive applications are related to laser-generated plasma diagnostics. Unlike traditional Silicon detector, SiC based devices do not suffer from the influence of visible light, the first noise contribution, due to the higher bandgap. This makes them particularly advantageous in the detection of particles emitted by plasma being able to simultaneously record both hard X-ray and fast ion signal. All these tests have demonstrated the extreme versatility of these devices and confirmed the qualities of SiC. In fact these detectors worked effectively under very different experimental conditions: starting from low-intensity laser-generated plasma

(10^9 Wcm^{-2}) to reach high laser intensity (10^{19}Wcm^{-2}). The energy spectrum that are able to cover and detect such detectors is therefore extremely large by some hundreds of eV obtained at low intensity up to a few hundred MeV obtained at high laser intensity. A great stimulation in the development of SiC technologies is given by the great opportunities and applications related to plasma. For example a very promising application concerns the possibility of considering plasma as a very compact particle source and accelerators by using the highly-intensive electric fields that are generated inside. Emitted radiations contain several ionic species each with a different speed and energy distribution. Depending on the specifications required by the particular application in which the plasma should be used, radiation can be filtered using suitable beam selection systems. Synthesisally the possible uses of plasmas include:

- astrophysics field applications;
- production of PET radionuclides and therapeutic treatments;
- applications in nuclear physics.
- deposition of thin films in industrial applications of microelectronics;
- ion implantation on various substrates;
- laser ion source (LIS).

But certainly the most important aspect concerns the possibility to realize fusion nuclear reaction. In an increasingly hungry world of energy resource, nuclear fusion becomes increasingly important. The tokamak project, for example, exploits the magnetic confinement of hydrogen isotopes to the plasma state, to create the conditions for thermonuclear fusion to be extracted from the produced energy. Not only in this case but in general in all of these area, SiC devices, coupled with other diagnostic techniques, become of crucial importance for the characterization of plasmas and generally for all those physical situations characterized by high temperatures and high doses. In this thesis, it was deliberately chosen to compare the SiC response only with that of a Faraday Cup (IC), IEA and scintillator. The Faraday Cup is by far the most widely used detector to have a fast diagnosis of plasma radiation due to its easy realization and reading of time of flight measurement. Also from a spectrum acquired with Faraday Cup, after deconvolution using the CBS function, it is possible to estimate the plasma temperature and the acceleration of the particles, similar to what was shown with SiC. However, unlike SiC detectors, these systems do not always effectively distinguish and separate between the photonic and ionic components and do not allow the simultaneous detection of ions and electrons, as can be done through SiCs. Finally, from the comparison of the solid angles between the two detectors, the response and sensitivity of the SiC detector is higher than that of the Faraday Cup. Through the IEA system it is possible to accurately define the energy distribution of ions by filtering incident radiations based on the E/z ratio. Among the disadvantages of this system there is the fact that, first of all, it is not possible to give any information about the neutral particles. Moreover in order to

have a good statistic it is necessary to shoot a lot of times on the target and it is not always possible. Finally, the data obtained with the scintillator photomultiplier system is very interesting. In fact, because the scintillators have low production costs, they can easily get large sensitive surfaces, one of the main goals that they try to achieve in the TOF measurements. A large useful surface would allow the detector to be positioned far away from the plasma by favoring the separation of the various ionic species and hence a better resolution in flight time measurements. The data shown demonstrate the feasibility of this approach but still highlight some critical points on which much work is still needed. An other important aspect is represented by the comparison between Diamond and SiC detectors. From the spectra analysis Diamond it is more sensitive to the electronic component and potentially more resistant to radiation-induced damage. However, the lower energy resolution and the still high production prices do not allow it to spread widely.

It was also characterize the SiC hardness studying effects due to radiation-induced damage. In this regard the state of the art has been shown, illustrating some literature works dealing with the formation of defects due to ion detection. Such detectors maintain a leakage current substantially unchanged up to ion fluence of the order of $10^{12}\,\mathrm{cm}^{-2}$. Respect to these work of literature we added a specific and in-depth characterization to the damage caused by the radiation emitted from the plasma. In such circumstances, we have distinguished the damage in surface damage, essentially due to the cluster's active surface coverage, and in depth damage due to the generation of defects in the device. As regards surface damage, an analysis procedure was carried out in order to evaluate the cluster size distribution and, thanks to the alpha spectroscopy measurements, the linearity and loss of efficiency of the detectors were evaluated as a function of the coverage of the cluster surface. The in depth damage was quantified by measuring the intensity of the leakage current as a function of laser shots. After 400 laser shot performed at PALS in which can be easily achieved high dose and particles energy, the the leakage current increase of a factor 100.

The overall work has put in evidence only some of the most important properties and benefits that SiC based technology offers. Certainly this is not a conclusion, but only a starting point because still a lot of work has to be done for a more complete and in-depth characterization of the devices, but also for the design and development of modern detectors. The elaborate is not exhaustive also because the research in this field is still in great development and very soon many steps forward will take place in the processes of realizing the diodes, in the optimization of the electronic read-out component and so on. An evident example of this is the X-ray measurements in the third chapter. In fact, because of the inappropriate electronic chain and the structure of the diodes, it was not possible to obtain the excellent results already reported in literature. However, the

preliminary data obtained by using SiC as a dosimeter are very encouraging because SiC detector shows an excellent linearity between the current of the diode and the dose both at low energies (20 keV) and at high energies (1.3 MeV). Moreover, concerning photon detection, it should be noted that in literature there are already several studies concerning the detection of UV rays where the advantages of the SiC are particularly significant [53, 54] for various applications in industrial, environmental, and even biological fields.

In the scenario of future challenges, as mentioned above, there is the realization of large array of SiC devices to build a detector wall but there is also the aim to develop a high-frame rate multi-pixel tracking and imaging detector, such as shown in Fig. 4.65, that would be very important in the medical and industrial field for imaging applications.

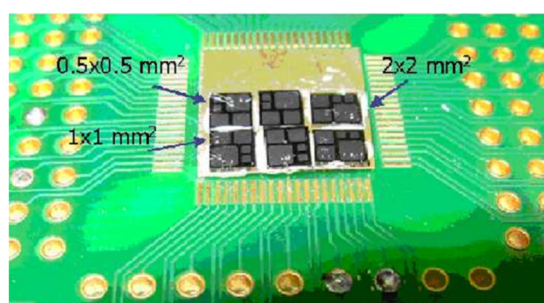

FIGURE 4.65: First attempt to realize a pixel detector, from Ref. [28].

Another ambitious project concerns the construction of an avalanche SiC detector. The interest in the realization of such device is testified also by the INFN project callaed CLASSiC: Cherenkov Light detection with Silicon Carbide. This detector would offer the great advantage of being able to reveal Cherenkov light (even a single photon) in the presence of visible radiation. Lastly, it should be mentioned the aim to realize new detector based on different polities such as the 6H-SiC. In the work proposed by A. Sciuto et al. in [69], is proposed the realization of a UV-A sensor based on 6H-SiC Schottky photodiode. These sensor would be integrated in some portable devices for UVI monitoring that is of fundamental interest to evaluate possible dangers to human health.

Appendix A

Common aspects of radiations detectors

At the basis of the operating principle of any particle detectors there is the transfer of all or a part of the energy of the radiation to the mass of the detector, where is converted to some other form, depending on the nature of the device. For example in the photographic emulsions the ionization of the interacting particles produces chemical reactions that allow the formation of an image, in gas detectors it produces ions which give rise to an electric signal, in scintillators it induces molecular energy transitions that leads to a light emission and so on. In a very simplified detector model, as a consequence of the radiation interaction, a net charge Q appears in the active volume of the detector. In order to form a suitable electrical signal, this charge is then collected in a certain time t_c that depends on the type of the detector. In ion chamber, for example, the collection time can take some milliseconds while in semiconductor detector can be few nanoseconds. In this model each interactions will give rise to a current $i(t)$ such that:

$$\int_0^{t_c} i(t)\, dt = Q \tag{A.1}$$

Logically in any real situation there are many interactions in a certain period of time and some of that can occur in the same instant if the radiation rate is too high. In this thesis both conditions will be presented, showing the differences and the necessary corrections that have to be done. However in this first chapter, reporting general considerations about radiations detectors, for simplicity, it will be assumed that the rate is low enough so that each interaction gives rise to a distinguishable signal.

Energy Resolution

One of the most important property of a detector, especially if radiation spectroscopy measurement has to be done, is the capability of the device to distinguish between two near monoenergetic pulse. It depends on the response function of the detector and reflects the ability to resolve fine detail in the incident radiation. In fact since the interaction of radiation with detector medium at the microscopic level involves stochastic processes, it is inevitable a fluctuation in the number of excitations and ionizations, causing the presence of a statistical noise. Therefore the response to a monoenergetic radiation will assume a gaussian shape rather than a Dirac delta function.

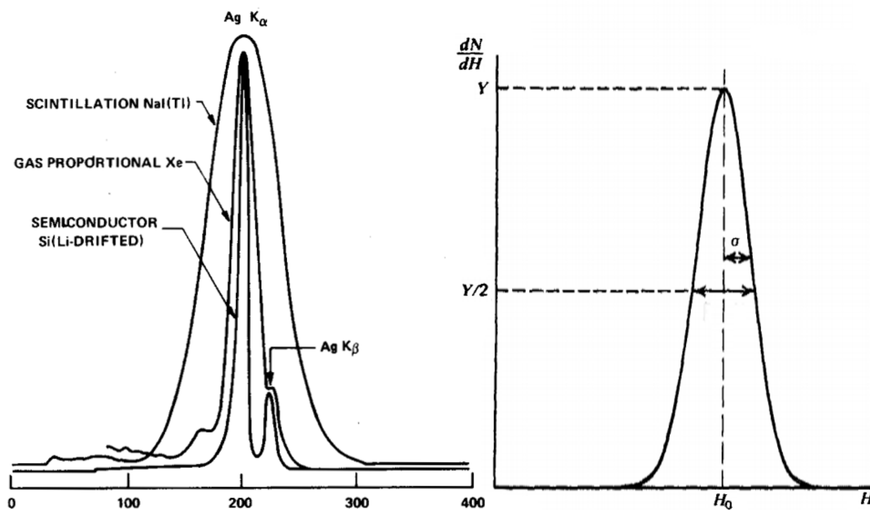

FIGURE A.1: Comparison between three types of X-Rays detector for the Silver K spectra (a). Definition of energy resolution (b).

The parameter that allows to estimate this response is called energy resolution, R, and is given by the dimensionless fraction:

$$R = \frac{FWHM}{H_0} \tag{A.2}$$

i.e. the ratio between the full width at half maximum ($FWHM$) and the peak centroid H_0. Semiconductor diode detectors for example can have an energy resolution less than 1 %, whereas in scintillation detector can ranging 5-10 % , as reportedin literature [59]. However the statistical noise, described above, is only one of the possible contribution that causes the worsening of the energy resolution. There are also other elements that have to be included:

- drift of the operating characteristics of the detector during measurements;
- unexpected fluctuations of the source;

- problems connected with the transport of the radiations;
- electrical noise due to instruments and connections between wires;
- constrains imposed by the geometry of the detector.

It is possible to connect these parameters through the sum quadrature rule [44]:

$$\Omega^2_{Exp} = \Omega^2_{Intr} + \Omega^2_{Elec} + \Omega^2_{Metal} + \Omega^2_{abs} \tag{A.3}$$

where Ω^2_{Exp} is energy spread in the experimental spectrum, Ω_{Intr} represents the intrinsic resolution of the device, Ω_{Elec} represents the noise of the employed electronic chain, Ω_{Metal} is the energy straggling due to top metallization in the entrance window of a semiconductor device and Ω_{abs} is the energy straggling due to the possible presence of an absorber placed in front of the detector.

Time response and dead time

Another important aspect of any detector is its temporal response, i.e. the time takenthe detector to form the signal after the arrival of the radiation. Also the duration of the signal is important, as it determines the dead time of the detector, i.e. the time during which the detector remains insensitive to a new event or detect a distorted signal due to the overlapping of signals, called "pile-up" phenomenon. The generated signal depends not only from the detector but also on the input characteristics of the circuit to which the detector is connected, that can be represented in the Fig. A.2.

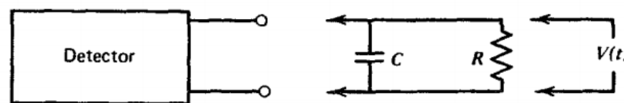

FIGURE A.2: Equivalent circuit connected to the detector.

It consists in an input resistance R and in a capacitance C representing the equivalent capacitance of both the detector itself and the measuring circuit. Using this simplified model it is possible to define a time constant τ given by the RC product. According to the relationship between τ and t_c, two different conditions can occur, as reported in Fig. A.3:

- when $RC \ll t_c$, the current flowing trough the resistance is the same current that flows within the detector, and the voltage $V(t)$ has a shape very near to that of the current $i(t)$;

- when an accurate energy information is required, the detector is connected in a circuit in which $RC \gg t_c$. Very little current flows in the load resistance during the collection time and the detector current is momentarily integrated on the capacitance. In low flux conditions, the capacitance will discharge through the resistance, before that a new pulses is recorded. In this approach the rise time, i.e. the time necessary to reach the maximum value, depends only by the collection time and not from the external circuit such as in high flux conditions. Another important aspect is the fact that the amplitude of the signal V_{max} is directly proportional to the corresponding charge generated in the active volume of the detector according to the relation:

$$V_{max} = \frac{Q}{C} \tag{A.4}$$

It should be noted that to obtain proportionality between V_{max} and Q the inherent capacitance has to be constant during operations. If this consideration is warranted for most kind of devices, the same is not true for semiconductor diodes in which the capacitance may change with variations in normal operating parameters. For this reason a type of preamplifier circuit know as a charge-sensitive configuration has been developed, in order to eliminate the dependence on the value of C preserving information carried by the magnitude of Q.

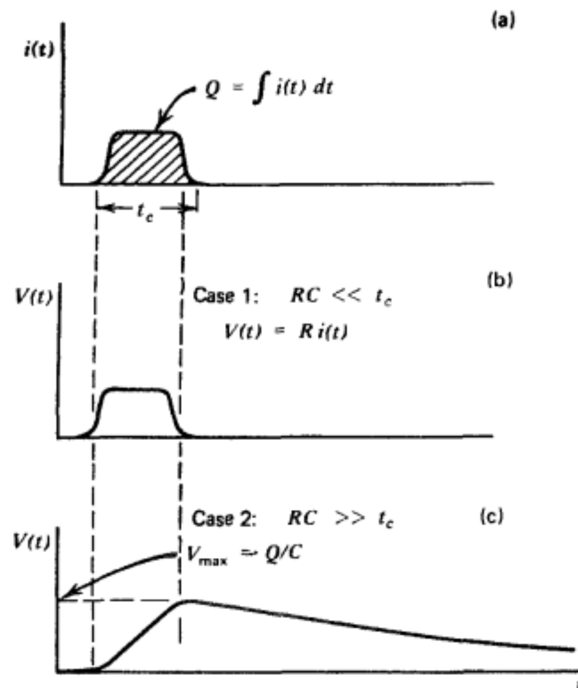

FIGURE A.3: (a) Hypothetical current pulse output. Signal voltage on the external circuit when $RC \ll t_c$ (b) panel or when $RC \gg t_c$ (c) panel.

Efficiency

Many aspects influence the capability of a detector to respond to a radiation quanta. First of all the nature of radiation influences the probability interaction within the detector. For example α-particles or massive ions are stopped in the first layers of the detector generating a huge number of charge pairs along their path, while for uncharged particles, like neutron or photon, the situation is quite different because they can travel large distances before interacting. Another aspects concerns the geometry of the overall apparatus: the shape of source (punctual or extended source), the isotropy of the emitted radiations, the source-detector distance, the dimension of the active volume. As can be seen in Fig. A.4a, supposing to have a detector with a surface $A = \pi a^2$ placed at a certain distance $d \gg a$ far from the source emitting isotropically, there will be a subtend solid angle Ω given by:

$$\Omega \approxeq \frac{A}{d^2} \tag{A.5}$$

However when these assumptions are not satisfied, like in Fig. A.4b, is it possible to express the solid angle in terms of the Bessel function.

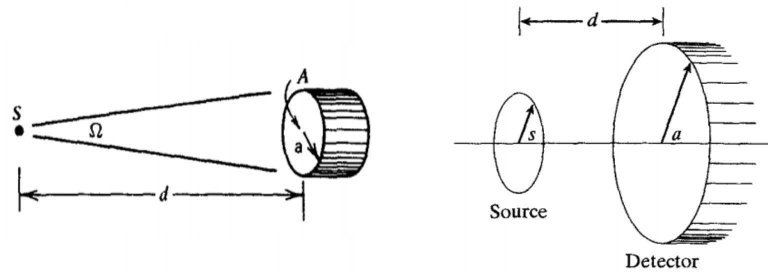

FIGURE A.4: Solid angle subtended by detector.

So in general it is defined an absolute efficiency conventionally expressed as:

$$\epsilon_{abs} = \frac{\text{number of recorded pulse}}{\text{number of radiation quanta emitted from the source}}$$

In particular circumstances it is useful to define also another kind of efficiency, the so called intrinsic efficiency:

$$\epsilon_{int} = \frac{\text{number of recorded pulse}}{\text{number of radiation quanta impinging on detector}}$$

It does not depend from the geometry, but only form the typology and energy of radiation, and form the material of the detector.

Appendix B

Physics of semiconductor material

The main subject of this work are solid state detectors and for this reason a detailed description about the physics of semiconductor is presented in this Appendix

Definition of band structure

The variations in the electrical conductivity among metals, semiconductors and insulators can be qualitatively described in terms of the differences in the band diagram and in the characteristics of the conduction and valence band. Metals present a very low value of resistivity because they can present or a partially filled conduction band (as in Cu), or an overlap between the valence band and the conduction (such as Zn or Pb). Consequently the valence electrons, when gain kinetic energy, for example through the application of an external electric field, can move freely from an energy level to the next one.
In the other hand insulators are characterized by a wide energy gap, conventionally grater than 5 eV. For this reason no electron can participate to current transport.
Semiconductors, from the point of view of the band structure, have similar characteristics of insulators, with a band gap lower than 5 eV. When T=0 K, all electrons are in the valence band and consequently at low temperatures semiconductors don't conduct current. Instead at room temperature and under standard pressure conditions a certain amount of electrons can be promoted to the conduction band due to the thermal energy. The conduction band is rich of accessible state in which electrons can be accepted, and also a very small external field will be able to move them.
More in details, the concept of the band structure can be explained in terms of the Pauli exclusion principle, [75]. Consider the energy levels of an isolated hydrogen atom,

according with the Bohr model, is given by:

$$E_n = -\frac{m_0 e^4}{8\varepsilon_0^2 h^2 k_n^2} = -\frac{13.6}{k_n^2} eV \tag{B.1}$$

where m_0 is the rest mass of the electron, e the electron charge, ε_0 is the permittivity in vacuum, h is the Planck's constant and k_n is a positive integer (principal quantum number). When $k_n > 2$ the energy levels split according to the number of the quantum moment ($\ell = 0, 1, 2, ..., k_n - 1$).
Considering two identical atoms, when they are distant, the allowed energy levels for a given quantum number ($k_n = 1$ for example), consist of a single state doubly degenerate, ie the atoms have exactly the same energy. If the two atoms are slowly brought in contact the doubly degenerate level will necessarily split in two distinct energy levels due to the interaction between the two atoms. The split can be explained in terms of the Pauli exclusion principle, which states that no more than two electrons (with antiparallel spins) in a given system can occupy the same energy level at the same time. Considering N atoms close together arranged to form a solid, the orbits of the outer electrons of different atoms will overlap and interact each other. This interaction, including attraction and repulsion forces, causes a shift in the energy levels, as in the case of two interacting atoms. However, instead of two levels, now N separate but closely spaced levels are formed. When N is large, the result is an essentially continuous band of energy. This band of N levels can extend over a few eV depending on the inter-atomic distance of the crystal. The electrons can no longer be treated as belonging to their parent atoms: they belong to the crystal as a whole. Fig. B.1 shows the effect, where the parameter a represents the equilibrium inter-atomic distance of the crystal.

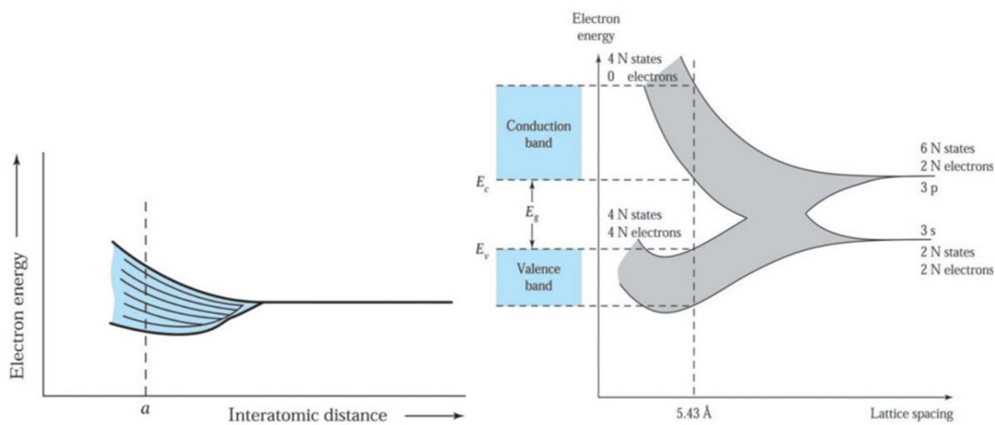

FIGURE B.1: The splitting of a degenerate state into a band of allowed energies a) and formation of energy bands for a silicon crystal.

In the case of semiconductor materials the splitting of the energy bands can be more complicated. For example silicon has 14 available electrons: 10 occupy the deeper energy

levels, strongly bound to the atoms, while the remaining 4 electrons, because they have a weak bond with may give rise to chemical bonds with other atoms. So only the outer shell with $k_n = 3$ has to be considered as valence electron. The four electrons are divided into two sub-shells 3s (or $k_n = 3$ and $\ell = 0$) and 2 in the 3p sub-shell (or $k_n = 3$ and $\ell = 1$) that have six possible quantum states. In Fig. B.1b is shown schematically what happens during the formation of the silicon crystal from N separated atoms. When the interatomic distance decreases, the 3s and 3p sub-shell of the N interacting silicon atoms form an energy band, for the same reasons reported before. Since the bands will grow, initially they will merge into one band containing $8\,N$ states, but at the equilibrium point of the interatomic distance, determined by the minimum of the total energy, the bands will split into two new bands each with $4\,N$ states: the valence band at lower energy and the conduction band at higher energy. When the temperature is close to 0, electrons will be only in the valence band occupying all its allowed states and leaving completely empty the conduction band.

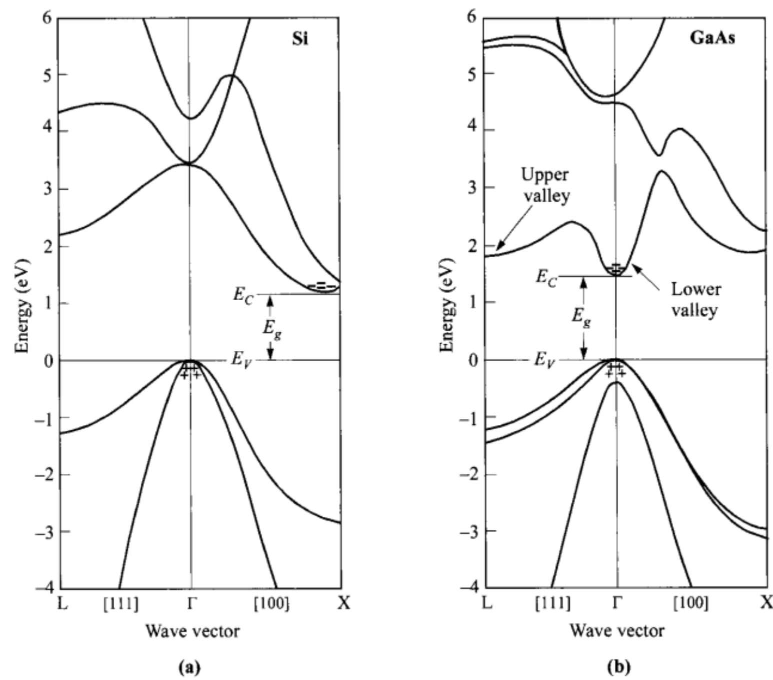

FIGURE B.2: Energy band structure for silicon a) and for gallium arsenide b), examples of indirect and direct semiconductor material, respectively

Between the top of the valence band and the bottom of the conduction bands there is an energy band with no allowed energy states, the so-called band gap, E_g. Physically to promote an electron from the valence band to the conduction band an energy equal to E_g is necessary. For this reason at higher temperatures, some electrons, as a result of the interaction with the lattice, can acquire enough energy to occupy more energetic levels. However it should be noted that semiconductors materials are divided into two classes: direct and indirect gap material. In fact, as reported in Fig. B.2, two different situation

can occur when the energy vs momentum curve is plotted. In silicon, the first case, the maximum point in the valence band is at $p = 0$, but the minimum in the conduction band occurs along the [1,0,0] direction at $p = p_c$. These materials are called indirect semiconductor, and when an electron makes a transition from the top of the valence band to the minimum of the conduction band, not only an energy change, greater than the energy gap, but also some momentum change greater than p_c is required. In the second case, such as for gallium arsenide, the maximum of the valence band and the minimum of the conduction band are in the same point at $p = 0$. These are the direct semiconductors and no momentum change is required for an electron transition.

Intrinsic carrier concentration

A semiconductor that contains relatively small amounts of impurities, compared with the thermally generated electrons and holes, is called intrinsic semiconductor. In such material at a given temperature, thermal agitation has the results to excite electrons from the valence band to the conduction band, leaving an equal number of holes in the valence band. In order to derive the carrier concentration in the thermal equilibrium condition the electron density n has to be firstly evaluated. It is given by the integral of the density of the occupied states $n(E)$ per unit volume and energy from the bottom E_C to the top E_{top} of the conduction band:

$$n = \int_{E_C}^{E_{top}} n(E)dE \tag{B.2}$$

Moreover the density of the occupied state $n(E)$ is determined by two factors:

- the density of the available states[1], $N_C(E)$, that depends on the considered material, for an electron which behaves as a free particle with effective mass m_e^* is:

$$N_C(E) = \frac{8\pi\sqrt{2}}{h^3} m_e^{*3/2} \sqrt{E - E_C}, \quad \text{for } E \geq E_C \tag{B.3}$$

- the probability that each states is occupied, given by the Fermi-Dirac distribution function, $F(E)$:

$$F(E) = \frac{1}{1 + \exp\left(\frac{E - E_F}{k_B T}\right)} \tag{B.4}$$

  in which k_B is the Boltzmann constant, and the quantity E_F, ie the Fermi level, represents the energy value in which $F(E_F) = 0.5$.

[1] for more information about the calculation of the density of the states see Appendix C

Using the Eq. B.3 and B.4, it is possible to rewrite Eq.B.2:

$$\begin{aligned} n &= \int_{E_C}^{\infty} N_C(E) \cdot F(E) dE = \\ &= \int_{E_C}^{\infty} \frac{8\pi\sqrt{2}}{h^3} m_e^{*3/2} \sqrt{E - E_C} \cdot \frac{1}{1 + \exp\left(\frac{E-E_F}{k_B T}\right)} dE \end{aligned} \tag{B.5}$$

in which the top limit of the integral was extended to infinity because Fermi function at higher energies becomes zero and so it is not important to know the top limit of the conduction band.

With the same consideration a similar equation can be obtained also for holes density in the valence band which can be considered as free particles with an effective mass m_h^*:

$$\begin{aligned} p &= \int_{-\infty}^{E_V} N_V(E)[1 - F(E)] dE \\ &= \int_{\infty}^{E_V} \frac{8\pi\sqrt{2}}{h^3} m_h^{*3/2} \sqrt{E_V - E} \frac{1}{1 + \exp\left(\frac{E_F-E}{k_B T}\right)} dE \end{aligned} \tag{B.6}$$

in which it was taken into account the density of states for holes in the valence band $N_V(E)$ that can be written:

$$N_V(E) = \frac{8\pi\sqrt{2}}{h^3} m_h^{*3/2} \sqrt{E_V - E}, \quad \text{for } E \leq E_V \tag{B.7}$$

This situation is clarified in Fig. B.3 where is evident that the carrier density n is represented by the crosshatched area, taking into account the density of the state N_C, N_V and the Fermi function $F(E)$.

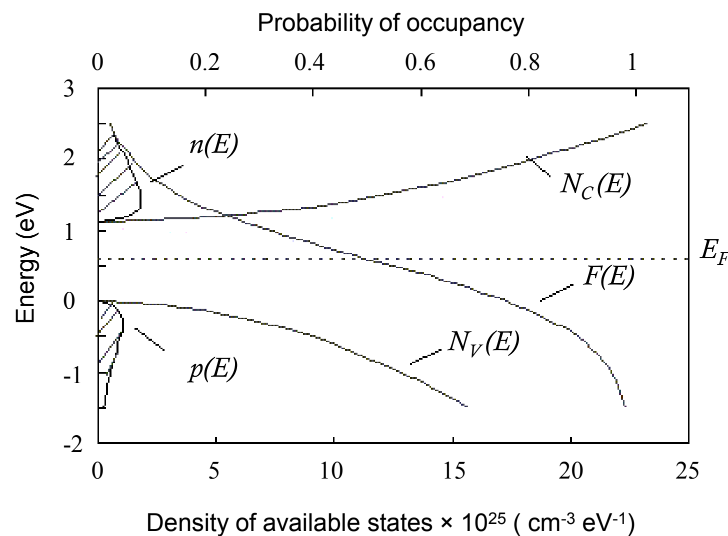

FIGURE B.3: Determination of carrier density in the conduction and valence band, [105].

Unluckily Eq.B.5 and B.6 can not be solved analytically, but only numeric or approximate solutions can be determined. However, there is a particular condition, ie when $T = 0$, whereby it is possible to solve the integral, thanks to the behaviour of the Fermi function:

$$F(E) = 1 \quad \text{when} \quad E < E_F$$
$$F(E) = 0 \quad \text{when} \quad E > E_F$$

For this reason at $T = 0$ eq. B.5 and eq. B.6 become:

$$n = \frac{\sqrt{8}}{3\pi^2}\frac{(m_e^*)^{3/2}}{\hbar^3}(E_F - E_C)^{3/2} \quad \text{in which} \quad E_F \geq E_C \tag{B.8}$$
$$p = \frac{\sqrt{8}}{3\pi^2}\frac{(m_h^*)^{3/2}}{\hbar^3}(E_V - E_F)^{3/2} \quad \text{in which} \quad E_V \geq E_F \tag{B.9}$$

Note that an important approximation can be done on the Fermi function when the energies are about $3kT$ above or below the Fermi energy, such as for non-degenerate semiconductors. In other words when the Fermi energy is at least $3k_BT$ away from either band the Fermi function can be replaced with a simple exponential function:

$$F(E) \cong \exp\left(\frac{E - E_F}{k_BT}\right) \quad \text{when}(E - E_F) > 3k_BT \tag{B.10}$$
$$F(E) \cong \exp\left(\frac{E - E_F}{k_BT}\right) \quad \text{when}(E - E_F) > 3k_BT \tag{B.11}$$

The carrier density integral can be solved again and eq. B.5 becomes:

$$n \cong \int_{E_C}^{\infty} \frac{8\pi\sqrt{2}}{h^3}(m_e^*)^{3/2}\sqrt{E - E_C}\exp\left(\frac{E_F - E}{k_BT}\right)dE = N_C^*\exp\left(\frac{E_F - E_C}{k_BT}\right) \tag{B.12}$$

where it was introduced N_C^* the effective density of state in the conduction band:

$$N_C^* = 2\left(\frac{2\pi m_e^* k_BT}{h^2}\right)^{\frac{3}{2}} \tag{B.13}$$

Similarly from eq. B.6, adopting the same approximations it is possible to obtain for holes:

$$p \cong \int_{-\infty}^{E_V} \frac{8\pi\sqrt{2}}{h^3}(m_h^*)^{3/2}\sqrt{E_V - E}\exp\left(\frac{E - E_F}{k_BT}\right)dE = N_V^*\exp\left(\frac{E_V - E_F}{k_BT}\right) \tag{B.14}$$

where the effective density of states in the valence band was introduced:

$$N_V^* = 2\left(\frac{2\pi m_h^* k_BT}{h^2}\right)^{\frac{3}{2}} \tag{B.15}$$

In order to evaluate the intrinsic concentration n_i at finite temperatures it is possible to

start from the latter approximation, because by definition an intrinsic semiconductor is non-degenerate. In this condition because of thermal agitation a continuous excitation of electrons from the valence band to the conduction band occurs. However this process is balanced by recombination between electrons in the conduction band and holes in the valence band and for this reason at the steady state:

$$n_i = n = p \tag{B.16}$$

Consequently from eq. B.12 and eq. B.14, n_i can be written:

$$n_i = N_C^* \exp\left(-\frac{E_C - E_F}{k_B T}\right) = N_V^* \exp\left(-\frac{E_F - E_V}{k_B T}\right) = \tag{B.17}$$

$$= \sqrt{N_C^* N_V^*} \exp\left(-\frac{E_g}{2k_B T}\right) \tag{B.18}$$

By using again the same equations also the Fermi Energy E_F can be determined:

$$E_F = \frac{E_C + E_V}{2} + \frac{k_B T}{2} \ln\left(\frac{N_V^*}{N_C^*}\right) \tag{B.19}$$

This equation shows that the Fermi level, for an intrinsic semiconductor, lies very close to, but not exactly at, the middle of the bandgap.

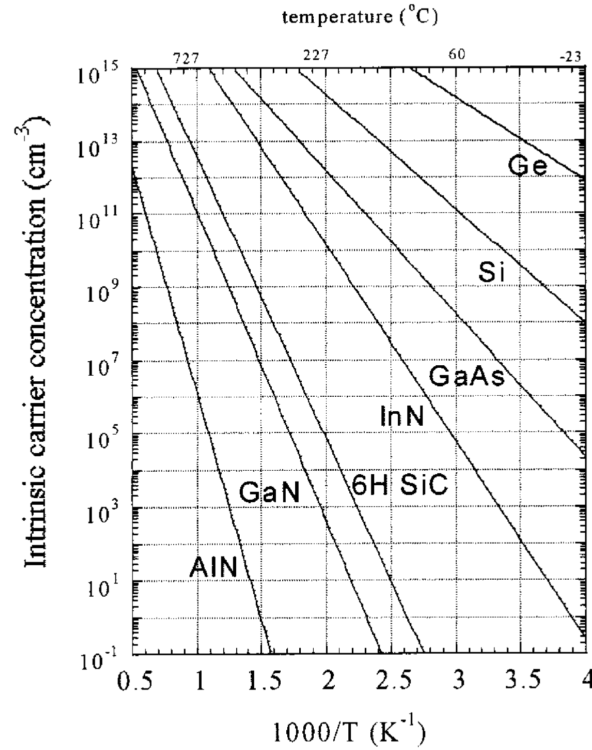

FIGURE B.4: Intrinsic carrier concentrations of germanium, silicon, gallium arsenide, indium nitride, silicon carbide, gallium nitride, aluminum nitride as a function of reciprocal temperature, [42].

In Fig. B.4 is reported the behaviour of the intrinsic concentration as a function of temperature for a wide class of semiconductor materials. From this figure it is evident that at any temperature, the intrinsic carrier concentration (and, thus, the intrinsic leakage current) is about 12 orders of magnitude lower in wide bandgap material than in the more common semiconductors (Si, Ge). Thus, as device temperature increases, the intrinsic carrier concentration eventually exceeds that of the impurity doping. This can be very deleterious in common semiconductors, while SiC and other wide bandgap materials maintain good performance also at temperatures exceeding 650°C [60].

Doping of semiconductor

The introduction of small amounts of impurities in an intrinsic semiconductor determines a radical change of the main properties of the material that becomes extrinsic. These impurities can be added on purpose with the aim to provide free carriers in the semiconductor or can be introduced accidentally during the grow phase of crystal. When pentavalent atoms (such as P, As, Sb) are added in the network, they replace old atoms in the lattice forming four covalent bonds. However an other electron remains free and not so bounded to the original atom. In fact also the effect of temperature will be able to liberate this electrons, making it free to participate to the conduction process. It's clear that increasing the number of the doping atoms, called donors, the number of free electrons will also increase and the material is n-type doped.
Similarly, it is called p-type doping, the situation in which in an intrinsic semiconductor are added trivalent impurities such as B, In. The atoms of the new chemical species should replace the original atoms of the crystal, but they are not able to saturate all four covalent bonds, creating an hole in the lattice. This hole can be filled by an electron coming from another near covalent bond, leaving in turn a new not saturated tetravalent bond. The result is a holes which moves in the opposite direction with respect to the electron so it is possible to say that also holes can move, participating in the conduction.

In both cases, as result of the introduction of impurities that break up the perfect periodicity of the crystal lattice, some new energy levels are generated. In terms of energy bands, the introduction of donor atoms corresponds to insert in the energy gap, a level close to the conduction band from which electrons can "jump" in the conduction band, participating to the conduction processes. Instead the introduction of acceptors atoms leads to a generation of a new energy level close to the valence band. In particular can be distinguished two class of impurities: shallow levels are impurities that require little amount of energy, of the order of $k_B T$ or less, to be ionized, or deep levels that instead require an energy much larger than

Note that even a single atom can introduce more levels, such as the oxygen in the silicon that has two donor levels and two acceptor levels in the band gap.

Again, in the case of a non-degenerate semiconductor, where the electron or hole concentration is much lower than the effective density of states in the conduction band or the valence band, respectively, under a complete ionization condition[2], the electron density can be written as:

$$n = N_D \tag{B.20}$$

where N_D indicates the donor concentration. Combing the last equation with eq. B.12 it is possible to obtain the Fermi level in terms of the effective density of states and donor concentration:

$$E_C - E_F = k_B T \ln\left(\frac{N_C}{N_D}\right) \tag{B.21}$$

Again, taking advantage of similar concentration, when there is complete ionization, the holes concentration is given by:

$$p = N_A, \tag{B.22}$$

N_A where is the concentration of acceptor atoms and the Fermi energy is:

$$E_F - E_V = k_B T \ln\left(\frac{N_V}{N_A}\right) \tag{B.23}$$

Eq. B.21 and eq. B.23 put in evidence the fact that the higher the concentration of the donor, the smaller will be the difference in energy between E_C and E_F and consequently the Fermi level will result near to the bottom of the conduction band. Similarly, increasing the acceptor concentration, the Fermi level will approach the top of the valence band.

In Fig. B.5 is presented an overview which shows the band diagram, the density of states, the Fermi distribution and the carrier concentration for intrinsic semiconductors, n-type and p-type. In every case the product of n and p is:

$$np = n_i^2 \tag{B.24}$$

This condition is usually called mass action law, and how can be also seen from eq. B.18 is valid for both intrinsic and extrinsic semiconductor under thermal equilibrium.

[2] The complete ionization condition occurs when there is enough thermal energy to ionize all impurities and consequently there is an equal number of electrons in the conduction band

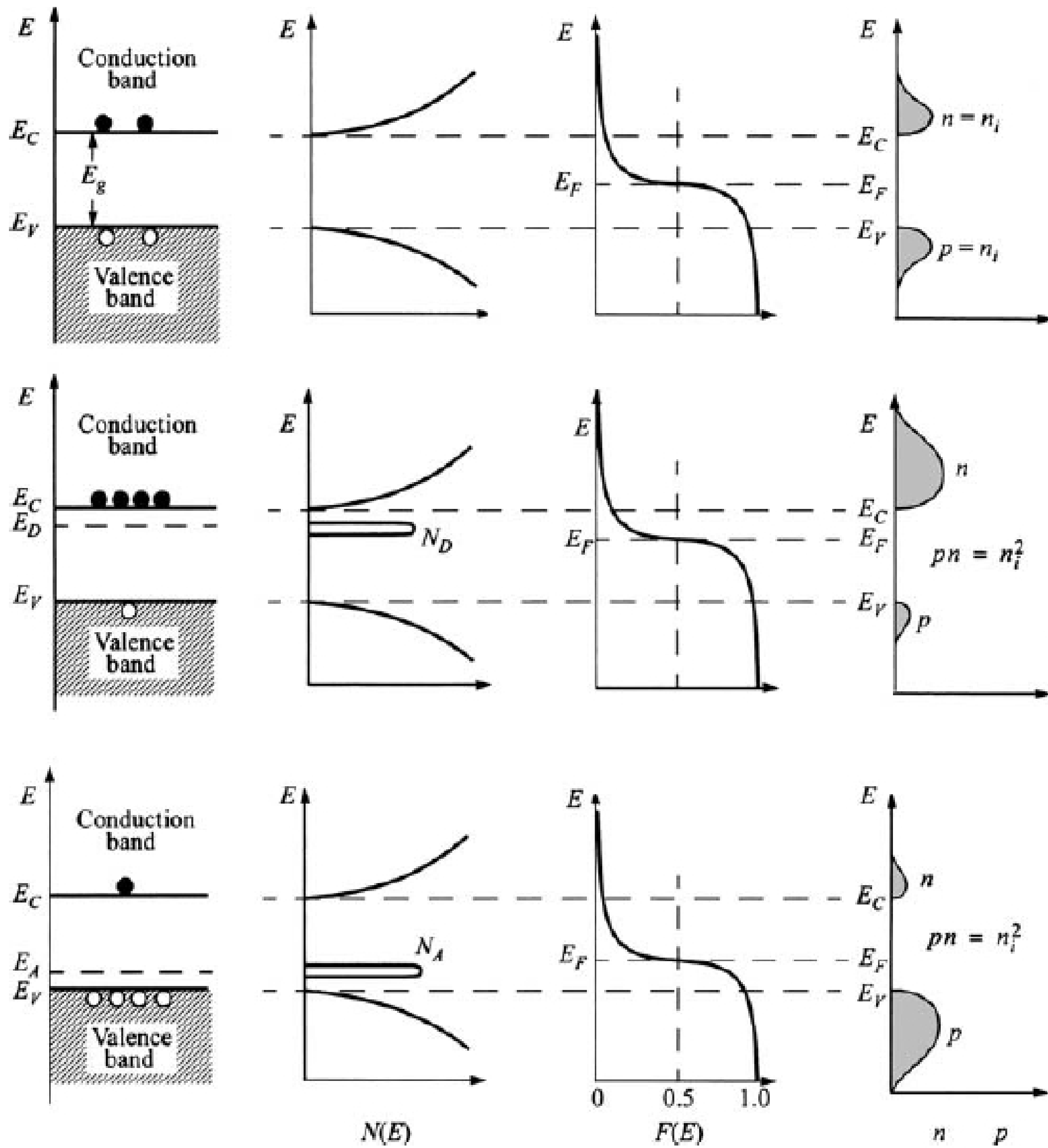

FIGURE B.5: Schematic band diagram, Density of states, Fermi distribution function, Carrier concentration for intrinsic, n-Type and p-Type semiconductor.

When the doping concentration is too high and the considerations concerning the non-degenerate conditions are not valid, the Fermi distribution can not be longer approximated and the electron density has to be integrated numerically. This condition is referred as degenerate semiconductor. Note that for very high doping concentration the Fermi levels can be above E_C or below E_F. Another important aspect is the reduction of the bandgap.

Another important aspect in the case of wide bandgap material, such as SiC or Diamond, is that at room temperature only a fraction of dopant atoms is ionized and consequently the complete ionization does not occur. However it is possible to consider the following

relationships, that describe the ionized concentration for donors N_D^+ and acceptors N_A^+:

$$N_D^+ = \frac{N_D^*}{1 + g_D \exp\left(\dfrac{E_C - E_D}{k_B T}\right)} \tag{B.25}$$

$$N_A^- = \frac{N_A^*}{1 + g_A \exp\left(\dfrac{E_A - E_V}{k_B T}\right)}, \tag{B.26}$$

where g_D is the ground-state degeneracy of the donor impurity level and equal to 2 because a donor level can accept one electron with either spin, while g_A is the ground-state degeneracy for acceptor level and equal 4 because each acceptor impurity level can accept one hole of either spin and the impurity level is doubly degenerate as a result of the two degenerate valence bands at $k = 0$ in most semiconductor.

Appendix C

Density of states $N(E)$

In a semiconductor, although the presence of a periodic potential of the nuclei, an electron in the conduction band can still be treated as a free electron, if the concept of electron effective mass is introduced:

$$m_e^* \equiv \left(\frac{d^2E}{dp^2}\right)^{-1} \tag{C.1}$$

using this approach, the solution of the Shröedinger equation, assuming to model the semiconductor as an infinite quantum well with a cubic shape and side L, can be written as sine and cosine functions:

$$\Psi = A\sin(k_x x) + B\cos(k_x x) \tag{C.2}$$

where the coefficients A and B have to be determined. This assumption does not affect the result since the density of states per unit volume should not depend on the actual size or shape of the semiconductor. The wave function must be zero at the infinite barriers of the well. At $x = 0$ the wave function must be zero so that only sine functions can be valid solutions or B must equal zero. At $x = L$, the wave function must also be zero yielding the following possible values for the wavenumber k_x:

$$k_x = \frac{n\pi}{L} \tag{C.3}$$

in which $n = 1, 2, 3....$ Repeating the same procedure also for the y and z direction, it's clear that each possible solution corresponds to a cube in k-space with size $n\pi/L$ as indicated in Fig.C.1. The total number of solutions with a different value for k_x, k_y and k_z and with a magnitude of the wavevector less than k is obtained by calculating the volume of one eighth of a sphere with radius k and dividing it by the volume corresponding to a single solution,$(\pi/L)^3$, yielding:

$$N = 2 \cdot \frac{1}{8} \cdot \left(\frac{L}{\pi}\right)^3 \cdot \frac{4}{3}\pi k^3 \tag{C.4}$$

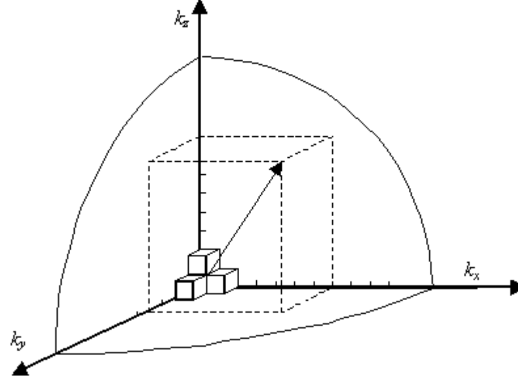

FIGURE C.1: Graphic representation of solutions in k-space.

where a factor two is added to take into account the two possible spins of each solution. The density per unit energy is then:

$$\frac{dN}{dE} = \frac{dN}{dk}\frac{dk}{dE} = \left(\frac{L}{\pi}\right)^3 \pi k^2 \frac{dk}{dE} \tag{C.5}$$

The kinetic energy E of a particle with mass m^* is related to the wavenumber, k, by:

$$E(k) = \frac{\hbar^2 k^2}{2m_e^*} \tag{C.6}$$

Consequently k is:

$$k = \frac{\sqrt{2m_e^* E}}{\hbar} \tag{C.7}$$

providing that:

$$\frac{dk}{dE} = \frac{m_e^*}{\hbar^2 k} \tag{C.8}$$

Finally the density of states per unit volume and per unit energy, $N(E)$, becomes:

$$N(E) = \frac{1}{L^3}\frac{dN}{dE} = \frac{8\pi\sqrt{2}}{h^3}(m_e^*)^{3/2}\sqrt{E} \tag{C.9}$$

for $E \geq 0$. The density of states is zero at the bottom of the well as well as for negative energies. The minimum energy of the electron is the energy at the bottom of the conduction band, called E_C, so that the density of states for electrons in the conduction band is given by:

$$N_C(E) = \frac{8\pi\sqrt{2}}{h^3}(m_e^*)^{3/2}\sqrt{E - E_C} \tag{C.10}$$

Similarly the density of states for holes in the valence band is given by:

$$N_V(E) = \frac{8\pi\sqrt{2}}{h^3}(m_h^*)^{3/2}\sqrt{E_V - E} \tag{C.11}$$

Bibliography

[1] Actual CXRO web sites, [Online]. Available:
henke.lbl.gov , 2017.

[2] Actual eSTATR web sites, [Online]. Available:
https://www.nist.gov/pml/stopping-power-range-tables-electrons-protons-and-helium-ions , 2017.

[3] Actual SRIM web sites, [Online]. Available:
www.srim.org , 2017.

[4] Actual Amptek web sites, [Online]. Available:
http://www.amptek.com/products/mini-x-ray-tube/ , 2017.

[5] Actual SiCILIA web sites, [Online]. Available:
www.tifpa.infn.it/projects/sicilia/ , 2017.

[6] Andò, L., Torrisi, L., Gammino, S., Beltrano, J., Percolla, C., and Parasole, O. Laser ion source for multiple ta ion implantation. In *Plasma Production by Laser Ablation* (2004), pp. 142–148.

[7] Atalay, B., Kenar, N., and Demir, A. Conversion efficiency calculations for euv radiation emitted from laser-produced tin plasmas. *Turkish Journal of Physics 33*, 6 (2010), 363–369.

[8] Badziak, J., Parys, P., Wolowski, J., Hora, H., Krasa, J., Laska, L., and Rohlena, K. Fast ion generation by a picosecond high-power laser. *Optica Applicata 35*, 1 (2005).

[9] Bakshi, V. *EUV sources for lithography*, vol. 149. SPIE press, 2006.

[10] Beg, F., Bell, A., Dangor, A., Danson, C., Fews, A., Glinsky, M., Hammel, B., Lee, P., Norreys, P., and Tatarakis, M. A study of picosecond laser–solid interactions up to 10^{19} w cm^{-2}. *Physics of plasmas 4*, 2 (1997), 447–457.

[11] Berger, M. J., Coursey, J., Zucker, M., and Chang, J. *Stopping-power and range tables for electrons, protons, and helium ions.* NIST Physics Laboratory Gaithersburg, MD, 1998.

[12] Bertuccio, G., Caccia, S., Puglisi, D., and Macera, D. Advances in silicon carbide x-ray detectors. *Nuclear Instruments and Methods in Physics Research Section A: Accelerators, Spectrometers, Detectors and Associated Equipment 652*, 1 (2011), 193–196.

[13] Bertuccio, G., and Casiraghi, R. Study of silicon carbide for x-ray detection and spectroscopy. *IEEE Transactions on Nuclear Science 50*, 1 (2003), 175–185.

[14] Bollanti, S., Albertano, P., Belli, M., Di Lazzaro, P., Faenov, A. Y., Flora, F., Giordano, G., Grilli, A., Ianzini, F., Kukhlevsky, S., et al. Soft x-ray plasma source for atmospheric-pressure microscopy, radiobiology and other applications. *NUOVO CIMENTO-SOCIETA ITALIANA DI FISICA SEZIONE D 20* (1998), 1685–1702.

[15] Borca, V. C., Pasquino, M., Russo, G., Grosso, P., Cante, D., Sciacero, P., Girelli, G., Porta, M. R. L., and Tofani, S. Dosimetric characterization and use of gafchromic ebt3 film for imrt dose verification. *Journal of applied clinical medical physics 14*, 2 (2013), 158–171.

[16] Bruzzi, M., Nava, F., Pini, S., and Russo, S. High quality sic applications in radiation dosimetry. *Applied surface science 184*, 1 (2001), 425–430.

[17] Calcagno, L., Musumeci, P., Zimbone, M., and La Via, F. Laser plasma monitored by silicon carbide detectors. *Radiation Effects and Defects in Solids 170*, 4 (2015), 303–324.

[18] Cannavò, A., and Torrisi, L. Sic detectors for radiation sources characterization and fast plasma diagnostic. *Journal of Instrumentation 11*, 09 (2016), C09005.

[19] Castaldini, A., Cavallini, A., Rigutti, L., Nava, F., Ferrero, S., and Giorgis, F. Deep levels by proton and electron irradiation in 4h–sic. *Journal of applied physics 98*, 5 (2005), 053706.

[20] Charpak, G., Rahm, D., and Steiner, H. Some developments in the operation of multiwire proportional chambers. *Nuclear Instruments and Methods 80*, 1 (1970), 13–34.

[21] Chen, X., Li, X., Ma, Y., Wu, Z., Li, J., and Zhu, W. Optimization of a femtosecond laser generated x-ray source for pulsed radiography. *Nuclear Instruments and Methods in Physics Research Section A: Accelerators, Spectrometers, Detectors and Associated Equipment 806* (2016), 378–382.

[22] Cheung, R. *Silicon carbide microelectromechanical systems for harsh environments.* World Scientific, 2006.

[23] Cirrone, G. A., Carpinelli, M., Cuttone, G., Gammino, S., Jia, S. B., Korn, G., Maggiore, M., Manti, L., Margarone, D., Prokupek, J., et al. Elimed, future hadrontherapy applications of laser-accelerated beams. *Nuclear Instruments and Methods in Physics Research Section A: Accelerators, Spectrometers, Detectors and Associated Equipment 730* (2013), 174–177.

[24] Clark, E., Krushelnick, K., Zepf, M., Beg, F., Tatarakis, M., Machacek, A., Santala, M., Watts, I., Norreys, P., and Dangor, A. Energetic heavy-ion and proton generation from ultraintense laser-plasma interactions with solids. *Physical Review Letters 85*, 8 (2000), 1654.

[25] Cowley, A., and Sze, S. Surface states and barrier height of metal-semiconductor systems. *Journal of Applied Physics 36*, 10 (1965), 3212–3220.

[26] Cutroneo, M., Malinsky, P., Mackova, A., Matousek, J., Torrisi, L., Slepicka, P., and Ullschmied, J. Ta-ion implantation induced by a high-intensity laser for plasma diagnostics and target preparation. *Nuclear Instruments and Methods in Physics Research Section B: Beam Interactions with Materials and Atoms 365* (2015), 384–388.

[27] De Boer, S., Beddar, A., and Rawlinson, J. Optical filtering and spectral measurements of radiation-induced light in plastic scintillation dosimetry. *Physics in Medicine and Biology 38*, 7 (1993), 945.

[28] De Napoli, M., Raciti, G., Rapisarda, E., and Sfienti, C. Light ions response of silicon carbide detectors. *Nuclear Instruments and Methods in Physics Research Section A: Accelerators, Spectrometers, Detectors and Associated Equipment 572*, 2 (2007), 831–838.

[29] Diver, D. A plasma formulary for physics. *Technology and Astrophysics (Hoboken, New Jersey: John Wiley)* (2001).

[30] Doyle, J., Linnarsson, M. K., Pellegrino, P., Keskitalo, N., Svensson, B., Schöner, A., Nordell, N., and Lindström, J. Electrically active point defects in n-type 4 h–sic. *Journal of applied physics 84*, 3 (1998), 1354–1357.

[31] Fernández, S. D. S., García-Salcedo, R., Mendoza, J. G., Sánchez-Guzmán, D., Rodríguez, G. R., Gaona, E., and Montalvo, T. R. Thermoluminescent characteristics of lif: Mg, cu, p and caso 4: Dy for low dose measurement. *Applied Radiation and Isotopes 111* (2016), 50–55.

[32] Gammino, S., Torrisi, L., Andò, L., Ciavola, G., Celona, L., Laska, L., Krasa, J., Pfeifer, M., Rohlena, K., Woryna, E., et al. Production of low energy, high intensity metal ion beams by means of a laser ion source. *Review of scientific instruments 73*, 2 (2002), 650–653.

[33] Gammino, S., Torrisi, L., Consoli, F., Margarone, D., Celona, L., and Ciavola, G. Perspectives for the eclisse method with third generation ecris. *Radiation Effects & Defects in Solids 163*, 4-6 (2008), 277–286.

[34] Ghergherehchi, M., Afarideh, H., Ghanadi, M., Mohammadzadeh, A., and Esmaeilnezhad, M. Proton beam dosimetry by cr-39 track-etched detector. *Iranian Journal of Radiation Research 6*, 3 (2008), 113–120.

[35] Giuffrida, L., and Torrisi, L. Post-acceleration of ions from the laser-generated plasma. *Nukleonika 56* (2011), 161–163.

[36] Giulietti, D., and Gizzi, L. A. X-ray emission from laser-produced plasmas. *La Rivista del Nuovo Cimento (1978-1999) 21*, 10 (1998), 1–93.

[37] Griem, H. Plasma spectroscopy, chap. 6, 1964.

[38] Hamamatsu Photonics, K. Photomultiplier tubes: Basics and applications. *Edition 3a 310* (2007).

[39] Hasselkamp, D. Secondary emission of electrons by ion impact on surfaces. *Comments At. Mol. Phys 21* (1988), 241–255.

[40] Henke, B. L., Gullikson, E. M., and Davis, J. C. X-ray interactions: photoabsorption, scattering, transmission, and reflection at e= 50-30,000 ev, z= 1-92. *Atomic data and nuclear data tables 54*, 2 (1993), 181–342.

[41] Izzo, G., Litrico, G., Severino, A., Foti, G., La Via, F., and Calcagno, L. Defects in high energy ion irradiated 4h-sic. In *Materials Science Forum* (2009), vol. 615, Trans Tech Publ, pp. 397–400.

[42] Kemerley, R. T., Wallace, H. B., and Yoder, M. N. Impact of wide bandgap microwave devices on dod systems. *Proceedings of the IEEE 90*, 6 (2002), 1059–1064.

[43] Khan, F. M. *The physics of radiation therapy.* Lippincott Williams & Wilkins, 2010.

[44] Knoll, G. F. *Radiation detection and measurement.* John Wiley & Sons, 2010.

[45] Kordina, O., Hallin, C., Henry, A., Bergman, J., Ivanov, I., Ellison, A., Son, N. T., and Janzén, E. Growth of sic by "hot-wall" cvd and htcvd. *physica status solidi (b) 202*, 1 (1997), 321–334.

[46] Kramida, A., Yu. Ralchenko, Reader, J., and and NIST ASD Team. NIST Atomic Spectra Database (ver. 5.3), [Online]. Available: http://physics.nist.gov/asd [2017, July 31]. National Institute of Standards and Technology, Gaithersburg, MD., 2015.

[47] Láska, L., Cavallaro, S., Jungwirth, K., Krása, J., Krouskỳ, E., Margarone, D., Mezzasalma, A., Pfeifer, M., Rohlena, K., Ryć, L., et al. Experimental studies of emission of highly charged au-ions and of x-rays from the laser-produced plasma at high laser intensities. *The European Physical Journal D-Atomic, Molecular, Optical and Plasma Physics 54*, 2 (2009), 487–492.

[48] Lees, J., Bassford, D., Fraser, G., Horsfall, A., Vassilevski, K., Wright, N., and Owens, A. Semi-transparent sic schottky diodes for x-ray spectroscopy. *Nuclear Instruments and Methods in Physics Research Section A: Accelerators, Spectrometers, Detectors and Associated Equipment 578*, 1 (2007), 226–234.

[49] Lotz, W. An empirical formula for the electron-impact ionization cross-section. *Zeitschrift für Physik A Hadrons and Nuclei 206*, 2 (1967), 205–211.

[50] Lotz, W. Electron binding energies in free atoms. *JOSA 60*, 2 (1970), 206–210.

[51] Lucas, G., and Pizzagalli, L. Ab initio molecular dynamics calculations of threshold displacement energies in silicon carbide. *Physical Review B 72*, 16 (2005), 161202.

[52] Mayer, J. W., and Rimini, E. *Ion beam handbook for material analysis*. Elsevier, 2012.

[53] Mazzillo, M., Condorelli, G., Castagna, M. E., Catania, G., Sciuto, A., Roccaforte, F., and Raineri, V. Highly efficient low reverse biased 4h-sic schottky photodiodes for uv-light detection. *IEEE Photonics Technology Letters 21*, 23 (2009), 1782–1784.

[54] Mazzillo, M., Sciuto, A., Catania, G., Roccaforte, F., and Raineri, V. Temperature and light induced effects on the capacitance of 4h-sic schottky photodiodes. *IEEE Sensors Journal 12*, 5 (2012), 1127–1130.

[55] Moser, S., Harder, W., Hurlbut, C., and Kusner, M. Principles and practice of plastic scintillator design. *Radiation Physics and Chemistry 41*, 1-2 (1993), 31–36.

[56] Musumeci, P., Cutroneo, M., Torrisi, L., Velyhan, A., Zimbone, M., and Calcagno, L. Silicon carbide detectors for diagnostics of ion emission from laser plasmas. *Physica Scripta 2014*, T161 (2014), 014021.

[57] Nigam, S., Kim, J., Ren, F., Chung, G., MacMillan, M., Dwivedi, R., Fogarty, T., Wilkins, R., Allums, K., Abernathy, C., et al. High energy proton irradiation effects on sic schottky rectifiers. *Applied physics letters 81*, 13 (2002), 2385–2387.

[58] Oliveira, M. L. d., Maia, A. F., Nascimento, N. C. d. E. S., Fragoso, M. d. C. d. F., Galindo, R. S., and Hazin, C. A. Influence of thermoluminescent dosimeters energy dependence on the measurement of entrance skin dose in radiographic procedures. *Radiologia Brasileira 43*, 2 (2010), 113–118.

[59] ORTEC, E. Experiments in nuclear science. *AN34* (1998).

[60] Palmour, J., Kong, H., and Davis, R. High-temperature depletion-mode metal-oxide-semiconductor field-effect transistors in beta-sic thin films. *Applied physics letters 51*, 24 (1987), 2028–2030.

[61] Raineri, V., Roccaforte, F., Libertino, S., Ruggiero, A., Massimino, V., and Calcagno, L. Correlation between leakage current and ion-irradiation induced defects in 4h-sic schottky diodes. In *Materials science forum* (2006), vol. 527, Trans Tech Publ, pp. 1167–1170.

[62] Robinson, A., Zepf, M., Kar, S., Evans, R., and Bellei, C. Radiation pressure acceleration of thin foils with circularly polarized laser pulses. *New journal of Physics 10*, 1 (2008), 013021.

[63] Roccaforte, F., La Via, F., Raineri, V., Calcagno, L., and Musumeci, P. Improvement of high temperature stability of nickel contacts on n-type 6h–sic. *Applied surface science 184*, 1 (2001), 295–298.

[64] Rubenchick, A., and Witkowsky, S. Handbook of plasma physics, 1991.

[65] Ryć, L., Dobrzański, L., Dubecký, F., Pfeifer, M., Pura, B., Riesz, F., and Słysz, W. Fast semiconductor detectors for detection of x-ray emission from plasmas.

[66] Ryc, L., Dubecky, F., Pfeifer, M., Pura, B., Riesz, F., and Slysz, W. Evaluation of gaas and inp msm detectors for detection of pulsed x-ray emission from laser plasmas. In *Semiconducting and Insulating Materials, 2002. SIMC-XII-2002. 12th International Conference on*, IEEE, pp. 280–283.

[67] Saha, M. N. On a physical theory of stellar spectra. *Proceedings of the Royal Society of London. Series A, Containing Papers of a Mathematical and Physical Character 99*, 697 (1921), 135–153.

[68] Schou, J. Secondary-electron emission from solids by electron and proton-bombardment. *Scanning Microscopy* (1988).

[69] Sciuto, A., Mazzillo, M. C., Di Franco, S., Mannino, G., Badalà, P., Renna, L., and Caruso, C. Uv-a sensor based on 6h-sic schottky photodiode. *IEEE Photonics Journal 9*, 1 (2017), 1–10.

[70] Sciuto, A., Torrisi, L., Cannavò, A., Ceccio, G., Musumeci, P., Mazzillo, M., and Calcagno, L. Sic interdigit detectors for post-accelerated ions generated by laser plasma. *Vacuum 131* (2016), 170–175.

[71] Sinenian, N., Rosenberg, M., Manuel, M., McDuffee, S., Casey, D., Zylstra, A., Rinderknecht, H., Gatu Johnson, M., Séguin, F., Frenje, J., et al. The response of cr-39 nuclear track detector to 1–9 mev protons. *Review of Scientific Instruments 82*, 10 (2011), 103303.

[72] Spencer, I., Ledingham, K., Singhal, R., McCanny, T., McKenna, P., Clark, E., Krushelnick, K., Zepf, M., Beg, F., Tatarakis, M., et al. Laser generation of proton beams for the production of short-lived positron emitting radioisotopes. *Nuclear Instruments and Methods in Physics Research Section B: Beam Interactions with Materials and Atoms 183*, 3 (2001), 449–458.

[73] Spohr, R. *Ion tracks and microtechnology: principles and applications.* Reimar Spohr, 1990.

[74] Staub, H. H. Detection methods. *Experimental nuclear physics 1* (1953), 1–165.

[75] Sze, S. M., and Ng, K. K. *Physics of semiconductor devices.* John wiley & sons, 2006.

[76] Takeyasu, N., Hirakawa, Y., and Imasaka, T. Elemental analysis using hard x-ray emission from a laser-produced plasma, induced by a femtosecond laser pulse. *Review of scientific instruments 72*, 10 (2001), 3940–3942.

[77] Tan, T., McCall, G., and Williams, A. Determination of laser intensity and hot-electron temperature from fastest ion velocity measurement on laser-produced plasma. *The Physics of fluids 27*, 1 (1984), 296–301.

[78] Toossi, M. B., Khorshidi, F., Ghorbani, M., Mohamadian, N., and Davenport, D. Comparison of ebt and ebt3 radiochromic film usage in parotid cancer radiotherapy. *Journal of biomedical physics & engineering 6*, 1 (2016), 1.

[79] Torrisi, L. Luminescence degrading in polyvinyltoluene by ion beam irradiations. *Radiation effects and defects in solids 154*, 2 (2001), 89–98.

[80] Torrisi, L. Radiation damage in polyvinyltoluene (pvt). *Radiation Physics and Chemistry 63*, 1 (2002), 89–92.

[81] Torrisi, L. Ion energy enhancement from tnsa plasmas obtained from advanced targets. *Laser and Particle Beams 32*, 3 (2014), 383–389.

[82] Torrisi, L. Ion acceleration from intense laser-generated plasma: methods, diagnostics and possible applications. *Nukleonika 60*, 2 (2015), 207–212.

[83] Torrisi, L. Coulomb-boltzmann-shifted distribution in laser-generated plasmas from 10^{10} up to 10^{19} w/cm^2 intensities. *Radiation Effects and Defects in Solids 171*, 1-2 (2016), 34–44.

[84] Torrisi, L., Calcagno, L., Cutroneo, M., Badziak, J., Rosinski, M., Zaras-Szydlowska, A., and Torrisi, A. Nanostructured targets for tnsa laser ion acceleration. *Nukleonika 61*, 2 (2016), 103–108.

[85] Torrisi, L., and Cannavò, A. Sic detector damage and characterization for high intensity laser-plasma diagnostics. *Journal of Instrumentation 11*, 05 (2016), P05009.

[86] Torrisi, L., and Cannavò, A. Silicon carbide for realization of "telescope" ion detectors. *IEEE Transactions on Electron Devices 63*, 11 (2016), 4445–4451.

[87] Torrisi, L., Caridi, F., Giuffrida, L., Torrisi, A., Mondio, G., Serafino, T., Caltabiano, M., Castrizio, E., Paniz, E., and Salici, A. Lamqs analysis applied to ancient egyptian bronze coins. *Nuclear Instruments and Methods in Physics Research Section B: Beam Interactions with Materials and Atoms 268*, 10 (2010), 1657–1664.

[88] Torrisi, L., Caridi, F., Margarone, D., Picciotto, A., Mangione, A., and Beltrano, J. Carbon-plasma produced in vacuum by 532nm–3ns laser pulses ablation. *Applied surface science 252*, 18 (2006), 6383–6389.

[89] Torrisi, L., Caridi, F., Picciotto, A., and Borrielli, A. Energy distribution of particles ejected by laser-generated aluminium plasma. *Nuclear Instruments and Methods in Physics Research Section B: Beam Interactions with Materials and Atoms 252*, 2 (2006), 183–189.

[90] Torrisi, L., Cavallaro, S., Cutroneo, M., Giuffrida, L., Krasa, J., Margarone, D., Velyhan, A., Kravarik, J., Ullschmied, J., Wolowski,

J., ET AL. Monoenergetic proton emission from nuclear reaction induced by high intensity laser-generated plasma a. *Review of Scientific Instruments 83*, 2 (2012), 02B111.

[91] TORRISI, L., CAVALLARO, S., ROSIŃSKI, M., NASSISI, V., PAPERNY, V., AND ROMANOV, I. Post acceleration of ions emitted from laser and spark-generated plasmas. *Nukleonika 57* (2012), 323–332.

[92] TORRISI, L., CUTRONEO, M., CALCAGNO, L., ROSINSKI, M., AND ULLSCHMIED, J. Tnsa ion acceleration at 1016 w/cm2 sub-nanosecond laser intensity. In *Journal of Physics: Conference Series* (2014), vol. 508, IOP Publishing, p. 012002.

[93] TORRISI, L., CUTRONEO, M., CECCIO, G., CANNAVÒ, A., BATANI, D., BOUTOUX, G., JAKUBOWSKA, K., AND DUCRET, J. Near monochromatic 20 me v proton acceleration using fs laser irradiating au foils in target normal sheath acceleration regime. *Physics of Plasmas 23*, 4 (2016), 043102.

[94] TORRISI, L., DESIDERIO, A., AND FOTI, G. High energy proton induced luminescence in f-doped polyvinyltoluene. *Nuclear Instruments and Methods in Physics Research Section B: Beam Interactions with Materials and Atoms 166* (2000), 664–668.

[95] TORRISI, L., FOTI, G., GIUFFRIDA, L., PUGLISI, D., WOLOWSKI, J., BADZIAK, J., PARYS, P., ROSINSKI, M., MARGARONE, D., KRASA, J., ET AL. Single crystal silicon carbide detector of emitted ions and soft x rays from power laser-generated plasmas. *Journal of Applied Physics 105*, 12 (2009), 123304.

[96] TORRISI, L., GAMMINO, S., AND ANDÒ, L. Non-equilibrium plasma production by pulsed laser ablation of gold. *Radiation effects and defects in solids 158*, 11-12 (2003), 757–769.

[97] TORRISI, L., GAMMINO, S., ANDÒ, L., AND LASKA, L. Tantalum ions produced by 1064 nm pulsed laser irradiation. *Journal of Applied Physics 91*, 7 (2002), 4685–4692.

[98] TORRISI, L., GAMMINO, S., ANDÒ, L., LASKA, L., KRASA, J., ROHLENA, K., ULLSCHMIED, J., WOLOWSKI, J., BADZIAK, J., AND PARYS, P. Equivalent ion temperature in ta plasma produced by high energy laser ablation. *Journal of applied physics 99*, 8 (2006), 083301.

[99] TORRISI, L., GAMMINO, S., ANDO, L., TORRISI, L., MEZZASALMA, A., BADZIAK, J., PARYS, P., WOLOWSKI, J., WORYNA, E., JUNGWIRTH, K., ET AL. Study of the etching process and crater formation induced by intense laser pulses at pals. *CZECHOSLOVAK JOURNAL OF PHYSICS 52* (2002), 329–334.

[100] Torrisi, L., Giuffrida, L., Cutroneo, M., Cirrone, P., Picciotto, A., Krasa, J., Margarone, D., Velyhan, A., Laska, L., Ullschmied, J., et al. Proton emission from thin hydrogenated targets irradiated by laser pulses at 1016 w/cm2 a. *Review of scientific instruments 83*, 2 (2012), 02B315.

[101] Torrisi, L., Giuffrida, L., Rosinski, M., and Schallhorn, C. Ge and ti post-ion acceleration from laser ion source. *Nuclear Instruments and Methods in Physics Research Section B: Beam Interactions with Materials and Atoms 268*, 17 (2010), 2808–2814.

[102] Torrisi, L., and Margarone, D. Investigations on pulsed laser ablation of sn at 1064 nm wavelength. *Plasma Sources Science and Technology 15*, 4 (2006), 635.

[103] Torrisi, L., Sciuto, A., Calcagno, L., Musumeci, P., Mazzillo, M., Ceccio, G., and Cannavò, A. Laser-plasma x-ray detection by using fast 4h-sic interdigit and ion collector detectors. *Journal of Instrumentation 10*, 07 (2015), P07009.

[104] Torrisi, L., Sciuto, A., Cannavò, A., Di Franco, S., Mazzillo, M., Badalà, P., and Calcagno, L. Sic detector for sub-mev alpha spectrometry. *Journal of Electronic Materials* (2017), 1–8.

[105] Van Zeghbroeck, B. Principles of electronic devices. *University of Colorado* (2011).

[106] Wachulak, P., Bartnik, A., Fiedorowicz, H., Kostecki, J., Jarocki, R., Szczurek, M., Szczurek, A., Feigl, T., and Pina, L. Nanoscale imaging using a compact laser plasma euv source. In *AIP Conference Proceedings* (2012), vol. 1437, AIP, pp. 79–82.

[107] Woryna, E., Parys, P., Wołowski, J., and Mroz, W. Corpuscular diagnostics and processing methods applied in investigations of laser-produced plasma as a source of highly ionized ions. *Laser and Particle beams 14*, 3 (1996), 293–321.

[108] Zat'ko, B., Dubecký, F., Boháček, P., Nečas, V., and Ryć, L. Detection of soft x-rays using semi-insulating gaas detector. In *Advanced Semiconductor Devices & Microsystems (ASDAM), 2010 8th International Conference on* (2010), IEEE, pp. 219–222.

[109] Zhang, Y., Milbrath, B. D., Weber, W. J., Elfman, M., and Whitlow, H. J. Radiation detector resolution over a continuous energy range. *Applied Physics Letters 91*, 9 (2007), 094105.

[110] Zhao, J. H., Sheng, K., and Lebron-Velilla, R. C. Silicon carbide schottky barrier diode. *International journal of high speed electronics and systems 15*, 04 (2005), 821–866.

[111] Ziegler, J. F., Biersack, J., and Littmark, U. The stopping and range of ions in matter, vol. 1. *1, Pergamon Press, New York* (1985).

[112] Ziegler, J. F., Ziegler, M. D., and Biersack, J. P. Srim–the stopping and range of ions in matter (2010). *Nuclear Instruments and Methods in Physics Research Section B: Beam Interactions with Materials and Atoms 268*, 11 (2010), 1818–1823.